Strongly Nonlinear Internal Waves in Near Two-Layer Stratifications: Generation, Propagation and Self-induced Shear Instabilities

Roxana Tiron

A dissertation submitted to the faculty of the University of North Carolina at Chapel Hill in partial fulfillment of the requirements for the degree of Doctor of Philosophy in the Department of Mathematics.

Chapel Hill
2009

Approved by

Advisor: Roberto Camassa
Reader: David Adalsteinsson
Reader: M. Gregory Forest
Reader: Richard M. McLaughlin
Reader: Brian L. White

ABSTRACT

ROXANA TIRON: Strongly Nonlinear Internal Waves in Near Two-Layer Stratifications: Generation, Propagation and Self-induced Shear Instabilities

(Under the direction of Roberto Camassa)

This thesis consists of three parts. In the first part, periodic travelling-wave solutions for a strongly nonlinear asymptotic model of long internal wave propagation in an Euler incompressible two-fluid system are derived and extensively analyzed. The class of waves with a prescribed mean elevation, and zero-average momentum and volume flux is studied in detail. We found that the domain of existence of these periodic waves contains that of their Euler solution counterparts as a subset, and the agreement is good on the common domain. Among other findings, the model predicts the existence of periodic waves of substantially larger amplitudes than those of limiting solitary waves. This is relevant for modeling realistic oceanic internal waves, which often occur in wavetrains with multiple peaks.

The second part consists of optimizing a two-layer system to approximate a continuously stratified one. This work aims at extending the applicability of two-layer asymptotic models. The strategy is validated by comparing long solitary wave numerical solutions in continuous stratification against their two-layer asymptotic counterparts.

The third part is a numerical study of the shear instability induced by internal solitary waves in near two-layer stratifications. We emulate numerically the generation of solitary wave in the experiments of [19], by using a variable density Navier Stokes solver [1]. We validate the numerical code by comparison against strongly nonlinear model [7], optimally adjusted for finite-width pycnocline developed in the second part. While the general dynamical features reported in [19] emerge from the simulations, there are significant discrepancies, which seem resolvable only by further laboratory work. Good agreement is however obtained for the self-induced shear instability for large waves. To assess whether this is an intrinsic property of the wave or an effect of the generation technique, we study the evolution of stationary solutions of Euler equations, found with a variant of the algorithm in [51]. We determine local stability characteristics and construct an amplitude threshold for manifestation of the instability. We discuss the implication of locally unstable shear for the global stability properties of traveling wave solutions.

Tatălui meu, Doru

ACKNOWLEDGEMENTS

First and foremost I want to express my deepest gratitude to my advisor, Dr. Roberto Camassa. Without his patience and encouragement through many of my self-doubt crisis this thesis wouldn't have been written. I found in Dr. Camassa a great role model, both as a scientist and as a human being. I feel really fortunate to have had the opportunity to work under his supervision. His rather unique mix of skepticism and excitement, that insatiable urge to continue to ask questions when, many times, I was feeling that I have reached the bottom of the problem at hand were truly inspirational and changed profoundly the way I view and approach science.

I also wanted to thank the members of my committee for all the suggestions they gave me in writing this thesis. I am greatly indebted to the entire applied math faculty and also to Dr. Patrick Eberlein, Dr. Michael Taylor and Dr. Mark Williams from which I took several courses in pure math. I have learned so much in my experience here at UNC, and their guidance was priceless. I want to thank Dr. Sorin Mitran for his sound advice in moments I needed it the most.

In my past experience as an undergraduate student at "Politehnica" University of Bucharest, I have had great mentors and professors, to whom I owe a great deal, especially Dr. Sterian Dănăilă and Dr. Marius Stoia-Djeska. I have the outmost respect and admiration for their commitment to do science in the difficult and shifting circumstances in my home country.

I am very grateful to Dr. Ann Almgren for her invaluable help with the numerical work and to Dr. Wooyoung Choi for illuminating discussions. I would also want to thank Dr. Avadh Saxena, who kindly hosted me during a summer internship at LANL and suggested one of the subjects of this thesis. During my stay at LANL, I had many useful discussions with Dr. Cory Hauck, for which I thank him.

For data analysis, I have used extensively DataTank. I thank its creator, Dr. David Adalsteinsson for all his help.

I also would like to thank the University of North Carolina at Chapel Hill, the UNC-CH Math Department, the Carolina Center for Interdisciplinary Applied Mathematics, and the following grants for financial support during my years at UNC: DMS-0509423 and CMG-0620687.

Teaching at UNC has been a rewarding and unforgettable experience. I thank Prof. Mark McCombs and Dr. Debra Ethridge for their wholehearted help and advice.

I would also like to thank the one that has been like a motherly figure for all us graduate students - Ms. Brenda Bethea. She has been always kind, always helpful even though I have always approached her at the last moment.

Dear Andrew, I wouldn't had achieved this without you. You have been my best friend, my family away from home. In the last few months, you have been feeding me, encouraging me, scolding me when I was tempted to renounce. I will always be grateful and I thank you from the bottom of my heart. I can only hope I will be for you the friend you have been for me.

My dear colleagues, office-mates and above all friends, Jen and Joyce, you have been such a support and inspiration for me. I will miss you very much, as I will miss all my friends here at UNC: Indrani, Christy, Longhua, Claudio, Martina to name a few.

At last but not at least, I thank my family for loving and supporting me no matter what, for believing in me in spite of my own doubts.

Dragele mele dragi, mama şi Ralu, vouă vă datorez saltul peste Atlantic. M-aţi împins (la început împotriva voinţei mele) să îmi urmez un vis - acela de a deveni un om de ştiinţă. Mai am mult până la a-mi îndeplini visul, dar acum sunt mai aproape cu un pas, şi vă mulţumesc din suflet.

Dragă tati, nu ştiu unde şi dacă eşti, dar ştiu ca o bucată din tine este în sufletul nostru. Blândeţea şi principialitea ta o voi purta cu mine mereu. Tare aş fi vrut să iţi spun: "Tata, sunt domnişoara doctor acum!". N-am apucat (şi eram atât de aproape) dar ştiu că tu nu aveai cea mai mică urmă de îndoială că o să reuşesc pentru că tu întotdeauna ai avut încredere în noi. Mereu spuneai că nu vrei ca fetele tale sa fie inginere. Nu te-am ascultat noi la început, dar iată că mai întâi Ralu, şi acum şi eu, am deviat un pic. Teza aceasta îţi este dedicată ţie, cu toată dragostea.

CONTENTS

LIST OF TABLES

LIST OF FIGURES

CHAPTER 1

General introduction

Internal waves are an important feature of geophysical fluid dynamics, as stratification is an inherent component of near equilibrium states of ocean and atmosphere. In this work we focus on internal waves of the type pertinent to the oceanic case.

Because of the relatively low viscosities and small differences in densities in these environments, energy penalties paid by natural forcing agents such as tides and winds in displacing fluid parcels from equilibrium are also relatively small, which can result in internal wave motion of large amplitudes, as recent improvements in instrumentation and observational techniques in the ocean are continuously revealing (Helfrich & Melville [21]).

From the earliest in-situ observations (Helfrich & Melville [21]), it became evident that these waves are not dispersive, since their typical amplitudes are too large with respect to the overall vertical scale of the stratification. Furthermore, in the early 1960s to 1970s, satellite imagery (recording scattering of radar signals from short surface waves induced by the strong currents associated with internal wave motion) revealed that these waves are in fact common occurrence in the near coastal waters. Thus, understanding their generation, propagation and breaking is crucial in understanding the overall dynamics of coastal processes.

This thesis studies three problems concerning large amplitude wave propagation in either two-layer or near two-layer density stratifications, each of which is essentially self contained:

(1) existence of periodic solutions in two-layer fluids,

(2) extension of two-layer models, which offer analytical predictions, to continuously stratified fluids,

(3) stability of large amplitude continuously stratified internal waves.

In order to proceed, it is necessary to assume a number of simplifications, while striving to maintain all the relevant features of the phenomena which are the target of this investigation.

Simplifying assumptions

We argue that an inviscid model suffices to capture the essential dynamics of internal wave propagation in lab experiments (and, to a greater extent, in a stratified ocean) since the scales associated with internal waves are large, and consequently the Reynolds number is typically high (ranging from 10^5 for laboratory setups to 10^8 in the ocean). In the lab, as in the ocean, the density stratification is the direct consequence of diffusing quantities such as temperature and salinity. However, since the time scales associated with diffusion processes are far larger than the time scale of internal wave propagation, we also neglect diffusion. Finally, we restrict the upper surface (the "rigid lid" assumption) arguing that the surface signature of the internal waves is typically 10^3 smaller than the displacement of the pycnocline and moreover the scales associated with internal wave

motion are greatly exceeding the scales of the surface (barotropic) waves - Vlasenko *et al.* [53].

Organization

In the first part, Chapter 2, periodic travelling wave solutions for a strongly nonlinear model of long internal wave propagation in a two-fluid system are derived and extensively analyzed, with the aim of providing structure to the rich parametric space of existence for the parent Euler system. The waves propagate at the interface between two homogeneous-density incompressible fluids filling the two-dimensional domain between rigid planar boundaries. The class of waves with a prescribed mean elevation, chosen to coincide with the origin of the vertical axis (parallel to the gravity direction), and prescribed zero-average momentum and volume flux is studied in detail. The constraints are selected because of their physical interpretation in terms of possible processes of wave generation in wave-tanks, and give rise to a quadrature formula which is analyzed in parameter space with a combination of numerical and analytical tools. The resulting model solutions are compared with those computed numerically from the parent Euler two-layer system with a boundary element method. It is found that the parametric domain of existence of model periodic waves, determined analytically, contains the existence domain of their Euler solution counterparts as a subset. The model existence domain in the amplitude-speed (A, c) parameter plane is determined by two functions $c(A)$ corresponding to infinite period limiting cases of fronts (conjugate states) and solitary waves, respectively. The front boundary is exact and coincides with that of fronts for Euler solutions, while the solitary-wave boundary is a close approximation to its Euler counterpart. A third functional relation between c and A indicates where the Euler

solutions cease to exist within the model's domain. This is found to be related to the phenomenon of "overhanging" wave profiles, whereby the interface between the two fluids becomes a multiply defined function of the horizontal coordinate. The model existence domain is further partitioned in regions where the model is expected to provide accurate approximations to Euler solutions based on analytical estimates from the quadrature. The resulting predictions are found to be in good agreement with the numerical Euler solutions, as exhibited by several wave properties, including kinetic and potential energy, over a broad range of parameter values, extending to the limiting cases of critical depth ratio and extreme density ratios. In particular, when the period is sufficiently long, model solutions show that for a given supercritical speed waves of substantially larger amplitude than the limiting amplitude of solitary waves can exist, and are good approximations of the corresponding Euler solutions. This finding can be relevant for modeling field observations of oceanic internal waves, which often occur in wavetrains with multiple peaks. Results concerning solitary wave solutions on background currents of the strongly nonlinear model, which are essential in constructing the periodic solutions are presented in Appendix A and B, respectively.

In the second part, Chapter 3, we construct an optimal two-layer approximation for a continuously-stratified system. The motivation behind this endeavor is to extend the use of two-layer asymptotic models (which are notably easier to explore analytically) to more realistic stratifications, especially for wave motion of *large* amplitude. The proposed strategy is validated by comparing traveling wave solutions of Euler equations in continuous stratification, obtained with a variant of the algorithm proposed in Turkington *et al.* [51] (described in detail in Appendix C) to solutions of the strongly nonlinear model

for long wave motion in a two-layer system Choi & Camassa [7]. The model furnishes good estimates for *global* properties of the wave motion in continuous stratification - such as phase speed, kinetic and potential energy, and displacement of the average density isoline. In §3.5, we propose a strategy for the reconstruction of the eulerian velocity field.

The third part (Chapters 4 and 5) is concerned with the breaking mechanism of internal solitary waves in a near two-layer continuous stratification. There is extensive evidence that such waves break via shear instabilities Grue *et al.* [19], Helfrich & Melville [21]. We first replicate numerically the experiments in Grue *et al.* [19]. The time evolution of the solitary wave from a step function in density initial condition is simulated using a variable density Navier Stokes solver described in Almgren *et al.* [1]. The numerical code is validated by comparison against strongly nonlinear model Choi & Camassa [7], adjusted for finite width pycnocline. While the numerical simulations capture the general features of the actual experiments in Grue *et al.* [19], there are signicant discrepancies, which seem resolvable only by further laboratory work. Good agreement is however obtained for the self-induced shear instability for large waves. To assess whether this phenomenon is an intrinsic property of the wave or an effect of the generation technique, we study the evolution of stationary solutions of Euler equations. We determine local stability characteristics and construct an amplitude threshold for manifestation of the instability. We conclude that the shear instability is indeed an inherent feature of large amplitude waves in a near two layer stratification, independent of the generation technique; we also present numerical evidence of the convective nature of the instability. Finally, in Chapter 5, we briefly comment on the use the two layer approximation (optimized for including the presence of a pycnocline of finite width as described in Chapter 3)

to get an analytical handle on the study of the stability properties of solitary waves in continuous stratification.

CHAPTER 2

Nonlinear periodic waves in a two layer system

2.1. Introduction

In the following we focus on what is possibly the simplest set-up capable of supporting internal wave motion of arbitrary amplitude, that of a two-layer inviscid and incompressible fluid of homogenous densities between plates of infinite horizontal extent. Despite its long history in the literature, it is only somewhat recently that attention has been paid, by experimental and theoretical investigations (Grue *et al.* [19], Choi & Camassa [7]), to the large amplitude motion that can be attained in this configuration. Among other findings, these studies have shown that the long wave assumption in a two-layer system makes it possible to develop models which can describe solitary wave motion of arbitrary amplitude, and provide closed form solutions that compare favorably with laboratory experimental data under appropriate circumstances (Camassa *et al.* [8]). While solitary waves are of interest in many practical situations, e.g., in field studies (Duda *et al.* [12]), a more extensive test of model fidelity is offered by the class of periodic travelling wave motion, which includes that of solitary waves as a limiting case. In this study, we examine periodic wave train solutions for a class of long-wave asymptotic models developed in Miyata [39, 40], Choi & Camassa [6, 7], and establish the parametric range where such solutions can be considered valid approximations to those of the parent Euler equations. This is carried out by a direct comparison with numerical computations of both two-layer

and continuous stratification solutions of the Euler equations, through a variety of wave properties, such as wave profiles, fluids velocity, wave speed and amplitude, etc.

Unlike the case of a solitary wave, whose physical parameters can be linked in the form of boundary conditions to a far-field reference configuration of the fluid, a periodic travelling wave train admits a richer class of such parameters, generally related to the invariants of motion. Unfortunately, the highly idealized nature of periodicity extending for all space and time does not allow one to identify a preferred (minimal) set of parameters that determines a unique periodic wave train, given that the physical processes necessary for its generation, as well as the physically necessary transition to far-field reference states, are neglected in this idealization. This, of course, is an issue that transcends the case of internal waves. The choice of the most convenient physical quantities that determine a given wave train already presents itself in the study of periodic irrotational waves at the free surface of a *single* fluid layer. It is remarkable that for these waves such questions appear to have been settled only relatively recently, and this only in the context of waves symmetric around their crests (see Benjamin [3] for a proof of a long-standing conjecture on this issue formulated in Benjamin & Lighthill [4]).

With this in mind, in deriving periodic travelling wave solutions to the asymptotic model in Choi & Camassa [7], we first make the assumption that the mean thickness of the fluid layers is prescribed at the outset. This choice makes the connection with previous work on solitary waves somewhat more transparent and allows us to follow easily the model's solutions in the distinguished limits of infinitesimal wave amplitudes, where the long wave critical speed is naturally defined from the general Euler internal wave dispersion relation for a two-fluid system (Lamb [33]). We proceed, in §2.2 to solve

by quadratures the system of four ordinary differential equations (ODE'S) resulting from the travelling wave ansatz. In this process, we accumulate four integration constants, which are constants of motion in the *wave frame*. Thus, at least within the realm of these asymptotic models, the minimal number of physical invariant quantities determining a unique period wave train is four. The phase speed of the wave can then be determined by specifying some integral property of the wave (e.g., total horizontal momentum) in the *lab frame*. In §2.3, we establish relationships between relevant physical quantities associated with the periodic wave train and the four constants of integration in the quadrature. A subset of these relationships can be chosen to determine the quadrature's constants. In particular, we show that two of these constants can be given a natural physical interpretation in terms of volume fluxes in each layer, while the remaining two integration constants can be determined, for instance, by seeking an *a priori* imposed peak-to-trough amplitude and from the prescribed mean layer thickness.

We proceed, in §2.4, to construct a particular class of periodic waves which limits correctly to the infinitesimal amplitude waves for the quiescent reference state. The final result will be a two parameter family of periodic solutions (e.g., speed and amplitude which determine the period). In particular, our approach allows us to deal with the technical difficulties posed by the quadrature solution which in general leads to hyper-elliptic integrals (as opposed to elliptic integrals as in the case of solitary waves). We study the properties of the periodic solutions of this two parameter family in §2.5. In an effort to establish the limitations on model's validity range through its periodic travelling wave solutions, §2.6 presents comparisons with numerically computed solutions of

both two-layer and near two-layer *continuously* stratified periodic traveling wave Euler solutions.

We remark that the choice of invariant physical quantities determining a periodic travelling wave solution is by no means unique. In the literature, various alternatives to the assumption of fixed mean level have been considered, and ultimately the issue of which among these is preferable must be related to the physical process by which (locally) periodic travelling wave trains are generated. We discuss some of these alternatives and their connection to our primary choice in §2.7.

The study of the limiting cases of solitary waves and fronts is fundamental to our construction of periodic solutions and it is interesting in its own right. However, to avoid distraction from the main focus of periodic solutions in our constrained class, we relegate the details of these studies to the appendices. In particular, in Appendix A we explore new solitary wave solutions of the asymptotic model in Choi & Camassa [7]. These are solitary waves on background uniform currents in each layer, which we found useful in the systematic study of various classes of periodic travelling wave solutions of the model. In Appendix B we present details of how such solitary waves can be used in studying the properties of the class of periodic waves described in §2.4.

2.2. The model equations and travelling wave system

We search for periodic wave solutions to the long wave strongly nonlinear asymptotic model (in the small parameter $\epsilon = H/L$, where L is a typical horizontal scale of the waves and H is the total thickness of the two layers) derived by Choi & Camassa [7] for

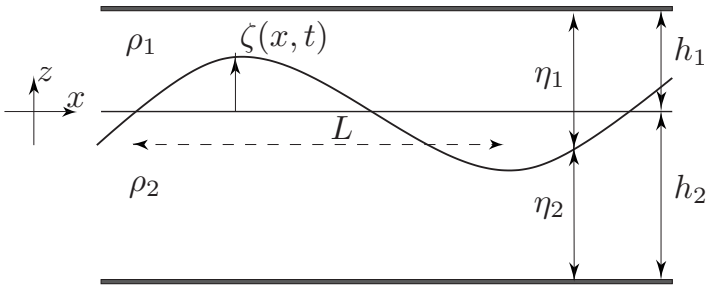

FIGURE 2.1. Schematics of the two-fluid system with main notation definitions.

a system of two inviscid, irrotational[1] fluid layers of constant densities under gravity (with $\rho_1 < \rho_2$ for stable stratification) – see Figure 2.1. We define the interface displacement between the two layers as the graph $z = \zeta(x,t)$ and choose the origin of our coordinate systems so that the two fluid layers are bounded above and below at $z = h_1$ and $z = -h_2$ respectively. We denote by $\eta_1(x,t) = h_1 - \zeta(x,t)$ and $\eta_2(x,t) = h_2 + \zeta(x,t)$, respectively, the thicknesses of each layer.

We interpret h_1 and h_2 as the fluid layer thicknesses of a reference quiescent state prior to wave generation and propagation, and assume that the mechanisms by which waves are generated do not add mass to either layer, so that the periodic wave trains we are seeking will have zero mean with respect to this state. We expect this to be the case for most common wave generation setups in experiments, although this is by no means assured, and there may be (small) departures from the zero mean assumption, for instance due to spatial transients. As mentioned in the Introduction, it is easy to adapt the model to different assumptions (as in the examples of §2.7), which can actually result in a simplified process of finding periodic solutions.

[1]In fact, the asymptotic model can accommodate for weak horizontal vorticity in each layer consistently with the long wave approximation.

The set of model equations that governs the dynamics of a two layer system under the long wave approximation is

$$\eta_{1t} + (\eta_1 \overline{u}_1)_x = 0\,, \tag{2.1}$$

$$\eta_{2t} + (\eta_2 \overline{u}_2)_x = 0\,, \tag{2.2}$$

$$\overline{u}_{1t} + \overline{u}_1 \overline{u}_{1x} + g\zeta_x = -\frac{1}{\rho_1}\partial_x P_I + \frac{1}{\eta_1}\partial_x\left(\frac{1}{3}\eta_1^3 G_1\right)\,, \tag{2.3}$$

$$\overline{u}_{2t} + \overline{u}_2 \overline{u}_{2x} + g\zeta_x = -\frac{1}{\rho_2}\partial_x P_I + \frac{1}{\eta_2}\partial_x\left(\frac{1}{3}\eta_2^3 G_2\right)\,, \tag{2.4}$$

where $\overline{u}_k(x,t)$ denote the layer mean velocities

$$\overline{u}_k(x,t) = \frac{1}{\eta_k}\int_{[\eta_k]} u_k(x,z,t)dz\,, \tag{2.5}$$

where the layer domains $[\eta_k]$ are defined as $\zeta \le z \le h_1$ and $-h_2 \le z \le \zeta$, for $k = 1, 2$ respectively, $P_I(x,t)$ is the pressure at the interface, and the *nonlinear* dispersive terms are defined, respectively, by

$$G_k\,(x,t) = \overline{u}_{kxt} + \overline{u}_k \overline{u}_{kxx} - (\overline{u}_{kx})^2\,, \qquad k = 1, 2\,. \tag{2.6}$$

The first pair is exact and is simply an expression of mass conservation per layer, while the second pair corresponds to horizontal momentum balance and is accurate up to terms in the long wave parameter asymptotics of order $O(\epsilon^4)$.

2.2.1. Traveling wave solutions. For a stationary wave moving from left to right with constant speed c, we make the change of variable

$$X = x - ct\,,$$

and consider

$$\zeta(x,t) \equiv \zeta(X)\,,\ \overline{u}_k(x,t) \equiv \overline{u}_k(X)\,,\ P_I(x,t) \equiv P_I(X)\,,$$

hence

$$\frac{\partial}{\partial t} = -c\frac{\partial}{\partial X}\,,\ \frac{\partial}{\partial x} = \frac{\partial}{\partial X}\,.$$

The equations of mass conservation and momentum for each layer therefore reduce to a system of four ODE's with respect to independent variable X. The system can be integrated by quadratures, which introduces four integration constants that represent an equal number of motion invariants.

Continuity.

Equations (2.1) and (2.2) become

$$-c\eta_{kX} + (\eta_k \overline{u}_k)_X = 0\,. \tag{2.7}$$

Integrating once with respect to X, we obtain

$$-c\eta_1 + \eta_1 \overline{u}_1 = C_1\,, \tag{2.8}$$

$$-c\eta_2 + \eta_2 \overline{u}_2 = C_2\,, \tag{2.9}$$

where C_1 and C_2 are manifestly the volume fluxes in the *wave frame*, in each layer.

Momentum.

Eliminating the pressure between (2.3) and (2.4) and with the help of (2.8) and (2.9), we obtain

$$\Gamma(\zeta)\,\zeta_X = \frac{\rho_1}{\eta_1}\left(\frac{1}{3}\eta_1^3 G_1\right)_X - \frac{\rho_2}{\eta_2}\left(\frac{1}{3}\eta_2^3 G_2\right)_X \tag{2.10}$$

where

$$\Gamma(\zeta) = \frac{\rho_1 C_1^2}{\eta_1^3} + \frac{\rho_2 C_2^2}{\eta_2^3} - \gamma\,, \tag{2.11}$$

and $\gamma \equiv g(\rho_2 - \rho_1)$. In order to separate variables we integrate the third order ODE (2.10) with two different integrating factors and eliminate the common second derivative ζ_{XX} between the resulting equations.

2.2.2. First integral. We note that with the traveling wave ansatz, the dispersive terms (2.6) become

$$G_k = -c\overline{u}_{kXX} + \overline{u}_k\overline{u}_{kXX} - (\overline{u}_{kX})^2 = C_k^2\left[-\frac{\eta_{kXX}}{\eta_k^3} + \frac{\eta_{kX}^2}{\eta_k^4}\right] = -\frac{C_k^2}{\eta_k^2}\left[\frac{\eta_{kX}}{\eta_k}\right]_X\,. \tag{2.12}$$

Thus, the terms in the RHS of equation (2.10) can be expressed as a total derivative

$$\frac{\rho_k}{\eta_k}\left(\frac{1}{3}\eta_k^3 G_k\right)_X = \frac{\rho_k C_k^2}{3}\left[\frac{1}{2}\frac{\zeta_X^2}{\eta_k^2} + (-1)^{k+1}\frac{\zeta_{XX}}{\eta_k}\right]_X,\ k = 1, 2\,. \tag{2.13}$$

From (2.13), integrating both sides of the equation (2.10) yields

$$M(\zeta) - C_3 = A_1(\zeta)\,\zeta_X^2 + B_1(\zeta)\,\zeta_{XX}\,, \tag{2.14}$$

with

$$M(\zeta) = \frac{1}{2}\frac{\rho_1 C_1^2}{\eta_1^2} - \frac{1}{2}\frac{\rho_2 C_2^2}{\eta_2^2} - \gamma\zeta\,, \tag{2.15}$$

$$A_1(\zeta) = \frac{\rho_1 C_1^2}{6\eta_1^2} - \frac{\rho_2 C_2^2}{6\eta_2^2}\,, \tag{2.16}$$

and

$$B_1(\zeta) = \frac{\rho_1 C_1^2}{3\eta_1} + \frac{\rho_2 C_2^2}{3\eta_2}\,, \tag{2.17}$$

respectively.

2.2.3. Second Integral. Another way of integrating equation (2.10) is to multiply it by η_1 and use

$$\eta_1 + \eta_2 = H\,. \tag{2.18}$$

We obtain

$$\Gamma(\zeta)\,\eta_1\zeta_X = \left[\frac{\rho_1\eta_1^3}{3}G_1 + \frac{\rho_2\eta_2^3}{3}G_2\right]_X - \frac{\rho_2 H}{\eta_2}\left[\frac{1}{3}\eta_2^3 G_2\right]_X\,. \tag{2.19}$$

The second term at the RHS of this equation can be expressed as a total derivative by using (2.13) again, and integrating both sides yields

$$N(\zeta) - C_4 = A_2(\zeta)\,\zeta_X^2 + B_2(\zeta)\,\zeta_{XX}\,, \tag{2.20}$$

where

$$N(\zeta) = \frac{\rho_1 C_1^2}{\eta_1} + \frac{\rho_2 C_2^2}{\eta_2}\left(1 - \frac{H}{2\eta_2}\right) - \gamma\left(\eta_1\zeta + \frac{\zeta^2}{2}\right), \tag{2.21}$$

$$A_2(\zeta) = \frac{\rho_1 C_1^2}{3\eta_1} + \frac{\rho_2 C_2^2}{3\eta_2}\left(1 - \frac{H}{2\eta_2}\right), \tag{2.22}$$

$$B_2(\zeta) = \frac{\rho_1 C_1^2}{3} + \frac{\rho_2 C_2^2}{3}\left(\frac{H}{\eta_2} - 1\right). \tag{2.23}$$

respectively.

2.2.4. Quadrature solution. By eliminating ζ_{XX} between equations (2.14) and(2.20) we obtain

$$\zeta_X^2 = \frac{(M(\zeta) - C_3)\, B_2(\zeta) - (N(\zeta) - C_4)\, B_1(\zeta)}{A_1(\zeta)B_2(\zeta) - A_2(\zeta)B_1(\zeta)}, \tag{2.24}$$

with the identity

$$B_2(\zeta) = \frac{\rho_1 C_1^2}{3} + \frac{\rho_2 C_2^2}{3}\frac{\eta_1}{\eta_2} = \eta_1 B_1(\zeta),$$

which yields the first order separable ODE for ζ

$$\zeta_X^2 = 3\frac{\rho_1 C_1^2\eta_2 + \rho_2 C_2^2\eta_1 - \gamma\zeta^2\eta_1\eta_2 + 2C_3\eta_1^2\eta_2 - 2C_4\eta_1\eta_2}{\rho_1 C_1^2\eta_2 + \rho_2 C_2^2\eta_1}. \tag{2.25}$$

2.2.5. Invariance with respect to choice of coordinate system. By making the traveling wave ansatz, we implicitly assume the translational invariance in horizontal direction. However, the translational invariance in the vertical direction may not be

immediately obvious, because of the presence of the ζ^2 term in the numerator, which depends on the choice of origin in the vertical. It is immediately clear from (2.8) and (2.9) that the constants of integration C_1, C_2 are independent of the coordinate system – since they are expressed in terms of the widths of the layers and the averaged velocities only. This is not the case with the other two constants of integration C_3 and C_4. However, from the definitions (2.14-2.23), observing that their RHS are invariant under z translations, it follows that the constants C_3 and C_4 must transform according to

$$C_3' = C_3 - \gamma z_0\,, \qquad C_4' = C_4 - \gamma z_0 \frac{2h_1 + z_0}{2}\,, \tag{2.26}$$

where z_0 is the amount of vertical translation of the new coordinate $z' = z + z_0$. With these rules, one can easily check that the quadrature (2.25) is frame invariant, because so is the denominator, while the numerator's translation dependent terms combine to give frame independence,

$$\begin{aligned} -\gamma\zeta'^2 + 2C_3'\eta_1 - 2C_4' &= -\gamma\zeta^2 - \gamma z_0^2 - 2\gamma z_0\zeta + 2C_3\eta_1 + 2\gamma z_0\eta_1 - 2C_4 - \gamma z_0(2h_1 + z_0) \\ &= -\gamma\zeta^2 + 2C_3\eta_1 - 2C_4\,. \end{aligned}$$

This essentially proves that the derivation of the quadrature is consistent with the physical requirements of frame independence.

2.2.6. Analysis of the quadrature. The quadrature (2.25) corresponds to the classical case of a particle in an unbounded potential well. The potential is a rational function

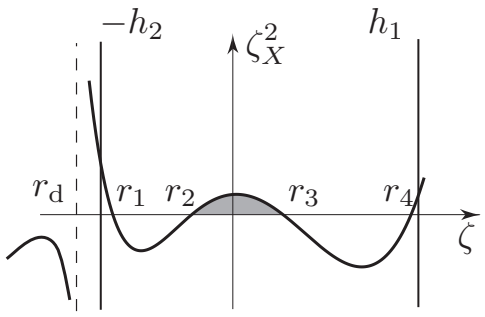

FIGURE 2.2. Potential for the quadrature (2.25). $r_1, \ldots, r_4$ are the roots of the quartic numerator while r_d is the root of the denominator, always located *outside* the physical domain.

of ζ with a quartic polynomial at the numerator (recall that $\eta_1 = h_1 - \zeta$ and $\eta_2 = h_2 + \zeta$)

$$P(\zeta) = \rho_1 C_1^2 \eta_2 + \rho_2 C_2^2 \eta_1 - \gamma \zeta^2 \eta_1 \eta_2 + 2C_3 \eta_1^2 \eta_2 - 2C_4 \eta_1 \eta_2 \,, \tag{2.27}$$

and a monomial at the denominator

$$\rho_1 C_1^2 \eta_2 + \rho_2 C_2^2 \eta_1 \,. \tag{2.28}$$

The numerator is positive for large ζ, with $\lim_{\zeta \to \pm\infty} P(\zeta) = +\infty$, while the denominator is always positive inside the physical domain (consequently the corresponding root, r_d say, is *outside* the physical domain), since $\rho_1 C_1^2 \eta_2 + \rho_2 C_2^2 \eta_1 > 0$. For periodic solutions to exist there needs to be two roots of the numerator $P(\zeta)$, with $P > 0$ between these roots. Hence, generically there must be four real roots of the polynomial $P(\zeta)$ to have periodic solutions. These roots can be ordered, $r_1 < r_2 < r_3 < r_4$ say, and periodic solutions will vary between the trough position r_2 and the crest position r_3 – see Figure 2.2. This structure – five real roots, four for numerator and one for denominator – give rise to

hyperelliptic integrals, in contrast to the elliptic integrals that arise in the solitary wave solutions, which correspond to the limiting situation of root collisions of P.

Unfortunately, manipulation of hyperelliptic integrals have not been completed to a level comparable to their elliptic counterparts. We remark that a modicum of information on the solutions of equation (2.25) can be obtained in terms of the twelve slotted, five variable, Lauricella D multiple hypergeometric function, $F_D^{(5)}$ Drociuk [11].

2.2.7. Physical interpretation of the quadrature. We now remark on the physical properties of the solutions obtained by the quadrature expression (2.25). First, the shape of the wave is described by a first order ODE that contains four constants of integration. By a careful examination of the quadrature, we note that the phase speed of the wave is no longer present, all the four integration constants being motion invariants in the wave frame. In particular, two of these constants of integration are mass fluxes in the wave frame for each layer, while the other two still have to be related to physical quantities. These four parameters span all possible traveling wave solutions in the reference frame where the wave motion is stationary. To connect the solution to a physical state of the fluid, one has to define a lab frame, independent of each specific wave realization. For instance, in laboratory experiments, in most circumstances (absent means of creating an overall current for all fluid layers) this reference frame will naturally be that of a stationary wave tank.

Second, in deriving the quadrature (2.25), we have not used any assumption of symmetry, yet this expression yields only symmetric wave shapes. Thus, we can infer that in the framework of the asymptotic model in Choi & Camassa [7], long periodic waves are symmetric up to $O(\epsilon^4)$ corrections. We also note that, since the root of the denominator

of the quadrature is, aside from special limits, always outside the physical domain, singular solutions with cusps (infinite derivative) can not exist, which is a desirable outcome as such solutions would violate the assumptions underlying the derivation of the long wave model. Degenerate limits of periodic waves thus occur only as limits to solitary waves or fronts corresponding to root collisions in the numerator of the quadrature (2.25). The only other degenerate limits correspond to the possibility of vanishing denominator in the quadrature (2.25). This happens when the root of the denominator (2.28) limits to either $\zeta = h_1$ or $\zeta = -h_2$ (from above or below, respectively), or this root migrates to infinity, which can happen when the coefficient $\rho_2 C_2^2 - \rho_1 C_1^2$ of ζ vanishes. In the former case, the potential becomes cubic, similar to the well known case of Korteweg-de Vries (KdV) solutions, while in the latter case the potential is a quartic, which is more akin to solutions of the modified-KdV-KdV (or Gardner) equation. We remark that the first degeneracy necessarily occurs when either $C_1 = 0$ or $C_2 = 0$, as well as in the limit of upper fluid density $\rho_1 = 0$. The latter will be discussed below together with the other physically extreme cases in the context of wave profile solutions.

2.3. Physical interpretation of the integration constants

The results of the previous section show that periodic wave solutions of the long wave model depend on four parameters that are wave frame quantities, with the phase speed of the wave not being present in the quadrature (2.25). However, in actual experimental setups for the generation of any kind of internal waves, there would be an unambiguously defined laboratory frame of reference. This compels us to consider the phase speed as an additional degree of freedom, and thus conclude that periodic wave solutions of the long wave model are a five parameter family. In general, we can expect some of these

five parameters to be fixed by the details of the experimental setup for an entire family of waves. For instance, in a closed wave tank, one would naturally try to create waves with a wavemaker that achieves various amplitudes and periods, while the mean level of the interface would stay close to that of the quiescent initial state. In addition, it is easy to envision a wavemaking mechanism that conserves horizontal momentum, such as the plunger used by Thorpe [49], because the horizontal component of the total force is zero. Moreover, incompressibility in a closed tank implies that the total volume flux in the lab frame has to be zero. The resulting wave class would thus be constrained to satisfy fixed mean interface (located at $z = 0$, say), zero total horizontal momentum and zero total volume flux. The first two constraints could be assumed to hold locally per period box. These constraints restrict the five parameter family of periodic waves to a two parameter family, e.g. amplitude and speed, with the period being functionally dependent on these. Other constraints among the five degrees of freedom are possible, regardless of the physical means of generating periodic waves on a given background state, and have been used in the literature.

With this in mind, in the present section, we establish connections between conserved quantities for periodic wave motion and the four constants of integration $C_1, \ldots, C_4$ and the phase speed c present in the quadrature (2.25). We will use the relations developed here primarily to construct various classes of periodic waves in §2.4 and §2.7, as well as to study the properties of these classes. We group these quantities in two categories: properties that are invariant with respect to a Galilean change of reference frame, and properties that depend on a particular inertial frame of reference.

2.3.1. Reference frame invariant quantities. Let $\boldsymbol{C}$ denote the set of integration constants $\{C_1, C_2, C_3, C_4\}$ and $R(\zeta, \boldsymbol{C})$ denote the rational function in ζ in the RHS of the quadrature (2.25), the potential function.

With the notations from §2.2.6, the amplitude (defined as distance peak to trough) is

$$\mathcal{A}(\boldsymbol{C}) = r_3(\boldsymbol{C}) - r_2(\boldsymbol{C})\,, \tag{2.29}$$

the period is given by the hyperelliptic integral

$$\mathcal{L}(\boldsymbol{C}) = \int_{-L/2}^{L/2} dX = \int_{-L/2}^{L/2} \frac{dX}{d\zeta} d\zeta = \int_{r_2(\boldsymbol{C})}^{r_3(\boldsymbol{C})} \frac{d\zeta}{\sqrt{R(\zeta, \boldsymbol{C})}}\,, \tag{2.30}$$

while the mean position of the interface is given by

$$\widetilde{\zeta}(\boldsymbol{C}) = \frac{1}{\mathcal{L}(\boldsymbol{C})} \int_{-L/2}^{L/2} \zeta dX = \frac{1}{\mathcal{L}(\boldsymbol{C})} \int_{-L/2}^{L/2} \frac{\zeta dX}{d\zeta} d\zeta = \frac{1}{\mathcal{L}(\boldsymbol{C})} \int_{r_2(\boldsymbol{C})}^{r_3(\boldsymbol{C})} \frac{\zeta d\zeta}{\sqrt{R(\zeta, \boldsymbol{C})}}\,, \tag{2.31}$$

and, consequently, the mean depths of the layers are

$$\widetilde{h}_1(\boldsymbol{C}) = \frac{1}{\mathcal{L}(\boldsymbol{C})} \int_{-L/2}^{L/2} \eta_1 dX = h_1 - \widetilde{\zeta}\,, \tag{2.32}$$

$$\widetilde{h}_2(\boldsymbol{C}) = \frac{1}{\mathcal{L}(\boldsymbol{C})} \int_{-L/2}^{L/2} \eta_2 dX = h_2 + \widetilde{\zeta}\,. \tag{2.33}$$

Thus, for instance, the requirement that the mean of the interface coincides with the interface of the background state, which we assume with no loss of generality to be located at the vertical origin of the coordinate system, can be met by imposing the

integral constraint

$$\widetilde{\zeta}(\boldsymbol{C}) = 0\,. \tag{2.34}$$

The mean potential energy for one layer is

$$V_k(\boldsymbol{C}) = \frac{1}{\mathcal{L}(\boldsymbol{C})}\int_{-L/2}^{L/2}\int_{[\eta_k]} \rho_k g z\; dz\; dX\,, \qquad k = 1, 2\,. \tag{2.35}$$

We obtain

$$V_1(\boldsymbol{C}) = \frac{g\rho_1 h_1^2}{2} - \frac{g\rho_1}{2\mathcal{L}(\boldsymbol{C})}\int_{r_2(\boldsymbol{C})}^{r_3(\boldsymbol{C})} \frac{\zeta^2 d\zeta}{\sqrt{R(\zeta, \boldsymbol{C})}}\,, \tag{2.36}$$

$$V_2(\boldsymbol{C}) = -\frac{g\rho_2 h_2^2}{2} + \frac{g\rho_2}{2\mathcal{L}(\boldsymbol{C})}\int_{r_2(\boldsymbol{C})}^{r_3(\boldsymbol{C})} \frac{\zeta^2 d\zeta}{\sqrt{R(\zeta, \boldsymbol{C})}}\,. \tag{2.37}$$

Finally, the total potential energy required for deforming the interface from the quiescent state to the wave shape, averaged over the period, is

$$V(\boldsymbol{C}) = \frac{\gamma}{2\mathcal{L}(\boldsymbol{C})}\int_{r_2(\boldsymbol{C})}^{r_3(\boldsymbol{C})} \frac{\zeta^2 d\zeta}{\sqrt{R(\zeta, \boldsymbol{C})}}\,. \tag{2.38}$$

2.3.2. Frame dependent quantities. In the following, we relate volume fluxes, momenta[2] and kinetic energy to the integration constants $\boldsymbol{C}$ and the phase speed and determine how these quantities transform with change of frame of reference. We denote by $\widehat{\cdot}$ quantities in the wave frame, frame where the motion is stationary. Two of the integration constants in the quadrature, C_1 and C_2, have a clear physical interpretation, namely volume fluxes in the wave frame in each layer. Indeed, the volume flux in the

[2]In deducing the relationships between these quantities and the quadrature constants we have not assumed irrotationality of the motion. Thus, they can be used in determining classes of long periodic waves under weak rotational approximations consistent with the model.

wave frame for the layer k is, by virtue of continuity in each layer (2.8) and (2.9),

$$\widehat{Q}_k = \int_{[\eta_k]} (u_k - c) dz = \overline{u}_k \eta_k - c\eta_k = C_k \,, \quad k = 1, 2 \,. \tag{2.39}$$

We note that volume the fluxes in each layer are conserved solely in the wave frame, and only the total volume flux is conserved in the lab frame. The total volume fluxes in the wave frame and in the lab frame are, respectively,

$$\widehat{Q}(C_1, C_2) \;=\; C_1 + C_2 \,, \tag{2.40}$$

$$Q(c, C_1, C_2) \;=\; C_1 + C_2 + cH \,. \tag{2.41}$$

Horizontal momentum per period in the layer k (in the lab frame) is given by

$$I_k = \frac{1}{L} \int_{-L/2}^{L/2} \int_{[\eta_k]} \rho_k u_k \; dz \; dX = \frac{1}{L} \int_{-L/2}^{L/2} \rho_k \eta_k \overline{u}_k \; dX \,, \quad k = 1, 2 \,. \tag{2.42}$$

Integrating (2.8), (2.9) over the period after multiplication with ρ_k yields

$$I_k - c\rho_k \widetilde{h}_k = \rho_k \widehat{Q}_k \,, \quad k = 1, 2 \,.$$

Thus, the mean horizontal momenta for the layer k in the wave frame and the lab frame, respectively, are

$$\widehat{I}_k(C_k) \;=\; \rho_k C_k \,, \tag{2.43}$$

$$I_k(c, \boldsymbol{C}) \;=\; \rho_k C_k + c\rho_k \widetilde{h}_k(\boldsymbol{C}) \,, \quad k = 1, 2 \,, \tag{2.44}$$

so that the mean *total* horizontal momenta in the wave frame and the lab frame are

$$\widehat{I}(C_1, C_2) = \rho_1 C_1 + \rho_2 C_2 \,, \tag{2.45}$$

$$I(c, \boldsymbol{C}) = \rho_1 C_1 + \rho_2 C_2 + c\left(\rho_1 \widetilde{h}_1(\boldsymbol{C}) + \rho_2 \widetilde{h}_2(\boldsymbol{C})\right) \,, \tag{2.46}$$

respectively. We remark that the above quantities are *exact* conservation laws for two-layer Euler equations which derive simply from conservation of mass (and volume, by incompressibilty). As such, they also hold exactly for the model, since mass is conserved with no asymptotic errors (cf. equations (2.1),(2.2)). We further remark that in general, for two-layer Euler periodic solutions even when expressed by a multiply-valued interface function (such as the case of "overhanging" waves in §2.6), incompressibility implies that the total flux is

$$L\,Q = \frac{I_1}{\rho_1} + \frac{I_2}{\rho_2} \,, \tag{2.47}$$

which, together with the total horizontal momentum $I = I_1 + I_2$, provides a one-to-one correspondence between constraints applied to total fluid domain-defined quantities I, Q and layer-defined quantities I_1, I_2. In particular, this implies that when these total quantities are chosen to be zero, so are the layer momenta I_1 and I_2 and vice-versa.

Next, we express the kinetic energy per period in terms of the quadrature constants and the phase speed. Mean kinetic energy for the layer k is given by

$$T_k = \frac{\rho_k}{2L} \int_{-L/2}^{L/2} \int_{[\eta_k]} (u_k^2 + w_k^2)\; dz\; dX \,, \tag{2.48}$$

with u and w denoting the horizontal and vertical velocity components. We use the asymptotic relationships for these components given in Camassa *et al.* [8], the horizontal velocity in layer k being given by, up to asymptotic errors of order $O(\epsilon^4)$,

$$u_k(X,z) = \overline{u}_k + \left(\frac{\eta_k^2}{6} - \frac{(z_k+h_k)^2}{2}\right)(\overline{u}_k)_{XX}\,, \tag{2.49}$$

with $z_k = (-1)^k z$, whereas the vertical velocity is given in the same asymptotics by

$$w_k(X,z) = -(\overline{u}_k)_X(z_k+h_k)\,. \tag{2.50}$$

Carrying out the integration across the layer in (2.48) yields

$$T_k = \frac{\rho_k}{2L}\int_{-\frac{L}{2}}^{\frac{L}{2}}\left[\overline{u}_k^2\eta_k + (\overline{u}_k)_X^2\frac{\eta_k^3}{3}\right]\,dX\,, \tag{2.51}$$

which, by using first (2.39) and subsequently (2.44), can be put in the form

$$\begin{aligned}
T_k &= \frac{\rho_k}{2L}\int_{-\frac{L}{2}}^{\frac{L}{2}}\left[\left(c+\frac{C_k}{\eta_k}\right)^2\eta_k + \frac{C_k^2\zeta_X^2}{\eta_k^4}\frac{\eta_k^3}{3}\right]\,dX \\
&= \frac{\rho_k C_k}{2}\frac{1}{L}\int_{-\frac{L}{2}}^{\frac{L}{2}}\left[c+\frac{C_k}{\eta_k}+\frac{C_k\zeta_X^2}{3\eta_k}\right]dX + \frac{c}{2}\left(\rho_k C_k + c\rho_k\widetilde{h}_k\right) \\
&= \frac{\rho_k C_k}{2}\frac{1}{L}\int_{-\frac{L}{2}}^{\frac{L}{2}}\left[c+\frac{C_k}{\eta_k}+\frac{C_k\zeta_X^2}{3\eta_k}-\frac{C_k\zeta_{XX}}{3}\right]dX + \frac{cI_k}{2}
\end{aligned}$$

$$= \frac{\rho_k C_k}{2}\frac{1}{L}\int_{-\frac{L}{2}}^{\frac{L}{2}} u_k(X,(-1)^k h_k)dX + \frac{cI_k}{2}\,,\quad k=1,2\,, \tag{2.52}$$

where we have used periodicity to add the null term $\int_{-\frac{L}{2}}^{\frac{L}{2}}\zeta_{XX}dX$ to the first integral and the asymptotic relation for velocity (2.49) again to write the first term of (2.52) in terms

of the fluid velocity evaluated at the boundaries $z = (-1)^k h_k$. Thus

$$\begin{aligned} \widetilde{u}_k(c, \boldsymbol{C}) &= \frac{1}{\mathcal{L}(\boldsymbol{C})} \int_{-L/2}^{L/2} \left(c + \frac{C_k}{\eta_k} + C_k \frac{\zeta_X^2}{\eta_k} \right) \, dX \\ &= c + \frac{1}{\mathcal{L}(\boldsymbol{C})} \int_{r_2(\boldsymbol{C})}^{r_3(\boldsymbol{C})} \frac{C_k \left(3 + R(\zeta, \boldsymbol{C})\right)}{3\eta_k \sqrt{R(\zeta, \boldsymbol{C})}} d\zeta \,, \end{aligned} \tag{2.53}$$

represents the mean value of the horizontal velocity at the boundaries over one period, with accuracy of up to terms of order $O(\epsilon^4)$. We recognize in the above expression another conserved quantity for an irrotational periodic wavetrain, namely the mean Eulerian velocity for the layer k, defined as

$$\widetilde{u}_k = \frac{1}{L} \int_{-L/2}^{L/2} u_k(X, z) dX \,, \tag{2.54}$$

where z is any location within the layer k that does not intersect the interface. Indeed, this quantity is invariant with z for a periodic and irrotational flow since its z derivative is

$$\frac{1}{L} \int_{-L/2}^{L/2} \frac{du_k(X, z)}{dz} dX = \frac{1}{L} \int_{-L/2}^{L/2} \frac{dw_k(X, z)}{dX} dX = 1/L \left[w_k(-L/2, z) - w_k(L/2, z) \right] = 0 \,.$$

Hence, the kinetic energy in the layer k in terms of the quadrature constants and the phase speed is

$$T_k(c, \boldsymbol{C}) = \frac{\rho_k \widehat{Q}_k \widetilde{u}_k}{2} + \frac{c I_k}{2} \,, \tag{2.55}$$

where $\widehat{Q}_k$, the flux in the wave frame in the layer k, is given by (2.39), $\widetilde{u}_k$, the mean Eulerian velocity in the layer k, is given by (2.53) and I_k, the horizontal momentum in the lab frame for the layer k, is given by (2.44).

We remark that the expression of the kinetic energy (2.55), being derived from an asymptotic approximation to the velocity field, is in principle affected by the accuracy of the asymptotic model. However, with this equation we retrieve the *exact* form deduced by Klopman [28] for irrotational periodic wave trains in *one layer* fluids, building upon previous work by Longuet-Higgins [34] who assumed that the lab frame was defined as the frame for which the mean Eulerian velocity is zero. It is worth reporting here the derivation for the general Euler equations for two layer fluids, without using the asymptotic model, and show that they lead to our same expression. If the flow is both irrotational and incompressible, a potential function and a stream function in the wave frame, ϕ and ψ, can be defined; we have:

$$u_k - c = (\phi_k)_X = (\psi_k)_z \,,$$

$$v_k = (\phi_k)_z = -(\psi_k)_X \,.$$

Hence, equation (2.48) becomes

$$\begin{aligned} T_k &= \frac{\rho_k}{2L}\left[\int_{-L/2}^{L/2}\int_{[\eta_k]} ((u_k-c)^2+v_k^2)\; dz\; dX \right. \\ &\qquad \left. +2c\int_{-L/2}^{L/2}\int_{[\eta_k]} (u_k-c)\; dz\; dX + c^2\int_{-L/2}^{L/2}\int_{[\eta_k]} dz\; dX\right] . \end{aligned} \tag{2.56}$$

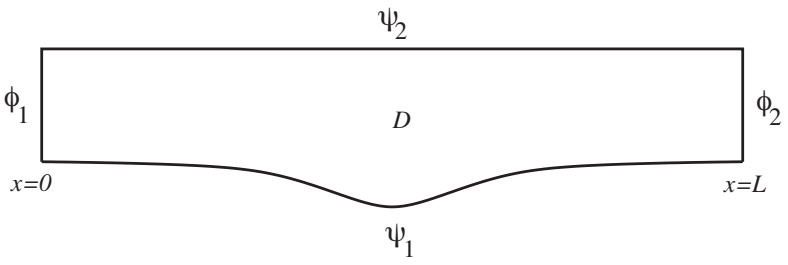

FIGURE 2.3. Domain of integration D

The first term in equation above is now replaced by

$$
\begin{aligned}
(2.57)\iint_D \left[(u_k-c)^2+v_k^2\right]\, dz\, dX \quad &= \iint_D \left[(\phi_k)_X(\psi_k)_z-(\phi_k)_z(\psi_k)_X\right]\, dz\, dX \\
&= \iint_{D^*} d\phi_k d\psi_k = \int_{(\phi_k)_1}^{(\phi_k)_2} d\phi_k \int_{(\psi_k)_1}^{(\psi_k)_2} d\psi_k \\
&= \int_{-L/2}^{L/2} (\phi_k)_X dX \int_{[\eta_k]} (\psi_k)_z dz \\
&= \int_{-L/2}^{L/2} \left[(u_k-c)\right]_{z=(-1)^k h_k} dX \int_{[\eta_k]} (u_k-c) dz \\
&= L(\widetilde{u}_k-c)\widehat{Q}_k\,,
\end{aligned}
$$

where $D^* = [(\phi_k)_1,(\phi_k)_2]\times[(\psi_k)_1,(\psi_k)_2]$ and D is specified in Figure 2.3. Thus, we obtain

$$
\begin{aligned}
(2.58) \qquad T_k = \quad & \frac{\rho_k}{2}\left[(\widetilde{u}_k-c)\widehat{Q}_k+2c\widehat{Q}_k+c^2\widetilde{h}_k\right] \\
&= \frac{\rho_k\widetilde{u}_k\widehat{Q}_k}{2}+\frac{c(\rho_k\widehat{Q}_k+c\rho_k\widetilde{h}_k)}{2}
\end{aligned}
$$

$$
(2.59) \qquad = \frac{\rho_k\widetilde{u}_k\widehat{Q}_k}{2}+\frac{cI_k}{2}\,.
$$

2.4. Periodic waves with zero total volume flux and horizontal momentum

We proceed with constructing the class of periodic waves we have alluded to in the previous section, satisfying three constraints: fixed mean level of the interface, total horizontal momentum in the lab frame zero and total volume flux in the lab frame zero. These constraints leave two free parameters. For our purposes, we found that the most advantageous choice to solve the system, and describe solution properties, is to parametrize the family with amplitude A and phase speed c. We will first describe how to determine particular solutions for prescribed amplitude and speed. We will then determine the domain of existence of periodic wave solutions in the parameter space $(A\,, c)$ and study their limiting forms.

2.4.1. Periodic solutions for prescribed speed and amplitude. By requiring that the total volume flux given by (2.41) and total horizontal momentum per period given by (2.46) are zero, the resulting linear system relates the two constants of integration in the quadrature C_1 and C_2 to the phase speed and mean heights

$$C_k = -c\widetilde{h}_k \qquad k = 1, 2\,. \tag{2.60}$$

Notice that it then follows from (2.44) that the mean horizontal momentum in each layer is zero. By choosing the coordinate system at the level of the quiescent state, the constraint of zero mean displacement of the interface implies

$$\widetilde{h}_k = h_k\,, \qquad k = 1, 2\,.$$

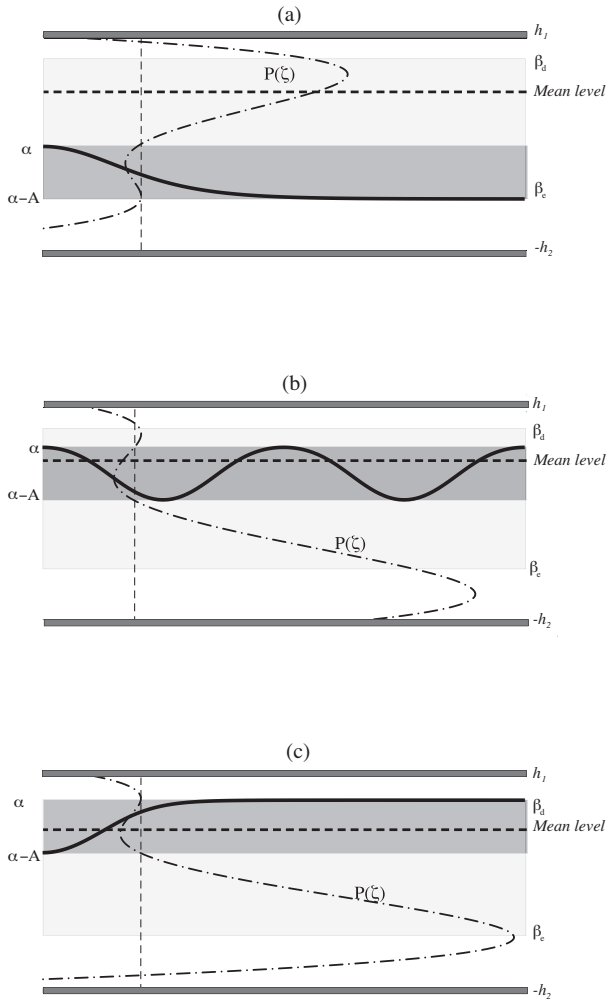

FIGURE 2.4. Schematic construction of constrained solutions with zero momenta and mean elevation for given amplitude A and speed c. The fluid is confined between the top and bottom walls at $z = h_1$ and $z = -h_2$, respectively. The dark grey strip "highlights" the range of the interface function $\zeta(X)$ between the roots at α and $\alpha - A$, while the light grey strip identifies the allowable range determined by root coalescence at $\alpha - A = \beta_e(A, c)$ and $\alpha = \beta_d(A, c)$, corresponding to solitary waves of elevation and depression, respectively. Solid curves depict travelling wave solution profiles (only the right half for solitary waves). The location of the targeted mean level is marked by the dashed horizontal line and the quartic function $P(\zeta)$, shown by the dash-dot curve, varies according to the placement of α in the allowable range from panel (a) to (c); (a) $\alpha = \beta_e(A, c) + A$, (b) $\beta_e(A, c) < \alpha < \beta_d(A, c)$ and (c) $\alpha = \beta_d(A, c)$. This construction is based on the actual configuration given by $h_1/h_2 = 1/3$, $\rho_1/\rho_2 = 0.99$, $c/c_0 = 0.55$, $A/h_1 = 1$.

The constants C_3 and C_4 can be determined by seeking waves of amplitude A and imposing the constraint of zero mean of interface displacement

$$\begin{aligned} \mathcal{A}(c, C_3, C_4) &= A\,, \\ \widetilde{\zeta}(c, C_3, C_4) &= 0\,. \end{aligned}$$

We first relate the two remaining constants of integration C_3 and C_4 to the position of the crest and the position of the trough, which are given by the middle roots of the quartic polynomial from the numerator of (2.25). By using (2.60) the quartic polynomial can be written as

$$P(\zeta) = \rho_1 c^2 h_1^2 \eta_2 + \rho_2 c^2 h_2^2 \eta_1 - \gamma \zeta^2 \eta_1 \eta_2 + 2C_3 \eta_1^2 \eta_2 - 2C_4 \eta_1 \eta_2\,. \tag{2.61}$$

If α is the position of the crest (so $\alpha - A$ is the position of the trough) C_3 and C_4 are functions of α since α and $\alpha - A$ must be roots of the polynomial $P(\zeta)$. By imposing this condition and solving the resulting linear system, we have

$$C_3(\alpha) = \frac{c^2 \rho_1 h_1^2}{2(h_1 - \alpha)(h_1 - \alpha + A)} - \frac{c^2 \rho_2 h_2^2}{2(h_2 + \alpha)(h_2 + \alpha - A)} - \gamma \left(\alpha - \frac{A}{2} \right)\,, \tag{2.62}$$

$$C_4(\alpha) = C_3(\alpha)(A + h_1 - \alpha) + \frac{c^2 \rho_1 h_1^2}{2(A + h_1 - \alpha)} - \frac{c^2 \rho_2 h_2^2}{2(A - h_2 - \alpha)} - \frac{\gamma}{2}(A - \alpha)^2\,. \tag{2.63}$$

With the explicit expressions for all the coefficients thus determined, the other two roots of the quartic $P(\zeta)$ can in turn be determined in terms of explicit (albeit lengthy) algebraic functions of α and A by solving the quadratic polynomial that results from

factoring the roots α and $\alpha - A$. Similarly, the mean of the interface becomes a function of α through (2.62), (2.63) in (2.31) (suppressing for ease of notation the arguments C_1 and C_2 of the rational function R in the quadrature expression (2.25))

$$\widetilde{\zeta}(\alpha) = \int_{\alpha-A}^{\alpha} \frac{\zeta\, d\zeta}{\sqrt{R(\zeta, C_3(\alpha), C_4(\alpha))}} \Bigg/ \int_{\alpha-A}^{\alpha} \frac{d\zeta}{\sqrt{R(\zeta, C_3(\alpha), C_4(\alpha))}} \quad . \tag{2.64}$$

Hence, the position of the crest of the periodic solution can be determined by finding the root of the nonlinear equation

$$\widetilde{\zeta}(\alpha) = 0\,. \tag{2.65}$$

Note that the denominator in (2.64) is a positive quantity, hence a necessary condition for existence of a solution is for the integrand of the function in the numerator

$$f(\alpha) \equiv \int_{\alpha-A}^{\alpha} \frac{\zeta}{\sqrt{R(\zeta, C_3(\alpha), C_4(\alpha))}} d\zeta \tag{2.66}$$

to change sign in the interval $(\alpha - A, \alpha)$, which implies $\alpha - A < 0 < \alpha$. This leads to a criterion for existence of a solution satisfying all the requirements so far imposed, by seeking the two limiting positions for the crest α when two roots of the polynomial (2.61) collide. Let

$$\alpha_{min}(A, c) \equiv \alpha(A, c)|_{r_1(\alpha;A,c)=r_2(\alpha;A,c)}\,, \tag{2.67}$$

and

$$\alpha_{max}(A, c) \equiv \alpha(A, c)|_{r_3(\alpha;A,c)=r_4(\alpha;A,c)}\,, \tag{2.68}$$

denote the α-range lower and upper limits, respectively, where the polynomial (2.61) has double roots $\beta_e(A,c) = r_1 = r_2 = \alpha_{min}(A,c) - A$ and $\beta_d(A,c) = r_3 = r_4 = \alpha_{max}(A,c)$. Notice that these would correspond to amplitude-A solitary waves of, respectively, elevation and depression. Notice also that these are not limiting forms of the class of periodic waves that satisfy our requirements. Thus, the necessary condition for existence of a periodic solution becomes

$$\beta_e(A,c) < 0 < \beta_d(A,c)\,, \tag{2.69}$$

– see Figure 2.4 for an illustration of the connection between the position of the crest α and the roots in such an instance. Moreover, as $\alpha \to \alpha_{min}(A,c)$, $f(\alpha) \to -\infty$, whereas as $\alpha \to \alpha_{max}(A,c)$, $f(\alpha) \to \infty$. It follows that $f(\alpha)$ will have a zero for some α in the range $(\alpha_{min}\,, \alpha_{max})$, so that the condition $\beta_e(A,c) < 0 < \beta_d(A,c)$ is also sufficient for existence of a periodic solution of mean zero. We remark that this argument does not guarantee uniqueness of zeroes of $f(\alpha)$ and hence of periodic solutions of mean zero. This would be guaranteed by the monotonicity of either $\widetilde{\zeta}(\alpha)$ or of the function $f(\alpha)$. Numerical results confirm that both these functions are monotonic in the interval $(\alpha_{min}\,, \alpha_{max})$, but a rigorous proof is still lacking. In Figure 2.5 we illustrate the dependence of the mean of the interface on the position of the crest for one particular configuration.

2.4.2. Domain of existence. The considerations of the previous section allow us to outline a strategy for determining periodic wave solutions of prescribed amplitude and speed, namely, given an A and a c, we can check whether the double roots $\beta_e(A,c)$ and $\beta_d(A,c)$ have opposite sign, which implies existence of the periodic train of that

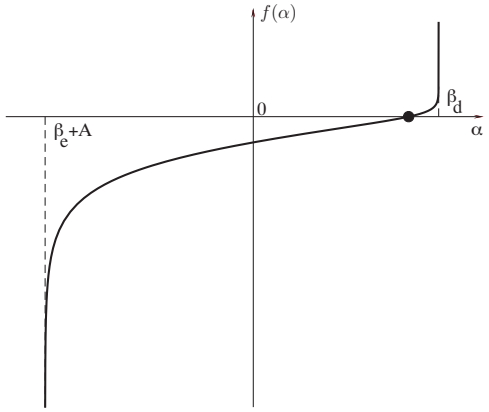

FIGURE 2.5. Dependence of $f(\alpha)$ given by (2.66) on the position of the crest α. The configuration is: $h_r = 1/3$, $\rho_r = 0.99$ and the parameters speed and amplitude are $c/c_0 = 0.55$, $A/h_1 = 1$.

amplitude and speed satisfying the constraints of zero mean displacement, zero total horizontal momentum and zero total volume flux. Of course, actual construction of the periodic train would have to rely on a numerical root finding algorithm. Hence, it would be desirable to know a priori and to determine analytically the portion of the (A, c) quadrant where the sufficiency condition (2.69) holds.

To this end, we use the two families of solitary wave solutions of elevation and depression corresponding to $\beta_e(A, c)$ and $\beta_d(A, c)$, respectively. In fact, the limiting forms β_d and β_e are nothing else than a generalization of the solitary waves (or fronts) solutions derived in Choi & Camassa [7], which admit an explicit analytical representation. In particular, the amplitude-speed relations of these families foliate the (A, c) quadrant and their limiting front solutions provide a boundary of existence in this quadrant, with the amplitude-speed relation given by an explicit quadratic expression. Notice that the quadrature is invariant with the change of the position of the coordinate system in the vertical direction, as shown in §2.2.5. Hence, we can represent the family of solitary waves corresponding to the double roots $\beta_e(A, c)$ and $\beta_d(A, c)$, with a new parametrization $(\beta\,, c)$,

with respect to "artificial" height configuration $h_1 - \beta, h_2 + \beta$ for $\beta \in (-h_2, h_1)$. The advantage of this new parametrization is that the polynomial at the numerator of the quadrature can be expressed as a product of ζ^2 times a quadratic polynomial, which provides the amplitude in closed form – see Choi & Camassa [7]. These "foliating" solitary wave solutions would then span a domain in the parameter space $(\beta\,, c)$, and this domain can in turn be mapped easily in the parameter space $(A\,, c)$.

Notice that in order to be useful for the construction of the periodic wave train that satisfies our constraints, these solitary waves of elevation and depression corresponding to double root β_e and β_d in the polynomial (2.61) must satisfy condition (2.60), and hence they have prescribed fluxes in the wave frame. By imposing the boundary conditions at infinity we obtain

$$(\overline{u}_k|_\infty - c)\eta_k|_\infty = -ch_k\,, \qquad k = 1, 2 \tag{2.70}$$

where $\overline{u}_k|_\infty$ can be interpreted as a current at infinity for the layer k in the lab frame while $\eta_k|_\infty$ is the height of layer k at infinity, since $\eta_k|_\infty \neq h_k$. Thus, these foliating solitary wave solutions are generalizations of the standard solitary waves in Choi & Camassa [7], for which the background state has zero currents in the lab frame. In Appendix A, we present an overview of this more general class of solitary waves, which are of independent interest than the present focus on periodic waves.

The domain of existence in $(\beta\,, c)$ of solitary waves with the prescribed fluxes (2.70) can be found by fixing β and determining the range of speed c for which solitary waves with property (2.70) exist. In Appendix B we present details for determining this range. For fixed β, the dependence between the maximum interface displacement a (or signed

amplitude, defined as difference between the zero level in the "artificial" parameters and the peak of the wave) and speed c is given by

$$a(c\,;\beta) = \frac{-q_1(c\,;\beta) + \mathrm{sgn}(\beta_0 - \beta)\sqrt{\Delta(c\,;\beta)}}{2} \qquad c \in [c_{min}(\beta), c_f(\beta)]\ . \tag{2.71}$$

Here the functions $q_1(c;\beta)$, $q_2(c;\beta)$, $\Delta(c;\beta)$ are given by (B.6-B.8), with the speeds $c_{min}(\beta)$ and $c_f(\beta)$ corresponding to limiting speeds of solitary wave of zero amplitude and front, respectively given by (B.10) and (B.11), and $z = \beta_0$ is a constant level in the physical domain $z \in [-h_2, h_1]$ determined solely by the "hardware" parameters h_k, ρ_k, $k = 1, 2$ – see definition (B.13).

For fixed β, the sign of the maximum displacement $a(c\,;\beta)$ shows the polarity of the class of solitary waves, with $a(c\,;\beta) > 0$ corresponding to waves of elevation, and $a(c\,;\beta) < 0$ to depression, respectively, for all $c \in [c_{min}(\beta), c_f(\beta)]$. In Appendix B we show that if $\beta < \beta_0$, then the corresponding maximum displacement branch $a(c\,;\beta)$ is positive (elevation), and, conversely, if $\beta > \beta_0$ then $a(c\,;\beta) < 0$ (depression). Thus, we can infer that the curves $a(c\,;\beta)$ with $\beta < \beta_0$ correspond to the foliating family β_e whereas the curves $a(c\,;\beta)$ with $\beta > \beta_0$ correspond to the foliating family β_d. These families span a domain in the (a, c)-semi-plane $c > 0$, bounded by a curve represented parametrically by

$$a\left(c_f(\beta)\,;\beta\right)\ , c_f(\beta)\,, \qquad \beta \in (-h_2, h_1)\,,$$

which corresponds to front solutions. By eliminating β, we can obtain an explicit formula for the front branch corresponding to $a\left(c_f(\beta)\right)$, with $\beta \in (-h_2, h_1)$. Let $h_r \equiv h_1/h_2$ and

$\rho_r \equiv \rho_1/\rho_2$. When $h_r\sqrt{\rho_r} \neq 1$, the front branch is given by

(2.72)
$$c_f(a) = \sqrt{Hg}\frac{(1+h_r)\sqrt{1-\rho_r}}{(h_r\sqrt{\rho_r}-1)^2}\left[h_r\sqrt{\rho_r}+1-\sqrt{\left(\frac{a}{H}\right)^2(h_r\sqrt{\rho_r}-1)^2+4h_r\sqrt{\rho_r}}\right],$$

whereas, for $h_r\sqrt{\rho_r} = 1$[1]

$$c_f(a) = \sqrt{Hg}\frac{(1+h_r)^2}{4h_r}\sqrt{\frac{1-\sqrt{\rho_r}}{1+\sqrt{\rho_r}}}\left[1-\left(\frac{a}{H}\right)^2\right]. \tag{2.73}$$

The curve $c_f(a)$ is symmetrical with respect to c axis. Returning to the original parameters A, c, for which $A > 0$, corresponds to "folding" the left half of the symmetric domain in a, c plane on top of the right half – see Figure 2.6, by taking $A = |a|$. Thus, for any point in the quadrant (A, c) with $c \in [0, c_f(A)]$ there are *two* foliating solitary waves of opposite polarity. These waves define a window for the possible locations of the crest and trough of a periodic wave of amplitude A that satisfies the flux condition (2.60). Moreover, the zero mean of the interface condition necessarily requires the crest location to be positive while the trough location must be negative, according to (2.69). This condition selects a limiting foliating curve

$$A(c;0) = |a(c;0)|\,, \qquad c \in [c_{min}(0), c_f(0)]\,, \tag{2.74}$$

when $\beta = 0$, which further restricts the allowable domain in the A, c plane. (For the region above this curve the two β parameters corresponding to the two families of foliating solitary waves have the same sign.) Notice that the curve $a(c;0)$ with $c \in [c_0, c_m]$

[1]We remark that this particular depth ratio, *different* than the critical depth ratio $h_r = 1/\sqrt{\rho_r}$, is associated with a mathematical degeneracy of the quadrature formula (2.25) to elliptic functions. This situation does not seem to have any particular physical interpretation.

Case I: $h_r < \sqrt{\rho_r}$

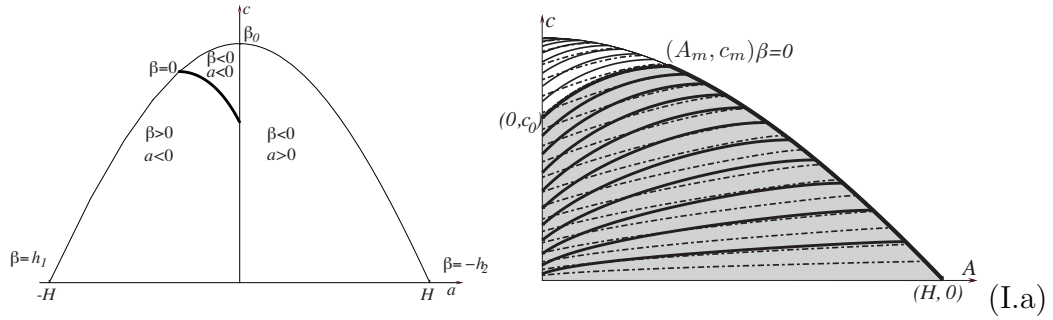

(I.a)

(I.b)

Case II: $h_r > \sqrt{\rho_r}$

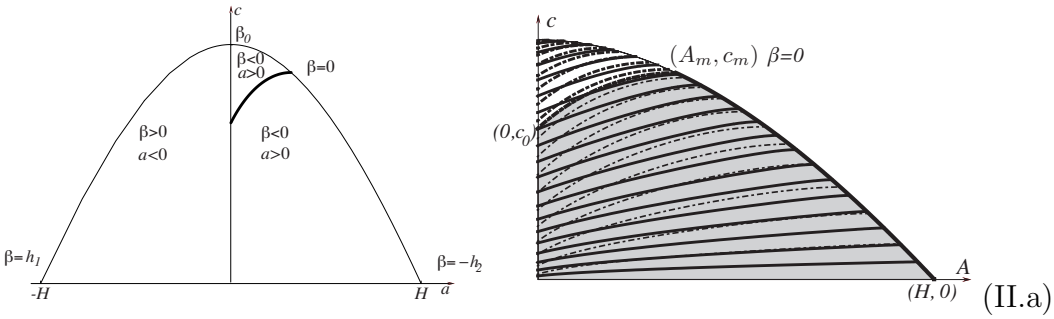

(II.a)

(II.b)

Case III: $h_r = \sqrt{\rho_r}$

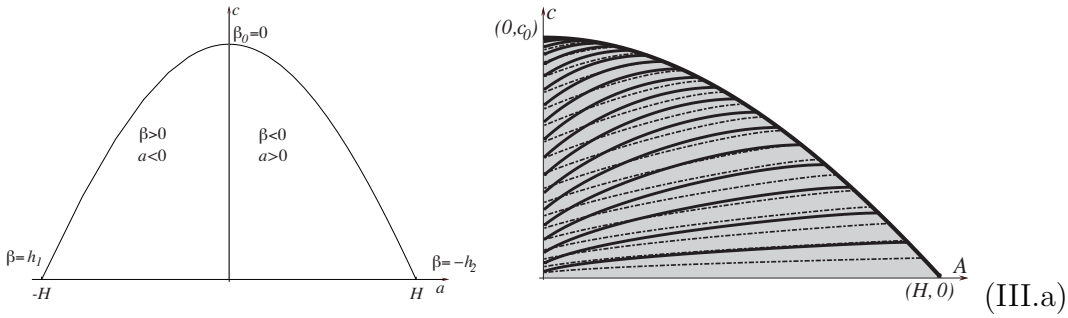

(III.a)

(III.b)

FIGURE 2.6. (I.a), (II.a) and (III.a) The front branch that marks the domain of existence of foliating solitary waves (2.71). (I.b), (II.b) and (III.b) Domain of existence for periodic waves of zero horizontal momentum and zero flux (gray areas). The thicker curves correspond to foliating solitary waves with $\beta > 0$ whereas thinner curves correspond to $\beta < 0$; continuous curves correspond to foliating solitary waves of depression, dashed curves to elevation. Periodic solutions can exist only in domains covered by solitary wave curves with opposite polarities and opposite positions (with respect to the mean level) of the interface at infinity.

corresponds to the standard solitary waves asymptotic to layer thicknesses h_1, h_2. Here c_0 is the long wave critical speed for this configuration,

$$c_0^2 = \frac{(1-\rho_r)h_r}{(\rho_r + h_r)(h_r+1)} gH\,, \tag{2.75}$$

and c_m is the speed of the highest travelling waves Choi & Camassa [7]

$$c_m^2 = \frac{1-\sqrt{\rho_r}}{1+\sqrt{\rho_r}} gH\,, \tag{2.76}$$

with the corresponding maximum amplitude

$$a_m = \frac{h_r - \sqrt{\rho_r}}{(h_r+1)(\sqrt{\rho_r}+1)} H\,. \tag{2.77}$$

Hence, the curve $A(c;0)$ corresponds to the infinite period limit to solitary waves of the periodic waves in our class, i.e., total horizontal momentum zero, total volume flux zero and mean zero. Indeed, these limiting solitary waves satisfy the mean zero of the interface condition in the limit, because in the process of taking the mean the finite mass is divided by an infinite period. We can represent this branch of the boundary as a function of amplitude A, by inverting (2.74)

$$c_{sw}(A) = c_0 \sqrt{\frac{(h_1 - \operatorname{sgn}(\beta_0)A)(h_2 + \operatorname{sgn}(\beta_0)A)}{h_1 h_2 - (c_0^2/g)\operatorname{sgn}(\beta_0)A}}\,, \qquad A \in [0, A_m]\,, \tag{2.78}$$

with $A_m = |a_m|$ and β_0 given by (B.13). The other boundary of the existence domain $A \in [|a_m|\,, H] \equiv [A_m, H]$, being the front limit of each foliating solitary wave curve, would correspond to the limit of our periodic waves to fronts.

Therefore, when the speed c increases with A fixed, $A \in [0, A_m]$, the periodic waves limit to infinite period in the form of solitary waves. Conversely, when c increases with $A \in [A_m, H]$, the periodic waves limit on fronts. The standard front limit of solitary waves (Choi & Camassa [7]) corresponds to the single point (A_m, c_m) at the vertex of the domain. Apart from this point, the front branch $[A_m, H]$ represents a new class of front solutions. Notice that for fixed $c \in [c_0, c_m]$ the domain of existence of periodic waves in our class consists of waves whose amplitude is larger than solitary waves of the same speed, and moreover a portion of the domain of existence consists of periodic waves of amplitude bigger than the maximum amplitude of the solitary wave (which limits to a front) for the same configuration.

We sketch the above discussion in Figure 2.6, for all three relevant cases: (I) $h_r < \sqrt{\rho_r}$ in which the solitary waves limiting branch corresponds to waves of depression, (II) $h_r > \sqrt{\rho_r}$, in which the limiting solitary waves are of elevation, (III) $h_r = \sqrt{\rho_r}$ – the critical density ratio – in which the solitary waves branch vanishes and the boundary of the domain of existence is marked only by the front branch. We remark, as shown in Appendix A, that the branch of front solutions which forms the right boundary of the existence domain is in fact *exact* for the parent two-layer Euler system, even though we arrive at it from within the asymptotic model. This property provides a validation test for the numerical solutions of two-layer Euler equations with large periods.

We also remark that the vertical and horizontal boundaries of the domain of existence correspond to infinitesimal amplitude waves, and to the singular limit of infinitesimal wave speed where the vanishing period shows that a neighborhood of the $c = 0$ axis is clearly outside of the model's validity regime. In fact, as we will see in the next section

and should be intuitive now given that the wave amplitude spans the whole gap between plates, the point $(H, 0)$ is extremely singular, and in its neighborhood wavetrains of any period can be found.

2.4.3. Extreme density limits. To complete this section, it is worth pointing out the limiting cases of equal density layers and that of vanishing upper layer density. For the first case, $\rho_r = 1$, the physics clearly can not support internal wave motion, and this is reflected in the model by the fact the boundary of the domain of existence collapses to zero, as the equation for the maximum speed (2.76) shows. For the second case, $\rho_r = 0$, which occurs for $\rho_1 = 0$ for a stably stratified fluid, the momentum equation governing the lower layer (2.4) decouples from that of the first layer, thus reducing the system to the single layer version (Su & Gardner [47], Green & Naghdi [18]). The effect of this limit on the quadrature (2.25) is to make the potential a cubic since the root at the denominator and a root of the quartic in the numerator collide at the upper boundary of the physical domain h_1. In the limit $\rho_r \to 0$ the family of foliating solitary waves of depression β_d vanishes and the right boundary of the domain of existence consisting of fronts degenerates to a branch of solitary waves that "scrape" the top wall with their crests. The left/top boundary consisting of solitary waves when $\rho_1 \neq 0$ remains a branch of solitary waves in the limit $\rho_r \to 0$ and coincides with the "classic" solitary wave solutions for the strongly nonlinear single layer model (Su & Gardner [47], Green & Naghdi [18]).

Curiously, the existence of maximum amplitude value A_m for $\rho_1 \neq 0$, which corresponds to the intersection of the two boundary branches for the existence domain, retains a meaning in the single layer case as the maximum amplitude of the solitary wave that

would fit within the domain walls at $z = -h_2$ and $z = h_1$. This apparent maximum amplitude contrasts the well known result that, for the single-layer case, the strongly-nonlinear model solitary-wave solutions do not possess a limiting amplitude, just as for the weakly nonlinear models such as KdV. Also, we remark that the degenerate front branch consists entirely of "scraping" solitary waves, and that these could still be thought of as fronts by cutting off half of the wave at the crest (at $z = h_1$). Also notice that for this degenerate front branch the dependence of the speed on amplitude becomes linear.

2.5. Properties of constrained periodic wave trains

Having determined the domain of existence in the A, c quadrant of our two-parameter family of periodic waves, we now turn to the study of the dependence of other relevant physical properties on these parameters.

2.5.1. Wave shapes. Determining a periodic wave solution for given amplitude and speed is a root finding problem (2.65) which involves evaluation of a hyperelliptic integral – see (2.64). We use a Newton scheme, whose quadratic convergence is desirable depending on a good initial guess (away from singularities injected into the integral by double roots). Here again the family of foliating solitary waves on artificial parameters becomes useful in identifying the position of the singularities.

Away from the critical depth ratio, when $h_r \neq \sqrt{\rho_r} \equiv h_{critical}$, the maximum amplitude A_m of the solitary wave branch marks a threshold amplitude that separates two regimes $A < A_m$ or $A > A_m$. The properties of the periodic solutions in these two cases are distinctively different.

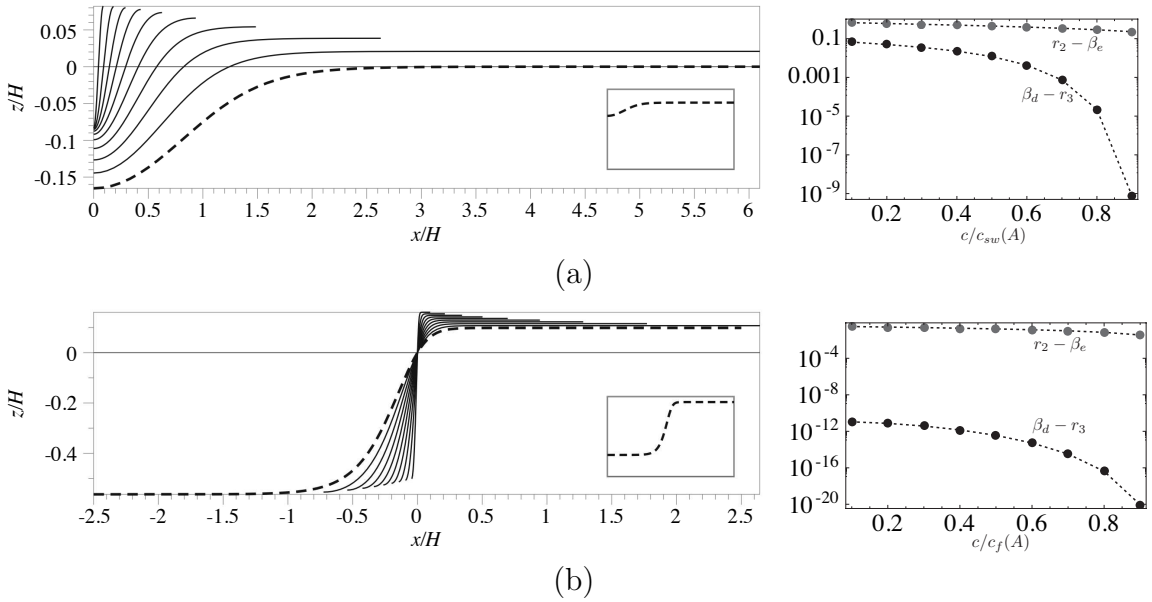

FIGURE 2.7. Wave profiles (half a period) along with the corresponding distances between the crest and the double root β_d and the trough and the double root β_e, respectively, for a configuration with $h_r < \sqrt{\rho_r}$ ($h_1/H = 1/6$, $h_2/H = 5/6$ and $\rho_r = 0.97$), for fixed amplitude (a) $A = A_m/2$ and (b) $A = 2A_m$ and phase speeds ranging from 10% to 90% of the corresponding maximum speed (a) $c_{sw}(A)$ and (b) $c_f(A)$, respectively. The dashed profiles correspond to the limiting (a) solitary wave of amplitude $A = A_m/2$ and (b) front of amplitude $A = 2A_m$; they are also depicted in the inserts where the physical boundaries $-h_2,\ h_1$ are included.

To fix ideas, let us focus on the case $h_r < h_{critical}$. For fixed amplitude $A < A_m$, as the phase speed increases, the position of the trough approaches the position of the foliating solitary wave of depression β_d while the distance between the trough and the other double root β_e remains bounded away from zero and set by the maximum speed for the corresponding solitary wave limiting form of the same amplitude.

For fixed amplitude $A > A_m$, with increasing phase speed the position of the crest once again approaches β_d, but the trough now also approaches the other double root β_e. However, we remark that for the configuration we are focusing on, $h_r < h_{critical}$, the

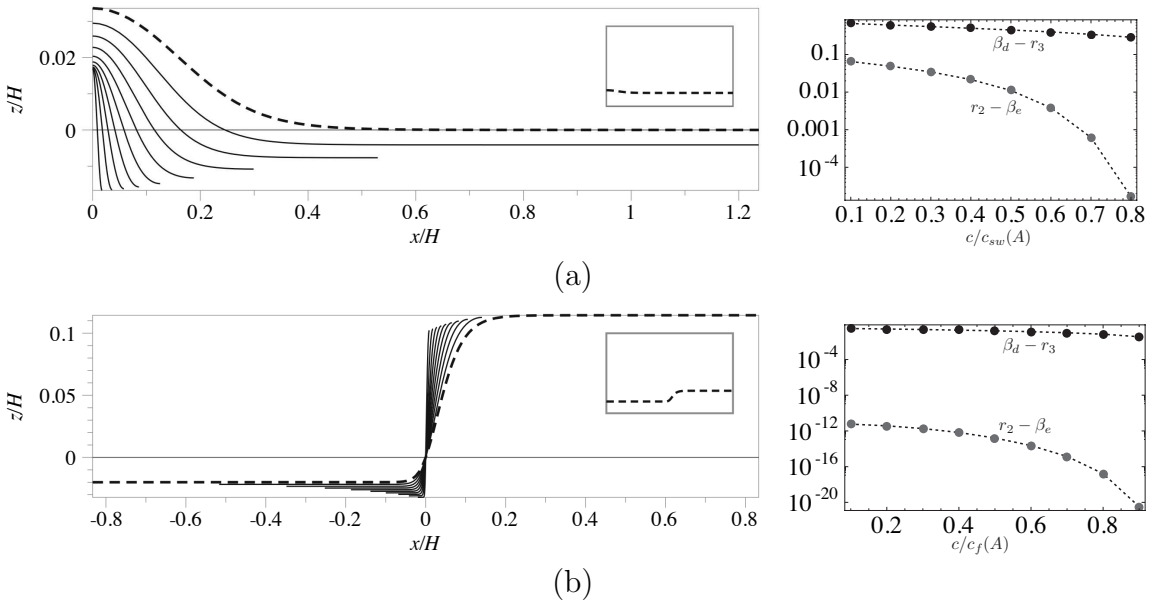

FIGURE 2.8. Same as in Figure 2.7 for a configuration with $h_r > \sqrt{\rho_r}$ ($h_1/H = 1/1.2$, $h_2/H = 0.2/1.2$ and $\rho_r = 0.97$).

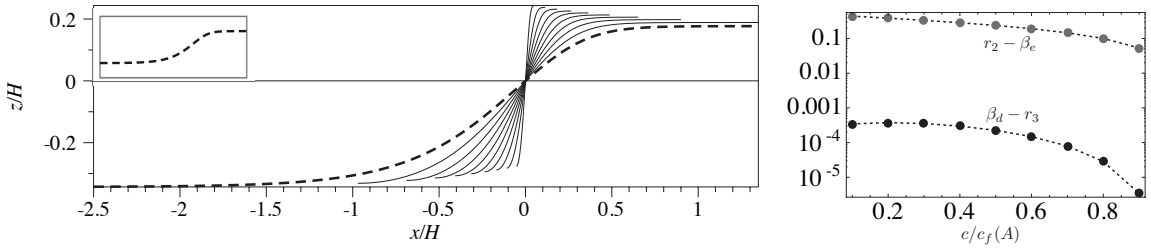

FIGURE 2.9. Same as in Figure 2.7(b) for a configuration corresponding to the critical case $h_r = \sqrt{\rho_r}$ ($h_1/H \simeq 0.24$, $h_2/H \simeq 0.76$ and $\rho_r = 0.1$). The waves have fixed amplitude $A = H/2$ and phase speeds ranging from 10% to 90% of the corresponding maximum speed $c_f(H/2)$.

approach of the trough position to this double root β_e occurs at a much slower rate than the approach of the crest to the other double root β_d.

For the other configuration $h_r > h_{critical}$ this happens in reverse. We illustrate these observations in Figure 2.7 for a configuration with $h_r < h_{critical}$, and in Figure 2.8 for $h_r > h_{critical}$, respectively.

For a configuration corresponding to the critical depth ratio $h_r = \sqrt{\rho_r}$, when the boundary of the domain of existence consists only of fronts, the position of the crest

approaches the limiting position β_d at a slightly faster rate than the position of the trough approaches β_e – see Figure 2.9.

We note that for large amplitudes, even when the pair speed/amplitude is away from the boundary of the domain of existence, the hyperelliptic integrals involved in the root finding process become nearly singular and consequently high precision computations are necessary. We remark that the root finding in this situation could be handled analytically via an asymptotic expansion in a small parameter representing the distance between roots approaching the double root locations β_d or β_e. This analysis, however, involves some subtleties that will be presented elsewhere.

2.5.2. Kinetic and potential energy. Once the quadrature solution is found, simple expressions for kinetic and potential energy can be derived for the periodic wavetrain, which allows us to examine how equipartition between these two forms of energy is lost as amplitude increases. By using the fact that for our class of periodic waves the horizontal momentum I_k in both layers $k = 1, 2$ is zero, the layer kinetic energy (2.55) in terms of the mean Eulerian velocity (2.54) is

$$T_k = -\frac{\rho_k}{2} c h_k \widetilde{u}_k \,. \tag{2.79}$$

This expression (which is exact for Euler equations) shows that the mean Eulerian velocity must be negative for periodic waves with zero horizontal momenta in both layers. Notice that the model expression for the kinetic energy (2.55) does not immediately show this property of sign definiteness. However, by replacing the integration constant C_k given by (2.60) in the asymptotic relation (2.53), the mean Eulerian velocity in the

layer k can be expressed as a sum of two integrals

$$\begin{aligned} \widetilde{u}_k &= \frac{c}{L}\int_{-L/2}^{L/2}\left[1-\frac{h_k}{\eta_k}-\frac{h_k\zeta_X^2}{3\eta_k}\right]\,dX \\ &= \frac{c}{L}\int_{-L/2}^{L/2}\left[1-\frac{h_k}{\eta_k}\right]\,dx-\frac{c}{L}\int_{-L/2}^{L/2}\frac{h_k\zeta_X^2}{3\eta_k}\,dX\,, \end{aligned} \tag{2.80}$$

with the second being manifestly negative definite. For the first integral, by using Cauchy-Schwartz inequality, we obtain

$$\left(\int_{-L/2}^{L/2}\sqrt{\eta_k}\frac{1}{\sqrt{\eta_k}}dX\right)^2 \le \int_{-L/2}^{L/2}\eta_k dX\int_{-L/2}^{L/2}\frac{1}{\eta_k}dX = h_k L\int_{-L/2}^{L/2}\frac{1}{\eta_k}dX\,, \tag{2.81}$$

which implies that the first term in (2.80) is also negative

$$\int_{-L/2}^{L/2}\left[1-\frac{h_k}{\eta_k}\right]dX\le 0\,.$$

Thus, the quadrature expression for the mean kinetic energy for layer k, up to terms of order $O(\epsilon^4)$,

$$T_k = c^2\frac{h_k\rho_k}{2}\left[\frac{1}{\mathcal{L}(\boldsymbol{C})}\int_{\alpha_0-A}^{\alpha_0}\frac{3+R(\zeta,\boldsymbol{C})}{\eta_k\sqrt{R(\zeta,\boldsymbol{C})}}d\zeta-1\right]\,, \tag{2.82}$$

is positive definite. Here the parameters $\boldsymbol{C}(\alpha)$ are evaluated at $\alpha=\alpha_0$, the position of the crest – a root of the nonlinear equation (2.65) – and depend on the speed c and the amplitude A (which determines the position of the root $\alpha_0 - A$ of $R(\zeta,\boldsymbol{C})=0$ corresponding to the trough).

This expression of the kinetic energy, together with the expression for the potential energy (2.38), allow us to test the resilience of the equipartition of energy for our class

of periodic waves as the amplitude increases. This property is well known to hold for infinitesimal amplitude waves Yih [54], and we show below, when direct comparisons with Euler solutions are presented, that this property in fact depends strongly on period for both model and Euler solutions, in agreement with the finding of Holyer [22] for the different setup of doubly infinite depths.

2.5.3. Period dependence on speed and amplitude. Period average expressions such as the kinetic energy evaluated in the previous section depend, of course, on knowing the length L of the period where the average is computed. This is determined through the quadrature by (2.30), and is therefore linked to the process of root finding for our class of solutions described above. Unfortunately, this prevents us from writing a simple and explicit functional dependence of period on A and c, and to find the level sets of L over the (A, c) domain we have to resort to numerical methods. To implement this, we determine the periodic wave solutions at the nodes of a grid covering the existence domain, then compute the corresponding period and construct the level sets by interpolation. Notice that for determining the periodic solutions at each node, we need the two limiting positions $\beta_e(A, c)$ and $\beta_d(A, c)$. This requires inversion of the function $a(c; \beta)$ given by (2.71), and the inversion can only be achieved numerically by solving the two equations $a(c; \beta) = A$, and $a(c; \beta) = -A$.

A strategy for reducing the computational cost is to cover the domain of existence with only one of the foliating family of solitary waves, β_d when $h_r < h_{critical}$ or β_e when $h_r > h_{critical}$, by taking into account the observations made in §2.5.1. These curves are given in closed form by equation (2.71) and provide a good initial guess for the position of the crest of periodic waves solutions. For constructing a constant period contour,

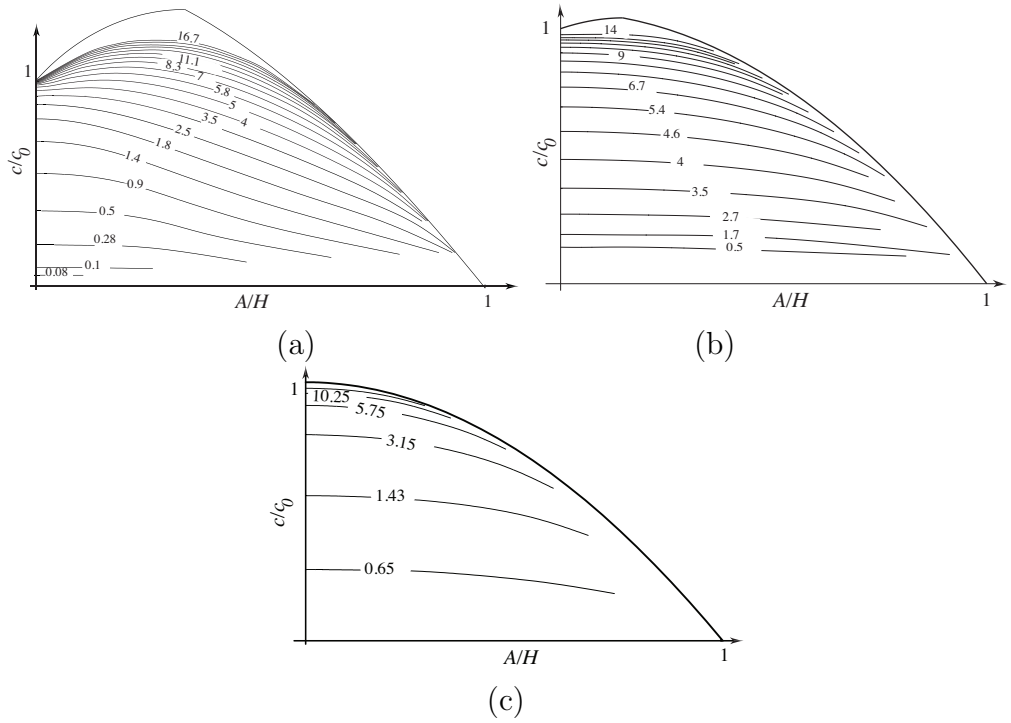

FIGURE 2.10. Level sets of period (nondimensionalized with the total height H) for a configuration with (a) $h_r < \sqrt{\rho_r}$ ($h_1/H = 1/6$, $h_2/H = 5/6$ and $\rho_r = 0.97$), (b) $h_r > \sqrt{\rho_r}$ ($h_1/H \simeq 0.56$, $h_2/H \simeq 0.44$ and $\rho_r = 0.5$), (c) $h_r = \sqrt{\rho_r}$ ($h_1/H \simeq 0.41$, $h_2/H \simeq 0.58$ and $\rho_r = 0.5$).

we: (i) determine solutions along the foliating solitary wave curves, by using parameter continuation techniques for accelerating the root finding process; (ii) interpolate the period as a function of speed c on these curves; (iii) determine for each curve the root c corresponding to that particular period; finally (iv) perform a spline interpolation for the (A, c) pairs found in the previous step.

In Figure 2.10(a)-(c) we present period isolines for three particular configurations corresponding to $h_r < h_{critical}$, $h_r > h_{critical}$ and $h_r = h_{critical}$, respectively. There are several interesting qualitative observations that can be made based on these numerical results. First, notice that the period increases with the increase of phase speed, which is in agreement with a general result for periodic waves in arbitrary stratification, proved

by Yih [54]. Second, all period isolines wrap along the front line as the amplitude increases, converging to a singular limit that corresponds to a steep front of amplitude equal to the total depth of the fluid. Although this limit is mathematically attainable, it is not of practical relevance since it lies outside of the domain of expected validity of solutions with respect to the parent Euler system, as we are going to see in the following section. Third, we note that away from critical depth ratio, we can identify two types of isolines: those along which the phase speeds are sub-critical and those that contain regions with super-critical speeds. On both sub- and super-critical isolines, the periodic solutions approach one of the two limiting foliating families (β_d for $h_r < h_{critical}$ or β_e for $h_r > h_{critical}$) at a much faster rate than the other as the amplitude increases – see Figure 2.11 for a configuration with $h_r > h_{critical}$. However, on sub-critical isolines, we can identify a region where both the position of the crest and the trough are nearly symmetrical with respect to the (zero mean) z-axis, and lie away from the bounds given by β_d and β_e. In these regions, the phase speed is comparable to the speed of waves of infinitesimal amplitude.

Finally, we mention that a good approximation to the actual location of the bounding roots α (for waves of depression) or $\alpha - A$ (for waves of elevation), respectively, for fixed amplitude A and period L can be found for sufficiently large period waves by a simple area criterion based on the effective wavelength λ_I (as defined by Koop & Butler [29] through the area integral of solitary wave profiles) of limiting foliating solutions, based on the closeness result illustrated by Figure 2.11 – see Appendix B, equation (B.19).

2.5.4. Limits of validity of the strongly nonlinear model. Our goal is to determine regions within the domain of existence of periodic solutions of the strongly nonlinear

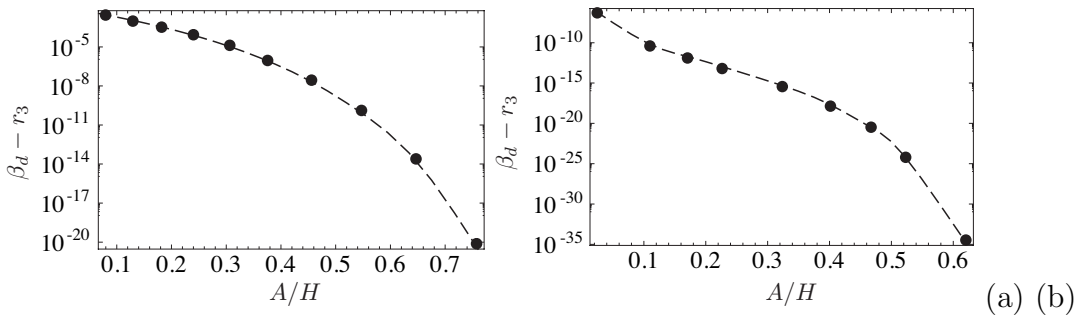

(a) (b)

FIGURE 2.11. Distance between the crest of the periodic solution and the corresponding foliating solitary wave $\beta_d - r_3$ along the constant period contours (a) $L/H = 3.25$, (b) $L/H = 16.67$ for the configuration from Figure 2.10(a).

model where we can expect good agreement with Euler solutions. We expect this agreement to be satisfactory when the long wave assumption at the basis of the asymptotic model is satisfied *in each layer*. Let $d_k = \max(\eta_k)$ denote the maximum thickness of layer k, $(k = 1, 2)$ and λ a characteristic wavelength. A condition that would insure that the long wave assumption holds in both layers is

$$\max(d_1, d_2)/\lambda \ll 1\,.$$

Thus, to establish a validity criterion we need an a priori estimate of a characteristic horizontal length-scale as well as upper bounds for the thickness of each layer. Once again, the limiting positions corresponding to the foliating solitary waves β_d and β_e prove to be useful.

First, we focus on the quasilinear regime. For the region within the domain of existence where $\beta_d/A > 1/2$ and $|\beta_e|/A > 1/2$, the position of the crest and trough of the periodic wave solutions are far from the corresponding limiting positions and quasi-symmetrical with respect to the interface, which translates in an almost-sinusoidal wave shape. The maximum layer-thickness is therefore well approximated by $d =$

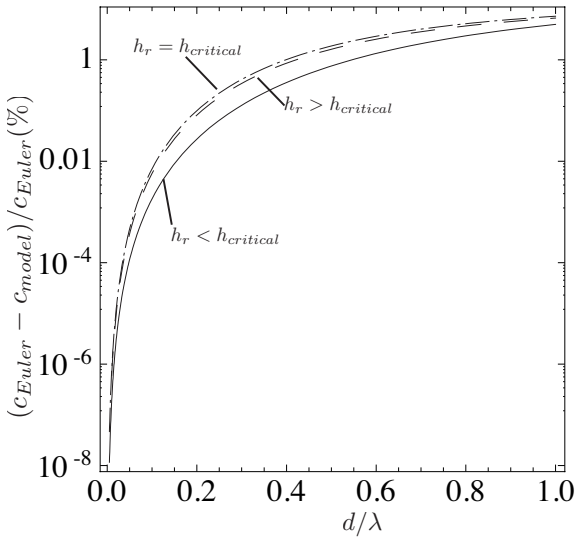

FIGURE 2.12. Error in the speed of waves of infinitesimal amplitude of the strongly nonlinear model with respect to Euler dispersion relation as a function of the long wave parameter d/λ for the configurations from Figure 2.10.

$\max(h_1 + A/2, h_2 + A/2)$. Furthermore, the dispersion relation for infinitesimal waves (relation (3.42) - Choi & Camassa [7]) offers a reasonable approximation for the dependence of the period on the phase speed for periodic solutions, hence a good estimate for the horizontal length scale is half the period of the infinitesimal waves with speed c. Note that the dispersion relation of the two layer model no longer agrees with the dispersion relation of Euler equations (Lamb [33], pag. 231) when the long wave parameter d/λ is not sufficiently small – see Figure 2.12 for typical errors in speed of the model with respect to Euler predictions. Thus, by using the discrepancy between Euler and model dispersion relation, we can infer a threshold long wave parameter that isolates the region of validity of the strongly nonlinear model from this first part of the domain.

For the region within the domain of existence where $\beta_d/A < 1/2$ (or $|\beta_e|/A < 1/2$), the position of the crest (or the position of the trough) of periodic solutions approaches

the limiting position β_d (or β_e). In this case, the maximum layer depth is well approximated by $d = \max(h_2 + \beta_d, h_1 - \beta_d + A)$ (or $d = \max(h_1 - \beta_e, h_2 + \beta_e + A)$) whereas the characteristic horizontal length scale of the foliating solitary waves provides a good estimate for the horizontal length scale of periodic solutions since the wave shapes are comparable. Obvious candidates for a characteristic length-scale of solitary waves are the effective wavelength λ_I and the ratio between the amplitude and the maximum slope of the interface ($\lambda_S = A/\max[\zeta_X]$). An analytical expression for the effective wavelength in terms of elliptic functions has been derived in Choi & Camassa [7] in the case of solitary waves with no currents at infinity. In Appendix A we report the relationships for effective wavelength corresponding to solitary waves on general currents at infinity (see Table 1) along with a strategy for computing the maximum slope of solitary waves and fronts – see (A.26). We can thus define two long wave parameters based on the effective wavelength

$$\epsilon_I = d/\lambda_I\,, \tag{2.83}$$

and on the wavelength derived from maximum slope

$$\epsilon_S = d/\lambda_S\,. \tag{2.84}$$

The condition $\epsilon_S \ll 1$ measures the *local* validity of the solutions and therefore is a much more restrictive criterion than $\epsilon_I \ll 1$, which is a an average of the steepness of the profile with respect to the thickness of the layer. We thus expect that for $\epsilon_I \ll 1$ and $\epsilon_S \sim O(1)$ to have a reasonable overall agreement with Euler solutions, while locally the

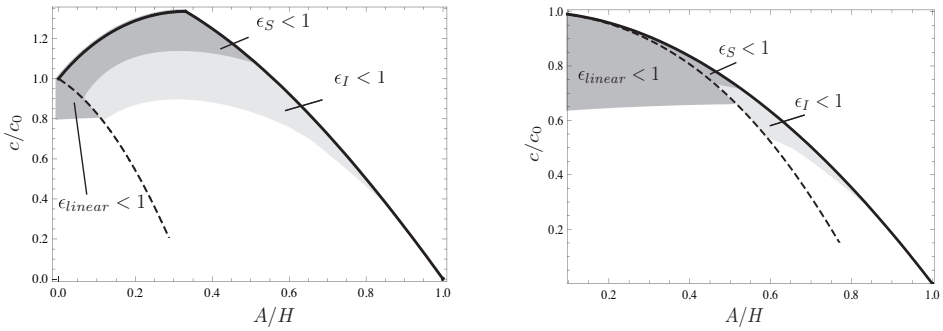

FIGURE 2.13. Regions in the domain of existence where we can expect a good agreement of the solutions of the strongly nonlinear model with Euler solutions for the configurations from Figures 2.10(a) and (c), respectively. The region at the left of the dashed line contains solutions with quasi-sinusoidal wave shapes whereas for the region at the right the periodic solutions approach the foliating family β_d.

model predicted profile does not match the Euler solution. We note that in the limit to fronts, however, the effective wavelength diverges to infinity, the only measure of a characteristic horizontal length-scale being provided by the maximum slope criterion. We summarize these ideas in Figure 2.13, where we depict the regions in the domain of existence of periodic solutions where the long wave parameter is smaller than unity.

We remark that some of the validity regimes we have identified could follow the classification of two-layer asymptotic models provided by Bona *et al.* [5], however we have not pursued this analysis here and work strictly with our model within their "shallow-shallow" configuration. In this context, it is worth mentioning that the strongly nonlinear model seems to work rather well (but not always) even outside this configuration.

2.6. Validation of the model by comparison to Euler solutions

In this section, we compare periodic solutions of zero horizontal momentum in each layer obtained by the strongly nonlinear model against numerical solutions of the full

Euler system under the same constraints. As remarked above, because of equation (2.47), this also implies that the layer horizontal momenta are zero, for both model and Euler solutions. We first concentrate on the parent two-layer Euler system, using the algorithm based on boundary integrals documented in Rusås [44], Grue *et al.* [19]. Convergence properties of this algorithm have been extensively studied in these references and others. We have performed further tests in the context of the present work within our constrained class. We have adapted this algorithm to seek solutions of a prescribed mean elevation, which requires a continuation search on the initial guesses for this iterative algorithm (the details of this continuation procedure are not important here and will be reported elsewhere). In particular, we focus here on the practical limitations of the asymptotic model in view of the validity estimates of §2.5.4, by testing the model with this class of periodic waves as well as their limiting forms of solitary waves and fronts, in various parametric regimes. Of course, the two-layer setup is highly idealized. In order to assess the relevance of this idealization, we next compare periodic solutions of Euler equations for *continuous* (but still near two-layer) stratification, obtained with a variant of the algorithm of Turkington *et al.* [51], by looking at relevant diagnostics such as wave profile and fluid velocities.

2.6.1. Two-layer Euler system vs. strongly nonlinear model. For a given density ratio ρ_r between the two layers, the subcritical and supercritical regimes ($h_r < \sqrt{\rho_r}$ and $h_r > \sqrt{\rho_r}$ respectively) will have many similarities, with the sole exception being the "polarity" of the waves. As pointed out before, this is reflected in the tendency of the crests or troughs, respectively, to flatten first with increasing amplitude. The critical

case on the other hand is special and deserves a separate study. Accordingly, in the next two sections we report results from the subcritical and critical case only.

$$h_r < h_{critical}.$$

First, we look at a subcritical configuration $h_r < h_{critical} \equiv \sqrt{\rho_r}$, whose speed vs. amplitude chart is illustrated by Figure 2.10(a). The corresponding chart with several constant-period curves computed with the full Euler two-layer system are reported in Figure 2.14, where the regions of validity discussed in the previous section are identified by shaded portions of the existence domain.

Some general features of the comparison between strongly nonlinear model and the full Euler solutions emerge from this figure. First, both strongly nonlinear and Euler models share the presence of two types of period isolines – isolines along which the phase speeds are subcritical $c < c_0$ and isolines that have a portion on which the phase speeds are supercritical $c > c_0$. As one can see from Figure 2.14, the agreement between model and Euler predictions is in general superior in the region where the phase speeds are supercritical (and the period is larger).

Next, the discrepancy between model and Euler period isolines amplifies with increasing amplitude, this tendency being enhanced by decreasing period. While the model isolines wrap on the right boundary of the existence domain (corresponding to the branch of fronts) as the amplitude increases, Euler isolines reach a maximum amplitude and overturn, which correspond to periodic wave profiles of the overhanging nature (multiple-valued interface for given x-locations) reported in the literature in different setups (either infinite depth fluids or front solutions, see e.g., Meiron & Saffman [37], Turner & Vanden-Broeck [52], respectively). Prolonging the constant period isolines past the overturning

seems to lead to periodic waves of smaller amplitude and larger speed with deeper overhangs, until this process terminates with a wave of a self-intersecting profile of extreme form – see Figures 2.15(a)–(d). We remark that this process of termination by self intersection can only be conjectured at this point and may not apply to long period waves, where we have not been able to achieve convergence of the Euler code. Moreover, this process may not apply to the infinite depth case, see Turner & Vanden-Broeck [52]. We further remark that both sub-critical and super-critical period isolines overturn in the region of subcritical phase speeds, and that the size of the overturning region decreases with increasing period. The phenomenon of overhanging periodic waves is connected with the existence of a maximum amplitude, single valued Euler wave profile for a given period. The envelope of constant period isolines for subcritical speeds defines a maximum amplitude boundary for single-valued solutions of two-layer Euler equations – see the dashed-dotted curve in Figure 2.14(a). It is remarkable that the strongly nonlinear model, for which all periodic solutions are naturally single valued, still manages to inform about this envelope through the setting of a threshold for model validity based on the slope achieved along the proper foliating solutions (computed with (A.26)) in the existence domain – see Figure 2.14(b).

Another important feature of the Euler solutions emerges from this plot, namely the nonuniqueness of periodic waves of given amplitude and speed. As can be seen from Figure 2.14(a), there exists a set of points in the parameters space $(A\,, c)$ at the left of the dashed-dotted curve, where at least two Euler solutions, one regular whose profile is a single-valued graph of x and one multiple-valued of the overhanging type, move at the same speed with the same amplitude (but with different periods).

In Figure 2.16 we compare the Euler solutions against model predictions for the points marked on Figure 2.14(a), while Figure 2.19 presents a comparison between model results and Euler results for the mean kinetic and potential energy. In particular, one can clearly see the equipartition of kinetic and potential energies for small amplitude waves for both strongly-nonlinear and full Euler solutions.

The progressive breakdown of the strongly nonlinear model's fidelity is captured reasonably well from the effective wavelength criterion discussed in the previous section. The condition $\epsilon_S \ll 1$ isolates the level sets of period predicted by the model which best match the Euler level sets. However, notice that the strongly nonlinear model performs well even in regions where $\epsilon_S \sim O(1)$ provided the long wave parameter based on effective wavelength ϵ_I is much smaller than unity. Also notice that for all period isolines of the model, the wave shapes are steepening and converging to a front of amplitude H with the "effective" wavelength $(h_r/(h_r+1))\,L$ selected by mass conservation. This horizontal length scale is a good estimate for the effective wavelength of both model and Euler wave profiles – see Figures 2.17 and 2.18.

$$h_r = h_{critical}.$$

For a configuration corresponding to the critical depth ratio, the domain of existence of solutions of the strongly nonlinear model contains only sub-critical speeds $c < c_0$, and the only limiting forms of periodic waves consist of fronts. In this instance the quasi-linear region (where the wave shapes are quasi-sinusoidal) occupies a larger portion of the domain of existence– see Figure 2.20(a). As expected, the agreement of the strongly

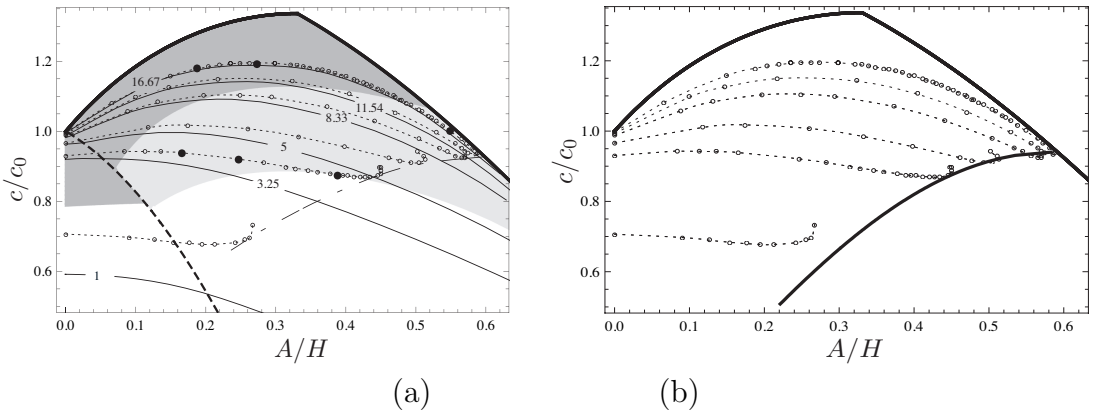

FIGURE 2.14. (a) Isolines of period (labeled with L/H) for the configuration from Figure 2.10(a); Continuous line - strongly nonlinear model, dotted line & data points - Euler solutions. The dashed-dotted curve marks the limiting amplitude, inferred from the numerical results obtained with the Euler code, before overhanging develops. The shaded areas are the estimated regions of validity of the strongly nonlinear model – see Figure 2.13(a). (b) Slope level set curve for foliating solutions and Euler period isolines, corresponding to the slope angle of approximately 40° degrees. The model tracks the location of the envelope from the numerically computed Euler isolines for most of the domain.

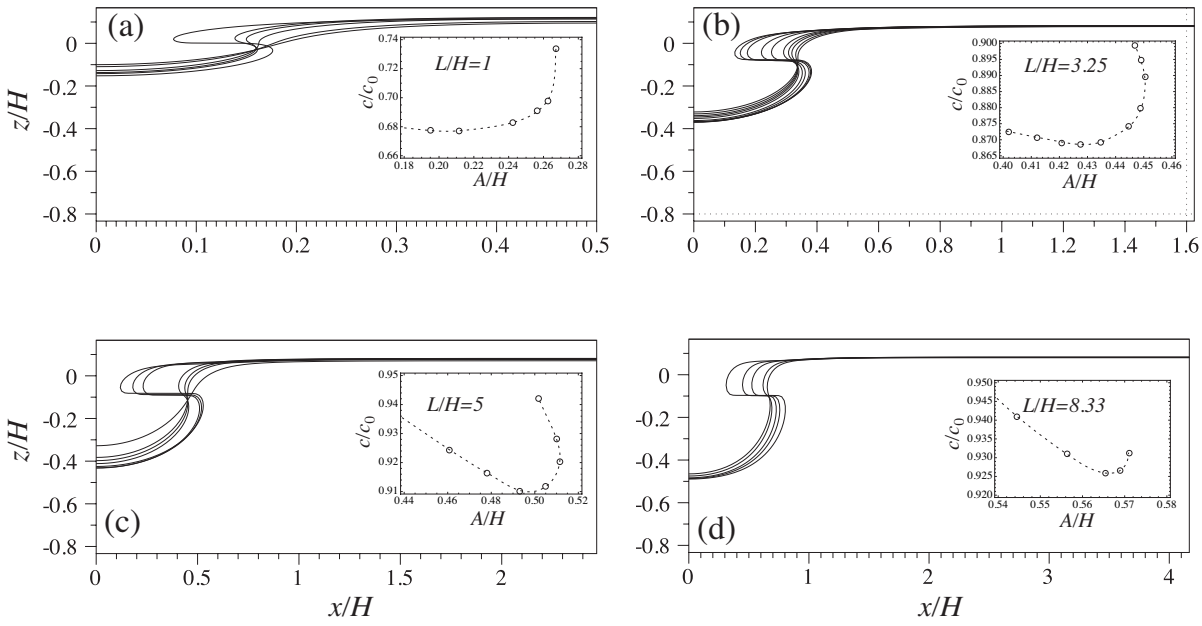

FIGURE 2.15. (a) – (d) Euler solutions of near maximal amplitude along four period isolines from Figure 2.14. The period and the corresponding pairs amplitude-speed are marked in the inserts.

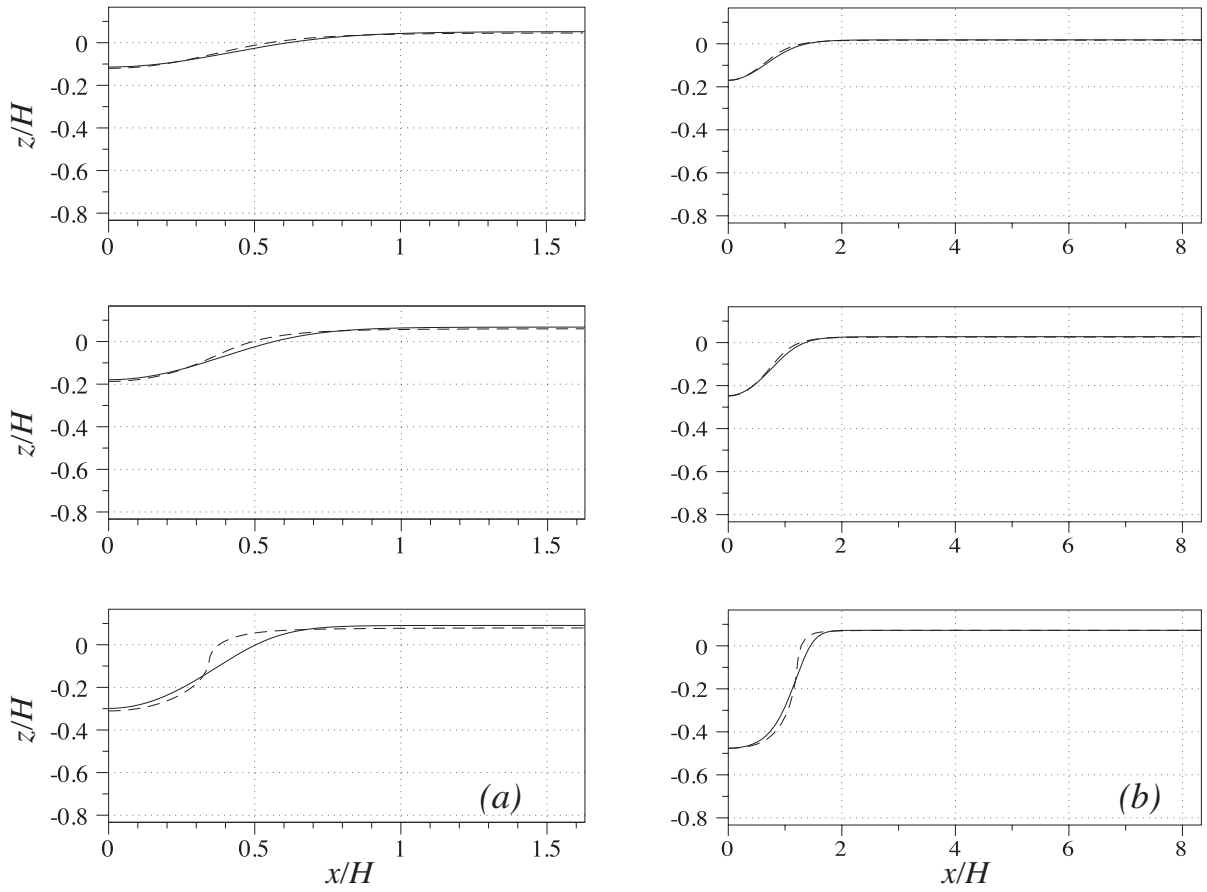

FIGURE 2.16. Comparison between model (continuous line) and Euler solutions (dashed line) corresponding to the points marked on Figure 2.14, for (a) $L/H = 3.25$ and (b) $L/H = 16.67$, respectively.

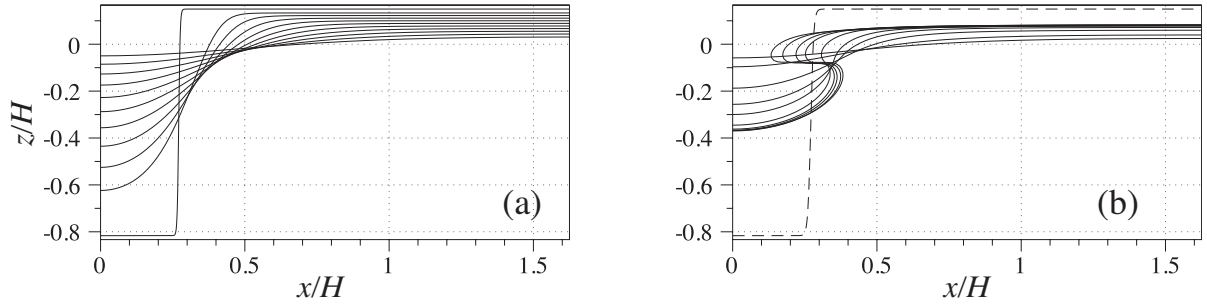

FIGURE 2.17. Waves shapes on an isoline of period $L/H = 3.25$. (a) Model, (b) Euler (the dashed line reports the model predicted limiting front with speed 0 and amplitude H from the left panel (a)).

nonlinear model with Euler is superior in the regions with $\epsilon_S \ll 1$. Notice that when the period increases, the isolines of period wrap along the front branch of the domain

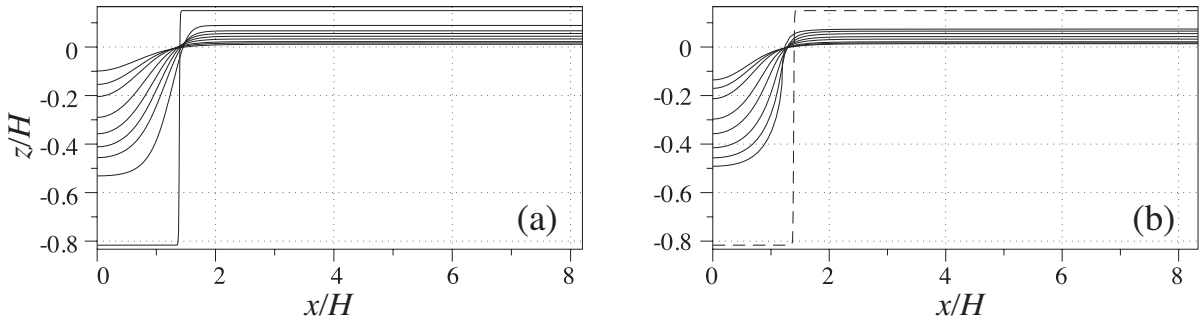

FIGURE 2.18. Same as Figure 2.17 for $L/H = 16.67$.

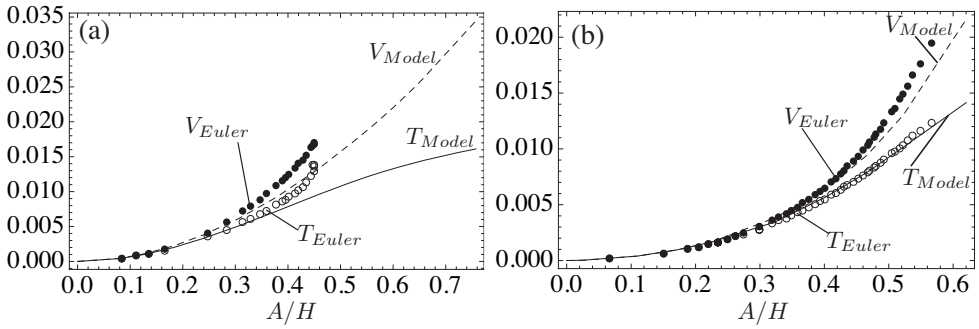

FIGURE 2.19. Mean kinetic energy (continuous - strongly nonlinear model, circles - Euler solutions) and mean potential energy (dashed - strongly nonlinear model, dots - Euler solutions) on two isolines of period from Figure 2.14: (a) $L/H = 3.25$ and (b) $L/H = 16.67$, respectively. The energies are nondimensionalized with γH^2.

of existence of the strongly nonlinear model solutions, which confirms that the front branch represents an actual branch of front solutions for the full Euler equations. We remark that these fronts are not the "classical" fronts on uniform currents studied in Dias & Vanden-Broeck [9]. In Figure 2.20(b)–(d), we compare the Euler wave shapes corresponding to points on the front branch to front solutions of the strongly nonlinear model, by matching the zero crossing points of the profiles. The agreement is quite reasonable even when ϵ_S is order $O(1)$.

2.6.2. Continuous stratification Euler system vs. strongly nonlinear model. We complete the study of our class of periodic waves with a limited comparison of results

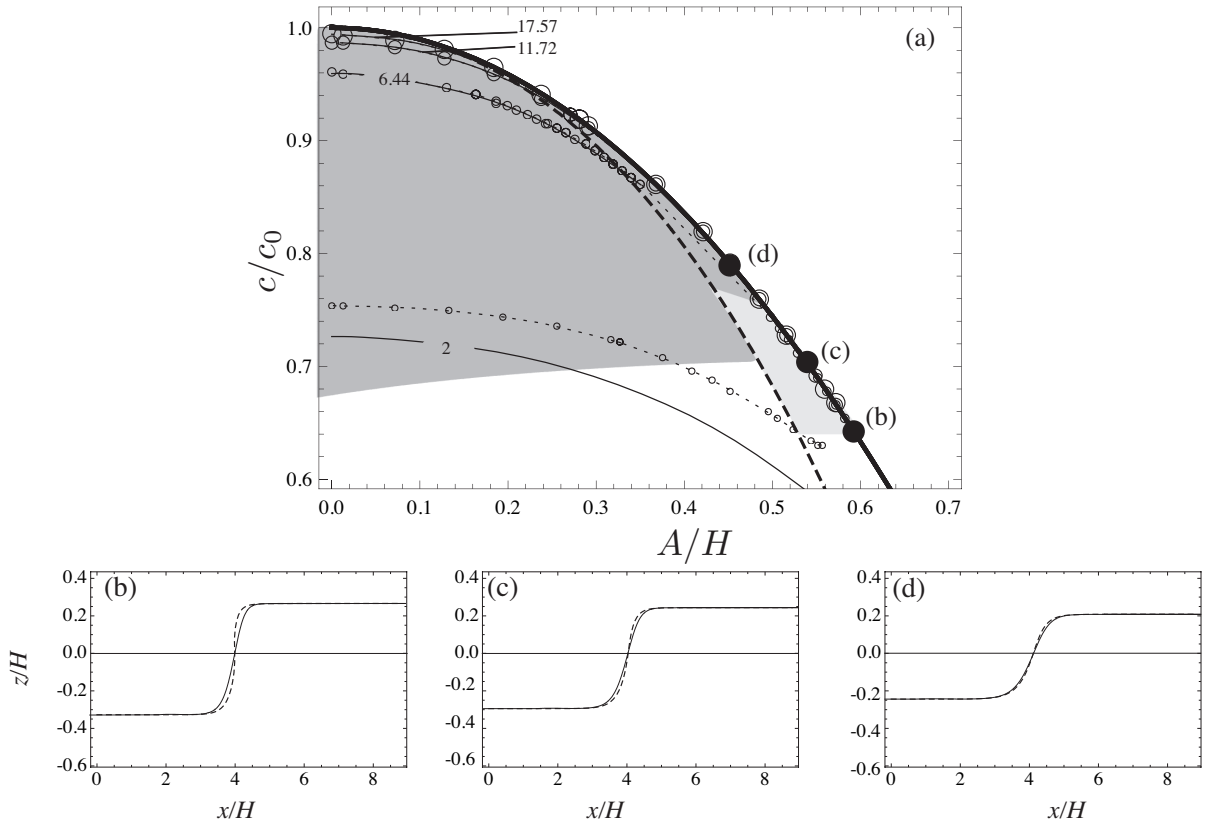

FIGURE 2.20. (a) Isolines of period (labeled with L/H) for the configuration from Figure 2.10(c); Continuous line - strongly nonlinear model, dotted line & data points - Euler solutions. The dashed curve corresponds to $\beta_d/A = 1/2$ whereas the shaded areas are the regions of validity of the strongly nonlinear model – see Figure 2.13(b). (b)-(d) Dashed line – Euler periodic solutions (half profile) with period $L/H = 17.56$ and with speed and amplitude corresponding to the points marked in Figure 2.20(a), continous line – front solution of the strongly nonlinear model with the same speed and amplitude. The profiles are aligned at the zero crossing points.

of the two-layer strongly nonlinear model with periodic wave solutions of Euler equations with *continuous* stratification. Stationary periodic solutions for the latter are determined by using an iterative scheme described in Turkington *et al.* [51]. This algorithm solves the Dubreil-Jacotin-Long (DJL) equation through minimization of kinetic energy for prescribed potential energy.

The unperturbed continuous stratification consists of two layers of constant density, separated by a thin diffused interface. Figure 2.21(a) displays the density field corresponding to a periodic wave solution in the presence of sharp stratification (pycnoline width relative to the height of the domain ~ 0.03). Following the strategy outlined in §3, we determine a two layer configuration which approximates the continuous stratification by optimizing with respect to critical speed, mass and potential energy of a reference equilibrium state. In Figure 2.21(b) we compare the isopycnal surface corresponding to $\overline{\rho}(h_2)$ from the Euler solution ($\overline{\rho}$ is the stratification of the equilibrium configuration, h_2 is the thickness of the bottom layer for the optimal two-layer approximation), versus the interface predicted by the strongly nonlinear model. Figure 2.21(c) compares the self-induced horizontal shear at the maximum displacement of the pycnocline with the horizontal velocity profiles predicted by the strongly-nonlinear model asymptotics, through the reconstructed z-dependence of the velocity field provided by equation (2.49). We remark that our implementation of the DJL solver, while allowing for the volume flux to be set to zero, does not impose the constraint of zero horizontal momentum for the resulting solution. However, for the solution shown here as well as for most of the ones we have studied, the momentum evaluated diagnostically after their computation turns out to be very close to zero.

2.7. Other classes of periodic waves

In this last section, we review a few alternatives of our choice of constraints as well as models reported in the literature for periodic wave motion in a two-layer system of finite depth. These alternatives, all share with our model the assumption of single-valuedness

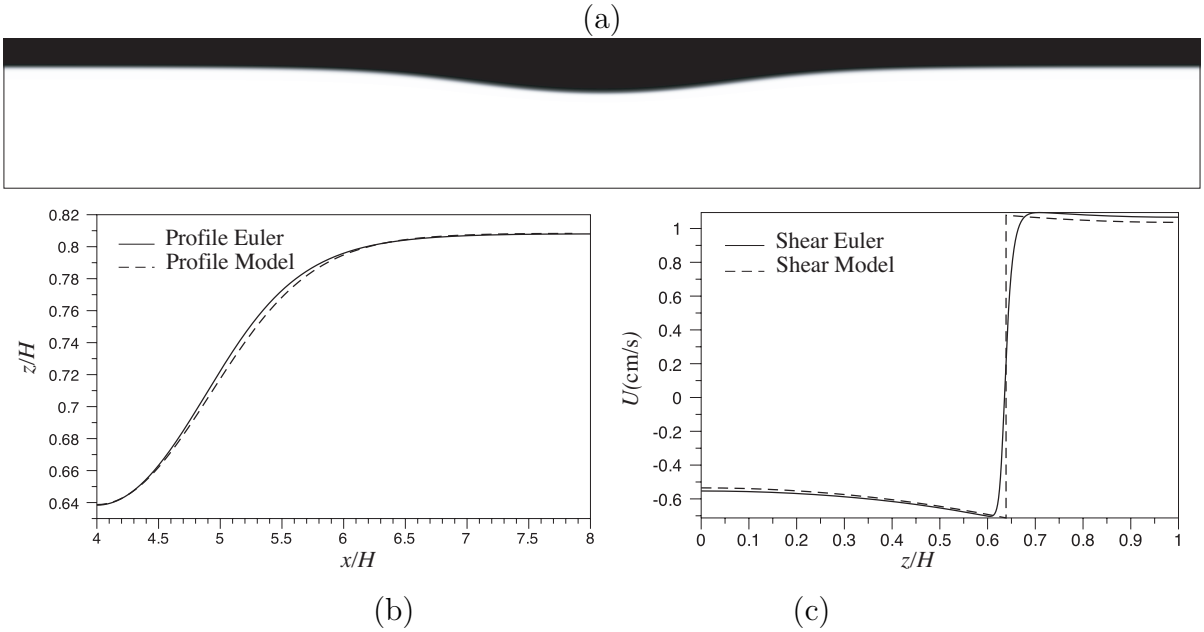

FIGURE 2.21. (a) Density field for a periodic wave in continuous stratification. $H = 77cm$, period $L/H = 8$, $\rho_r \sim 0.977$. (b) Wave profile comparison. (c) Shear at the wave trough.

of the interface between the two layers, thereby excluding overhanging wave solutions. With this functional assumption, the minimal number of quantities needed to determine a unique wave train is five for all cases, just as in our study of the strongly nonlinear model.

We remark that the majority of these alternative studies are aimed at the limiting forms of periodic waves corresponding to solitary waves on zero currents at infinity, the issue of the possible generation mechanisms of periodic wave trains thus being circumvented. These alternatives leave the mean position of the interface a priori undetermined, and seek some other constraints fixing the five quantities that determine the periodic wave-train. In the following, we show how to cast these different constraints in the framework of the strongly nonlinear model.

2.7.1. Periodic waves with prescribed fluxes, total flow force and Bernoulli constants. We note that there appears to be no rigorous proof regarding the minimal set of constants of motion for general symmetric periodic solutions of Euler equations in *two-layer* systems. Such a proof has been provided in recent years by Benjamin [3] for the *one-layer* case, addressing a long-standing conjecture by Benjamin & Lighthill [4] based on a model of small-amplitude, long-wave periodic motion. Thorpe [49] presents a similar construction for a two-layer (weakly nonlinear) system; in his approach five wave-frame invariants generalizing those in Benjamin & Lighthill [4] would completely characterize a periodic wave-train, viz., mass fluxes in each layer, Bernoulli constants in each layer and total flow force.

In the following we use the fact that the Bernoulli constants, being related by continuity in pressure at the interface, are not independent, and only the difference between them (which we will denote by $\mathcal{R}$) can be regarded as a true motion invariant. Moreover, in the periodic setting there is no reference state to which an asymptotic pressure head can be related, thereby fixing (one of) the Bernoulli constants. An additional invariant (the total flow-force $\mathcal{S}$ in our notation) can then be obtained by relating the flow force to the Bernoulli constants. Thus, we retrieve the same count of constraints in the *wave frame* as the one previously found with the strongly nonlinear model, viz., $\mathcal{R}\,,\mathcal{S}$ and the wave frame volume fluxes in each layer $\widehat{Q}_1$ and $\widehat{Q}_2$. The phase speed, which defines the lab frame of reference, can be viewed as an additional degree of freedom.

Integrating (A.29) over the wave period at $z = h_1$ and $z = -h_2$ for each layer, respectively, yields

$$R_1 = \frac{1}{L}\int_0^L p_1|_{z=h_1} dX + \frac{1}{2}\widetilde{\widehat{u}^2}|_{z=h_1} + \rho_1 g h_1 \,, \tag{2.85}$$

$$R_2 = \frac{1}{L}\int_0^L p_2|_{z=-h_2} dX + \frac{1}{2}\widetilde{\widehat{u}^2}|_{z=-h_2} - \rho_2 g h_2 \,, \tag{2.86}$$

where $\widetilde{\widehat{u}^2}|_{z=h} = \frac{1}{L}\int_0^L (\widehat{u}|_{z=h})^2 dX$. We compute the integrals of the pressure at the two walls (first terms in the RHS of the above relations), by integrating over one periodic box domain the vertical momentum equation in the wave frame in each layer

$$\rho_k(\widehat{u}_k\widehat{v}_{kX} + \widehat{v}_k\widehat{v}_{kz}) = -p_{kz} - \rho_k g \,, \qquad k = 1\,, 2\,. \tag{2.87}$$

By incompressibility, the kinematic condition at the interface ($\zeta_X\widehat{u}_k = \widehat{v}_k$) and the periodicity of the motion shows that the LHS integrates to zero,

$$\int_0^L \int_{[\eta_k]} (\widehat{u}_k\widehat{v}_{kX} + \widehat{v}_k\widehat{v}_{kz}) dz\, dX = \int_0^L \int_{[\eta_k]} ((\widehat{u}_k\widehat{v}_k)_X - \widehat{v}_k\widehat{u}_{kX} + \widehat{v}_k\widehat{v}_{kz}) dz\, dX$$

$$= \int_0^L \frac{\partial}{\partial X}\left(\int_{[\eta_k]} \widehat{u}_k\widehat{v}_k dz\right) dX + \int_0^L (-\zeta_X(\widehat{u}_k\widehat{v}_k)|_\zeta + \widehat{v}_k^2|_\zeta) dX = 0\,.$$

The RHS for the bottom layer is

$$\int_0^L \int_{-h_2}^{\zeta} (-p_{2z} - \rho_2 g) dz\, dX = \int_0^L (p_2|_{z=-h_2} - p_2|_\zeta)\, dX - \rho_2 g \widetilde{h}_2 L\,,$$

while for the upper layer we have

$$\int_0^L \int_{\zeta}^{h_1} (-p_{1z} - \rho_1 g) dz\, dX = \int_0^L (p_1|_\zeta - p_1|_{z=h_1}) dX - \rho_1 g \widetilde{h}_1 L\,,$$

and therefore

$$\int_0^L p_2|_{z=-h_2} dX - \int_0^L p_2|_{z=\zeta} dX = \rho_2 g \widetilde{h}_2 L \,, \tag{2.88}$$

$$\int_0^L p_1|_{z=\zeta} dX - \int_0^L p_1|_{z=h_1} dX = \rho_1 g \widetilde{h}_1 L \,, \tag{2.89}$$

where $\widetilde{h}_k$ is the mean depth of layer k. Summing up the above relations and using the continuity of pressure across the interface yields

$$\int_0^L (p_2|_{z=-h_2} - p_1|_{z=h_1}) dX = (\rho_1 \widetilde{h}_1 + \rho_2 \widetilde{h}_2) g L \,.$$

The difference between equations (2.85) and (2.86) then provides a first motion invariant $\mathcal{R} \equiv R_2 - R_1$

$$\mathcal{R} = \gamma \widetilde{\zeta} + \frac{\rho_2}{2} \widetilde{\widehat{u}^2}|_{z=-h_2} - \frac{\rho_1}{2} \widetilde{\widehat{u}^2}|_{z=h_1} \,, \tag{2.90}$$

where $\widetilde{\zeta}$ is the mean position of the interface.

To determine a second motion invariant connecting the flow force to the Bernoulli constants, we rewrite the wave-frame Bernoulli equation in each layer as

$$(p_k + \rho_k \widehat{u}_k^2) + \rho_k \widehat{v}_k^2 + (p_k + \rho_k g z) + \rho_k g z = 2R_k \,, \qquad k = 1, 2 \,.$$

For the bottom layer, by multiplying the momentum equation (2.87) by $(h_2 + z)$ and adding it to the Bernoulli equation we obtain

$$(p_2 + \rho_2 \widehat{u}_2^2) + \frac{D\left[(h_2 + z)\widehat{v}_2\right]}{Dt} + \left[(h_2 + z)(p_2 + \rho_2 g z)\right]_z + \rho_2 g z = 2R_2 \,, \tag{2.91}$$

where $D[\cdot]/Dt \equiv \widehat{u}_2\partial_X(\cdot) + \widehat{v}_2\partial_z(\cdot)$ is the usual definition of material derivative.

In this equation, the integral of the second term in the LHS over the periodic box domain for this bottom layer is zero. Indeed, we have, by completing derivatives and by carrying out a z-integration,

$$\int_0^L \int_{-h_2}^{\zeta} [\widehat{u}_2((h_2+z)\widehat{v}_2)_X + v_2((h_2+z)\widehat{v}_2)_z]\, dz\, dX = \int_0^L \int_{-h_2}^{\zeta} (\widehat{u}_2(h_2+z)\widehat{v}_2)_X dz\, dX -$$

$$- \int_0^L \int_{-h_2}^{\zeta} \widehat{u}_{2X}(h_2+z)\widehat{v}_2\, dz\, dX + \int_0^L (\widehat{v}_2|_\zeta)^2\, \eta_2\, dX - \int_0^L \int_{-h_2}^{\zeta} (h_2+z)\widehat{v}_2\widehat{v}_{2z}\, dz\, dX\,.$$

The second and last term of the above expression cancel by continuity, while the first term can be rewritten by chain rule with integration to yield

$$\int_0^L \frac{\partial}{\partial X}\left(\int_{-h_2}^{\zeta} \widehat{u}_2(h_2+z)\widehat{v}_2 dz\right) dX - \int_0^L \zeta_X \widehat{u}_2|_\zeta \widehat{v}_2|_\zeta \eta_2\, dX + \int_0^L (\widehat{v}_2|_\zeta)^2\, \eta_2\, dX = 0\,,$$

where the cancellation is due to periodicity (first term) and to the kinematic condition at the interface (second and third term).

As to the other three terms in equation (2.91), carrying out the integration over the period box domain, yields

(2.92)
$$\int_0^L \int_{-h_2}^{\zeta} (p_2 + \rho_2 \widehat{u}_2^2) dz dX + \int_0^L \left[(\zeta+h_2)(p_2|_\zeta + \rho_2 g\zeta) + \rho_2 g \frac{\zeta^2 - h_2^2}{2}\right] dX = 2R_2\widetilde{h}_2 L\,.$$

For the upper layer, by multiplying the momentum equation by $(z-h_1)$ and following the same procedure, we obtain

(2.93)
$$\int_0^L \int_{\zeta}^{h_1} (p_1 + \rho_1 u_1^2) dz dX + \int_0^L \left[(h_1-\zeta)(p_1|_\zeta + \rho_1 g\zeta) + \rho_1 g \frac{h_1^2 - \zeta^2}{2}\right] dX = 2R_1\widetilde{h}_1 L\,.$$

By adding (2.92) and (2.93) and dividing by the period length we obtain for the total flow force S

$$S+\frac{1}{L}\int_0^L Hp|_\zeta dX+\frac{g(\rho_1 h_1^2-\rho_2 h_2^2)}{2}+\frac{3\gamma}{2}\,\widetilde{\zeta^2}+\frac{g(\rho_1 h_1+\rho_1 h_1)}{2}\,\widetilde{\zeta}=2(\widetilde{h}_1 R_1+\widetilde{h}_2 R_2)\,, \tag{2.94}$$

where we have defined the mean-square wave elevation

$$\widetilde{\zeta^2}=\frac{1}{L}\int_0^L \zeta^2(X)dX\,. \tag{2.95}$$

Using equations (2.85-2.88) we obtain

$$\frac{1}{L}\int_0^L p_1|_\zeta dX = R_1-\frac{\rho_1}{2}\widetilde{\widehat{u}^2}|_{z=h_1}-\rho_1 g\widetilde{\zeta}\,, \tag{2.96}$$

$$\frac{1}{L}\int_0^L p_2|_\zeta dX = R_2-\frac{\rho_2}{2}\widetilde{\widehat{u}^2}|_{z=-h_2}-\rho_2 g\widetilde{\zeta}\,. \tag{2.97}$$

Continuity of pressure at the interface $p_1|_\zeta = p_2|_\zeta = p|_\zeta$, by adding the above relations after multiplication with $\widetilde{h}_1$ and $\widetilde{h}_2$, respectively, yields

$$\frac{1}{L}\int_0^L Hp|_\zeta dX=\widetilde{h}_1 R_1+\widetilde{h}_2 R_2-\frac{\rho_1\widetilde{h}_1}{2}\widetilde{\widehat{u}^2}|_{z=h_1}-\frac{\rho_2\widetilde{h}_2}{2}\widetilde{\widehat{u}^2}|_{z=-h_2}-g(\rho_1\widetilde{h}_1+\rho_2\widetilde{h}_2)\widetilde{\zeta}\,,$$

and by substituting the above relation in equation (2.94) we finally obtain the motion invariant $\mathcal{S}\equiv S-R_1\widetilde{h}_1-R_2\widetilde{h}_2$

$$\mathcal{S}=\frac{\rho_1\widetilde{h}_1}{2}\widetilde{\widehat{u}^2}|_{z=h_1}+\frac{\rho_2\widetilde{h}_2}{2}\widetilde{\widehat{u}^2}|_{z=-h_2}+\frac{3}{2}(\rho_1\widetilde{h}_1+\rho_2\widetilde{h}_2)\widetilde{\zeta}-\frac{3\gamma}{2}\widetilde{\zeta^2}+\frac{g(\rho_1\widetilde{h}_1^2-\rho_2\widetilde{h}_2^2)}{2} \tag{2.98}$$

(where we have used the identities $h_1=\widetilde{h}_1+\widetilde{\zeta}$ and $h_2=\widetilde{h}_2-\widetilde{\zeta}$).

The motion invariants $\mathcal{R}$ and $\mathcal{S}$ are defined in terms of period averages of kinematic and geometric wave properties in the wave frame of reference, and do not contain arbitrary pressure constants. Together with the two motion invariants provided by the volume fluxes in the wave frame, this set of four invariants can be used to specify the periodic wave train for Euler two-layer system.

Until this point we have defined motion invariants which are exact for the Euler equations. We now compute these quantities within the asymptotic approximation consistent with strongly nonlinear model. First, we notice that layer-fluxes are exact within this approximation, and correspond to the constants of integration C_1, C_2 in (2.25).

The remaining two motion invariants $\mathcal{R}$ and $\mathcal{S}$, can be approximated for the strongly nonlinear model and linked to the quadrature constants by using the asymptotic relations for the horizontal velocity (2.49) and the equation for the mean of the interface (2.31), while $\widetilde{\zeta^2}$ can be expressed in terms of the quadrature constants by replacing the numerator of the integrand in (2.31) with ζ^2.

We remark that a systematic study of existence and uniqueness of solutions of the strongly nonlinear model in the parameter space $\widehat{Q}_1$, $\widehat{Q}_2$, $\mathcal{R}$ and $\mathcal{S}$ seems difficult, given that the constraints between these parameters and the integration constants of the quadrature (2.25) are defined nonlocally through singular integrals with variable limits of integration.

2.7.2. Periodic waves with prescribed fluxes. Miyata [41] proposed the same strongly nonlinear long wave model and studied a class of periodic waves that limit on solitary waves on zero current at infinity. The position of the crest is located at *fixed* distance h_2 from the bottom wall, (thus at distance $h_1 = H - h_2$ from the top wall). The fluxes

in each layer are set to zero in a particular frame of reference which is designated as the "lab" frame, so that in the wave frame they are $\widehat{Q}_k = -ch_k$, $k = 1, 2$, where c is the phase speed. Thus, Miyata obtains a two parameter family of periodic solutions parametrized by the phase speed c and amplitude A, which, in the limit of infinite period, recovers the solitary wave solution with asymptotic behavior at infinity $\eta_k \to h_k$ and zero current in both layers.

These constraints (fixed position of the trough and zero volume fluxes in each layer) yield a distinct class of waves with respect to the one we have concentrated on and defined in §2.4 (waves of momentum zero in the frame for which the total volume flux is zero).

While the total volume flux in the lab frame is zero for this particular class of waves,

$$Q = \eta_1 \overline{u}_1 + \eta_2 \overline{u}_2 = 0\,, \tag{2.99}$$

the total horizontal momentum is different than zero.

Indeed, integrating this relation over one period after multiplication with ρ_k yields

$$-c\rho_k \widetilde{h}_k L + I_k L = -ch_k \rho_k L\,,$$

where $\widetilde{h}_k = 1/L \int_0^L \eta_k \, dX$ is the period average of the k-layer depth and I_k is the momentum per period in the lab frame. Thus

$$I_k = c\rho_k(\widetilde{h}_k - h_k)\,,$$

and therefore

$$I_1 + \rho_r I_2 (\neq I_1 + I_2) = 0\,. \tag{2.100}$$

Miyata derived his periodic solutions for the particular depth ratio $h_r \equiv h_1/h_2 = \frac{1}{\sqrt{\rho_r}}$, which is different than the critical case $h_r = \sqrt{\rho_r}$. For this particular ratio, his periodic solutions are expressible via elliptic functions.

We can cast Miyata's solutions in our notation in the general case (for arbitrary h_r), by looking at the class of waves for which the position of the trough is not constrained. Again, the strongly nonlinear model yields solutions which are expressible via hyperelliptic functions except for the particular case $h_r\sqrt{\rho_r} = 1$, when the root in the denominator for the quadrature (2.25) vanishes and the hyperelliptic integral associated with the quadrature degenerates into an elliptic integral. In addition to generalizing Miyata's class of periodic waves, we will also determine their domain of existence following a similar strategy as for our main constrained class of periodic solutions. We remark that by not enforcing the mean position of interface constraint, the analysis is greatly simplified for Miyata's class with respect to that of our main class. Notice also that the interpretation of the constants C_1 and C_2 as layer fluxes and the property of the root of the denominator in the quadrature formula (2.25) remain the same for Miyata's class.

Following the same procedure as in §2.4, the constants C_3 and C_4 can be determined uniquely by imposing the conditions that 0 and $-A$ are roots of the polynomial at the numerator in (2.25)

$$P(\zeta) = \rho_1 c^2 h_1^2 \eta_2 + \rho_2 c^2 h_2^2 \eta_1 - \gamma \zeta^2 \eta_1 \eta_2 + 2C_3 \eta_1^2 \eta_2 - 2C_4 \eta_1 \eta_2\,. \tag{2.101}$$

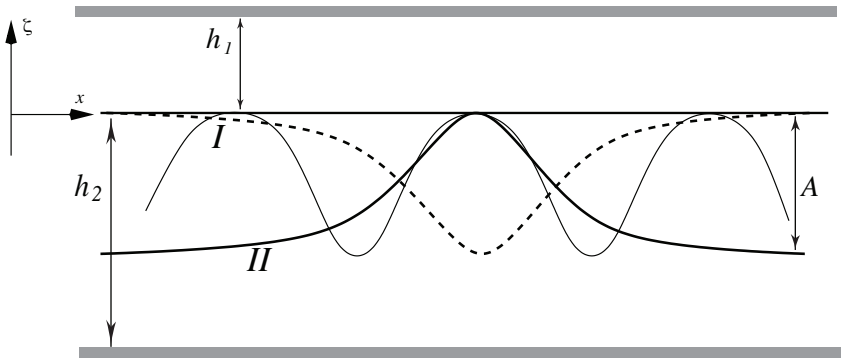

FIGURE 2.22. Limiting forms (solitary waves) for the the class of periodic waves with constrained fluxes and position of the crest.

Thus

$$C_3 = \frac{c^2}{2}\left[\frac{\rho_1 h_1}{h_1 + A} - \frac{\rho_2 h_2}{h_2 - A}\right] + \frac{\gamma A}{2}\,, \tag{2.102}$$

$$C_4 = C_3 h_1 + c^2 \frac{\rho_1 h_1 + \rho_2 h_2}{2}\,. \tag{2.103}$$

With all the constants C_i, $i = 1, \ldots, 4$, thus determined, we can construct the periodic solution from the quadrature (2.25), and determine the domain of existence of this class of periodic waves in the parameter space c and A. We restrict our attention to the case $h_1 < h_{critical}$. Once again, there are two bounding curves for this domain, which correspond to limiting cases of solitary waves with the prescribed fluxes. One limiting branch consists of the "classic" solitary waves that satisfy the asymptotic condition, $\eta_k \to h_k$ and $\overline{u}_k \to 0$ as $|X| \to \infty$ – type *I* in Figure 2.22. The other limiting branch – type *II* in Figure 2.22 – is given by solitary waves of opposite polarity superimposed on different non-zero currents at infinity (since the position of the interface at infinity is in

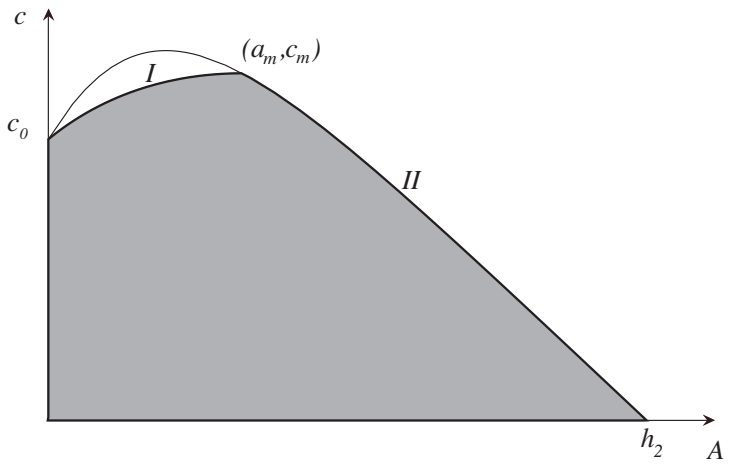

FIGURE 2.23. Domain of existence for periodic waves with prescribed fluxes for $h_1 < h_c$. Branch I represents solitary waves on zero current, asymptotic depth of upper layer h_1. Branch II corresponds to solitary waves on currents.

this case is $(h_1 + A, h_2 - A)$), which can be determined by imposing the flux condition

$$(\overline{u}_1 - c)\,\eta_1 = (\overline{u}_1|_\infty - c)(h_1 + A) = -ch_1\,, \tag{2.104}$$

$$(\overline{u}_2 - c)\,\eta_2 = (\overline{u}_2|_\infty - c)(h_2 - A) = -ch_2\,. \tag{2.105}$$

Using the notation from Appendix A yields

$$U_1 = \frac{c^2h_1^2}{(h_1 + A)^2}\,,\ U_2 = \frac{c^2h_2^2}{(h_2 - A)^2}\,. \tag{2.106}$$

The coefficients q_1, given by (A.8), and q_2, given by (A.9), respectively, in the quadratic polynomial from the numerator of (A.7) become

$$q_1(A,c) = -h_1 + h_2 - 2A + \frac{c^2}{\gamma}\left[\frac{\rho_1 h_1^2}{(h_1 + A)^2} - \frac{\rho_2 h_2^2}{(h_2 - A)^2}\right]\,, \tag{2.107}$$

$$q_2(A,c) = -(h_1 + A)(h_2 - A) + \frac{c^2}{\gamma}\left[\frac{\rho_1 h_1^2(h_2 - A)}{(h_1 + A)^2} + \frac{\rho_2 h_2^2(h1 + A)}{(h_2 - A)^2}\right]\,.$$

For a given amplitude A we want to determine the velocity c of the solitary wave on the current U_1, U_2 given by (2.106). That is equivalent to requiring that A is the root of the equation

$$A^2 + q_1(A, c)A + q_2(A, c) = 0\,,$$

which determines the square of the phase speed c^2,

$$c(A)^2 = \gamma \left(\frac{\rho_1 h_1}{(h_1 + A)^2} + \frac{\rho_2 h_2}{(h_2 - A)^2} \right)^{-1} . \tag{2.108}$$

In order to select from the curve (A, c) given by equation (2.108) the part that corresponds to actual solitary waves, we need to make sure that the second root of the equation

$$r^2 + q_1(A, c(A))r + q_2(A, c(A)) = 0\,,$$

say B, satisfies the condition $B > A$. Thus, we need the condition

$$q_1 = -(A + B) < -2A\,,$$

Replacing equation (2.108) in (2.107) and imposing the above condition we obtain

$$-\frac{\rho_2 h_1 h_2}{(h_2 - A)^2} + \frac{\rho_1 h_1 h_2}{(h_1 + A)^2} < 0\,,$$

which allows to conclude that relation (2.108) defines the branch *II* of the limiting solitary waves for

$$A > a_m = \frac{h_2\sqrt{\rho_r} - h_1}{\sqrt{\rho_r} + 1}\,,$$

where a_m is the maximum amplitude of the usual front for layer thicknesses (h_1, h_2), see Figure 2.23 for a sketch of the existence domain. We remark that what we have effectively done by looking at the solutions of Miyata's class is to take a different constraint surface through the five-dimensional parameter space of periodic solutions, and that the domain of existence on these surfaces coincide with our main class along the segment of boundary corresponding to the classical solitary wave solutions terminating in the maximum amplitude degenerate front solution (besides the straight boundary segments of zero amplitude and the artificial zero phase speed waves). We also remark that the critical depth ratio case follows a similar fate as that of our main constrained class, namely the classic solitary wave branch at the top of the existence domain shrinks to the point $(0, c_0)$ and only the type *II* solutions survive.

2.7.3. Periodic waves with prescribed mean Eulerian velocities. [15] study the two-layer Euler system numerically, and compute a class of periodic waves under the constraint that the period average of the Eulerian wall-velocity (defined in the lab frame) be zero for both top and bottom walls. Their other two constraints are to fix the position of the crest and the period length (thus fixing five independent parameters, phase speed, two mean-Eulerian wall-velocities, crest position and period). We first show that this class of periodic waves is different than our main class. In fact, the kinetic energy equation (2.55) with mean Eulerian wall-velocity zero in each layer yields

$$T_k = c\frac{I_k}{2}\,, \tag{2.109}$$

so that the horizontal momenta I_k must be nonzero, violating the constraint of our main class defined in §2.4.

Similarly to the previous sections, we now use the strongly nonlinear model to find how these different constraints relate to the quadrature constants C_i, $i = 1, \cdots 4$. By fixing the position of the crest of the wave, we specify one of the four roots in the polynomial at the numerator (2.27), say r_2, which constitutes a constraint among the integration constants C_i, $i = 1, \ldots, 4$, or $P(r_2, \boldsymbol{C}) = 0$, where P is the polynomial in the numerator of (2.25). By fixing the period, we obtain another integral constraint involving the constants C_i, $i = 1, \ldots, 4$,

$$L = \mathcal{L}(\boldsymbol{C})\,, \tag{2.110}$$

see relation (2.30). By using the asymptotic expressions (2.53) for the mean Eulerian velocities and setting them to zero for both layers, we obtain two more integral constraints for the constants $C_1, \ldots, C_4$ involving the wave speed c (prescribed from the onset)

$$\widetilde{u}_k(c, \boldsymbol{C}) = 0\,, \quad k = 1, 2\,.$$

We remark that, just as for the constraints of §2.7.1, it seems difficult to study analytically the existence and uniqueness of this class of waves, even with the power afforded by the strongly nonlinear model because of the nonlocal expression for of the physical quantities in terms of the quadrature constants.

Among the class of periodic solutions that can be constructed for two-layer systems, a special mention goes to those derived through weakly nonlinear, unidirectional models.

Funakoshi & Oikawa [15] also derived a KdV-mKdV equation for waves of small amplitude, whence periodic solution of standard elliptic functional form derive. However, we remark that this particular class of waves does not recover the correct asymptotic limit of the dispersion relation (as evidenced by Fig. 9(b,c) on that paper).

In fact, an asymptotically consistent KdV-mKdV model is a particular case of a unidirectional model that can be obtained from our strongly nonlinear model (Choi & Camassa [7]). This reduction of degrees of freedom for the wave motion, from bi- to unidirectional, has the effect of reducing the number of parameters that define a periodic wave train from five to three. We can thus anticipate that the constraints that rely on the definition of a lab-frame (through its connection to wave speed) for the full Euler two-layer system as well as for the strongly nonlinear model will be violated, in general, albeit possibly only by asymptotically small errors arising from the unidirectional limit process.

The traveling wave solution ansatz in the unidirectional model in (Choi & Camassa [7], Appendix A, equation (A 14)) results in the quadrature formula

$$\zeta_X^2 = \frac{c_3}{4(c_4-c_5)} \frac{\zeta^4 + \frac{2}{3}\frac{c_1}{c_3}\zeta^3 + \frac{2(c_0-c)}{c_3}\zeta^2 + C_1\zeta + C_2}{\zeta + \frac{c_2c_1 + (c_0-c)(2c_4-c_5)}{2c_1(c_5-c_4)}}\,, \tag{2.111}$$

where C_1 and C_2 are constants of integration which are related to purely geometric wave properties such as amplitude, period, and mean level, and c_1, c_2, c_3, c_4 and c_5 "hardware" constants determined by the densities and layer thicknesses (Choi & Camassa [7], Appendix A, equations (A 7a) and (A 7b)). The quadrature (2.111) has the same structure as its bidirectional analog (2.25), but only two constants of integration are needed. While

we have not extensively studied this class here, it is interesting to note that at least for small-amplitude wavetrains, well within the range of validity of the unidirectional model, its periodic solutions are in good agreement with those of the bidirectional model in the constrained class of zero period-averaged momentum for each layer.

2.8. Discussion

We have presented a study of finite-depth periodic traveling wave solutions of a strongly nonlinear model for internal wave propagation in two-layer inviscid, incompressible fluid systems. Periodic solutions clearly constitute a much richer class than their limiting forms, such as solitary wave solutions, which have been the main focus of previous model investigations in both theory and experiments. In contrast with these limiting forms, the lack of an asymptotic spatial reference state opens up additional parametric freedom, and the distinction of which parameter subsets constitute solutions relevant for physical situations becomes less clear. With our study we have provided some order in the various results established in the literature on two-layer finite-depth periodic internal wave solutions, by examining in detail the role of the physical constraints on such waves, and by studying their transition to the limiting infinite-period forms. In particular, we have shown how such solutions constitute a five parameter family, which we conjecture holds for the general two-layer Euler periodic single-valued solutions of symmetric type. Moreover, we have provided examples that show non-uniqueness within this family, associated with "overhanging" (multiple-valued) solutions of the Euler system.

In this work, we have chosen to focus on the particular parametric subset corresponding to waves that generate no horizontal mean momentum in each layer, with respect to some inertial reference frame defined to be that of the laboratory. Additionally, we

impose that these waves maintain a prescribed period average interface height, which can be thought of as that of an undisturbed reference state. We chose these constraints with a past asymptotic *temporal* reference state in mind, in which the process of wave generation proceeds from a quiescent state with well defined uniform layer thicknesses, in closed (but long) domains with wave-generators that do not apply a net horizontal force. While these conditions do not necessarily guarantee the exact enforcement of our choice of constraints, it is plausible to assume that under these circumstances our two sets of constraints can be approximately satisfied. True periodicity could be approximated by a section of the wave train far from both the generation region and from the leading wave region, where the displaced interface connects with the flat surface between undisturbed fluids. (Other parametric subsets have been proposed in the literature for Euler and weakly nonlinear systems. We looked at some of them in the context of our model in §2.7.)

Several results have emerged from our study. First, we have identified analytically the domain of existence of the periodic waves in the two-parameter space of amplitude and speed. The boundary of this domain is represented by the limiting curves of speed vs. amplitude of solitary waves and fronts. While the solitary wave branch is a long-wave approximation to the corresponding full two-layer Euler branch (but practically indistinguishable from it as shown in the previous work of Camassa *et al.* [8]), the front branch is exact and coincides with that of the full Euler system, as we show in Appendix A. Thus, the domain of existence we have identified thanks to the model informs us on the corresponding domain for the full Euler system, even though not every existing model

solution within the domain can be expected to be a good approximation of an Euler solution.

The numerical solutions of the full Euler two-layer system have also brought forth the feature of overhanging periodic waves of higher speed than single valued waves of the same amplitude, within the same class of constrained zero momenta and fluxes for solutions for the strongly nonlinear model. Similar overhanging solutions of Euler equations have been the subject of previous studies, however most of these have concentrated on the case of infinite thickness of either both or one fluid layer. In contrast, our study has concentrated on finite depth of both layers, and in particular we locate the domain of existence of overhanging periodic solutions for these configurations. Moreover, our Euler solutions explore the transition from finite period to infinite period front solution of the overhanging type. It is interesting to speculate that the point at which the envelope of maximum amplitudes for given period intersects the boundary of the existence domain along the front branch separates this branch between single valued front profiles and overhanging ones similar to those found by Dias & Vanden-Broeck [9]. If so, it is remarkable that the model maximum slope curves can offer an estimate of this transition amplitude along the front branch.

By comparing with numerical solutions of the full Euler system, we have shown that two model solutions are accurate approximations whenever certain criteria of asymptotic accuracy based on definitions of "long-waveness" and departure from near-linear regimes are satisfied. This first and most stringent application of these criteria excludes from the existence domain the region where overhanging waves are found, and the model predictions are very good approximations of the full Euler solution. It is remarkable

that with a second criterion based on a nonlocal definition of effective wavelength the model is still able to pick up with some accuracy the location of flattening crests and/or troughs, even though the wave profile may fail to offer a good local approximation. In particular, the Euler computations show that a portion of the existence domain from the model needs to be removed as Euler solutions do not exist in this region. Euler periodic waves of the constrained class we have studied have a (single valued regular) wave of maximum amplitude for a given period. The envelope of all the constant period curves in the (A, c) plane gives rise to a curve marking the boundary of existence of these Euler periodic solutions. Here again the model is able to inform about the boundary of this region by examining the maximum slope curve of its solutions in the existence domain.

A large portion of the existence domain is taken by periodic waves which are de facto the spatially truncated version of solitary waves or fronts. These are not the classic cases of such internal waves, which are asymptotic to quiescent states. Instead, these infinite-period limiting waves are defined on background relative currents between the two layers. This situation has not been given much attention in previous work, presumably due to lack of physical interest for a velocity jump to be sustained over an infinite interface. However, the length of this interface becomes finite when clipped in the process of constructing periodic waves, thus justifying the more in-depth study of such limiting cases presented in Appendix A and B.

A result of possible relevance in applications, where solitary waves rarely occur in true solitary fashion and are more commonly members of wavetrains with multiple crests, is exhibited by the supercritical speed region near the vertex of the existence domain. There, for a fixed supercritical speed and relatively long period waves, there exist two

different amplitude waves, with the larger one attaining an amplitude that can be substantially larger than the maximum wave front limit of the classic solitary wave branch.

Several future directions could stem from our study of the periodic solutions for the two-layer strongly nonlinear model. Perhaps the one most physically relevant is the modulated wavetrains that can be obtained perturbatively by allowing the quadrature integration constants to be slowly varying functions of space and time. To this end, asymptotics of the quadrature formula for nearly flat crests or troughs would have to be established and are in progress. Such a study would be of relevance in geophysical applications, where near-solitary wave trains are a common occurrence. On a more mathematical level, the overhanging solutions and their model approximations provide a starting point for continuation studies to explore the issue of multiplicity for this class of two-layer Euler solutions, as well as their stability properties.

CHAPTER 3

Optimal two-layer approximation for continuous density stratification

3.1. Introduction

A rather ubiquitous density stratification encountered in geophysical applications consists of two layers of constant density fluids separated by an intermediate, diffused layer (the *pycnocline*) in which the density varies continuously. When the pycnocline is thin, a two layer system describes wave motion supported by such configurations successfully, as comparisons between theory and experiments (e.g. in Grue *et al.* [19]) reveal. Typically, the interface position of the two layer system is chosen at the inflection point of the density profile, while the densities of the two layers are set by the extrema of the density profile. As discussed in §2.1, the two layer system is by far the simplest configuration supporting internal wave motion, and consequently both asymptotic and full Euler models for wave motion in such a system have been developed and analyzed extensively. In particular, asymptotic models that take advantage of typical long horizontal scale of the motion with respect to the widths of the fluid layers, are notably much easier to study than their full Euler counterparts. For instance, the two layer strongly nonlinear model for long waves of arbitrary amplitude described in Miyata [39], Choi & Camassa [7], reduces the full Euler system of partial differential equations to a system of evolution

equation for interface position, layer mean velocities and pressure at the interface, which are evidently more amenable to analytical investigations.

For thick pycnoclines, the aforementioned modality of prescribing the two layer system approximation for the continuous stratification is no longer satisfactory. Various simplified models that take into consideration the presence of a pycnocline of finite width have been studied (e.g. intermediate layer of constant density Rusås [44], Rusås & Grue [43] or linear stratification Fructus & Grue [14], Fructus *et al.* [13]). However, studying time evolution and determining stationary solutions in the framework of such models is substantially more difficult than the equivalent analysis using the two layer models (in particular the asymptotic models for long waves). Thus, in the present chapter, we aim to extend the two layer approximation to density stratifications with a single finite-width pycnocline. The results of this chapter are relevant for the study in Chapter 4, where the shear instability of solitary waves in near two-layer stratification is considered. In this study, we assume the fluid to be inviscible, incompressible and non-diffusive. Furthermore, we confine the upper surface by a rigid lid.

The chapter is organized as follows: in §3.2 we propose several models for constructing two-layer approximations for an arbitrary continuous stratification. In §3.3 we outline a simple strategy for comparing the performance of these models, in order to select the optimal one among them, by studying the propagation of waves of infinitesimal amplitude and of internal bores. We also explore the range of pycnocline thicknesses for which the proposed models furnish reasonable estimates. In §3.4, in an effort to further validate our strategy, we compare the solitary wave solutions of Euler equations in continuous stratification (obtained by the fixed point iteration algorithm described in Appendix C)

with solitary waves solutions of the strongly nonlinear long-wave model Choi & Camassa [7], solutions available in closed form. Finally, In §3.5 we construct an approximation of local fluid velocities, based on a long wave assumption.

3.2. Model

Let $\overline{\rho}(z)$ denote a continuous density stratification for which we aim to determine an equivalent two-layer system. The two-layer system is fully determined by specifying three quantities: the height of the bottom layer, z_0 and the densities in each layer (ρ_1 upper, ρ_2 bottom) - see Figure 3.1 for general notation. Hence, we need three matching criteria that would connect the two stratifications.

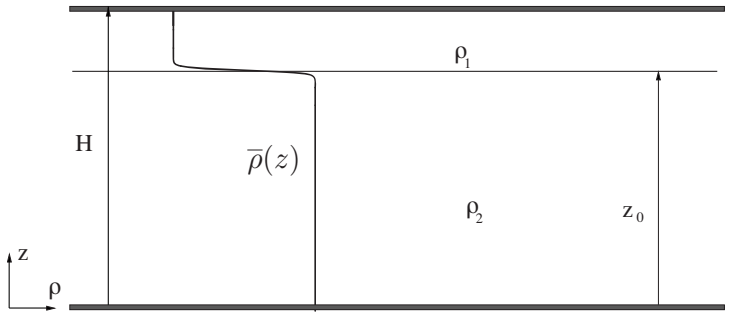

FIGURE 3.1. Schematics of two layer system and its continous stratification counterpart with the main notations.

Dispersion is a fundamental aspect of wave motion in stratified fluids, and thus furnishes a natural criterion for selection of a two-layer system that would correctly capture wave dynamics in continuous stratification. The most significant physical quantity that characterizes dispersion in both two-layer and continuously stratified systems is the speed of waves of infinitesimal amplitude and infinite wavelength – *linearized long wave speed*.

The linearized long wave speed for *continuous stratification* corresponds to the first eigenmode (baroclinic mode) of the linearized Euler equations. Assuming sinusoidal

waves propagating in the horizontal direction x, the stream function can be expressed as

$$\psi(x,z) = F(z)e^{ik(x-ct)}\,,$$

with c being the phase speed of the wave whereas k is the wave number. The boundary conditions are $\psi(x,0) = \psi(x,H) = 0$ (no-slip at the vertical boundaries) and thus $F(0) = F(H) = 0$. The equation for the amplitude F (that results from the linearization of Euler equations) is

$$(\overline{\rho}F')' - \left[\frac{g\overline{\rho}'}{c^2} + \overline{\rho}k^2\right]F = 0\,,$$

or equivalently

$$F'' - \frac{N(z)^2}{g}F' + \left[\frac{N(z)^2}{c^2} - k^2\right]F = 0\,, \tag{3.1}$$

with $N(z) \equiv \sqrt{\dfrac{-\overline{\rho}'g}{\overline{\rho}}}$ being the Brunt-Väisälä frequency. We thus obtain a Sturm-Liouville eigenvalue problem with the eigenvalue $1/c^2$, parametrized by k. The linearized critical long wave speed is determined by the limit $k \to 0$. Equation (3.1) becomes

$$F'' - \frac{N(z)^2}{g}F' + \frac{N(z)^2}{c^2}F = 0\,. \tag{3.2}$$

The first eigenvalue of equation (3.2) gives the linearized long wave speed ($\equiv c_0^{cont}$).

The linearized long wave speed for *a two layer system* (Lamb [33]) with height of the bottom layer z_0, total height H and densities ρ_1, ρ_2 is

$$c_0^{two\ layers} = \sqrt{\frac{gz_0(H-z_0)(\rho_2-\rho_1)}{\rho_1 z_0 + \rho_2(H-z_0)}}\,. \tag{3.3}$$

Other relevant physical quantities that characterize a stratified configuration in quiescent state are the masses and potential energies of the two layers. In the following, we define functions representing differences between the quantities that characterize the continuous stratification and two layer configuration (mass in each layer, respectively potential energies in each layer)

$$f_1(z_0,\rho_1) \equiv \rho_1\,(H-z_0) - \int_{z_0}^{H} \overline{\rho}(z)dz = \rho_1\,(H-z_0) + r(z_0) - \overline{r}\,, \tag{3.4}$$

$$f_2(z_0,\rho_2) \equiv \rho_2 z_0 - \int_{0}^{z_0} \overline{\rho}(z)dz = \rho_2 z_0 - r(z_0)\,, \tag{3.5}$$

$$f_3(z_0,\rho_1) \equiv \frac{\rho_1}{2}(H^2-z_0^2) - \int_{z_0}^{H} z\overline{\rho}(z)dz = \frac{\rho_1}{2}(H^2-z_0^2) + W(z_0) - \overline{W}\,, \tag{3.6}$$

$$f_4(z_0,\rho_2) \equiv \frac{\rho_2}{2}z_0^2 - \int_{0}^{z_0} \overline{\rho}(z)zdz = \frac{\rho_2}{2}z_0^2 - W(z_0)\,, \tag{3.7}$$

where

$$\overline{r} = \int_0^H \overline{\rho}(z)dz$$

is the total cross-section mass for the continuous stratification,

$$\overline{W} = \int_0^H z\overline{\rho}(z)dz$$

is the total cross-section potential energy for the continuous stratification ($/g$) and

$$r(z_0) \equiv \int_0^{z_0} \overline{\rho}(z)dz\,, \qquad W(z_0) \equiv \int_0^{z_0} z\overline{\rho}(z)dz\,.$$

There are of course, multiple ways of prescribing the matching criteria. Since the equivalent two-layer system should accurately capture small amplitude motion, we assert that the linearized speed should be matched exactly. This allows elimination of one of

the unknowns - for instance ρ_2 in favor of ρ_1 and z_0. Let $h_0 \equiv (c_0^{cont})^2/g$. From (3.3) we obtain

$$\rho_2(z_0\,,\rho_1) = \frac{(z_0 - h_0 - H)z_0\rho_1}{(H - z_0)(h_0 - z_0)}\,. \tag{3.8}$$

We thus rewrite the functions (3.4)-(3.7) as

$$f_1(z_0,\rho_1) = \rho_1\,(H - z_0) + r(z_0) - \overline{r}\,, \tag{3.9}$$

$$f_2(z_0,\rho_1) = \frac{(z_0 - H - h_0)z_0^2\rho_1}{(H - z_0)(h_0 - z_0)} - r(z_0)\,, \tag{3.10}$$

$$f_3(z_0,\rho_1) = \frac{\rho_1}{2}(H^2 - z_0^2) + W(z_0) - \overline{W}\,, \tag{3.11}$$

$$f_4(z_0,\rho_1) = \frac{(z_0 - H - h_0)z_0^3\rho_1}{(H - z_0)(h_0 - z_0)} - W(z_0)\,, \tag{3.12}$$

In the present study, we are investigating three matching strategies. For all of these modalities, the first criterion is, as mentioned above, matched linearized speed. Additionaly, we match: (I) mass in each layer, (II) potential energy in each layer, (III) least square fit for masses in the two layers and energies in the two layers. In all three cases, we reduce the determination of the equivalent two-layer system problem to a nonlinear equation for the position of the interface z_0 (the width of the bottom layer). In most cases, this nonlinear equation has multiple solutions. In §3.3 we will present prescriptions for selecting only one of the roots in each instances, in the context of a specific density stratification.

3.2.1. Matched mass in each layer. Matching mass in each layer amounts to solving the nonlinear system of equations $f_1(z_0,\rho_1) = 0\,, f_2(z_0,\rho_1) = 0$ ($f_1\,, f_2$ given by (3.9),

(3.10)) in the unknowns z_0, ρ_1. By eliminating ρ_1 in favor of z_0 from the first equation

$$\rho_1(z_0) = \frac{(H - z_0)(h_0 - z_0)\overline{r}}{H\,(z_0^2 - (H + 2h_0)z_0 + Hh_0)}\,,$$

we can reduce the system to a single equation in z_0

$$F_1(z_0) \equiv \frac{(z_0 - h_0 - H)z_0^2\overline{r}}{H\,(z_0^2 - (H + 2h_0)z_0 + Hh_0)} - r(z_0) = 0\,. \tag{3.13}$$

Note that $z_0 = H$ is a solution.

3.2.2. Matched potential energy in each layer. We need to solve the nonlinear system of equations: $f_3(z_0, \rho_1) = 0\,, f_4(z_0, \rho_1) = 0$ ($f_3\,, f_4$ given by (3.11), (3.12)) in the unknowns z_0, ρ_1. By eliminating ρ_1 in favor of z_0 from the first equation,

$$\rho_1(z_0) = \frac{2(H - z_0)(z_0 - h_0)\overline{W}}{H\,(H^2h_0 - H(H + h_0)z_0 + (H - h_0)z_0^2)}\,,$$

we can reduce the system to a single equation in z_0

$$F_2(z_0) \equiv \frac{(z_0 - h_0 - H)z_0^3\overline{W}}{H\,(H^2h_0 - H(H + h_0)z_0 + (H - h_0)z_0^2)} - W(z_0) = 0\,. \tag{3.14}$$

Note that $z_0 = H$, $z_0 = 0$ are solutions.

3.2.3. Least square fit for potential energies and masses. We define the residue function

$$S(z_0, \rho_1) = \frac{f_1^2(z_0, \rho_1) + f_2^2(z_0, \rho_1)}{2r^2} + \frac{f_3^2(z_0, \rho_1) + f_4^2(z_0, \rho_1)}{2\overline{W}^2}\,. \tag{3.15}$$

In order to minimize the residual S, we determine the critical points, thus solving the system

$$\frac{\partial S}{\partial z_0}(z_0\,,\rho_1)=0,\ \frac{\partial S}{\partial \rho_1}(z_0\,,\rho_1)=0\,. \tag{3.16}$$

and select the local minima. We record here the partial derivatives of $f_1(z_0,\rho_1)$ - $f_4(z_0,\rho_1)$:

$$\begin{aligned}
\frac{\partial f_1}{\partial z_0} &= \overline{\rho}(z_0)-\rho_1\,,\\
\frac{\partial f_1}{\partial \rho_1} &= H-z_0\,,\\
\frac{\partial f_2}{\partial z_0} &= \frac{(z_0^3-2(H+h_0)z_0^2+(H^2+5Hh_0+h_0^2)z_0-2Hh_0(H+h_0))\,z_0\rho_1}{(H-z_0)^2(h_0-z)^2}-\overline{\rho}(z_0)\,,\\
\frac{\partial f_2}{\partial \rho_1} &= \frac{(H+h_0-z_0)z_0^2}{(H-z_0)(z_0-h_0)}\,,\\
\frac{\partial f_3}{\partial z_0} &= z_0\,(\overline{\rho}(z_0)-\rho_1)\ ,\\
\frac{\partial f_3}{\partial \rho_1} &= \frac{1}{2}\left(H^2-z_0^2\right)\ ,\\
\frac{\partial f_4}{\partial z_0} &= \frac{(2z_0^3-4(H+h_0)z_0^2+2(H^2+4Hh_0+h_0^2)z_0-3Hh_0(H+h_0))\,z_0^2\rho_1}{2(H-z_0)^2(h_0-z)^2}-z_0\overline{\rho}(z_0)\,,\\
\frac{\partial f_4}{\partial \rho_1} &= \frac{(H+h_0-z_0)z_0^3}{2(H-z_0)(z_0-h_0)}\,,
\end{aligned}$$

where we have used

$$\frac{\partial r}{\partial z_0}=\overline{\rho}(z_0)\,,\qquad \frac{\partial W}{\partial z_0}=z_0\overline{\rho}(z_0)\,.$$

In order to solve the system (3.16) we first solve the two corresponding root finding problems in ρ_1 for the entire range $z_0\in(0\,,H)$. Usually, we obtain several branches for

both from which we select the ones that intersect - say $\rho_1^{(1)}(z_0)$ and $\rho_1^{(2)}(z_0)$. We define

$$F_3(z_0) = \rho_1^{(1)}(z_0) - \rho_1^{(2)}(z_0)\,. \tag{3.17}$$

The roots of the above equation determine the critical points of the the residual, from which we will select the global minima.

3.3. Limits of validity

The strategy outlined above can be expected to suffer from several limitations, which can be expected to become more prominent as the extra degrees of freedom of the continuously stratified fluids with respect to two-layer approximations become dynamically accessible. We focus next on some of these limitations and on diagnostics to quantify them.

3.3.1. Density stratification and resulting two layer approximations. In the present section, we explore the performance and the limits of validity of the matching strategies introduced above.

We use as benchmark for validation the antisymmetric density stratification

$$\overline{\rho}(z) = \rho_{min} + \frac{\rho_{max} - \rho_{min}}{2}\left(1 + \tanh\left[\frac{\ln\ 9}{d}(z_p - z)\right]\right)\,, \tag{3.18}$$

where ρ_{min}, ρ_{max} are the densities below and above the pycnocline (unless the pycnocline is close to the upper or lower vertical boundaries), z_p is the location of the inflection point (the center) of the density stratification, whereas d is the thickness of the pycnocline defined as usual (the distance between the vertical locations in the

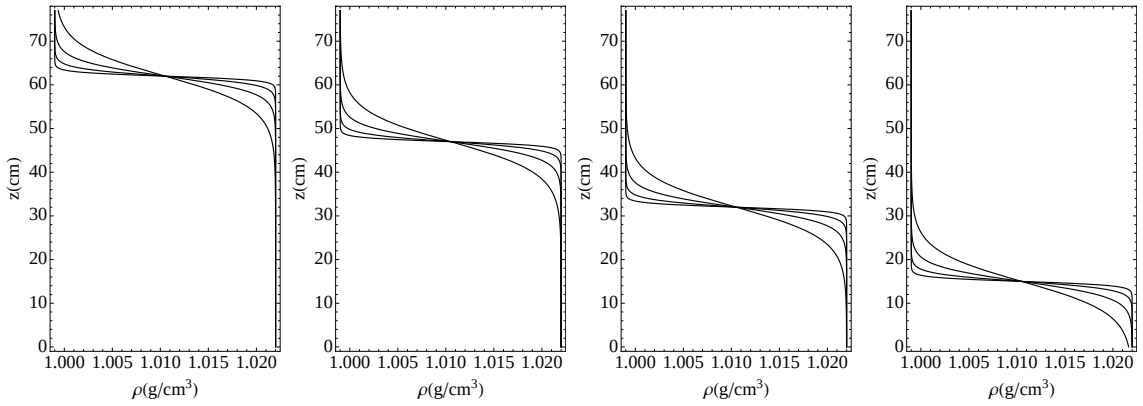

FIGURE 3.2. Density stratifications analyzed in the current section, corresponding to the general stratification (3.18), for the position of the inflection point z_p at (a) 62 cm, (b) 47 cm, (c) 32 cm and (d) 17 cm and for the widths of the pycnocline of 2 cm , 4 cm , 8 cm and 16 cm respectively.

density stratification corresponding to $\rho_{min} + 0.1\Delta\rho$ and $\rho_{max} + 0.9\Delta\rho$ respectively). Note that $\overline{\rho}(z_p) = \rho_{med} \equiv 1/2(\rho_{min} + \rho_{max})$. We fix the densities $\rho_{min} = 0.999$ g/cm^3, $\rho_{max} = 1.022$ g/cm^3 and the total height of the fluid column $H = 77$ cm. This choice of physical parameters is motivated by the experiments in Grue *et al.* [19], to which we are going to refer extensively in Chapter 4. In the present study, we aim at monitoring the effectiveness of the matching strategy for various relative thicknesses of the intermediate layer, with respect to the widths of the two layers situated above and below the pycnocline. Thus, we study the two parameter family of the density profiles (3.18) in the parameters $d\,, z_p$. We consider four widths of the pycnocline: 2 cm , 4 cm , 8 cm and 16 cm and four positions of the center of the pycnocline: 62 cm , 47 cm , 32 cm and 17 cm - see Figure 3.2 for the corresponding density profiles.

By matching either the masses in each layer or the potential energies in each layer, the corresponding nonlinear equation for the height of the bottom layer z_0 has two real

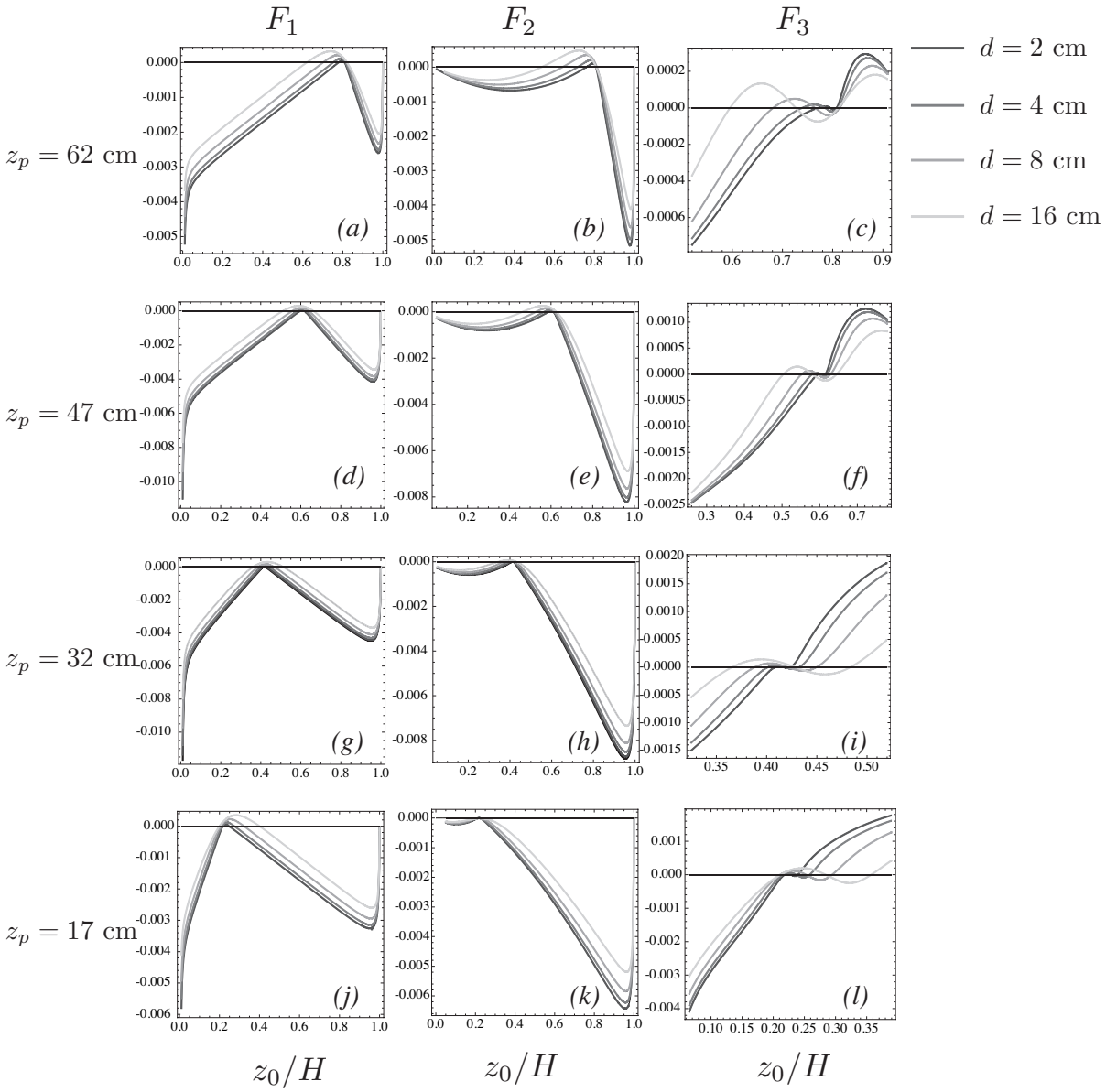

FIGURE 3.3. Functions $F_1(z_0)$, $F_2(z_0)$ and $F_3(z_0)$ corresponding to the three matching conditions (3.13), (3.14) and (3.17) (matched mass in each layer, matched potential energy in each layer, least square for mass and potential energy in each layer, respectively), for the density stratifications from Figure 3.2. The width of the pycnocline d varies between 2 cm and 16 cm whereas the inflection point of the continuos density stratification is located at (a)-(c) $z_p = 62$ cm, (d)-(f) $z_p = 47$ cm, (g)-(i) $z_p = 32$ cm and (j)-(l) $z_p = 17$ cm.

solutions (besides $z_0 = H$ for the matched masses strategy, and $z_0 = 0\,, H$ for matched potential energies). We select the root closest to the inflection point of the density

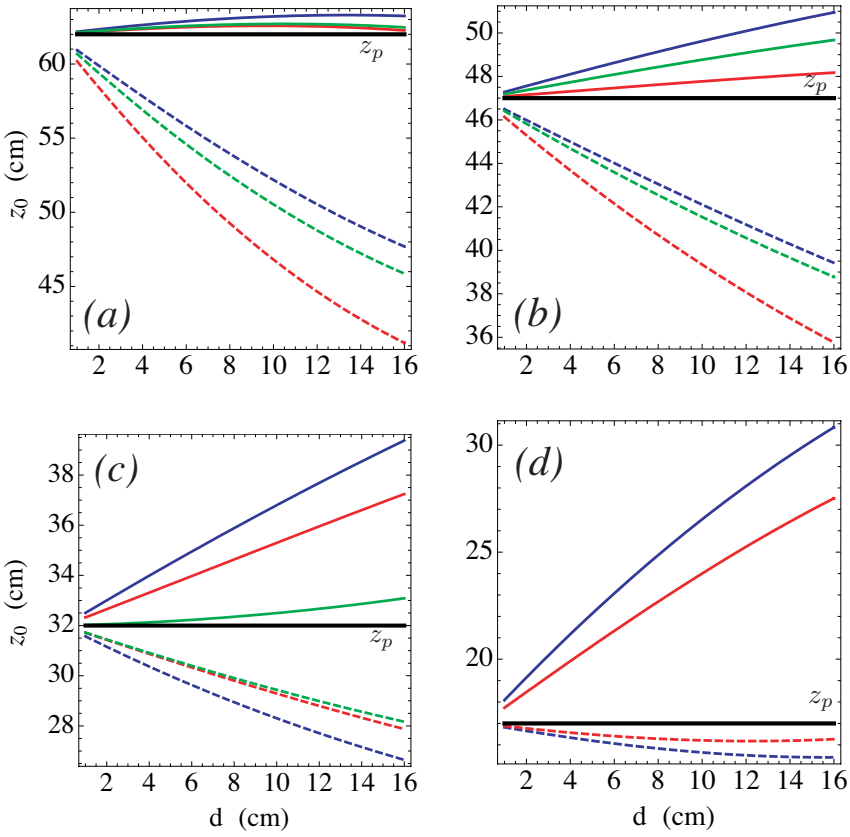

FIGURE 3.4. Roots of the equations $F_1(z_0) = 0$ (blue), $F_2(z_0) = 0$ (green), $F_3(z_0) = 0$ (red) as functions of the width of the pycnocline d, for the density stratifications from Figure 3.2, with the inflection point of the density stratification located at (a) $z_p = 62$ cm, (b) $z_p = 47$ cm, (c) $z_p = 32$ cm and (d) $z_p = 17$ cm.

profile z_p (which will translate in a better prediction for the speed of the conjugate states, described in the following section). Note also that for $z_p = 17$ cm the matching modality corresponding to matched potential energy in each layer does not admit real solutions – see Figure 3.3(k).

By using the third matching strategy we obtain three roots (see Figure 3.3). The second root corresponds to a saddle point, and only the first and the third correspond to points of local minimum of the residual S (3.15). In this instance, we select the root corresponding to the global minimum which for the stratifications analyzed in this

section corresponds to the root closest to the position of the inflection point of the density stratification z_p.

In Figure 3.4 we depict the roots as functions of the width of the pycnocline for the four values of the inflection point of the density stratification.

3.3.2. Conjugate states. As already referenced in Chapter 2, Euler equations in two layer systems admit front solutions (internal bore solutions), which represent an upper bound for the amplitude of internal solitary waves. As solitary waves approach this limit, they become very long and flat. The uniform flow at the peak of such flat waves is said to be *conjugate* to the upstream flow. In fact, this upper bound together with the speed of propagation are predicted exactly by the strongly nonlinear model proposed by Miyata [40], Choi & Camassa [7]. (We have reported these formulas in Chapter 2, relations (2.77) and (2.76).) Conjugate flows exist for any combination of densities ratios $\rho_r = \rho_1/\rho_2$ of the two layers and depth ratios $h_r = h_1/h_2$, *except* when the depth ratio becomes critical $h_c = \sqrt{\rho_r}$.

On the other hand, to our knowledge, there is no analogous analytical prediction on the existence of internal bore solutions in the case of continuously stratified flows. In fact, there are density stratifications that do not seem to support conjugate flows, as investigated by a series of numerical investigations (Lamb & Wan [31], Kubota [30]).

Lamb & Wan [31] have derived a numerical method for determining conjugate flows for arbitrary stratifications. By imposing conservation of mass, horizontal momentum and energy, they reduce the Euler equations to a nonlinear boundary value problem for for the isopycnal displacement $\eta(z)$, with the speed of propagation as the eigenvalue. Furthermore, they have extensively analyzed the density stratification (3.18), and show

that it admits conjugate flow solutions except for a critical depth ratio z_c, in perfect analogy with two-layer systems.

In light of the above-mentioned facts, the conjugate states concept becomes a key feature of our investigation. We conjecture that a continuous density stratification that does not admit conjugate states cannot be approximated reasonably by a two-layer system, since finite-amplitude effects such as narrowing of solitary wave solutions in such stratifications for increasing amplitude are not correctly captured by the two layer system. Conversely, for a continuous stratification that admits conjugate states, the speed and amplitude of the bore solutions become relevant matching criteria.

We point out that the eigenvalue problem for determining the conjugate states can be solved numerically via a standard shooting method, with relatively small computational cost. Following the strategy outlined in Lamb & Wan [31], we compute the conjugate flows in continuous stratification (3.18) for the parameters z_p and d specified in the previous sub-section, and compare against the two-layer predictions with the parameters ρ_1 , ρ_2 and z_0 chosen via the three proposed matching strategies. Figure 3.5 illustrates the front speed dependence on the width of the pycnocline. We remark that better agreement is achieved in general by employing the third strategy (least square fit for masses and potential energy in each layer), except in the case (c) $z_p = 32$ cm. This particular depth is close to the *critical* depth of the continuous stratification, depth that does not support a conjugate state. One can estimate the critical depth by interpolating the maximum displacement of the conjugate states for various positions of the center of the pycnocline z_p, and subsequently determine the depth for which the maximum displacement is zero.

For our stratification, the critical depth ranges between 38.714 cm for the pycnocline thickness $d = 2$ cm and 38.645 cm for $d = 16$ cm.

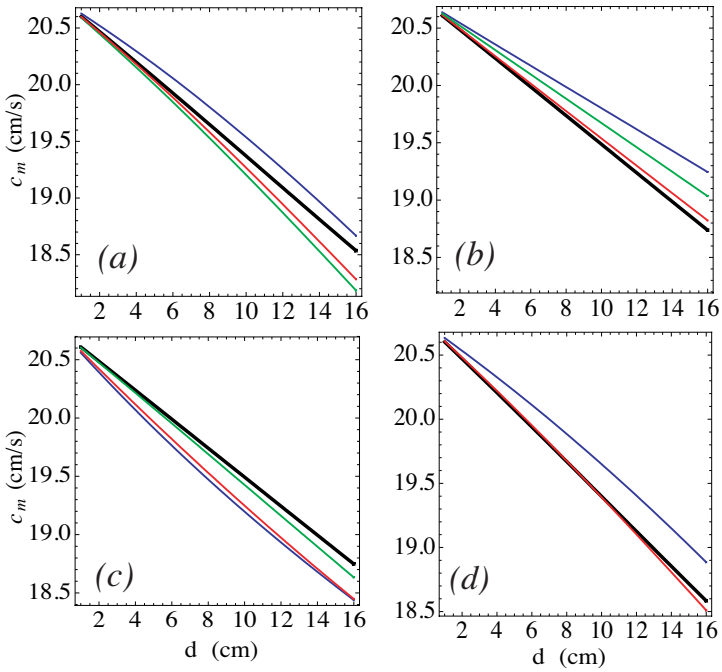

FIGURE 3.5. Black - speed corresponding to the conjugate state for stratifications from Figure 3.2 (with the inflection point of the density stratification located at (a) $z_p = 62$ cm, (b) $z_p = 47$ cm, (c) $z_p = 32$ cm and (d) $z_p = 17$ cm, respectively) as a function of the width of the pycnocline d; blue - the two layer predictions with matched masses; green - matched potential energies; red - least square fit for the masses and potential energy.

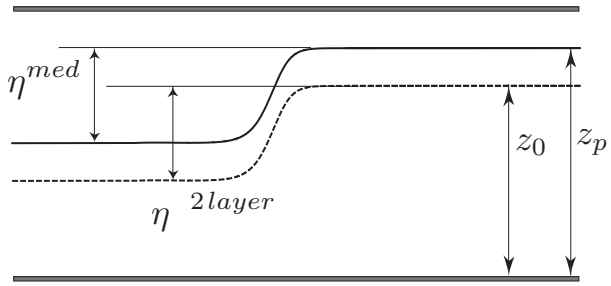

FIGURE 3.6. Schematics of the displacement of the average density isoline η^{med} and displacement of the interface of the two layer model $\eta^{2\ layer}$. z_0 is the undisturbed position of the interface of the two layer system, z_p is the position of the pycnocline center, afferent to the continuous stratification.

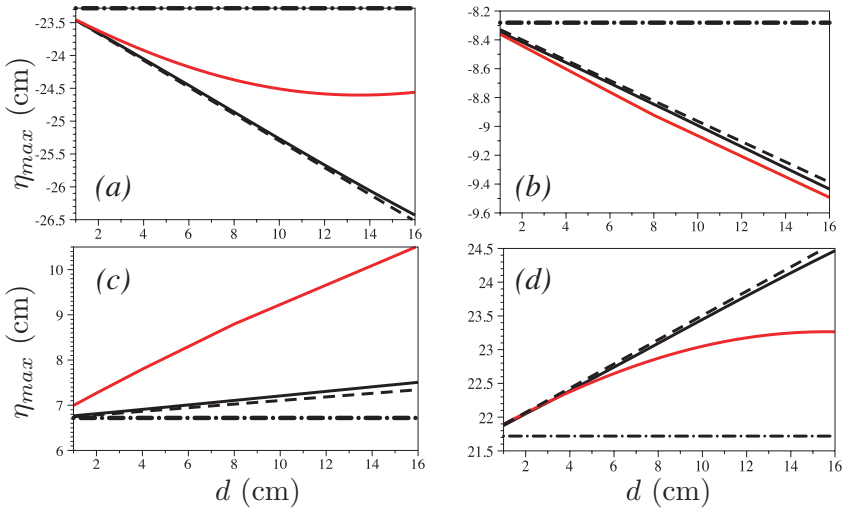

FIGURE 3.7. Black - maximum displacement of the average density isoline corresponding to the conjugate state for stratifications from Figure 3.2 (with the inflection point of the density stratification located at (a) $z_p = 62$ cm, (b) $z_p = 47$ cm, (c) $z_p = 32$ cm and (d) $z_p = 17$ cm, respectively) as function of the width of the pycnocline d; black dot-dashed - regular two-layer model; red - maximum displacement for the interface corresponding to the conjugate state of the optimal two layer system. The dashed black curve represents the maximum displacement of the density isolines $\rho(x,z) = \overline{\rho}(z_0)$ of the conjugate states in the continuos stratifications, with $\overline{\rho}(z)$ being the background stratification and z_0 being the interface position for the optimal two layer system.

In Figure 3.7 we compare the vertical displacement of the average density isoline to the displacement of the interface predicted by the two layer model (see Figure 3.6 for a simple schematics). We also display for comparison the vertical displacement of the density isolines for the continuous stratification corresponding to $\rho(x,z) = \overline{\rho}(z_0)$. Notice that the displacement of these isolines is close to the displacement corresponding to the average density profile, for the entire range of pycnocline widths. Based on this observation, we can construct an estimate of the average density isoline position for the continuous stratification by simply translating the interface predicted by the two-layer model $z = \zeta(x,t)$ in the vertical direction with $z_p - z_0$.

3.3.3. Dispersion. We conclude the section by assessing how accurately the optimal two-layer system that we have constructed captures the propagation of waves of infinitesimal amplitude and *finite* wave number.

In Figures 3.8-3.11 we compare the dispersion relation for the continuous density stratification $c = c(k)$ ($L = 2\pi/k$ period, c phase speed) (which can be easily be computed by solving the Sturm-Liouville problem (3.1) with zero boundary conditions, via a standard shooting method) against the dispersion relation for the two-layer systems, given by

$$c = k\sqrt{\frac{g(\rho_2 - \rho_1)}{\rho_1 \coth(h_1 k) + \rho_2 \coth(h_2 k)}}\,, \tag{3.19}$$

see Lamb [33]. Note that for periods comparable to the total height of the fluid H,

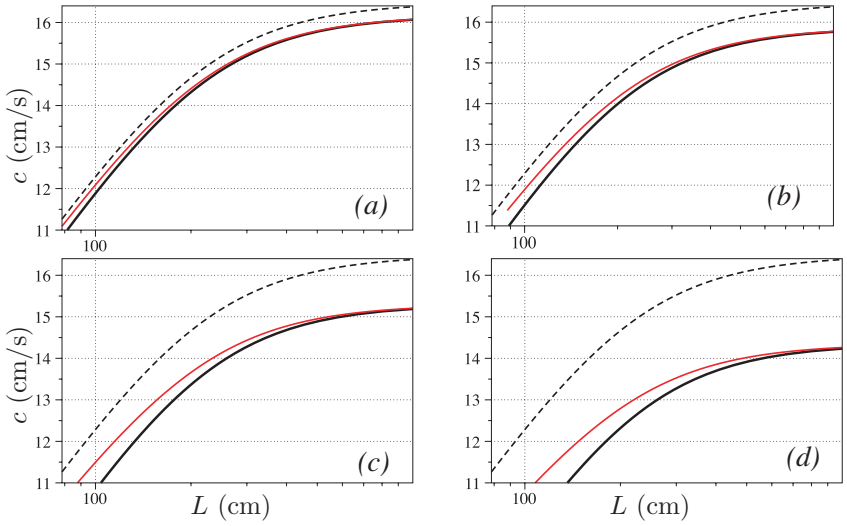

FIGURE 3.8. Dispersion relation for infinitesimal waves (L, period as a function of c, speed). Black - continuous stratification, black dashed - regular two layer, red - optimal two layer approximation. The width of the pycnocline d is (a) 2 cm, (b) 4 cm, (c) 8 cm and (d) 16 cm, whereas the inflection point of the density stratification located at $z_p = 62$ cm.

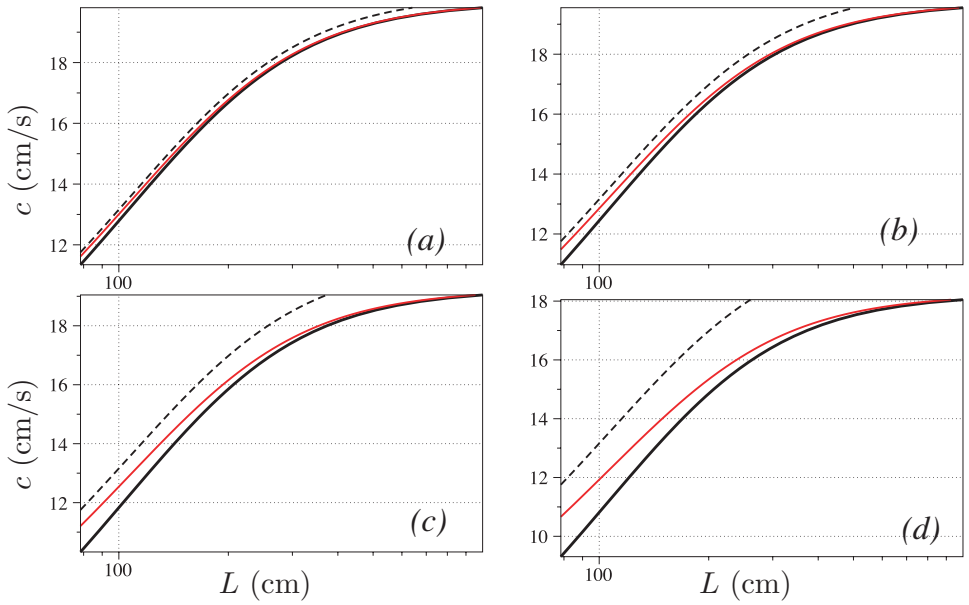

FIGURE 3.9. Same as Figure 3.8, with the inflection point of the density stratification located at $z_p = 47$ cm.

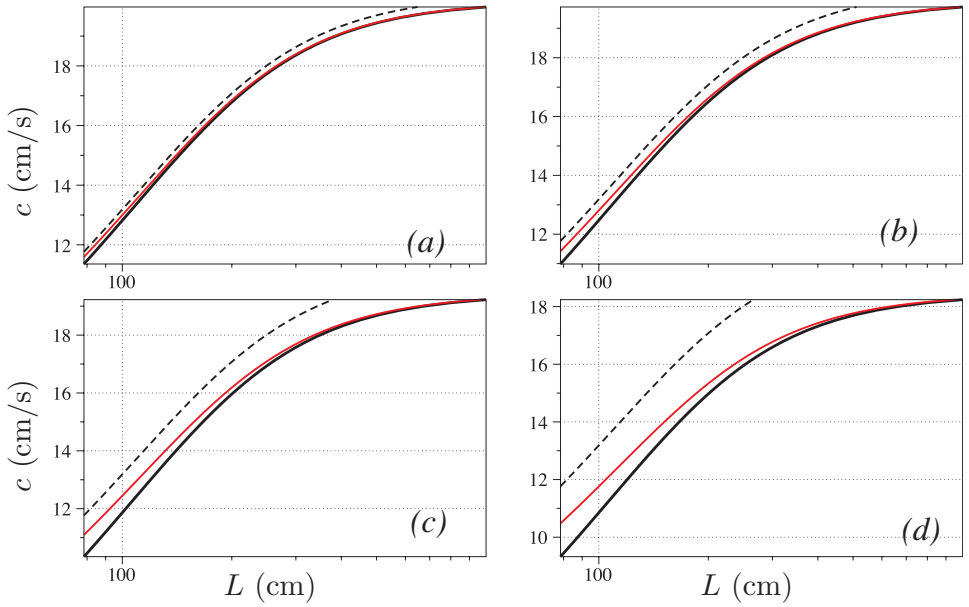

FIGURE 3.10. Same as Figure 3.8, with the inflection point of the density stratification located at $z_p = 32$ cm.

the optimal two-layer model fails to accurately capture the dispersion in the continuous stratification, this effect being enhanced by increasing the pycnocline width d. However, its prediction is always superior to the prediction of the regular two-layer model. We

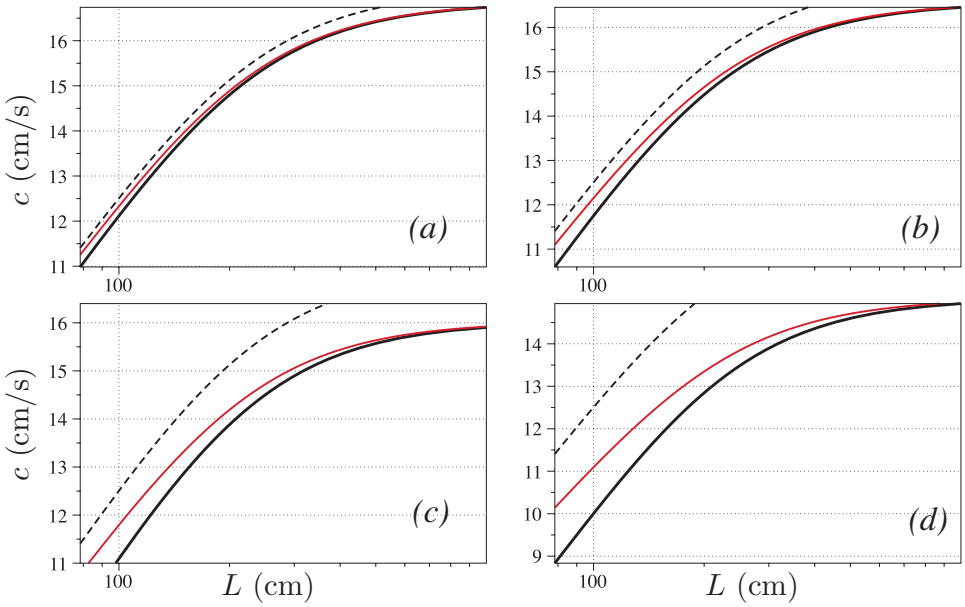

FIGURE 3.11. Same as Figure 3.8, with the inflection point of the density stratification located at $z_p = 17$ cm.

also point out that the agreement is excellent for $L/H > 1$, hence these strategies can be used in conjunction with asymptotic models for long wave motion, such as Choi & Camassa [7].

3.4. Validation

We test the performance of the optimal two-layer approximation described in the previous section in the case of solitary wave solutions. We will compare fundamental properties of the waves (wave speed, shape, kinetic and potential energy) in continuous stratification (as solutions as full Euler system, using a variant of the algorithm constructed by Turkington *et al.* [51], as described in Appendix C) versus properties of the waves in a two layer system (for which asymptotic solutions, in closed form are available Choi & Camassa [7]).

We consider the density stratifications in Figure 3.2(a) (the center of the pycnocline located at $z_p = 62$ cm and widths of the pycnocline ranging between 2 cm and 16 cm).

In Figures 3.12-3.15 we show the amplitude, kinetic energy and potential energy as functions of the speed of the solitary wave solutions in continuous stratification versus the two-layer approximations. The regular two-layer model over-predicts the speed of propagation of the solutions in continuous stratification, even for narrow pycnoclines, as evidenced in Figure 3.12(a). Note the excellent agreement of the integral properties (kinetic and potential energy) as predicted by the optimal two-layer model with the properties of the solutions in continuous stratification. An accurate estimate of the potential energy is particularly useful in the context of determining specific solitary wave solutions (e.g. waves of prescribed speed and amplitude) using the algorithm proposed by Turkington *et al.* [51], since the potential energy is an input of the corresponding iterative scheme.

By comparing the wave shapes of the solitary wave solutions against waves of same amplitude obtained with the two-layer approximations, we observe that the optimal two-layer approximation does not outperform the regular two-layer model, except in the large amplitude regime – see Figures 3.17(I.a-III.a), 3.19(I.a-III.a), 3.21(I.a-III.a) and 3.23(I.a).

However, when matching for speed, we notice a much better performance of the optimized two layer model. Finally, all solitary wave solutions in continuous stratification exhibit the behavior referenced in §3.3.2: flattening for increasing amplitude – see Figures 3.16, 3.18, 3.20 and 3.22. In particular for $d = 16$ cm we have computed a solitary wave solution close to the maximal amplitude which is bigger than the maximal amplitude predicted by the optimized two layer model – see Figure 3.15(a). In this instance, we

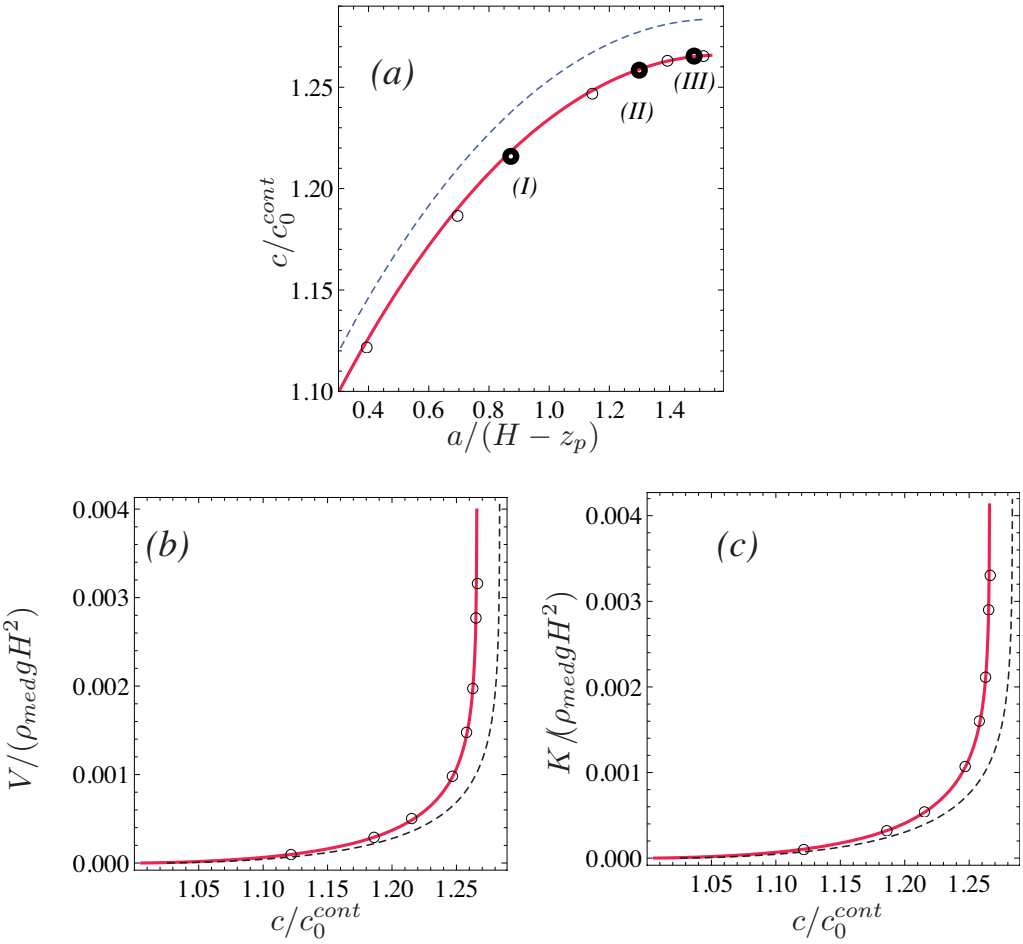

FIGURE 3.12. Properties of solitary wave solutions for the density stratification (3.18) with $H = 77$ cm, the inflection point located at $z_p = 62$ cm and the thickness of the pycnocline $d = 2$ cm. (a) Speed versus the maximum displacement of the average density isoline. (b) Potential energy versus speed. (c) Kinetic energy versus speed. Circles - Euler solutions in continuous stratification, black dashed - regular two layer, red - equivalent two layer least square for masses and potential energy in each layer. ρ_{med} is the average density for the continuous stratification.

cannot compare wave shapes for matched amplitude; nonetheless, the integral properties of the waves are still well captured by the optimized two-layer model.

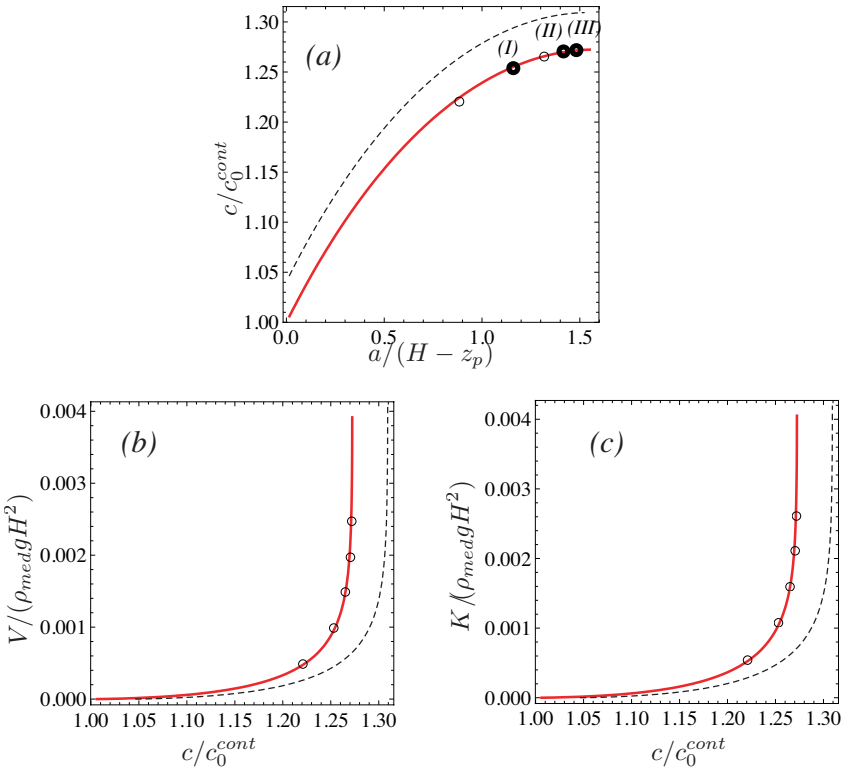

FIGURE 3.13. Same as Figure 3.12, for the thickness of the pycnocline $d = 4$ cm.

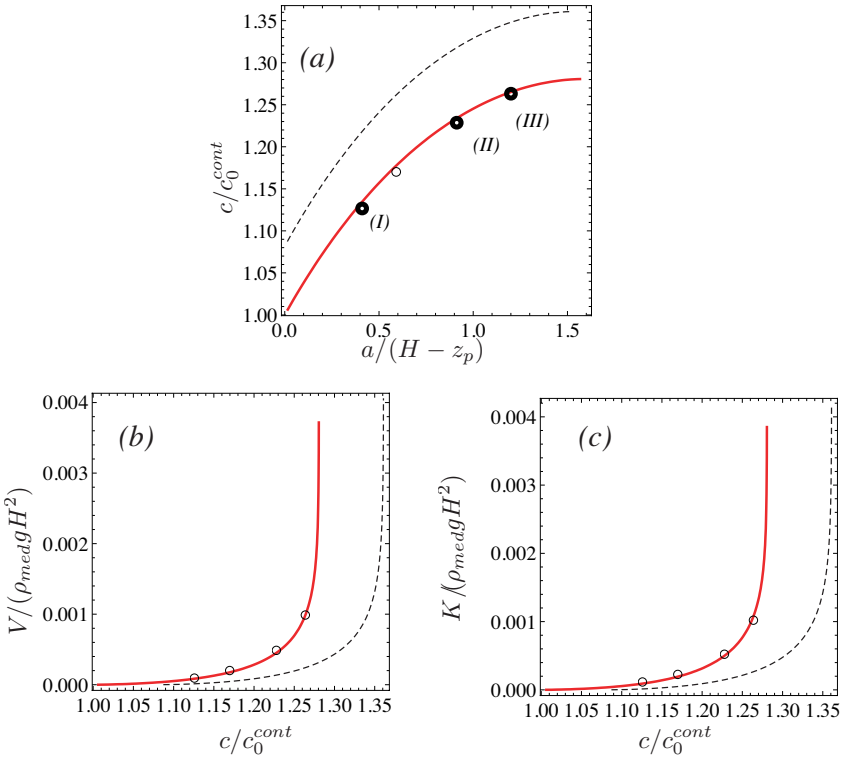

FIGURE 3.14. Same as Figure 3.12, for the thickness of the pycnocline $d = 8$ cm.

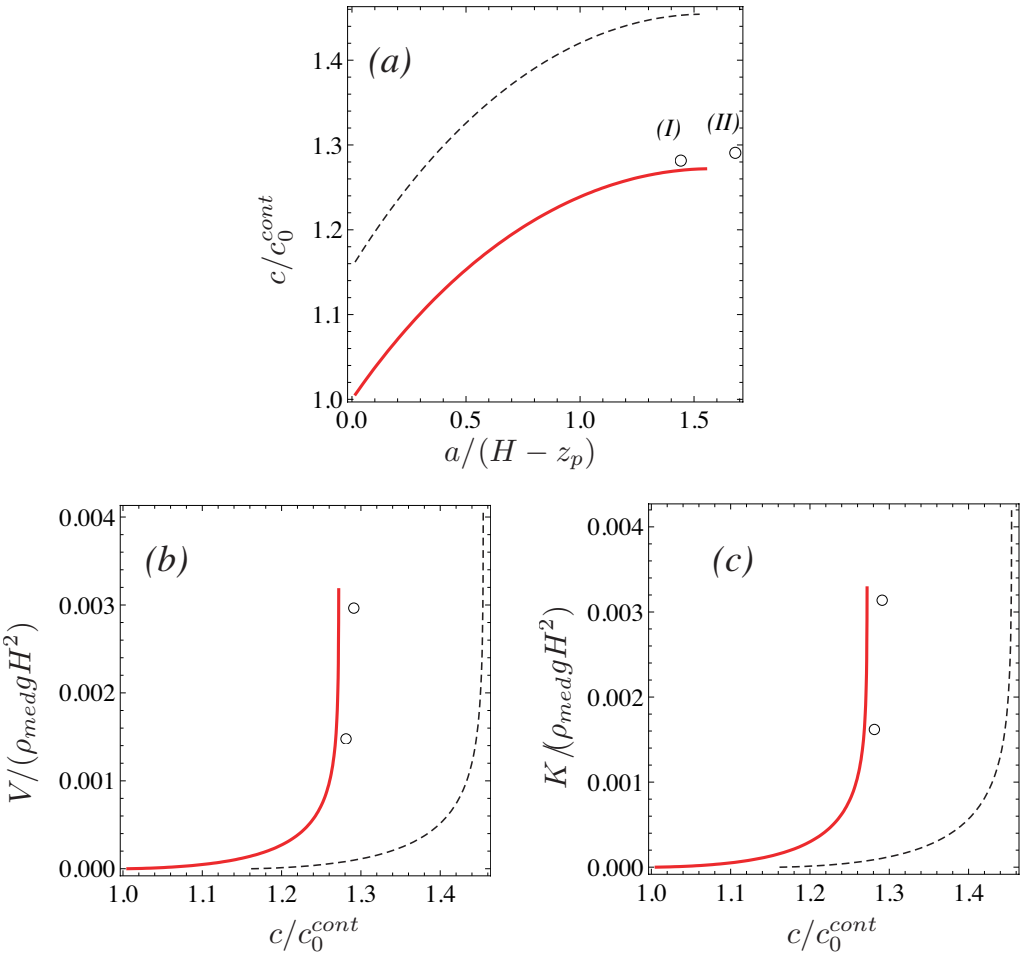

FIGURE 3.15. Same as Figure 3.12, for the thickness of the pycnocline $d = 16$ cm.

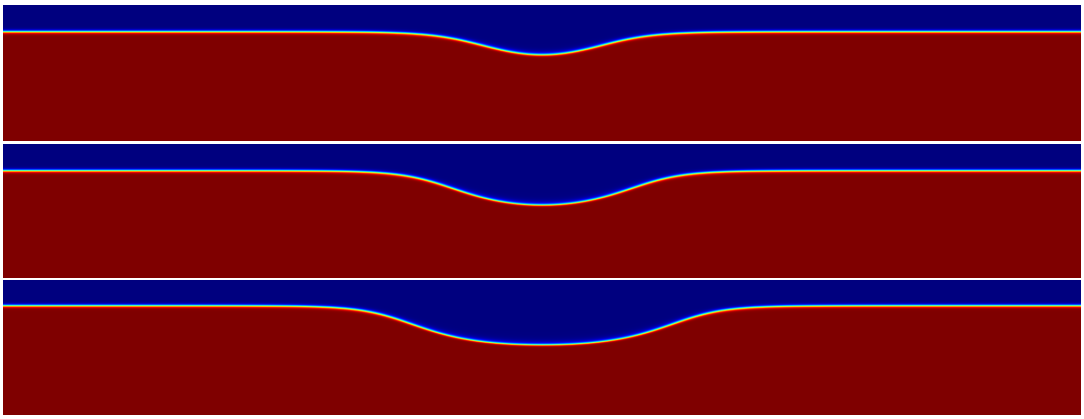

FIGURE 3.16. Density field for solitary wave solutions corresponding to the points marked in Figure 3.12(a) ($d = 2$ cm).

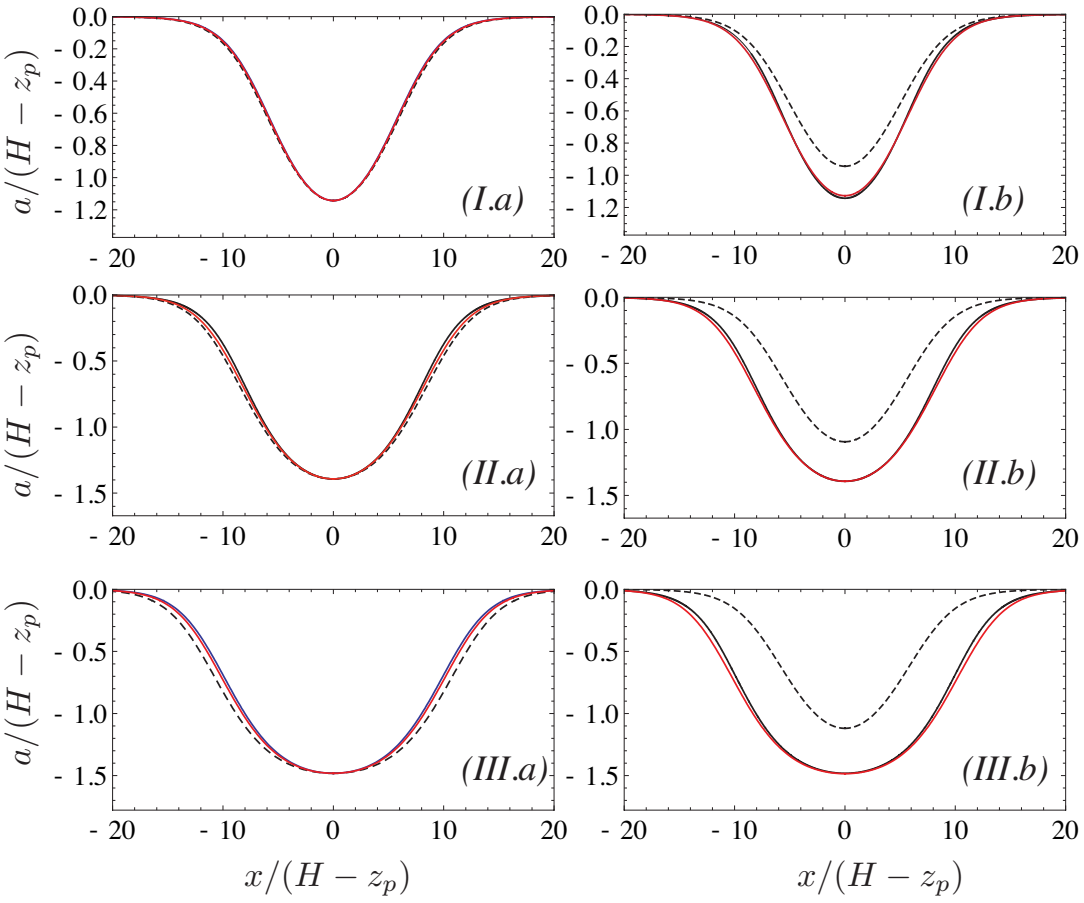

FIGURE 3.17. Comparison between the wave profiles of solitary wave solutions in continuous stratification (corresponding to the points marked in Figure 3.12(a)) and the two-layer approximations. Left - matched amplitude; right - matched speed. Black - Euler solutions, black dashed - regular two layer, red - equivalent two layer least square for masses and potential energy in each layer.

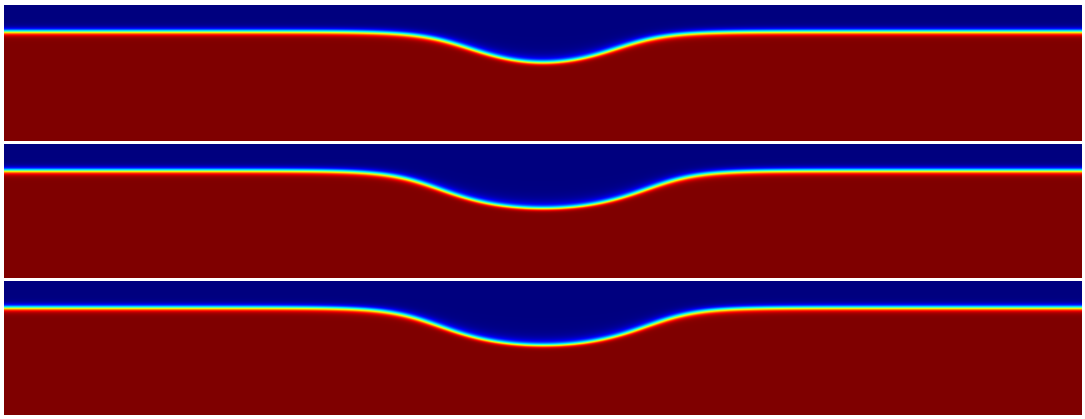

FIGURE 3.18. Density field for solitary wave solutions corresponding to the points marked in Figure 3.13(a) ($d = 4$ cm).

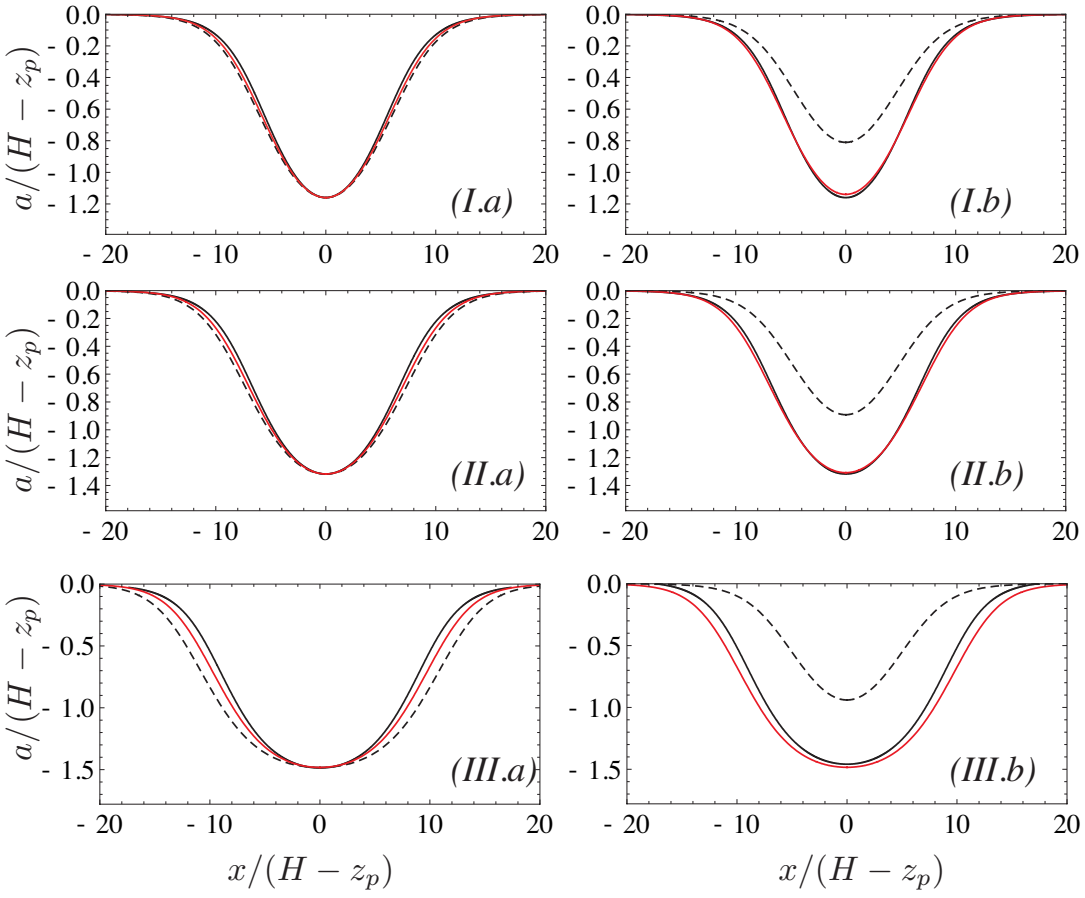

FIGURE 3.19. Comparison between the wave profiles of solitary wave solutions in continuous stratification (corresponding to the points marked in Figure 3.13(a)) and the two-layer approximations. Left - matched amplitude; right - matched speed. Black - Euler solutions, black dashed - regular two layer, red - equivalent two layer least square fit for masses and potential energy in each layer.

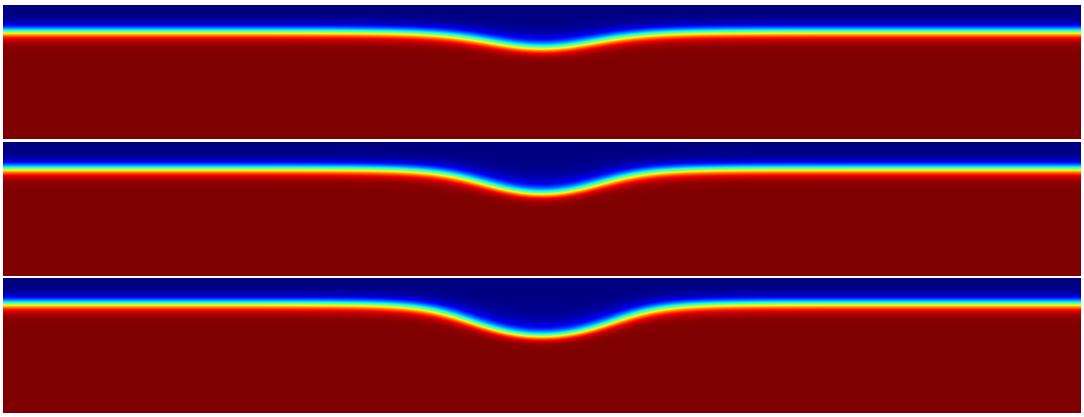

FIGURE 3.20. Density field for solitary wave solutions corresponding to the points marked in Figure 3.14(a) ($d = 8$ cm).

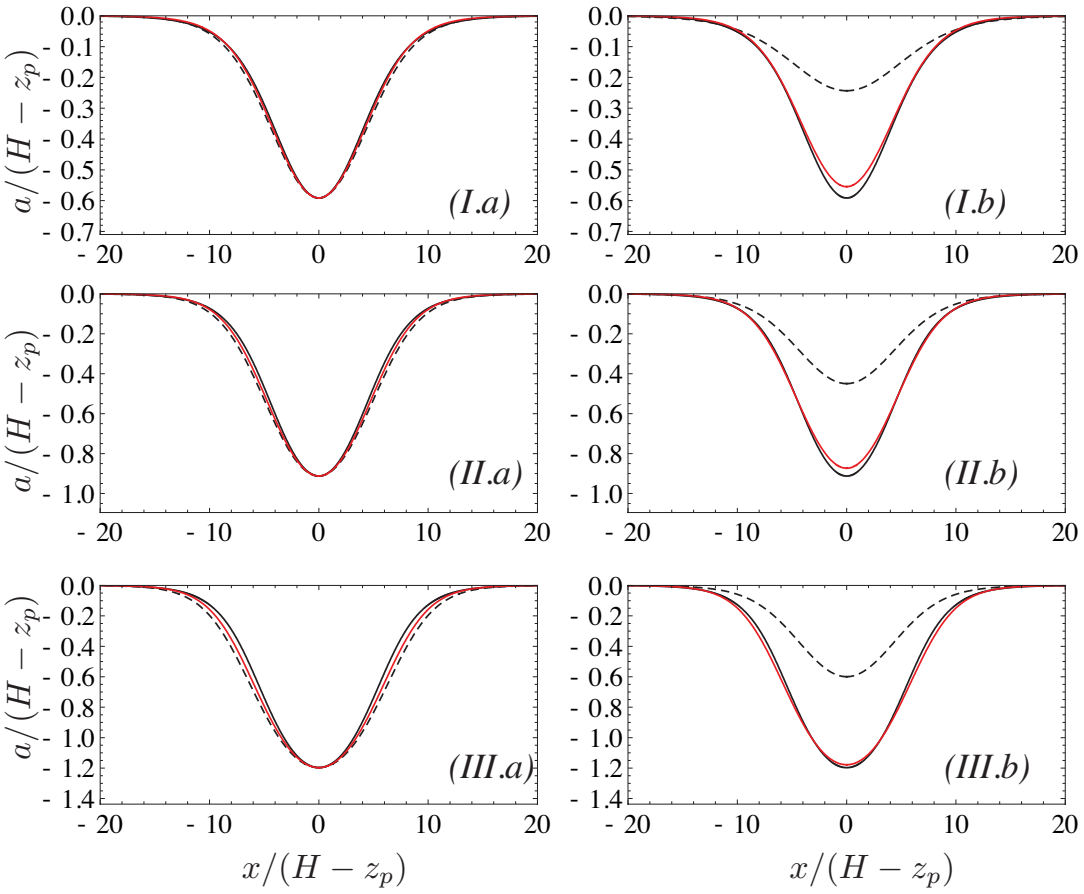

FIGURE 3.21. Comparison between the wave profiles of solitary wave solutions in continuous stratification (corresponding to the points marked in Figure 3.14(a)) and the two-layer approximations. Left - matched amplitude; right - matched speed. Black - Euler solutions, black dashed - regular two layer, red - equivalent two layer least square for masses and potential energy in each layer.

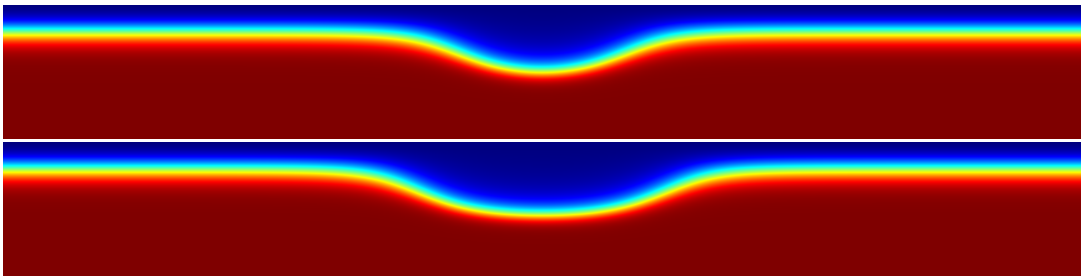

FIGURE 3.22. Density field for solitary wave solutions corresponding to the points in Figure 3.15(a)($d = 16$ cm).

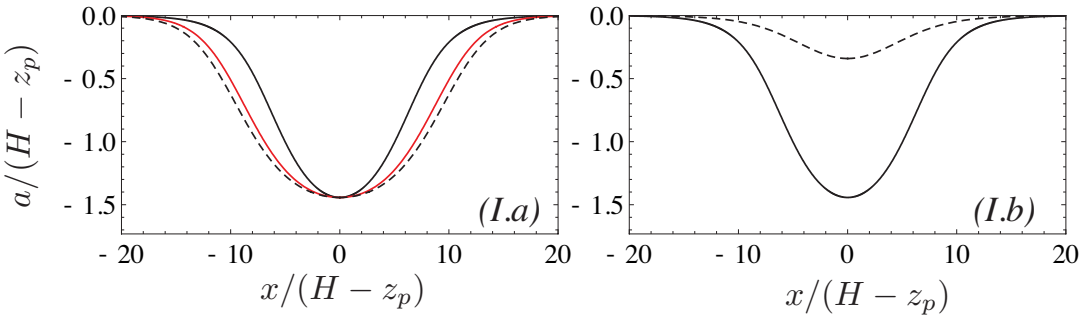

FIGURE 3.23. Comparison between the wave profiles of solitary wave solutions in continuous stratification (corresponding to the points marked in Figure 3.15) and the two-layer approximations. Left - matched amplitude; right - matched speed. Black - Euler solutions, black dashed - regular two layer, red - equivalent two layer least square for masses and potential energy in each layer.

3.5. Reconstruction of the velocity field from the two-layer approximation

In the current section, we estimate the velocity field induced by long wave motion in continuously stratified fluid, based on the two-layer approximation we have discussed in the previous section. As seen in above, when optimally selecting for the parameters of the two-layer system, we obtain good estimates for the isopycnal displacement corresponding to the average density and for the speed of propagation. Local velocities can be estimated using the strongly nonlinear model (relationships of $O(\epsilon^4)$ for long waves in a *two layer* system provided by Camassa *et al.* [8], where $\epsilon = H/L$ is the long wave parameter with H a typical vertical scale and L a typical horizontal scale). However, when the thickness of the pycnocline is large, these estimates under-predict the fluid-velocity, since they cannot capture the structure of the shear in the pycnocline region (the velocity predicted by the two layer theory exhibits a jump across the interface). In the following, we include the

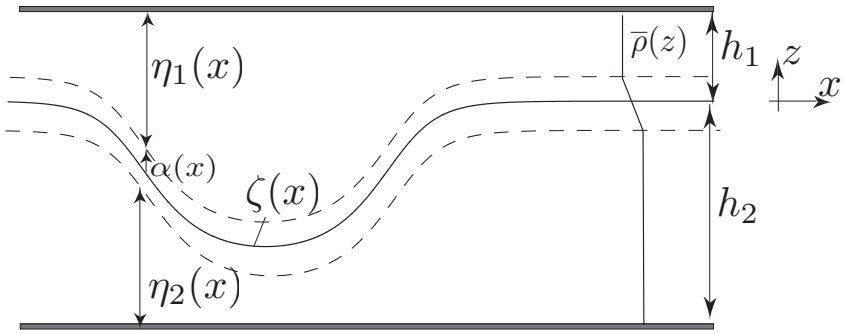

FIGURE 3.24. Schematics of the three-layer system with main notations definitions.

effect of the finite pycnocline by assuming linear density stratification and shear in the pycnocline region and imposing volume conservation; we reconstruct the velocity field from the isopycnal displacement and the speed of propagation predicted by the two layer model. We restrict our attention on the case of waves of permanent form, propagating

with constant speed c. Nonetheless, this analysis is easily extendable to time dependent wave evolution.

Let $\zeta(x,t)$ denote the displacement of the average density isoline, as predicted by the two layer model – see Figure 3.24 for a simple schematics. For a stationary wave moving from left to right with constant speed c, we make the change of variable

$$X = x - ct\,,$$

and consider

$$\zeta(x,t) \equiv \zeta(X)\,,\ u(x,t) \equiv u(X)\,,\ w(x,t) \equiv w(X)\,,$$

where $u\,, w$ are the horizontal and vertical fluid velocities. We place the coordinate system at the level of the pycnocline center of the background stratification $\overline{\rho}(z)$, which implies

$$\overline{\rho}(0) = \rho_{med} = (\rho_{min} + \rho_{max})/2\,.$$

We approximate the background density profile in the intermediate layer by using a linear stratification that passes through the center of the pycnocline and has the same slope as the continuous stratification in the quiescent state. The corresponding thickness is thus given by

$$2\widetilde{\alpha} = \frac{\rho_{min} - \rho_{max}}{2\overline{\rho}'(0)}\,.$$

Let $\alpha(X)$ denote half the thickness of the pycnocline at location X. We allow the pycnocline thickness to vary in the horizontal direction, however we assume that the variation is slow and also that the thickness is smaller than any of the outer layers widths. We thus assume $\alpha = \alpha(\epsilon X)$ and $\alpha/H = \delta \ll 1$.

Then, the density field is

$$\rho(X,z) = \begin{cases} \dfrac{\rho_{min}-\rho_{max}}{2\alpha(X)} z + \dfrac{\rho_{min}+\rho_{max}}{2} & \text{if } z \in [\zeta(X)-\alpha(X)\,,\zeta(X)+\alpha(X)]\,, \\ \rho_{min} & \text{if } z \in [\zeta(X)+\alpha(X), h_1]\,, \\ \rho_{max} & \text{if } z \in [-h_2, \zeta(X)-\alpha(X)]\,. \end{cases}$$

We denote by

$$\eta_1(X) = h_1 - \zeta(X) - \alpha(X)\,, \qquad \eta_2(X) = h_2 + \zeta(X) - \alpha(X)\,, \tag{3.20}$$

the widths of the two layers of constant densities.

We approximate the horizontal velocity with a linear profile in the pycnocline region $z \in [\zeta(X)-\alpha(X)\,,\zeta(X)+\alpha(X)]\,,$

$$u_{pyc}(X,z) = \frac{u_1(\alpha(X)) - u_2(-\alpha(X))}{2\alpha(X)} z + \frac{u_1(\alpha(X)) + u_2(-\alpha(X))}{2}\,, \tag{3.21}$$

where we have imposed continuity of the horizontal velocity at the two interfaces. In the constant density layers, assuming irrotationality, we can connect the local velocities to the layer-averaged velocities

$$\overline{u}_k(X) = \int_{[\eta_k]} u_k(X,z)dz \quad k = 1,2\,,$$

by using the asymptotic relation derived in Camassa *et al.* [8].

Thus, we have accumulated three unknown functions dependent on X, that would completely specify the density and local-velocity fields: the thickness of the pycnocline α and the two layer-averaged velocities in the outer layers $\overline{u}_1$ and $\overline{u}_2$. We can relate the

layer-averaged velocities to the thickness α by imposing volume conservation in the outer layers

$$(\overline{u}_k - c)\eta_k = -c(h_k - \widetilde{\alpha})\,, \qquad k = 1, 2\,, \tag{3.22}$$

which implies

$$\overline{u}_k = c\left(1 - \frac{h_k - \widetilde{\alpha}}{\eta_k}\right)\,, \qquad k = 1, 2\,. \tag{3.23}$$

Then, imposing continuity of the horizontal velocity at the two interfaces, we can express the velocity in the pycnocline region as a function of the thickness of the pycnocline only. Finally, imposing conservation of volume for the intermediate layer, we obtain an equation involving only the thickness of the pycnocline $\alpha(X)$. In the following, we deduce the above equation, as an *algebraic* equation in $\alpha(X)$, by taking advantage of the scaling $\alpha/H \equiv \delta \ll 1$. We introduce the scaled independent variables

$$X^* = \frac{X}{L}\,, \quad z^* = \frac{z}{H}\,, \quad t^* = t\frac{U_0}{L}\,,$$

and the scaled dependent variables

$$u_i^* = \frac{u_i}{U_0}\,, \quad \rho_i^* = \frac{\rho_i}{\rho_{med}}\,, \quad \delta\alpha^* = \frac{\alpha}{H}\,,$$

where $U_0 \equiv \sqrt{gH}$.

The horizontal velocities in the constant density layers are

$$u_1^*(X^*, z^*) = \overline{u}_1^*(X^*) + \epsilon^2\left(\frac{\eta_1^*(X^*)^2}{6} - \frac{(h_1^* - z^*)^2}{2}\right)\partial_{X^*}^2\overline{u}_1^*(X^*) + O(\epsilon^4)\,, \tag{3.24}$$

if $z^* \in [\zeta^* + \delta\alpha^*, h_1^*]$, and

$$u_2^*(X^*, z^*) = \overline{u}_2^*(X^*) + \epsilon^2 \left(\frac{\eta_2^*(X^*)^2}{6} - \frac{(h_2^* + z^*)^2}{2} \right) \partial_{X^*}^2 \overline{u}_2^*(X^*) + O(\epsilon^4)\,, \tag{3.25}$$

if $z^* \in [-h_2^*\,, \zeta^* - \delta\alpha^*]$, respectively. Using relation (3.23), the second derivative of the mean-layer velocities $\overline{u}_k$ can be expressed as

(3.26)

$$\partial_{X^*}^2 \overline{u}^*{}_k = c^* \left[\frac{(h_k^* - \delta\widetilde{\alpha}^*)\eta_k^{*\prime\prime}}{\eta_k^{*2}} - \frac{2(h_k^* - \delta\widetilde{\alpha}^*)\eta_k^{*\prime 2}}{\eta_k^{*3}} \right] = c^* \left[(-1)^k \frac{h_k^* \zeta^{*\prime\prime}}{\eta_k^{*2}} - \frac{2h_k^* \zeta^{*\prime 2}}{\eta_k^{*3}} \right] + O(\delta)\,,$$

recalling relation (3.20) that defines the outer layer widths.

By replacing (3.26) in (3.24)-(3.25) and discarding terms of order $O(\delta\epsilon^2)$, we thus obtain the following asymptotic relation for the horizontal shear in the layers of constant densities, rewritten in dimensional form,

$$u_k(X, z) = c \left[1 - \frac{h_k - \widetilde{\alpha}}{\eta_k} + \left(\frac{\eta_k^2}{6} - \frac{(h_k + (-1)^k z)^2}{2} \right) \left(\frac{(-1)^k h_k \zeta^{\prime\prime}}{\eta_k^2} - \frac{2h_k \zeta^{\prime 2}}{\eta_k^3} \right) \right]\,, \tag{3.27}$$

which has an algebraic dependence on the thickness of the pycnocline α. Substituting the velocities at the two interfaces

$$u_k|_{\eta_k} = c \left[1 - \frac{h_k - \widetilde{\alpha}}{\eta_k} + h_k \left(\frac{(-1)^k \zeta^{\prime\prime}}{3} - \frac{2\zeta^{\prime 2}}{\eta_k} \right) \right]\,, \quad k = 1, 2\,, \tag{3.28}$$

in the formula for the inner layer velocity (3.21) yields a relation between the shear in the pycnocline region that depends algebraically on the unknown width α. Finally, imposing

volume conservation in the inner layer

$$\int_{-\alpha(X)}^{\alpha(X)} (u_{pyc}(X,z) - c)dz = -2c\widetilde{\alpha}\,,$$

we obtain an algebraic, *cubic*, equation for $\alpha(X)$, which can be solved for any fixed X location

$$\alpha\left[\frac{h_1-\widetilde{\alpha}}{\eta_1} - h_1\left(\frac{\zeta''}{3} + \frac{2\zeta'^2}{3\eta_1}\right) + \frac{h_2-\widetilde{\alpha}}{\eta_2} + h_2\left(\frac{\zeta''}{3} - \frac{2\zeta'^2}{3\eta_2}\right)\right] = 2\widetilde{\alpha}\,. \tag{3.29}$$

In Figure 3.25 we present shear and density profiles for conjugate states for the stratification (3.18) (with $z_p = 62$ cm and pycnocline widths ranging from $d = 4$ cm to $d = 10$ cm) constructed using the strategy described above. Note that when including the effect of finite pycnocline, the agreement for the velocity between the smooth stratification case and its linear approximation degrades with increasing effective thickness of the pycnocline more visibly for the top layer (albeit while maintaining a superior agreement with respect to the strictly two-layer prediction throughout). Nonetheless, the maximum slope of the shear in the pycnocline region is very well captured.

Finally, in Figure 3.26 we present the shear profiles for an internal solitary wave solution in continuous stratification at three horizontal locations along the wave profile, compared against the two-layer predictions.

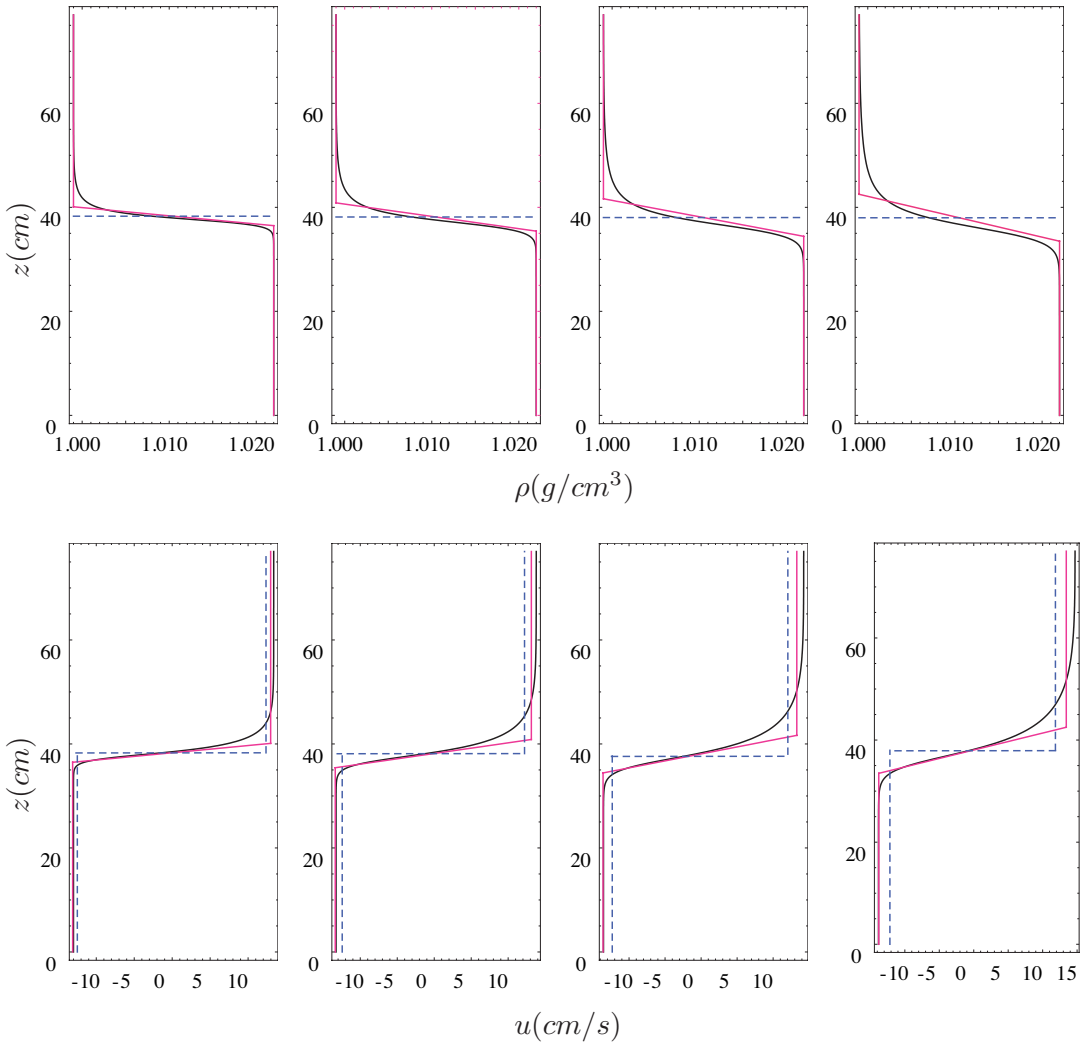

FIGURE 3.25. Density and horizontal shear for conjugate states in a stratification (3.18) with total depth of the fluid layer $H = 77$ cm, center of the pycnocline located at $z_p = 62$ cm, densities in the outer layers $\rho_{min} = 0.999$ g/cm^2 , $\rho_{max} = 1.022$ g/cm^2 and thickness of the pycnocline (defined, as usual, as the distance between the vertical locations in the density stratification corresponding to $\rho_{min} + 0.1\Delta\rho$ and $\rho_{max} + 0.9\Delta\rho$ respectively) of $4\,, 6\,, 8$ and 10 cm. Black - Euler solution in continuous stratification, dashed - prediction of the strongly nonlinear model for optimized choice of parameters, red - predictions of the optimized two layer model with correction that includes the presence of the finite width pycnocline.

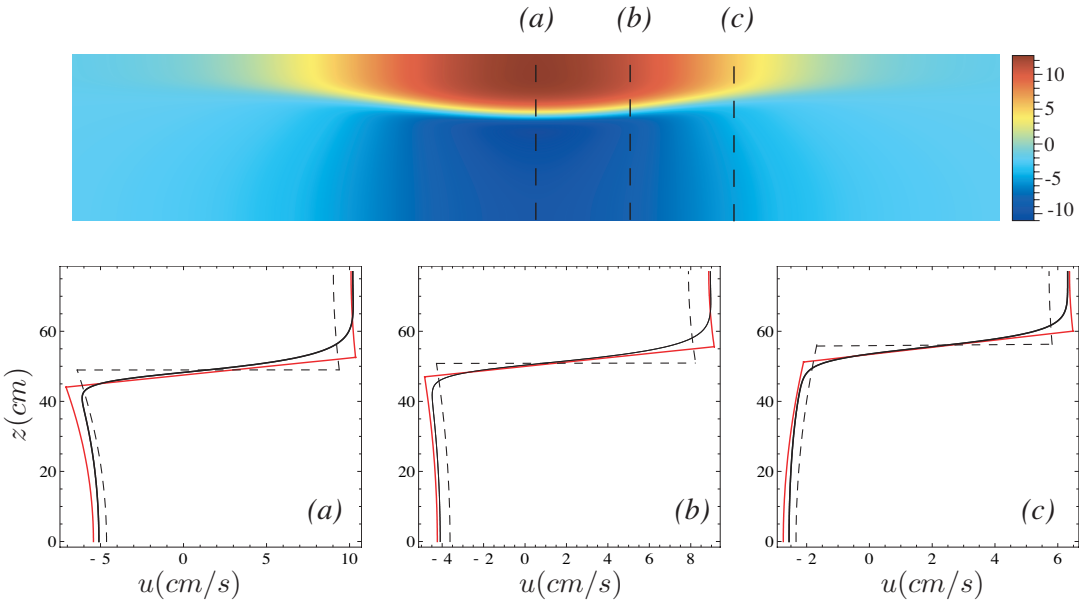

FIGURE 3.26. Black - horizontal shear for a solitary wave solution in a stratification (3.18) (with total depth of the fluid layer $H = 77$ cm, center of the pycnocline located at $z_p = 62$ cm, densities in the outer layers $\rho_{min} = 0.999$ g/cm^2 , $\rho_{max} = 1.022$ g/cm^2 and thickness of the pycnocline of 8 cm) at (a) maximum displacement of the pycnocline, (b) at a distance $X = 44$ cm from the maximum displacement and (c) $X = 79$ cm respectively. Black - Euler solution in continuous stratification, dashed - prediction of the strongly nonlinear model for optimized choice of parameters, red - predictions of the optimized two layer model with correction that includes the presence of the finite width pycnocline.

3.6. Discussion

We have constructed an optimal two-layer approximation for continuous stratification with one pycnocline that accurately captures the speed of propagation of both dispersive waves and nonlinear solitary wave solutions (including internal bores). We use the conjugate state concept to select the optimal two-layer configuration, among other possible choice for parameters. When choosing the optimal equivalent two-layer system, the isopycnal displacement of the center of the pycnocline is very well approximated up to thicknesses comparable to the widths of the two layers. Integral properties of the motion, such as kinetic and potential energy are also very well predicted.

Local properties of the waves such as eulerian velocity are also of practical interest. We note that the two-layer model provides a good estimate of layer averaged velocities, but fails to describe the structure of the velocity field in the pycnocline region. In §3.5 we construct the velocity field based on the long wave assumption, by taking into account the effect of the finite pycnocline.

This study would be made more complete by assessing the influence of an asymmetry of the density stratification. Moreover, a more accurate testing for the robustness of the proposed model would be provided by the study of time evolution – which will be investigated in future work.

The current investigation could be easily adapted to configurations with multiple pycnoclines as well as to the case of a free (as opposed to rigid lid) upper surface.

CHAPTER 4

Propagation of large amplitude internal waves and their instabilities

4.1. Introduction

Recent progress in field measurements (Moum *et al.* [42]) as well as experiments (Grue *et al.* [19], Fructus *et al.* [13]) have confirmed that in large amplitude regimes one of the most common mechanisms of internal wave breaking is shear-instability. In this work, we focus on the experiments of Grue *et al.* [19], which provided early evidence of large-amplitude wave instabilities, identified by the authors to be of Kelvin-Helmholtz type. For this set of experiments, the instabilities are only observed for near maximal amplitude waves, despite the fact that a (parallel) shear stability theory would predict that Kelvin-Helmholtz instability should be observable at wave amplitudes smaller than those reported. However, for experiments, and to an even greater extent for their field counterparts, an unambiguous determination of the onset of instability may be affected by several unrelated causes, which motivates our effort to study numerically, and to interpret analytically, the instabilities of large amplitude internal waves.

The study of Kelvin-Helmholtz instability onset and its ensuing evolution can be pursued in the framework of the Euler equations for incompressible inviscid and stratified fluid. This is because typical Reynolds numbers, from both the experimental and field

observation set-ups, are very large, and diffusion of stratifying agents such as salt and heat is expected to take place on time scales much larger than those of the dynamics of both the internal waves and their instabilities. Moreover, the spatial (vertical) scales of free-surface internal-wave-induced motion is small in comparison to the internal wave scales, which allows us to constrain the free surface by a rigid lid. Of course, the full set of stratified Euler equations are not easily amenable to analytical investigations. However, we can get fundamental help from the far simpler physical situation capable of supporting internal wave motion – that of a two-layer fluid under gravity – which we have studied in the previous chapters. In particular, for large amplitude waves, the strongly nonlinear asymptotic model developed in Miyata [39, 40], Choi & Camassa [6, 7] is in overall good agreement with the full Euler equations as well as experimental data, and this can be used as a predictive tool for the onset of instabilities whenever the underlying stratification is approximates that of a two layers. The purpose of this investigation is thus to study numerically the instabilities of large amplitude internal waves in stratification with narrow pycnoclines.

The chapter is organized as follows: in §4.2, we replicate numerically the experiment in Grue *et al.* [19], by using an incompressible Euler (and Navier-Stokes) variable density solver based on a conservative projection method for the time-dependent flows in two-dimensions (VARDEN), described in detail in Almgren *et al.* [1]. We validate the numerical scheme by comparison against the strongly nonlinear model and monitor the correlation between the shear instability and amplitude regimes. We complement this study, in §4.3, by initializing the evolution code with solitary wave solutions of Euler equations (found through a variant of the iterative scheme developed in Turkington

et al. [51], which we present in Appendix C). By determining true travelling wave solution for the continuously stratified Euler system, we can discern between instabilities that are an intrinsic property of travelling wave dynamics and those that are induced by the experimental generation technique in the course of evolution towards a true travelling wave of a given amplitude.

4.2. Simulated wave tank

4.2.1. Experiments for generation and propagation of internal waves of large amplitude Grue *et al.* [19]. The propagation and breaking of solitary waves in a near two-layer stratification with narrow pycnocline were investigated experimentally in Grue *et al.* [19]. The velocity field associated with the waves, the phase speed and the wave profiles were measured using particle tracking velocimetry (PTV) and image analysis. The experiments were performed in a stratification consisting of a layer of fresh water of density $\rho_1 = 0.999$ g/cm^3 over a layer of brine of density $\rho_2 = 1.022$ g/cm^3. With respect to the quiescent initial state and the pycnocline location, the depth of the (bottom) layer of brine and that of (top) layer of fresh water were 62 cm and 15 cm, respectively. Salt diffusivity and pouring techniques naturally generated a stratified interfacial region in which the density varied smoothly between the two layers. The undisturbed interfacial thickness of about 2 cm was used for most of the experimental runs; we use this thickness for the majority of our numerical simulations as well. We assume that the thickness of the pycnocline referred in Grue *et al.* [19] is defined, as usual, as the distance between the two constant density profiles with densities given by $\rho_1 + 0.1\Delta\rho$ and $\rho_1 + 0.9\Delta\rho$.

In all experiments, the waves were generated by releasing a volume of fresh water trapped behind a gate. This volume was varied to obtain a single internal wave of desired

amplitude. At the other end of the tank the waves were reflected by a vertical wall. The measurements allowed the evaluation of the local Richardson number due to the wave induced shear flow in the pycnocline region. Kelvin-Helmholtz instability was observed only for the largest amplitude waves near the theoretical maximal amplitude set by the initial equilibrium configuration.

4.2.2. Set-up for numerical experiments. We replicate numerically the experiments mentioned above by using the same technique of Grue *et al.* [19] for initialization. Moreover, we mimic as closely as possible the measuring procedure of wave parameters they reported in their paper. As argued before, we neglect diffusivity and viscosity as matter of scales, and restrict the upper surface by a rigid lid. The computational domain is thus a rectangular box (with length of the tank $L = 1232\,\mathrm{cm}$ and height $H = 77\,\mathrm{cm}$, similar to Grue *et al.* [19]), with slip boundary conditions for all four rigid walls. Of course, the geometry of a real tank would have a third (width) dimension. Grue *et al.* [19] chose the width ($L = 50\,\mathrm{cm}$) to minimize three dimensional effects from lateral boundary layers. The skewed width/length aspect ratio then produced essentially two-dimensional (width-independent) dynamics in all their lab experiments sufficiently far from the generation region. In the numerical experiments, we simulate the gate by a step function in density (see Figure 4.1). The fluid is initially at rest, and the smooth pycnocline is approximated by a hyperbolic tangent function. Thus, initially, the center of the pycnocline is located at

$$\zeta(x, t = 0) = \begin{cases} H - h_1 - h_{gate} & \text{if } x < L_{gate} \\ h_2 & \text{if } x > L_{gate} \end{cases},$$

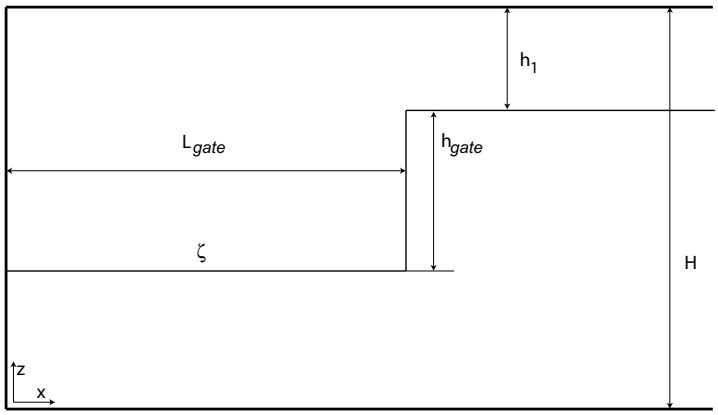

FIGURE 4.1. Numerical gate in the form of a step function.

where $h_2 = 62\,\text{cm}$, $h_1 = H - h_2 = 15\,\text{cm}$ and the density field is given by

$$\rho(x, z, t = 0) = \rho_1 + \tfrac{1}{2}(\rho_2 - \rho_1)\,(1 + \tanh\,[\ln(9)/d(\zeta(x, t = 0) - z)])\,.$$

where $d = 2.1\,\text{cm}$ is the thickness of the pycnocline. The step function eventually evolves into a rightward-propagating depression wave. Its amplitude and speed of propagation depends on the height h_{gate} and the length L_{gate} of the gate. Following Grue *et al.* [19]'s experimental techniques, we mimic their reconstruction of spatial wave profiles from two time-series of the vertical position of the pycnocline, recorded at two fixed locations along the tank, at half length $x = 450\,\text{cm}$ and at the end of the tank, $x = 1050\,\text{cm}$, respectively. The initial gate parameters for each wave realization were not reported in [19]. The data in this reference focus on the resulting traveling waves for five typical relative amplitudes (as measured at the $x = 1050\,\text{cm}$ recording location) a/h_1 of 0.22, 0.36, 0.91, 1.23 and 1.51 respectively. Gate parameters assuring repeatability of realization for these wave amplitudes were achieved by a trial-and-error procedure (Sveen, private communication). Once again, we mimic this to obtain waves of comparable amplitudes.

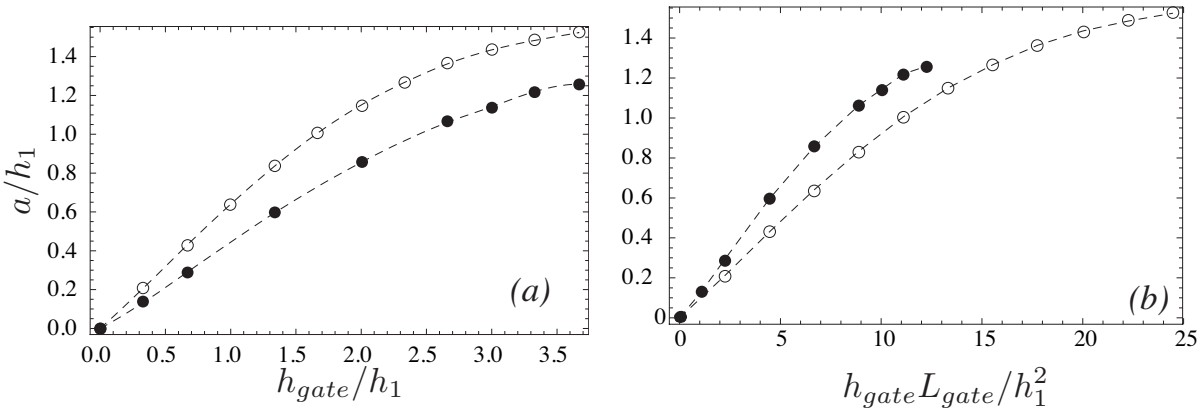

FIGURE 4.2. (a) Dependence of the amplitude of the wave at $x = 1050\,\text{cm}$ on the height of added volume of fresh water h_{gate}. (b) Dependence of the amplitude of the wave on the volume of added volume of fresh water. ◯ $L_{gate} = 100\,\text{cm}$, • $L_{gate} = 50\,\text{cm}$.

By fixing the length of the gate to $L_{gate} = 100\,\text{cm}$ and realizing a series of experiments for h_{gate} ranging from 5 cm to 55 cm, we determine numerically the dependence $a|_{1050\,\text{cm}} = f\,(h_{gate})$. We can then determine, via interpolation, the heights of the gate that would render the targeted amplitudes. While this procedure is effective, we see evidence of a trailing nonlinear wave train close to the emanating traveling wave in some cases, also noticeable in some of the laboratory data. To investigate the influence of the initialization parameters, we perform a series of numerical experiments for the length of the gate $L_{gate} = 50\,\text{cm}$. In Figure 4.2 we show the dependence of amplitude (as measured at $X = 1050\,\text{cm}$) on the height of the gate (a) and on the added volume of fresh water (b). Note that the wave amplitude depends on both parameters of the gate, rather than on just the added volume. The sensitivity of the amplitude and separation for trailing waves on gate parameters is tested by generating two waves of relative amplitude $a/h_1 = 0.91$ and $a/h_1 = 1.23$ respectively, for a gate length $L_{gate} = 50\,\text{cm}$ and of the gate heights

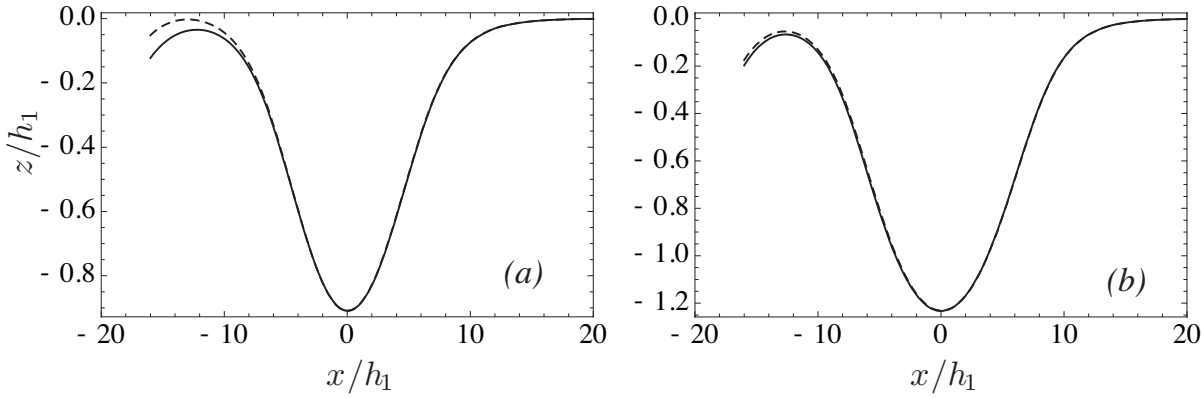

FIGURE 4.3. (a) Two wave profiles of same amplitude (as recorded at $x = 1050\,\text{cm}$) $a/h_1 = 0.91$ are shown for two numerical experiments with initial conditions $L_{gate} = 100\,\text{cm}$, $h_{gate} = 23.39$ cm (dashed) and $L_{gate} = 50$ cm, $h_{gate} = 32.37$ cm (continuous). (b) Same as (a), for relative amplitude $a/h_1 = 1.23$, the height of the gate being in each case $h_{gate} = 33.3\,\text{cm}$ and $h_{gate} = 50.7\,\text{cm}$, respectively.

$h_{gate} = 32.37\,\text{cm}$ and $50.767\,\text{cm}$ respectively. As shown in Figure 4.3, the wave shape is overall maintained except for slightly different height recovery a the trailing end.

4.2.3. Validation of the experiment. We present numerical results for the three main types of results presented in Grue *et al.* [19]: wave profiles, horizontal velocity profiles, and wave speeds. We have performed the majority of the numerical experiments using a resolution of 128 points in the vertical direction. We have also performed runs at resolutions of 256 and 512 for a large amplitude wave, in order to assess the convergence of the numerical scheme. More detailed analysis of the resolution study are given in §4.2.6.

In Grue *et al.* [19], the wave profile is reconstructed by multiplying the time series measured at the location $x = 1050$ cm with the phase speed. We thus need an estimate for the phase speed of the wave, which can be constructed using the other time series,

measured at location 450 cm. In the following, we describe the strategy for obtaining such an estimate.

The wave profile corresponds to a surface in the space (x, z, t), defined by $\rho(x, z, t) = \rho_{med}$. On such a surface we have

$$\frac{d\rho}{dt} = \frac{\partial\rho}{\partial x}\frac{dx}{dt} + \frac{\partial\rho}{\partial z}\frac{dz}{dt} + \frac{\partial\rho}{\partial t} = 0\,.$$

For a curve $z =$ constant, we obtain

$$\frac{\partial\rho}{\partial x}\frac{dx}{dt} + \frac{\partial\rho}{\partial t} = 0\,.$$

Furthermore, the density field for an exact traveling wave satisfies $\rho(x - ct, z, t) = \rho(x, z, t)$, with c being the phase speed of the wave. Hence, the phase speed is

$$c = -\frac{\partial\rho}{\partial t}\Big/\frac{\partial\rho}{\partial x} = \frac{dx}{dt}(z = \text{constant}\,, \rho = \text{constant})\,.$$

Hence

$$c(t) = \frac{dx}{dt}(z = \text{constant}\,, \rho = \text{constant})\,,$$

represents the instantaneous speed of an isoline of density and thus it is an estimate for the phase speed, its time variation quantifying the departure from the traveling wave solution. We compute the speeds of points located on the wave profile, at multiple heights between the maximum displacement and the wing of the wave, and take an average of these values. We note that Grue *et al.* [19] have estimated the phase speed based on *one* such vertical location, close to the inflection point of the wave profile.

This phase speed estimate can be performed by using any constant density profiles corresponding to densities in the range (ρ_1, ρ_2). In order to get a better estimate of the phase speed, we extract isolines densities corresponding to the average ρ_{med} and to an additional density, $\rho_{opt} = 1.0077$ g/cm^3. We note however that the wave is not fully detached from the wake at the first wave recording position, 450 cm, and thus the phase speed computed using the strategy outlined above does not completely capture the dynamics of the wave. In order to obtain information on the wave evolution *between* the two wave gate locations, and assess whether the wave detaches as a wave traveling at constant speed, we extract wave profiles corresponding to the two densities mentioned above for a series of time steps (t_j). Hence, we can determine a more accurate measure of the instantaneous phase speed of the wave, by taking a range of heights between the maximum displacement and the front wing of the wave, computing speeds corresponding to these heights $\left(\left(x_{t_{j+1}} - x_{t_j}\right)/(t_{j+1} - t_j)\right)$, and taking the average across the range of heights.

In Figure 4.4(a) we depict the instantaneous horizontal speed of points on the front of the density isoline corresponding to ρ_{med}. Note that the velocity profile flattens in time - which is another indication that the wave is in the process of becoming a traveling wave, but does not reach a purely traveling wave state before interacting with its reflection from the tank's end. We also show the phase speed estimate based on the two time series. As expected, this estimate is not particularly accurate, since it represents a time average of the wave speed between the two wave recording locations. In Figure 4.4(b) we present the evolution in time of the instantaneous phase speed mentioned above, for the two constant density profiles (corresponding to ρ_{med} and ρ_{opt}, respectively). For a "pure"

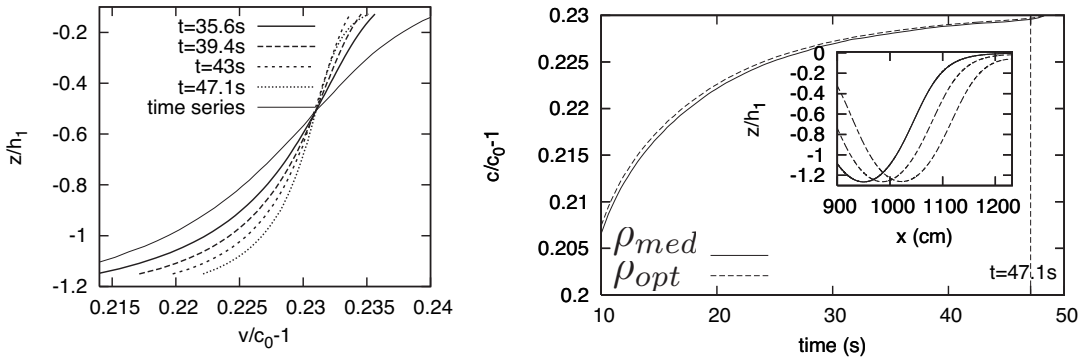

FIGURE 4.4. Phase speed evolution in time for a numerical experiment with initial conditions $h_{gate} = 34.5\,\text{cm}$ and $L_{gate} = 100\,\text{cm}$. (a) Continuous line - phase speed constructed from the two time series measured at 450 and 1050 cm, dashed lines - instantaneous speed for points on the front of the constant density profile corresponding to ρ_{med} at various time steps. (b) Instantaneous wave speed evolution in time for the two constant density profiles, corresponding to ρ_{med} and ρ_{opt}. At time $t = 47.1\,\text{s}$, the wave interacts with the right vertical boundary, as evidenced in the insert, where the isoline of density ρ_{med} is depicted (continuous line).

traveling wave, these quantities should coincide and remain constant in time. Although this is definitely the trend, their variation is still significant when the wave interacts with the right boundary, as evidenced in the insert.

In an attempt to obtain traveling waves of permanent form, we carry out a series of experiments with the same initial conditions in a tank of double length $L = 2464\,\text{cm}$. We look at yet another indicator of the wave tendency (or lack thereof) to become a traveling wave – the evolution in time of its amplitude. As evidenced in Figure 4.5(a) (where we present amplitude decay in time for the short tank experiments versus the double tank experiments with the same initial conditions) the amplitude levels off in the tank of double length, indicating that the solutions are much closer to being permanent-form traveling waves.

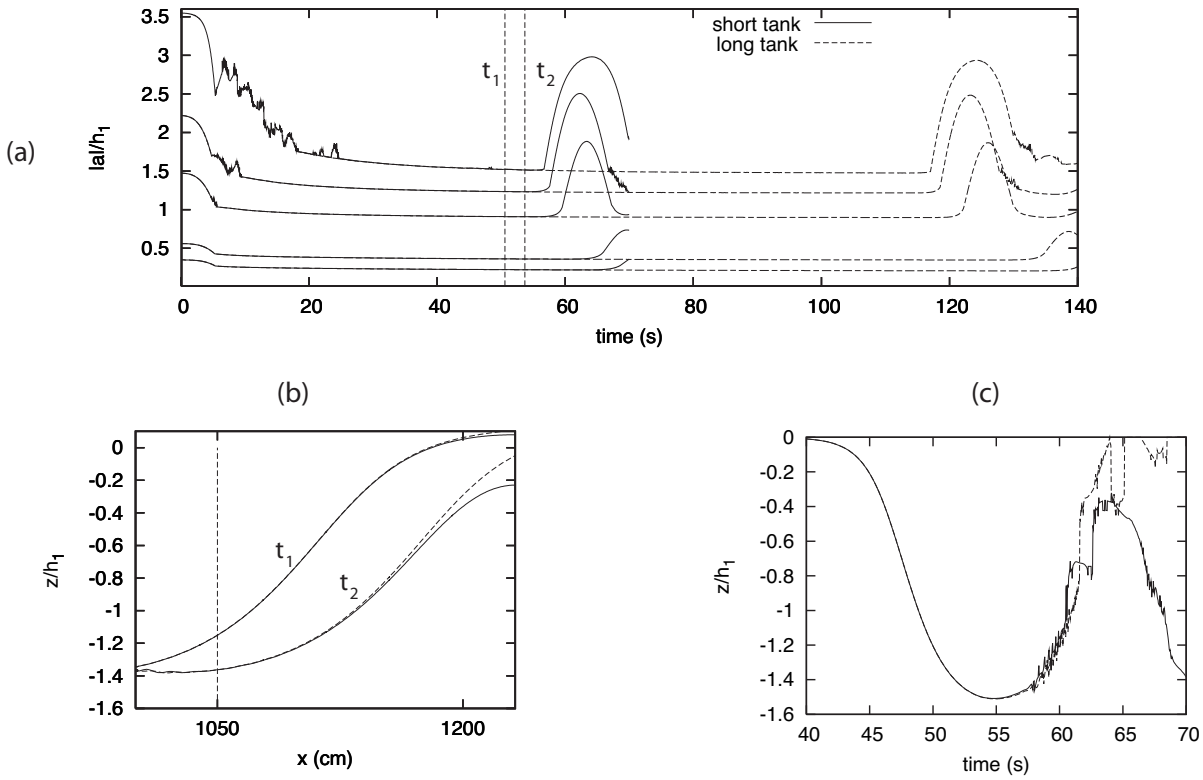

FIGURE 4.5. Reflection. (a) Amplitude decay in time for various initial conditions in the tank of length $L = 1232$ cm versus $L = 2464$ cm. (b) wave profiles at $t_1 = 50.6$ s and $t_2 = 53.5$ s for the largest amplitude wave. (c) Time series at $x = 1050$ cm in the tank of length $L = 1232$ cm versus $L = 2464$ cm, for the largest amplitude wave.

These experiments also allow us to determine the influence of wall reflection on the time series measured at 1050 cm and also on the instantaneous wave profiles. Note the time series profile is affected by reflection only in the trailing edge, as Figure 4.5(c) shows. In Figure 4.5(b) two wave profiles corresponding to the average density are shown at the times when reflection from the short tank end-wall begins to affect the front of the wave. We can conclude the front of the wave shape reconstructed from the time series for the experiments in the short tank is not affected by reflection, but at the same time the length of the short tank is not sufficient for waves to completely evolve into permanent-form traveling waves.

Wave shapes comparison.

Given the agreement documented in [8] between the strongly nonlinear model [7] and the experimental data of [19], we compare our results against the predictions of the strongly nonlinear model. We remark that the strongly nonlinear model, for all solution computed with the parameters of the experimental set-up, are practically indistinguishable from *two-layer* numerical full Euler solutions.

In Figure 4.6, we show the wave profiles obtained from the numerical experiments compared against on those predicted by the strongly nonlinear theory. When matching for amplitude, we note a moderately good agreement on the leading edge of the waves, but some evidence of trailing wave trains to the left, evidenced by the asymmetry in height when comparing the left and right tails of the wave. This effect can be furthermore enhanced by the reflection of the wave at the right boundary. We also note the clear discrepancy in the largest amplitude wave, where the numerics were able to detect Kelvin-Helmholtz instabilities in the form of roll-up to the left of the wave crest. We remark that in the actual experiment of Grue *et al.* [19], instabilities have been observed in the same amplitude regime. When matching for speed, we note the clear superiority of the strongly nonlinear model with optimized choice of parameters. However, in the above section we have concluded that the waves in the tank of length $L = 1232\,\text{cm}$, for the entire range of amplitudes explored, do not completely reach a permanent-form traveling wave state. In Figure 4.7 we compare the waves generated from the same initial conditions, but in the tank with double the length; the wave profiles are generated from time series recorded at $x = 2000\,\text{cm}$. Note that the trailing edge of the waves has recovered a height

of the front edge (corresponding to that of the quiescent pycnocline), and the profiles are closer to the prediction of the strongly nonlinear model.

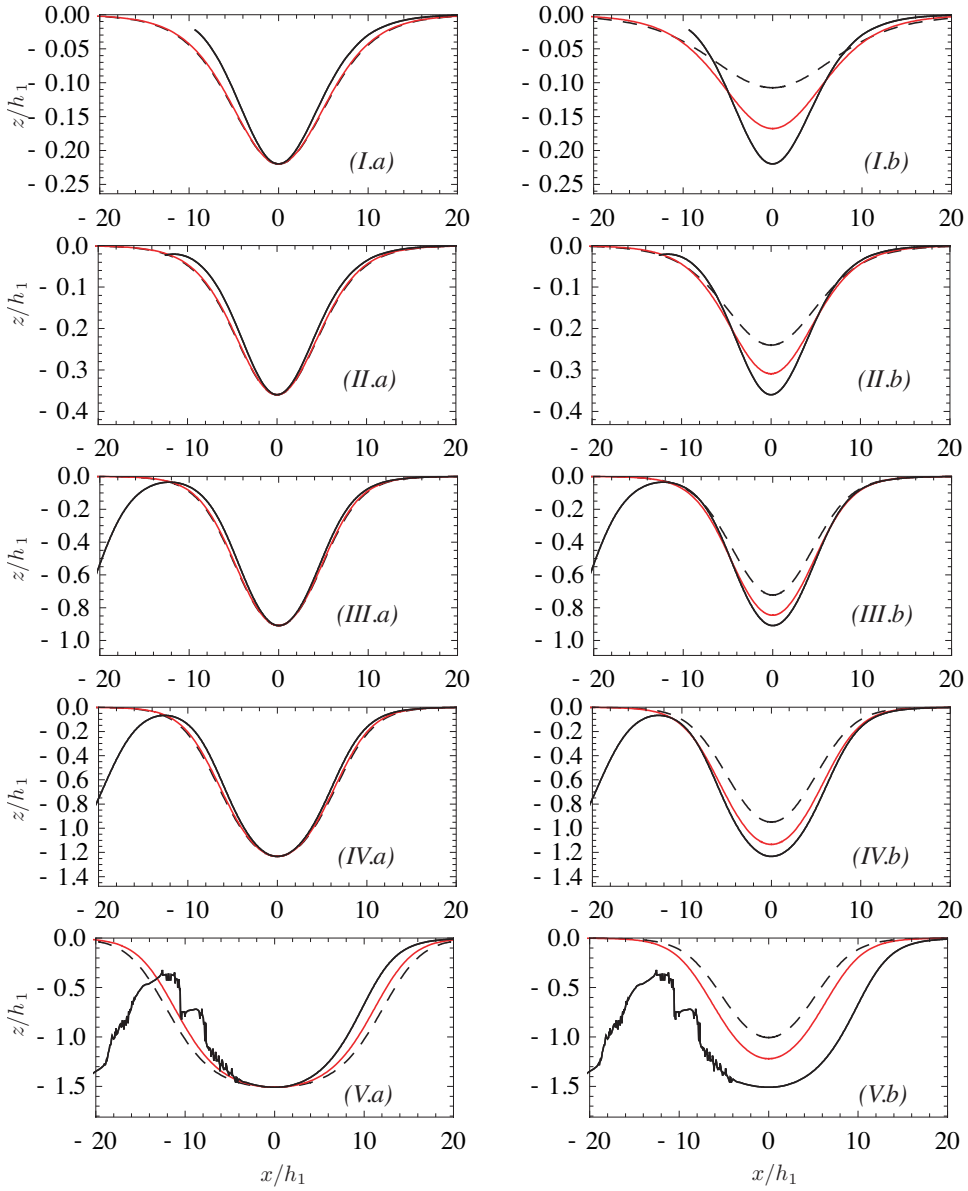

FIGURE 4.6. Wave profiles corresponding to the average density isoline, constructed from the time series at location $x = 1050\,\text{cm}$, in the tank of length $1232\,\text{cm}$, with phase speed computed based on time series at $x = 450\,\text{cm}$ and $x = 1050\,\text{cm}$. The amplitudes of the waves (a/h_1) at $x = 1050\,\text{cm}$ are (I) 0.22, (II) 0.36, (III) 0.91, (IV) 1.23 and (V) 1.51. Continuous - experimental profile; Dashed - strongly nonlinear model, regular; Red - strongly nonlinear model, optimized. Left - the solutions of the strongly nonlinear model for matched amplitude; right - matched phase speed.

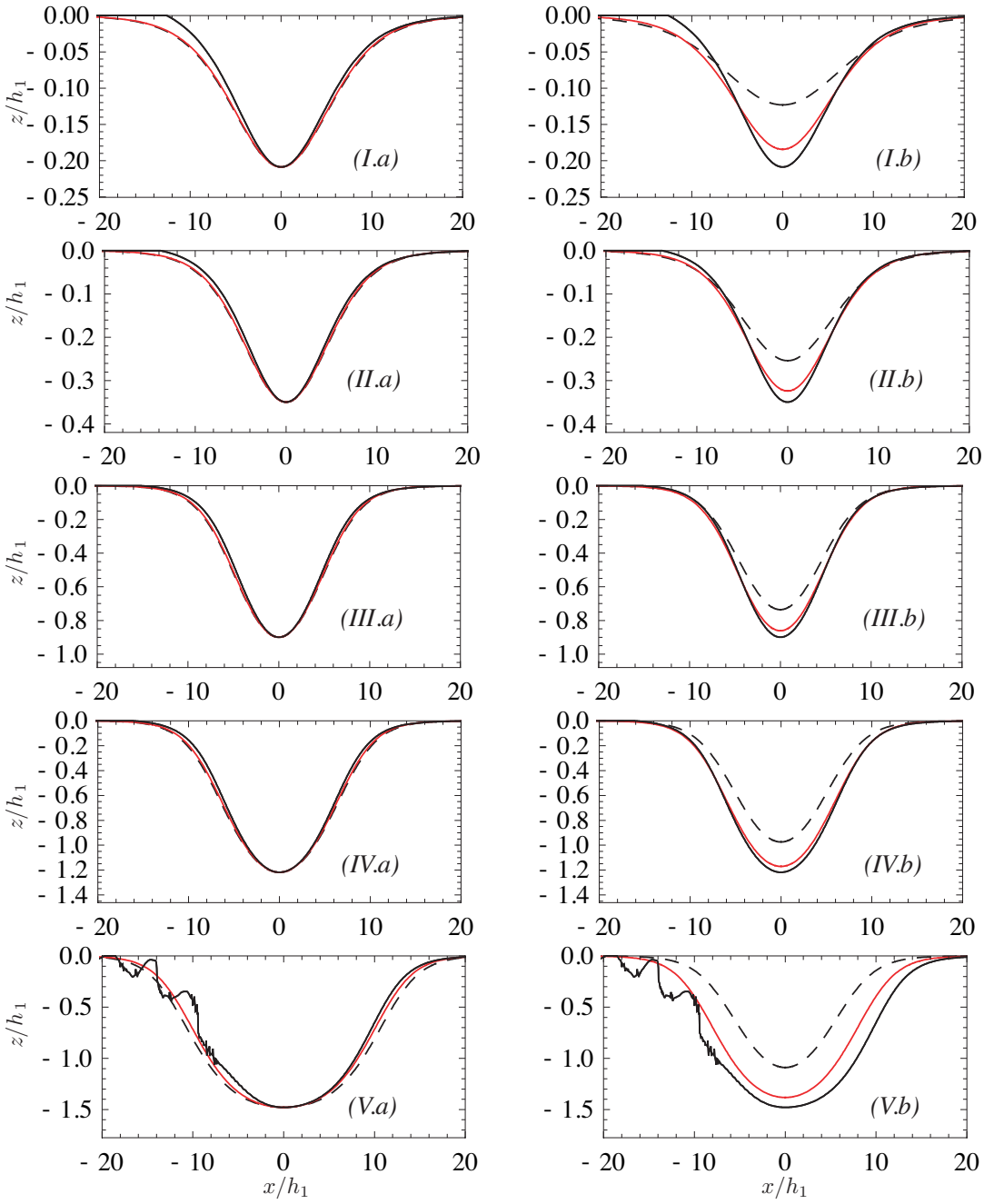

FIGURE 4.7. Wave profiles corresponding to the average density isoline, constructed from the time series at location $x = 1050\,\text{cm}$, in the tank of length 2464 cm, with phase speed computed based on time series at 450 cm and 2000 cm. The initial conditions for (I)-(V) are the same as for the waves in Figure 4.6. Continuous - experimental profile; dashed - regular strongly nonlinear model; red - optimized strongly nonlinear model. Left - the solutions of the strongly nonlinear model for matched amplitude; right - for matched phase speed.

Phase speed dependence on amplitude.

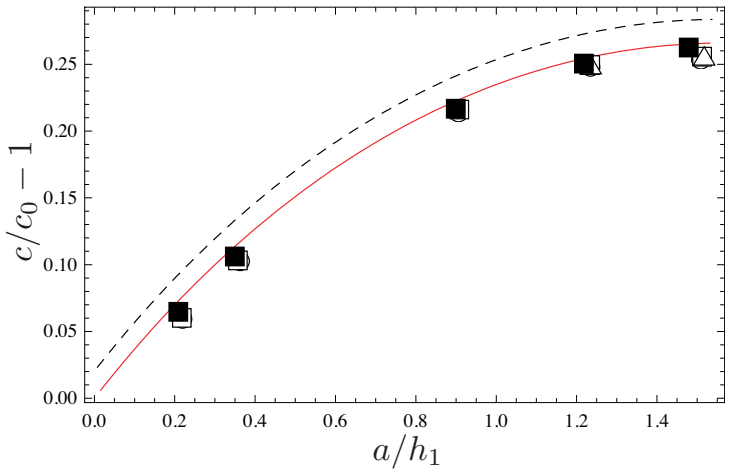

FIGURE 4.8. Phase speed dependence on amplitude. Phase speed computed from time series at locations 450 cm and 1050 cm for the short tank, 1050 cm and 2000 cm for the long tank. The amplitude corresponds to the wave profile constructed from time series at location 1050 cm for the short tank, 2000 cm for the long tank. ◯ experiments in tank of length 1232 cm, simulation using 128 points in the vertical, □ 256 and Δ 512, respectively; ■ experiments in tank of length 2464 cm using 128 points in the vertical. Dashed - regular strongly nonlinear model; Red - optimal strongly nonlinear model.

In Figure 4.8, we present the dependence of the phase speed on the amplitude, compared against strongly nonlinear model predictions. As before, we notice the excellent agreement with the optimal two layer model; furthermore, the double-tank data points confirm that the wave, as recorded at $x = 2000$ cm, is closer to becoming a permanent-form traveling wave. We also show numerical results for three resolutions of the evolution code. We note that a resolution of 128 points in the vertical is sufficient for accurately capturing the evolution of the wave front.

Horizontal velocity profiles.

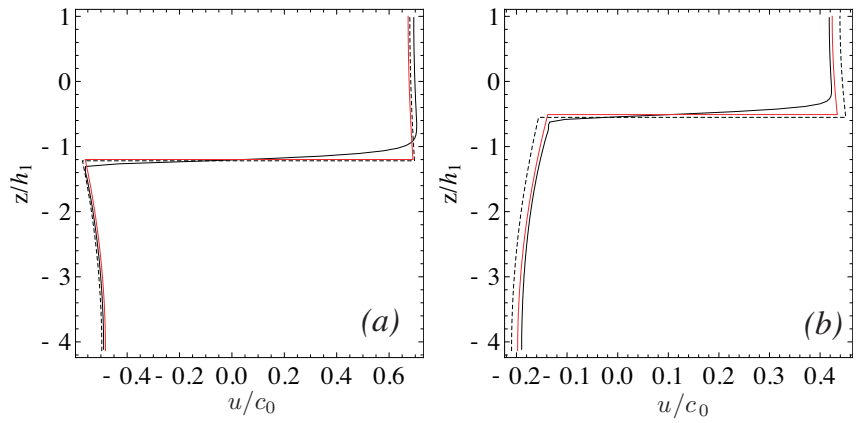

FIGURE 4.9. Horizontal velocity profiles for a wave of intermediate amplitude. (a) Horizontal velocity profile at maximum displacement of the pycnocline at time 101.23 s (time when this point is located at $X = 2000\,\text{cm}$); (b) Horizontal velocity profile measured at the same time, at a station located at $X = 2106\,\text{cm}$. Black - the experimental profile; dashed line - regular two layer model; red - optimal two layer model.

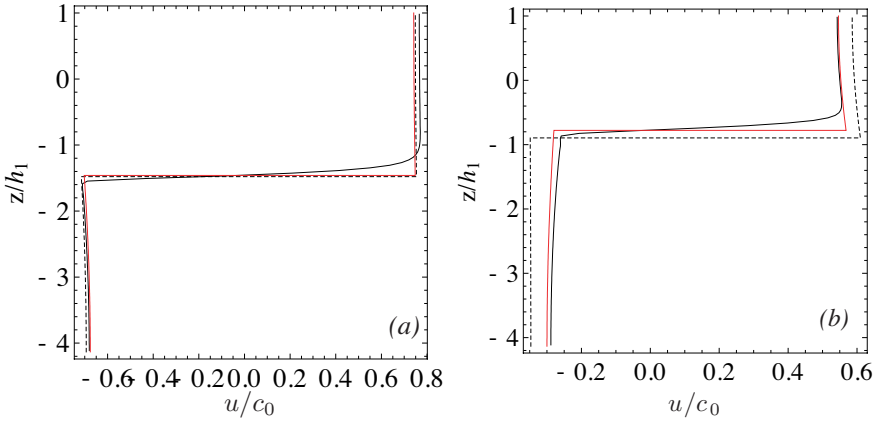

FIGURE 4.10. Horizontal velocity profiles for a wave of large amplitude. (a) Horizontal velocity profile at maximum displacement of the pycnocline at time 100.139 s (time when this point is located at $X = 2000\,\text{cm}$); (b) Horizontal velocity profile measured at the same time, at a station located at $X = 2140\,\text{cm}$. Black - the experimental profile; dashed line - regular two layer model; red - optimal two layer model.

We show horizontal velocity profiles for a wave of moderate amplitude (1.23 at $x = 1050\,\text{cm}$) and for a large amplitude wave (1.51 at $x = 1050\,\text{cm}$) – see Figure 4.9 and Figure 4.10, respectively. In both cases, comparison against the two layer model is done for the maximum displacement of the pycnocline and for a point located in the front of the wave (close to the inflection point of the wave profile). For the maximum displacement of the pycnocline, we see very good agreement with the strongly nonlinear model - both regular and optimized. For the front of the wave, the agreement with the optimized two layer is noticeably better. We note the smoothing of the profile across the interface that is due to its finite thickness; again this is consistent with smoothing seen in the experimental data. We also note that in constructing the velocity profiles from the predictions of the strongly nonlinear model, we have neglected the effect of the finite pycnocline (which is negligible for the density stratification we are considering in the current chapter). However, this effect is substantial for thicker pycnoclines, and can easily be included by following the strategy outlined in Chapter 3, §3.5.

4.2.4. Convergence study. Even though second order convergence for the variable density numerical scheme had been verified for smooth initial conditions, the order of convergence reduces drastically when we start with non-smooth initial data. We can infer the order of convergence from monitoring the variation of total energy in the system – which should be conserved by an Euler scheme, in a potential force field such as our configuration. In Figure 4.11 we present the variation of total energy (and its components: kinetic - initially zero - and potential) for the three resolutions considered - 128, 256 and 512 grid points in the vertical direction (for a square grid), respectively. It can be inferred that the order of convergence if approximately first order. We note that the

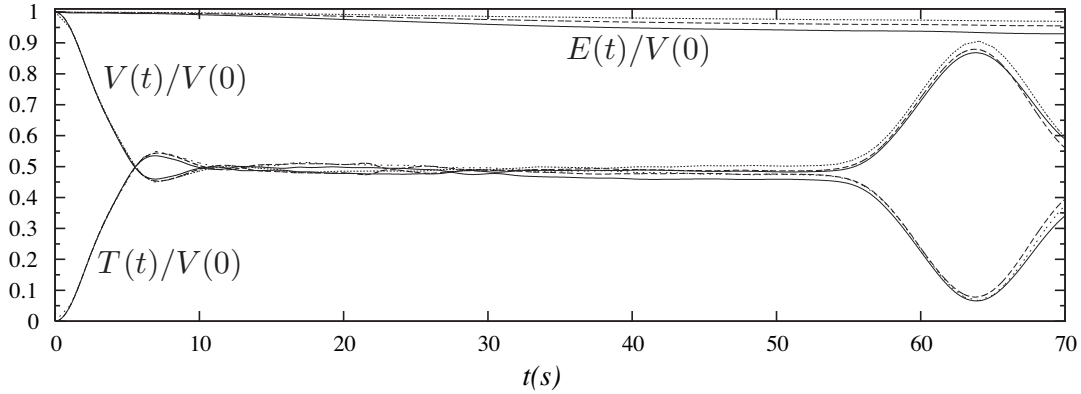

FIGURE 4.11. Kinetic T, potential V and total $E = T+V$ energies during the evolution of large amplitude wave $a/h_1 = 1.51$ for 128 (continuous), 256 (dashed), 512 (dotted) points in the vertical, respectively.

maximum values of the relative error among various resolutions are concentrated mostly in the wake, as seen in Figure 4.12. We also monitor the time series at location 450 cm

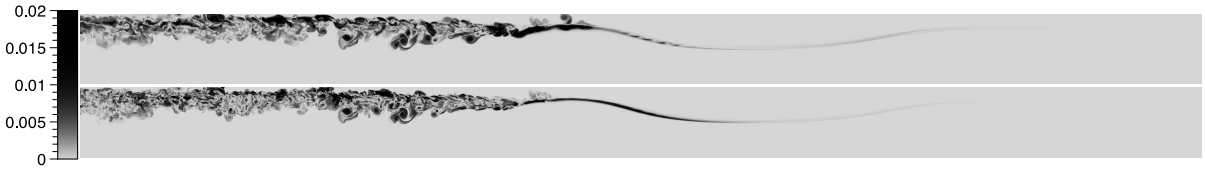

FIGURE 4.12. Relative error in the density field at $t = 39.45$ s (for the numerical experiment from Figure 4.19) between coarse (128) and medium (256) grid and the medium and fine (512) grid, respectively.

and 1050 cm; the coarsest grid seems to be sufficient for accurately capturing the front of the wave - as seen in Figure 4.13(a)-(d). In small to intermediate amplitude regimes, the coarsest grid (128) captures accurately also the trailing edge (Figure 4.13(a),(b)), whereas for large amplitude waves we notice significant differences in the trailing edge.

4.2.5. Effects that might justify observed differences with respect to Grue *et al.* [19] experimental results. The discrepancy between the strongly nonlinear model predictions and the numerical experiments (in particular for large amplitude, and in the (shorter) tank of length 1232 cm) is more pronounced than the discrepancy noted

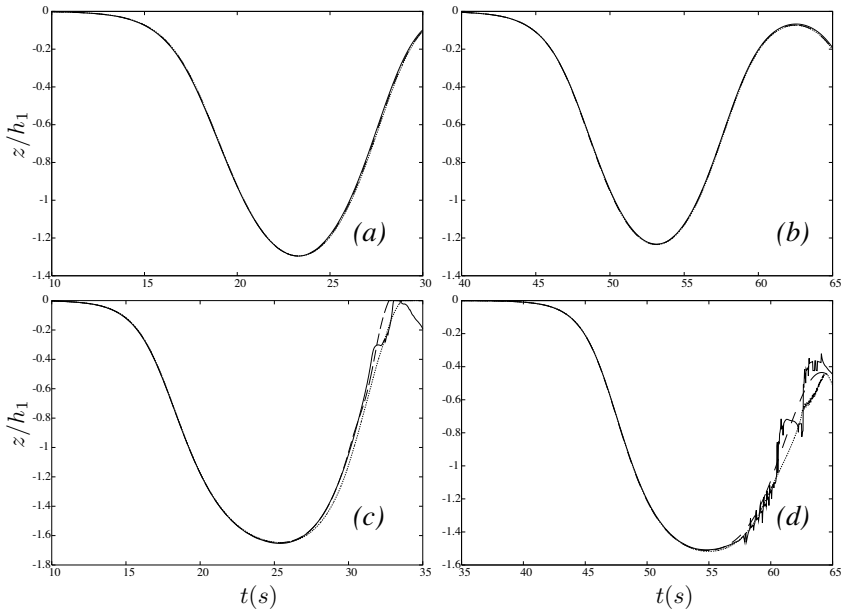

FIGURE 4.13. (a), (b) Time series of the average density profile at 450 cm and 1050 cm, respectively at resolutions 128 (continuous), 256 (dashed) and 512 (dotted) for intermediate amplitude wave ($a/h_1 = 1.23$); (c), (d) large amplitude wave ($a/h_1 = 1.51$).

in Grue *et al.* [19], where the experimental wave profiles are compared against full Euler solutions in two layer system. As already remarked, any discrepancy cannot be attributed to the asymptotic approximation of long-waves, since the model agreement with the full Euler numerical solutions in two-layer systems is remarkable in all diagnostics as shown in Camassa *et al.* [8]. We also note that in Grue *et al.* [19] the agreement of the phase speed-amplitude dependence as predicted by the two-layer model when compared to the experimental data was much noisier than the agreement with wave profiles. We conjecture that one of the possible explanations for the discrepancy in the wave shapes comparison lays in the way the phase speed of the wave is determined, given how sensitive the time series reconstruction of the spatial wave profile is with respect to the phase speed determination. Notice that in [19], the experimental wave shapes are compared against

their two-layer counterparts by matching for amplitude exclusively – which is likely to mask discrepancies in phase speeds, with the consequences shown above.

It is useful to summarize in a list some of the effects that might justify the aforementioned discrepancy in wave profiles between experiment and the two layer theory. These effects could be consequences of physical phenomena neglected in the numerical results presented so far. Whenever possible, we adapt our numerical implementation to account for these phenomena and address their effects.

Initial condition. The initialization technique employed in our numerical experiment differs slightly from that in Grue *et al.* [19], where the waves are created by adding a volume of fresh water behind a gate which is not completely lowered to the bottom of the tank. In order to let hydrostatic pressure equilibrate at the deep fresh water interface to the left of the gate, a very small difference in height between free surfaces to the left and the right of the gate must exist. Given the smallness of this height difference (proportional to that of the layer densities) and the minimal impact of free surface effects on internal waves, we believe that this effect has minimal influence on the traveling wave propagation.

Free surface. The actual experiments in Grue *et al.* [19] are performed in a tank with a free surface, whereas our numerical experiments bound the upper surface with a rigid lid. However, the surface displacement induced by internal solitary waves is small by comparison to the pycnocline deformation, and the pycnocline position is far from the surface in our setup. We note that the Euler simulations used for validation in Grue *et al.* [19] also employ the rigid-lid assumption.

Three dimensional (3D) effects . The experiments in Grue *et al.* [19] have been performed in a tank with width 0.5 m, whereas the numerical simulations are two-dimensional ($2D$). The most important consequence of three-dimensionality is enhanced dissipation through friction with the lateral walls. Nonetheless, the Euler results used for validation in Grue *et al.* [19] were also $2D$ simulations.

Viscosity. We have tested the effects of bulk viscosity (considering a water viscosity of $\mu = 0.01$ Poise). We note that even though the evolution code allows for implementation of no-slip boundary condition, high grid resolution is necessary to accurately resolve the resulting thin boundary layers. The variant of the VARDEN code we have used in this study does not support adaptive mesh refinement, which would be required to treat our setup (where the aspect ratio of the tank is rather skewed in the horizontal direction). As shown in Figure 4.14, viscosity alone does not affect either the wave shape nor the manifestation of shear instability.

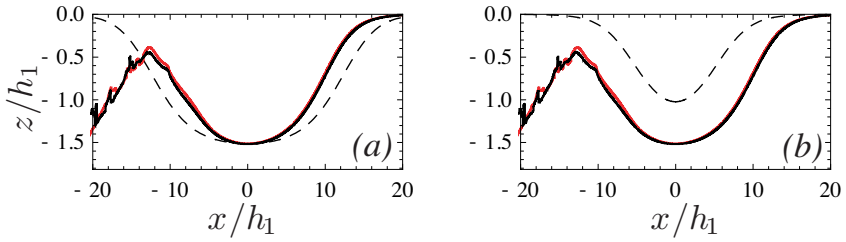

FIGURE 4.14. Continuous lines - wave shapes constructed from the time series at $x = 450$ cm and $x = 1050$ cm for two numerical experiments with the same initial conditions (added volume of fresh water $L_{gate} = 100$ cm $h_{gate} = 50.203$ cm): red curve - bulk viscosity $\mu = 0.01$ Poise, black curve - inviscid. The dashed curves correspond to the regular strongly nonlinear model for (a) matched amplitude, (b) speed.

Details of the stratification. Changing the background stratification by using an error-function density distribution for the pycnocline region, while keeping the thickness the

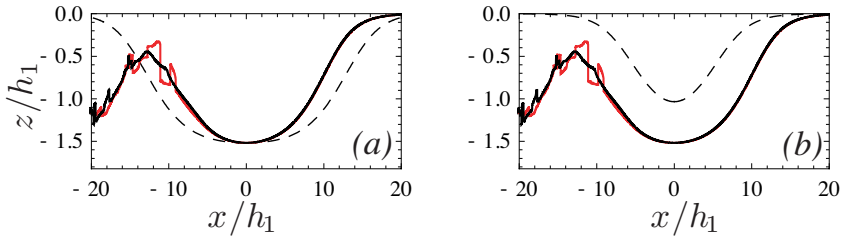

FIGURE 4.15. Continuous lines - wave shapes constructed from the time series at $x = 450\,\text{cm}$ and $x = 1050\,\text{cm}$ for two numerical experiments with the same initial conditions (added volume of fresh water by $L_{gate} = 100\,\text{cm}$ $h_{gate} = 50.203\,\text{cm}$): red curve - error function background density stratification, black curve - tangent hyperbolic density stratification. The dashed curves correspond to the regular strongly nonlinear model for (a) matched amplitude, (b) speed.

same, does not modify the wave shape substantially, as seen in Figure 4.15. As expected, and a further validation of the numerical scheme, reducing the thickness of the pycnocline by half results in a better agreement with the strongly nonlinear model. Moreover, as expected from the two-layer limit, shear instability for thinner pycnoclines manifests itself at lower amplitude waves than those reported in the experiments in Grue *et al.* [19], as seen in Figure 4.16.

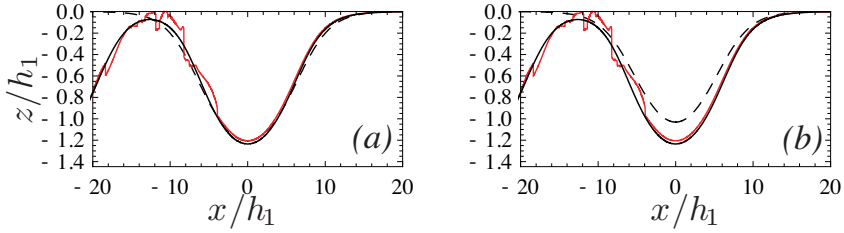

FIGURE 4.16. Continuous lines - wave shapes constructed from the time series at $x = 450\,\text{cm}$ and $x = 1050\,\text{cm}$ for two numerical experiments with the same initial conditions (added volume of fresh water by $L_{gate} = 100\,\text{cm}$, $h_{gate} = 32.3\,\text{cm}$): red curve - thickness of the pycnocline $d = 1\,\text{cm}$, black curve - $d = 1\,\text{cm}$ (wave IV in Figure 4.6). The dashed curves correspond to the regular strongly nonlinear model for (a) matched amplitude, (b) speed.

4.2.6. Shear instability within the experiment.

Richardson number criteria.

Accurately predicting the self-induced internal wave shear flow at the pycnocline allows us to develop a sufficient condition for the local stability properties of the flow, based on the predictions of the strongly nonlinear model. First, we recognize that the effective wavelength of the solitary wave is relatively large in comparison to the vertical length scale, and correspondingly both the shear and stratification are slowly varying in the horizontal direction. The first order approximation in these circumstances is therefore that of a *parallel shear*.

The main measure of stability of parallel heterogeneous flows is the Richardson number, which measures the relative magnitude of the buoyancy effects of the density gradient with respect to the inertial effects of shear velocity

$$Ri(z) = \frac{\beta(z)g}{u'(z)^2} \ , \tag{4.1}$$

where $\beta(z) = -\rho'(z)/\rho(z)$ indicates the static stability of the density stratification ($\beta < 0$ implying static instability). As follows from Miles [38] and Howard [23] (which have build on previous investigations of Taylor [48], Goldstein [17]), a *sufficient* condition for spectral linear stability of a heterogenous parallel shear flow is $Ri > 1/4$ everywhere.

We can obtain a relatively good estimate of the Richardson number by using the strongly nonlinear model (Appendix D) as shown by Figure 4.17, where the comparison of this estimate against the Richardson number from a numerical experiment is plotted against the horizontal location to the right of the wave's maximum interface

displacement. We can thus identify the regions with $Ri < 1/4$ as regions of *potential* local instability in the flow field However, there are instances for which, even though

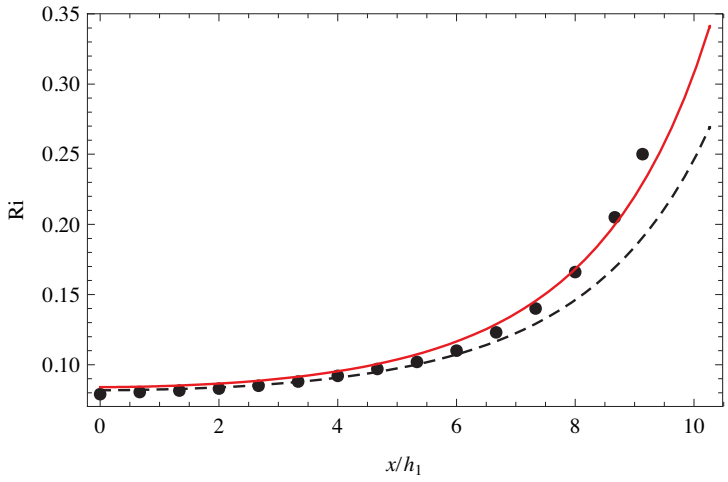

FIGURE 4.17. Minimum Richardson distribution for half of the wave profile of a large amplitude wave $a/h_1 = 1.51$ (wave V in Figure 4.6). Red -predictions using the optimal two layer approximation; dashed - regular two layer approximation; dots - measured from the numerical wavetank experiment experiment.

we identify regions of Richardson number under the 1/4 threshold within the flow field, we do not observe formation of Kelvin-Helmholtz roll-ups (see Figure 4.18 for such an example). While for this particular wave $Ri \approx 0.15$ at the peak of the wave, Grue *et al.* [19] reported the Richardson number at the peak of the wave with the same amplitude attained in the actual experiments to be 0.23 (hence falling into the window of potential instability, though close to meeting the sufficient stability criteria $Ri > 0.25$).

Experimental observations of internal waves that do not exhibit shear instability but have areas with $Ri < 1/4$ in their flow field have been reported in Troy & Koseff [50], for small amplitude periodic waves in a smooth, tangent-hyperbolic density stratification

FIGURE 4.18. Density field at time $t = 45\ s$, for a numerical experiment in which no shear instability has been observed. The amplitude (a/h_1) of the solitary wave constructed from the second time series is 1.23 (wave IV in Figure 4.6). Regions in the flow field with $Ri < 1/4$ are marked with red.

and in Fructus *et al.* [13] for large amplitude solitary waves in three layer stratification, with the intermediate layer linearly stratified.

The fact that $Ri < 1/4$ is not a *sufficient* condition for spectral instability could in fact explain our observations of lack of instability evidence in these regimes. We would have to refer to the normal modes corresponding to each horizontal locations and see if the flow supports normal growing modes. However, it might also be the case that what we are seeing is an effect of the horizontal spatial variations of the shear flow. We are going to address these issues in §4.3.

Influence of the resolution on the instability behaviour.

In good agreement with the experiments in Grue *et al.* [19], we observe the development of Kelvin-Helmholtz roll-ups for waves of near-maximal amplitude; these rolls develop behind the maximum displacement of the interface by the wave. In Figure 4.19 and Figure 4.20, we present the density plots at times $t = 39.45\,\mathrm{s}$ and $t = 53.3\,\mathrm{s}$, respectively, for an experiment with initial conditions $L_{gate} = 100\,\mathrm{cm}$ and $h_{gate} = 53.21\,\mathrm{cm}$, in a tank of length $L = 1232\,\mathrm{cm}$. These initial data yield a near-travelling wave of amplitude $a/h_1 = 1.51$ (wave V in Figure 4.6). The results are presented for three vertical resolutions (with square grids): $N = 128,\ 256,\ 512$. We notice that instability development within the

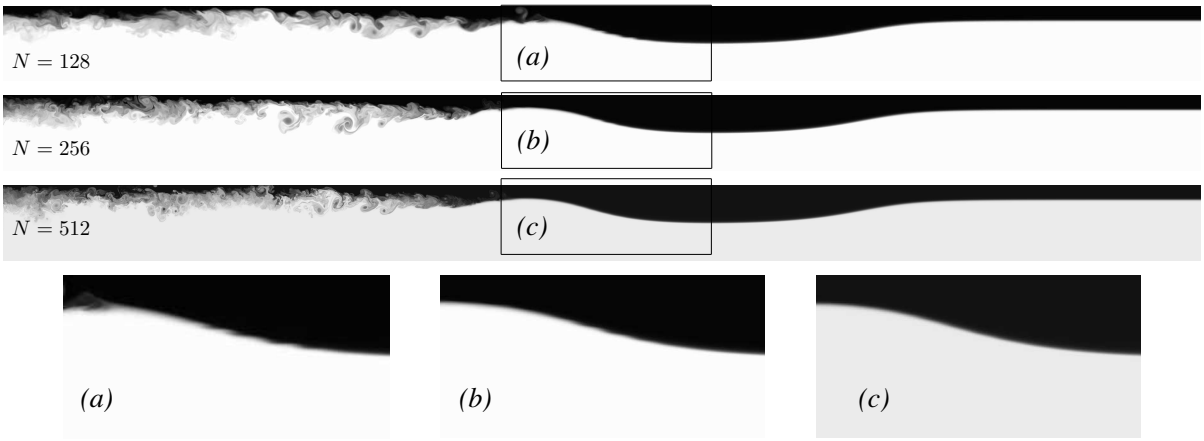

FIGURE 4.19. Density plots at $t = 39.45\,\mathrm{s}$ for initial condition $L_{gate} = 100\,\mathrm{cm}$, $h_{gate} = 53.21\,\mathrm{cm}$ at resolutions 128, 256 respectively 512.

numerical experiment is related to resolution. We therefore can assert that the order

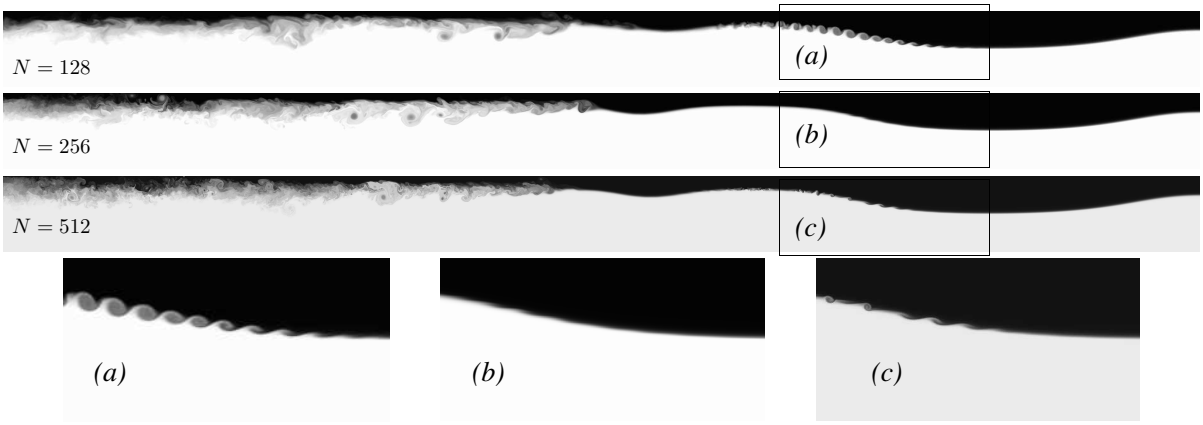

FIGURE 4.20. Same as in Figure 4.19, at time $t = 53.3\,\mathrm{s}$.

of the scheme is responsible for the noticeable differences in the wake. The reduction of the convergence order due to the highly turbulent wake and the non-smooth initial condition can translate in significant errors in capturing the onset and time evolution of the instability episodes.

Influence of reflection on instability development.

In Figure 4.19, which refers to the 1232 cm-long tank, we can observe that the trailing side of the wave has detached from the wake, the onset of shear instability occurring after

this detachment. In order to determine whether the interaction with the right boundary induces shear instability we perform an experiment in a longer tank, of length 1386 cm and monitor the time of onset. These experiments are performed at 512 resolution. In Figure 4.21 we show that the time of onset of instability in the longer tank is roughly the same as in the shorter tank, hence the instability manifestation is not induced by reflection of the wave at the right boundary.

FIGURE 4.21. Density plots for numerical experiments with the same initial condition $L_{gate} = 100$ cm, $h_{gate} = 53.21$ cm. (a) Density plots at $t = 39.45$ s (a.I) tank of length 1232 cm, (a.II) tank of length 1386 cm (b) Density plots at $t = 53.3$ s (b.I) tank of length 1232 cm, (b.II) tank of length 1386 cm.

We have seen how for the particular experimental set-up of [19], the trailing edge does not fully recover the height of the quiescent state (as can be seen in Figure 4.21). Thus, one cannot be sure that the wave in the simulated tank can be truly considered as permanent form (solitary) traveling wave. This fact undermines the task of assessing whether the shear instability development is an intrinsic property of the wave, or it is rather linked to the initial condition (and hence generation mechanism). This motivates us, next, to study the time evolution from initial data corresponding to a traveling wave solution.

4.3. Time evolution of solitary wave solutions

For sufficiently large amplitudes, solitary waves emerging from the experimental initialization process never fully develop into symmetric shapes and achieve traveling wave form. While the highly fluctuating fluid motion in their wakes is traveling at a slower group speed and is eventually left behind by the large waves, its upstream influence is not clear and cannot be completely ruled out, as evidenced by the slightly asymmetric shape of the precursor large wave. In order to assess whether the asymmetry originates in the initial conditions or is related to an inherent instability of large waves, we seek to initialize the evolution code with a permanent form solitary wave solution. For this, we use the algorithm developed in Turkington *et al.* [51]. Our implementation of this algorithm, adapted to handle relatively thin pycnoclines, is described in detail in Appendix C. The boundary conditions for the evolution code are zero vertical velocity at the top and bottom boundary and periodic in the horizontal direction. We initially perform our study on a long *periodic* wave (near the solitary wave limit) with period $L = 1232\,\mathrm{cm}$ and large amplitude ($a/h_1 = 1.51$).

4.3.1. Convergence study. Instabilities induced by lack of resolution. There are two interconnected issues that we address in this section: one is the convergence of the evolution code itself for large density gradients, and the second is the correctness of the initialization (how far is the initial condition from a traveling permanent form solution supported by the evolution code).

We have tested the order of convergence of the code both for initialization with experimental setup and for solitary wave initialization. In the first instance, we obtain order convergence of first order – due to the fact that the initial condition is not smooth.

As described in the previous section, the coarsest resolution that we have used ($N = 128$ points in the vertical) manages to capture fairly well the front of the wave.

We have verified second order convergence of the evolution code in the case of smooth initialization, by initializing the evolution code with a solitary wave solution obtained with the iterative scheme ([51]) at resolution $N = 1024$, and running three time evolution simulations at resolutions $N = 256\,, 512$ and 1024 respectively. We have monitored the infinite norm of the error in the velocity and density fields. The numerical error is concentrated in the pycnocline region, where we register the highest gradients of density- see Figure 4.22.

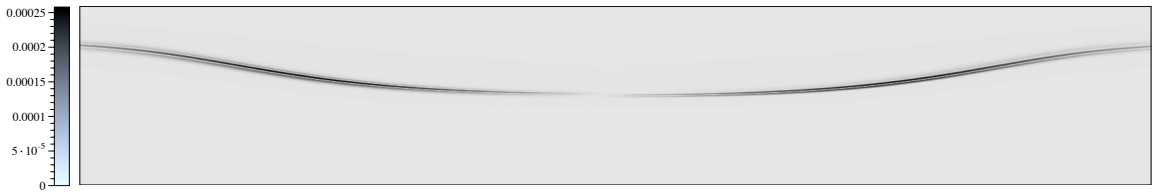

FIGURE 4.22. Magnitude of the relative error in the density field after 5 s, between two runs performed at resolutions 256 and 512, respectively, for the time evolution of the solitary wave solution in continuous stratification of amplitude $a/h_1 = 1.51$.

One other indicator of the magnitude of the numerical error induced by the sharp stratification is the total energy – this should be conserved in our setup (periodic boundary conditions in horizontal direction, slip in the vertical). Figure 4.23 shows the variation of the total energy for three resolutions $N = 256$, 512, 1024, respectively. We note that the total energy decays (due to numerical diffusion) and that the resolution $N = 1024$ is satisfactory for the time scales we are interested in.

To address the second issue – namely how far the initial condition is from a stationary solution – we monitor the wave amplitude, the phase speed (using the strategy outlined

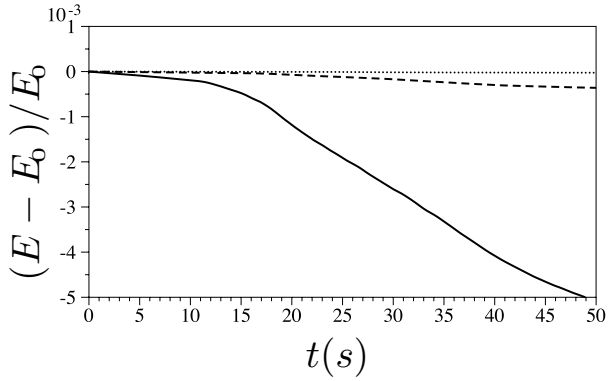

FIGURE 4.23. Variation of the total energy for the time evolution of the solitary wave solution in continuous stratification of amplitude $a/h_1 = 1.51$ (normalized with the energy at time $t = 0$ s).

in §4.2.3) and the potential and kinetic energy, respectively. All of these quantities should be constants of motion for a stationary solution. As we see in Figure 4.24, the variation of these quantities decreases with resolution.

We found evidence of shear instability for all the resolutions we have tested, as noticeable in Figures 4.25 - 4.27, where we present several time snapshots of the density field during the evolution of the wave. (The simulations presented are performed in the wave frame, a frame of reference moving at the speed c_{it} – the speed of the wave as predicted by the iterative code.) Nonetheless, the magnitude of the roll-ups decreases with increased resolution (to the point that there are not easy to identify visually, as the insert (a) in Figure 4.27 shows), which can be interpreted as yet another confirmation of convergence of the iterative code to actual traveling wave solutions of Euler equations. Moreover, the instabilities are manifest only on the trailing side of the wave, a fact also noticed in the experiments of Grue *et al.* [19], Fructus *et al.* [13].

In all three simulations, we have observed (qualitatively) three episodes of shear instability: an initial episode triggered by numerical error (followed by a period in which

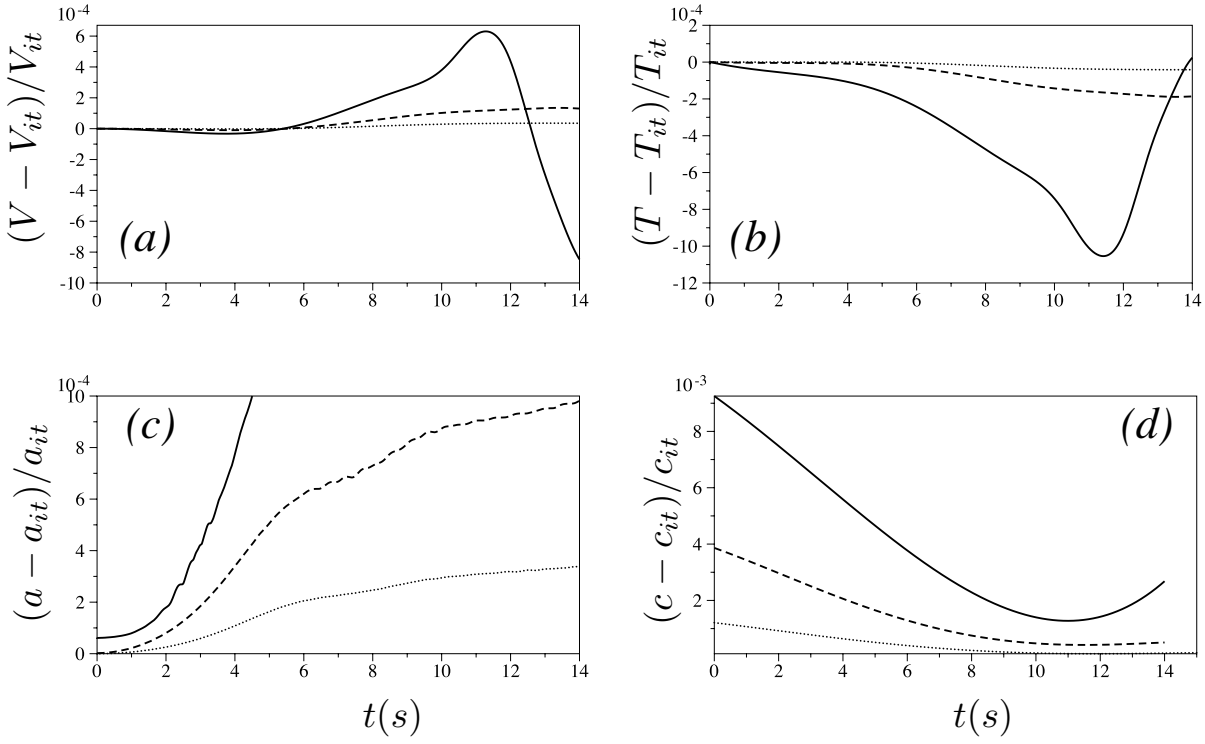

FIGURE 4.24. Variation of (a) potential energy, (b) kinetic energy, (c) amplitude, (d) phase speed – for the time evolution of the solitary wave solution in continuous stratification of amplitude $a/h_1 = 1.51$. Continuous - resolution $N = 256$, dashed $N = 512$, dotted $N = 1024$. All quantities are nondimensionalized with the corresponding quantities at time $t = 0$ s.

the wave travels at quasi-constant speed and amplitude), a second episode of instability of smaller magnitude (which occurs roughly in the interval $30 - 40$ s) and finally the interaction with the turbulent wake created by the first episode, which wraps around the periodic box – see Figure 4.25 (resolution $N = 256$), where the first two episodes are clearly visible, and Figure 4.26 (resolution $N = 512$) where the second episode is barely discernible in the density field (the insert (a) magnifies the region where growing modes are detected).

We argue that the simulations, at all the resolutions we have tested, retain important physical features of the actual phenomenon. Thus, the first episode of instability is

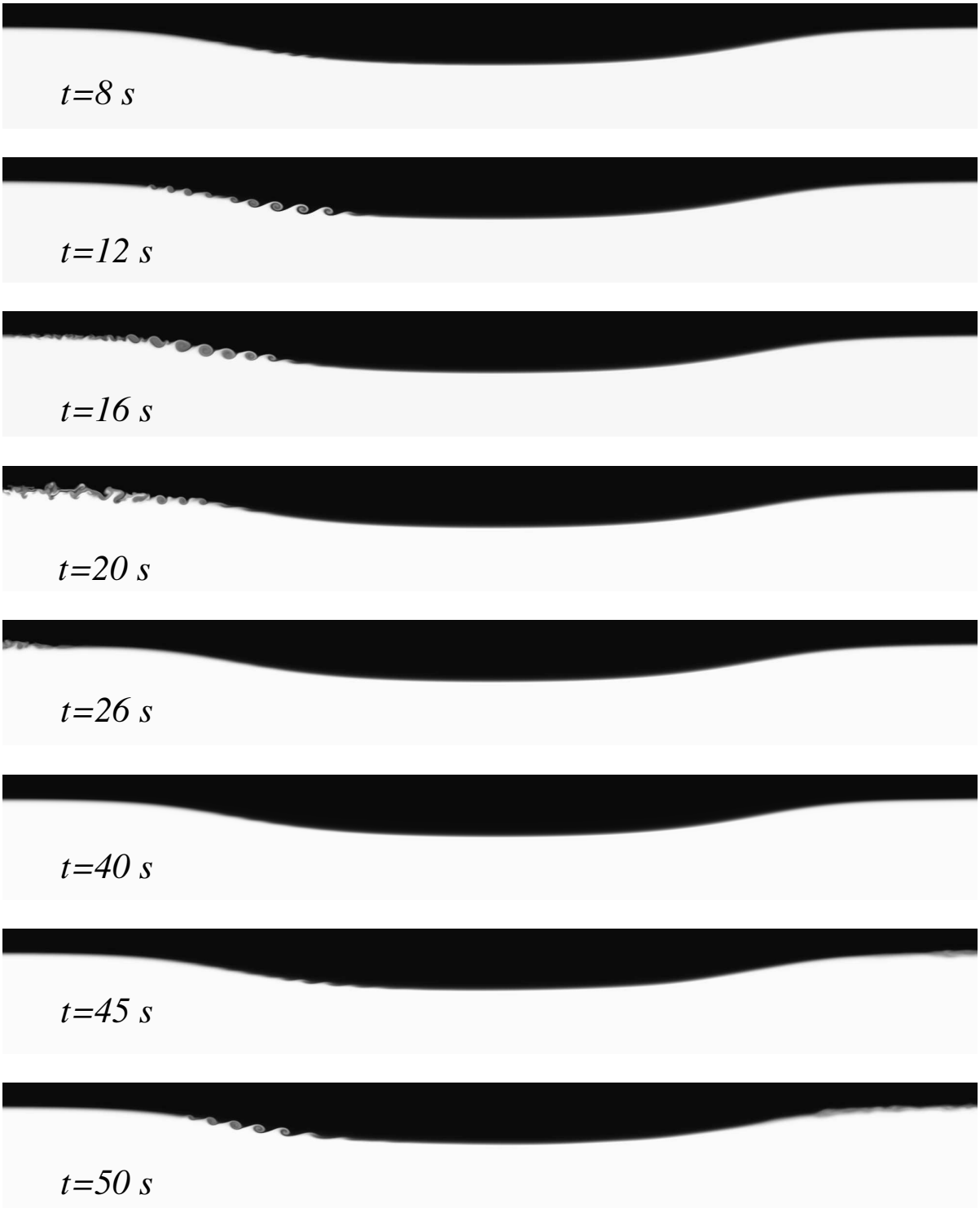

FIGURE 4.25. Time snapshots of the density field during the propagation of a large amplitude solitary internal wave $a/h_1 = 1.51$. We show a section of the computational domain, centered at the peak of the wave, with dimension 3000 cm. Resolution 256.

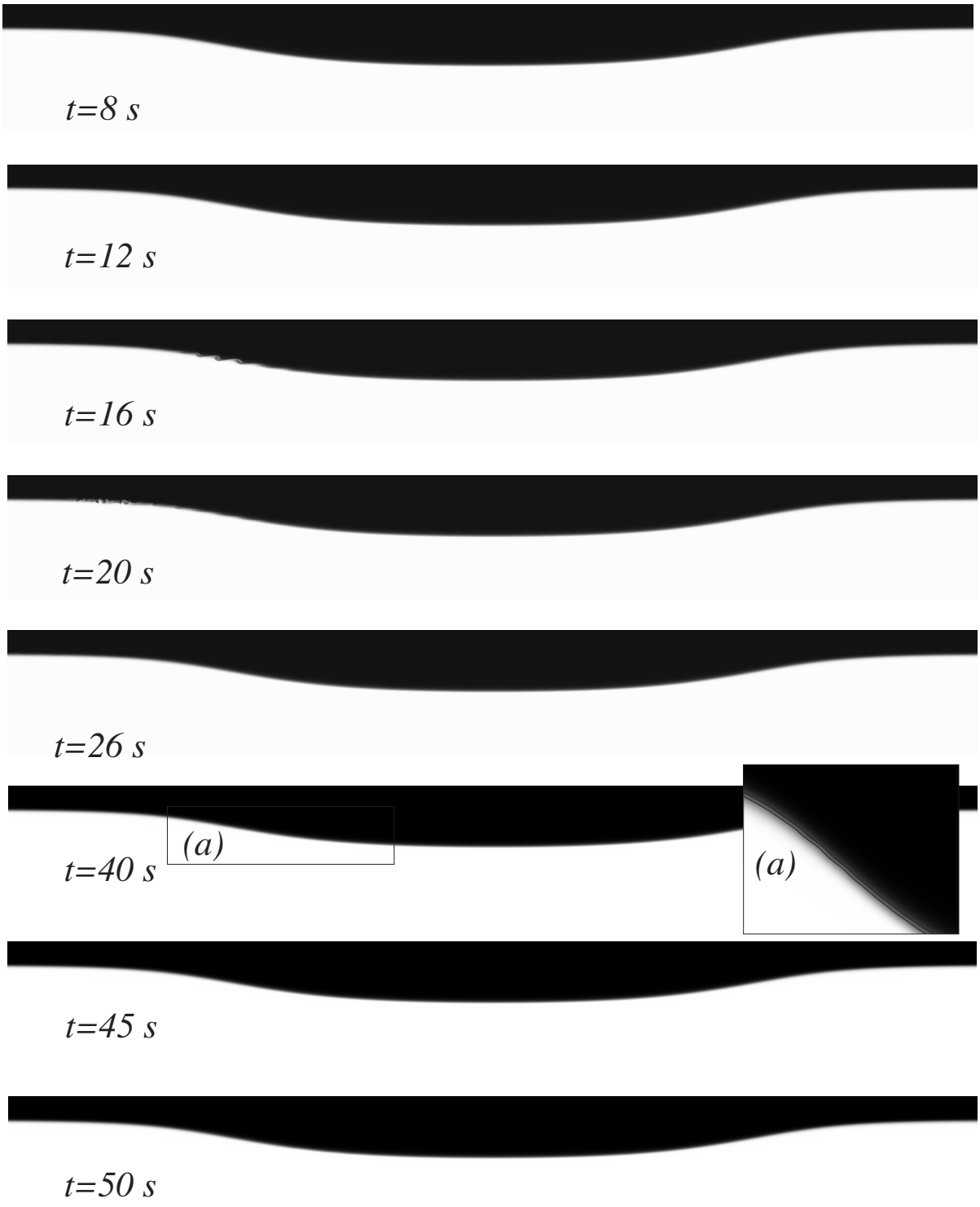

FIGURE 4.26. Same as Figure 4.25, resolution 512.

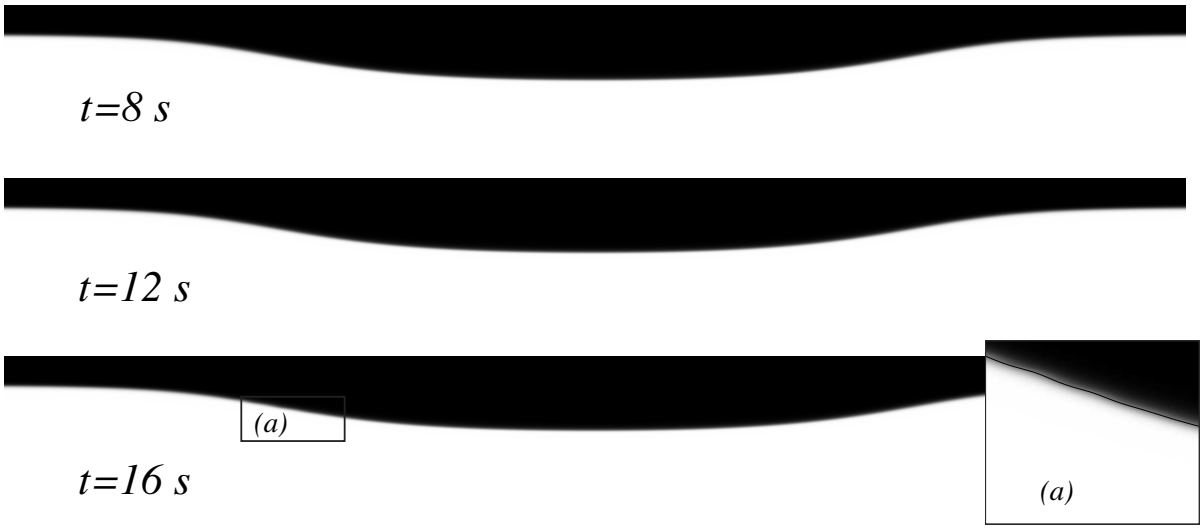

FIGURE 4.27. Same as Figure 4.25, resolution 1024.

induced by numerical error in both the evolution code and the initial condition, which can be viewed as an *initial perturbation* superimposed on the traveling wave solution of the discrete operator associated with the evolution code. Simultaneously with the growth in the unstable region of the wave, this perturbation is shed downstream (in the wave-frame), and starts propagating in a stable region of the flow field. The shear in this region on the downstream side of the wave decays to zero exponentially fast for solitary waves, with the density stratification limiting to that of the quiescent state. The perturbation therefore propagates mainly as a dispersive (weakly nonlinear for sufficiently large time) wave train governed by the dispersion relations determined by the background stratification. One can show that in the frame of reference of the wave, all normal modes in this region are traveling from right to left, both their phase speed and group velocity being thus bounded below by $c_0 - c$ and above by $c_0 + c$, where c_0 is the *critical* speed in the background stratification and c is the speed of the wave (with $c > c_0$) - see Figure 4.28 for the two branches of the dispersion curves.

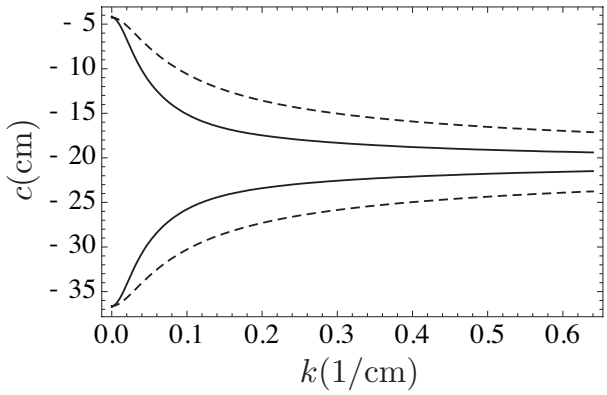

FIGURE 4.28. The two branches of the dispersion relation for the background stratification. Continuous line - group velocity, dashed line - phase speed, both in the frame of the wave, as function of the wave number.

We remark here that all time simulations for propagation of solitary wave solutions (independent of whether they exhibit shear instabilities or not) exhibit a wake that is shed behind the wave, which is visible in both the density and the velocity field. Its magnitude decreases with resolution, indicating that the wake is a result of the initial perturbation (localized in the region of maximum displacement) that is shed downstream. In fact, we can identify qualitatively the superposition of normal modes of the background stratification (see Figure 4.30) in the velocity field associated with the wake – see Figure 4.29. For a rigorous quantitative comparison of the normal modes with the features in the wake, knowledge of the initial perturbation is needed.

At the front of the wave train however, as shown in Figure 4.29(c), the fastest traveling normal mode emerges.

Thus, we argue that the second episode of instability is triggered by the fastest traveling normal mode of the background stratification (which travels with a group velocity bounded above by $c_0 + c$) and it is not part of the instability triggered by the initial evolution of the perturbation.

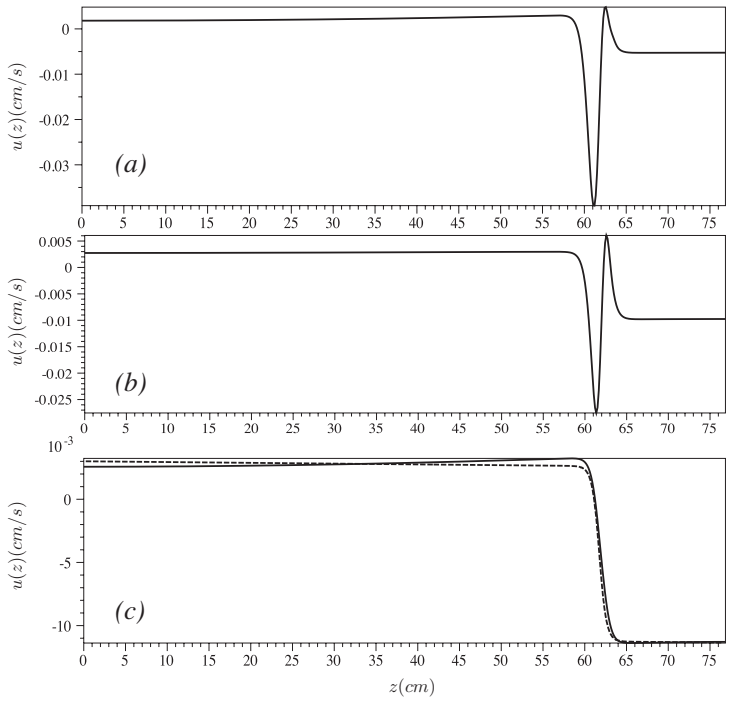

FIGURE 4.29. Horizontal velocity (in the lab frame) profiles during the propagation of a large amplitude solitary internal wave $a/h_1 = 1.51$ at time $t = 17.5$ s at locations downstream from the peak of the wave (a) $X = 516$ cm, (b) $X = 566$ cm and (c) $X = 716$ cm. In (c) the dashed contour corresponds the fastest traveling normal mode of the background stratification.

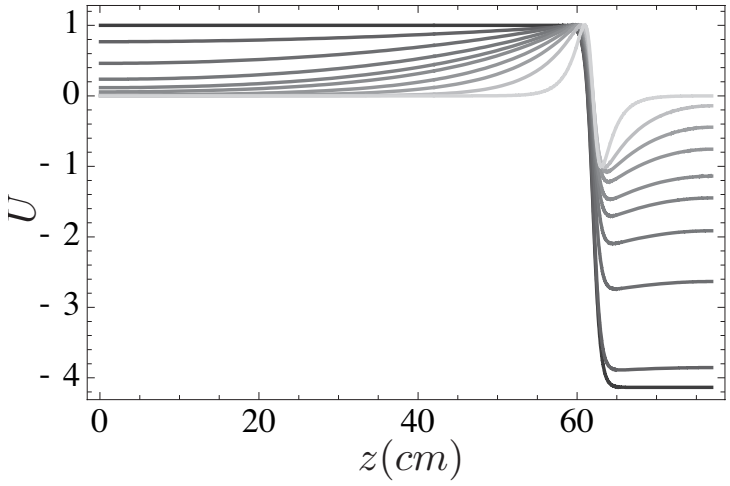

FIGURE 4.30. Horizontal velocity profiles for normal modes of the background stratification with wavenumbers ranging from 0 (black) to 0.4 cm^{-1} light gray.

We test this conjecture by doubling the length of the computational domain – thus initializing the evolution code with a long periodic wave solution of the iterative code,

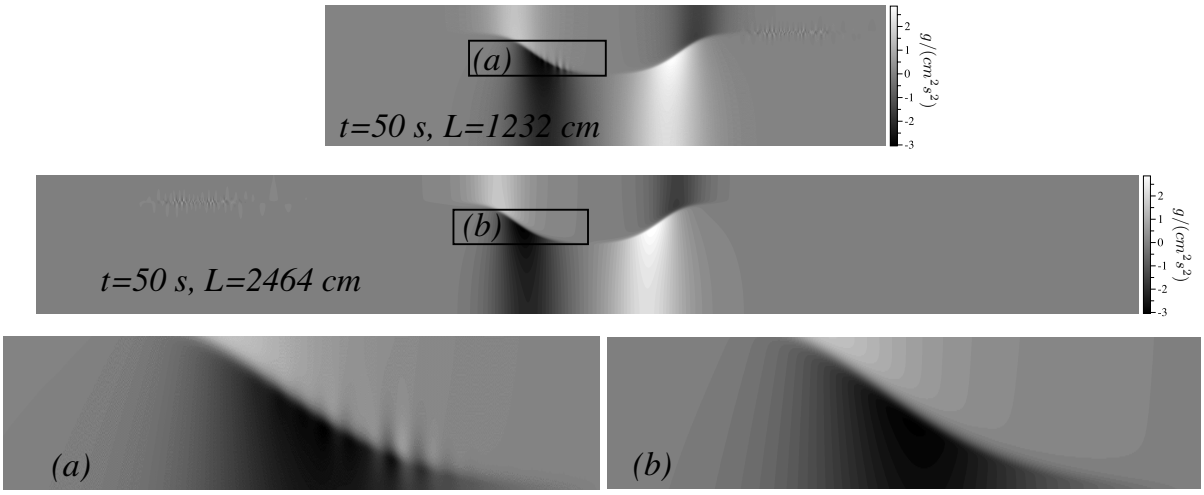

FIGURE 4.31. Horizontal pressure gradient p_x at time $t = 50\,\mathrm{s}$ for two waves of same amplitude $a/h_1 = 1.51$, with periods $L = 1232\,\mathrm{cm}$, top and $L = 2464\,\mathrm{cm}$, bottom.

with double the period and same amplitude and speed. We perform simulations at the resolution $N = 512$. Since, for this resolution, the shear instability is not immediately apparent in the density field, we monitor and display the horizontal pressure gradient. In Figure 4.31 we show the horizontal pressure gradient at time $t = 50\,\mathrm{s}$ for both the wave of period $L = 1232\,\mathrm{cm}$ and of period $2464\,\mathrm{cm}$, respectively. Note that the wave with period $2464\,\mathrm{cm}$ does not exhibit roll-up, as opposed to the wave of shorter period. In fact, we can estimate the minimum time of travel of the aforementioned normal mode as $(c_0 + c)/L$, where L is the period. In particular, for the long wave of period $L = 1232\,\mathrm{cm}$ (taking into account that the critical speed c_0 is $\approx 16\,\mathrm{cm/s}$, whereas the speed of the wave c is $\approx 20.4\,\mathrm{cm/s}$) this estimate is $\approx 34\,\mathrm{s}$ which falls in the range $30 - 40\,\mathrm{s}$ observed in the simulations.

All numerical experiments we have performed suggest, apart from the convergence of the stationary solution, some interesting stability properties of the flow. In the limit of infinite period, the internal waves investigated seem to be globally linearly stable since the

initial perturbation (after some growth in the unstable region located at the peak of the wave) is advected away, leaving the wave in an equilibrium state, close to the unperturbed solitary wave (in a norm appropriately defined to mode out translations, as appropriate for orbital stability of traveling waves (see, e.g., Benjamin [2] for the analagous case of the Korteweg-de Vries equation). For finite period, however, the dispersive train generated by the first episode of instability wraps around the periodic box triggering subsequent episodes of instability. One can then expect the traveling wave to relax to a state where the dispersive wave trains no longer excite shear instabilities, by effectively reducing the amplitude of the wave and simultaneously stirring the pycnocline region to a larger thickness. Such a state would ultimately be dependent on the background stratification only, thus indicating overall instability of the original wavetrain.

In the following section, in order to shed some light on these observations, we look at the local spectrum of the flow.

4.3.2. Local stability analysis of the solitary wave solution. As argued before, both the shear and the density stratification of the solitary wave have slow variation in the horizontal direction, hence the first order approximation reduces to the case of a parallel heterogeneous shear flow (slowly varying with the horzontal location).

Taylor-Goldstein stability equation.

Starting with Kelvin [27], a considerable body of work has been dedicated to the stability of horizontal flows of incompressible fluid with *piecewise-constant* density and shear distribution – see Drazin & Howard [10], for an excellent review. Taylor [48] and Goldstein [17] were the first to consider the stability of heterogeneous shear flow with *smoothly* varying density and shear, from the perspective of normal modes. By linearizing the

Euler equations

$$\rho(u_t + uu_x + wu_z) = -p_x\,, \tag{4.2}$$

$$\rho(w_t + uw_x + ww_z) = -p_z - \rho g\,, \tag{4.3}$$

$$\rho_t + u\rho_x + w\rho_z = 0\,, \tag{4.4}$$

$$u_x + w_z = 0\,, \tag{4.5}$$

with respect to small perturbation of the parallel basic flow with stratification $\rho_0(z)$ and shear $u_0(z)$

$$u = u_0 + \delta u\,, w = \delta w\,, \rho = \rho_0 + \delta\rho\,, p = p_0 + \delta p\,,$$

and assuming that any perturbation can be decomposed in independent wave components

$$\boldsymbol{\phi}(x,z,t) = \{\delta u\,, \delta w\,, \delta\rho\,, \delta p\} = \widehat{\boldsymbol{\phi}}(z)\mathrm{Exp}\left[i\boldsymbol{k}\cdot\boldsymbol{x} - \omega t\right]\,,$$

they derived a linear eigenvalue problem for the stability problem. They further conjectured that the fastest growing component is two-dimensional, conjecture which has been rigorously proven later by Squire [46]. The eigenvalue problem governing the stability of parallel heterogeneous flows (often refer to as Taylor-Goldstein equation) is thus

$$\psi'' + \left[\frac{2u_0'}{u_0 - c} - \beta\right]\psi' + \left[\frac{\beta g}{(u_0 - c)^2} - k^2\right]\psi = 0\,, \tag{4.6}$$

where $\psi(z)$ is the magnitude of the perturbation stream function, $\beta(z) = -\rho_0'(z)/\rho_0(z)$, where $k\,, c$ are the wave number phase speed of the perturbation, respectively. The

boundary conditions, assuming a flow confined between two rigid walls at 0 and H, are

$$\psi(0) = 0\,, \psi(H) = 0\,. \tag{4.7}$$

In this work, we focus on the *initial value* problem, hence we are interested in the *temporal* evolution of a initial perturbation superimposed on the base flow. Hence, we seek so solve equation (4.6) with boundary conditions (4.7), for *real* wave number k and with the phase speed $c = c_R + ic_I$ as the eigenvalue, which can be *complex*. The flow is unstable if $c_I > 0$, and the associated normal mode has the rate of growth $\omega_I = kc_I$. We note that equation (4.6) becomes singular for c real and in the range of u_0. Eigenvalues c with this property correspond to singular neutral modes, and usually correspond to the boundaries of linear stability.

We remark that the influence of viscosity on the stability properties is expected to be minimal, slightly reducing the growth rates – as numerical investigations of viscous shear flows have revealed. In fact, Maslowe & Thompson [36] have shown that the viscosity effects on the maximum growth rates are very small for Reynolds number above 100 (recall that in our investigation typical Reynolds numbers are $\approx 10^5$).

Numerical implementation.

We solve equation (4.6), with boundary conditions (4.7), by employing a shooting method as follows: for fixed wave number k, we integrate from the center of the pycnocline location z_p to left and right by imposing continuity of both the eigenfunction ($\psi_L(z_p) = \psi_R(z_p) = \psi_p$, with ψ_p a normalization constant for the eigenfunction) and its derivative in the center ($\psi'_L(z_p) = \psi'_R(z_p) = \psi'_p$). We thus define two functions depending on the slope of the eigenfunction ψ'_p and on the eigenvalue c. We determine the eigenvalue c and

the slope of the eigenfunction by imposing the boundary conditions (4.7), and by solving the corresponding nonlinear system. Our strategy follows closely the one reported in Hazel [20], who was the first to investigate numerically the stability of a class of parallel shear flows with *smooth* density stratification and shear. We point out that in this case the integration is done from the boundaries inwards. We choose to integrate from the center outwards in order to control the magnitude of the eigenfunction.

In order to locate numerically all unstable modes, we search within a domain of the complex c plane, which we isolate by applying the result of Howard [23] (often referred to in the literature as the *semicircle theorem*). The theorem states that the complex wave velocity of any unstable mode must lie inside the semicircle in the upper half-plane of the complex c plane which has as diameter the range of the horizontal shear. We have determined numerically one unstable branch for all configurations investigated.

Local spectrum of the solitary wave solution.

In this section we present detailed spectrum calculations for the large amplitude wave $a/h_1 = 1.51$. We compute local unstable spectrum for a series of horizontal locations in between the point of maximum displacement of the wave and the end of the region of potential instability $Ri < 1/4$ (noting that both the horizontal velocity and the density stratification are symmetric with respect to the point of maximum displacement) – see Figure 4.32, where we show the general setup, and Figure 4.33, where we show a contour plot of the Richardson number for the area of potential instability.

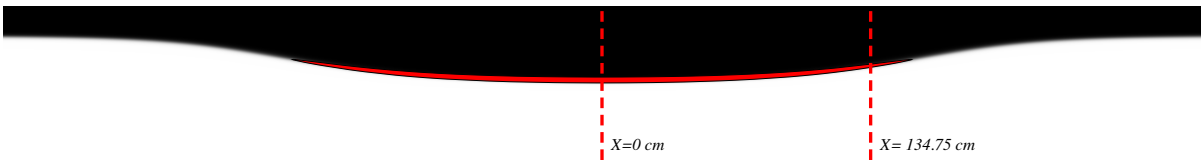

FIGURE 4.32. Density field for a solitary wave solution of amplitude $a/h_1 = 1.51$. Marked with red the area of $Ri < 1/4$. Local spectrum calculations are performed for locations in between $X = 0$ cm (peak of the wave) and $X = 134.75$ cm.

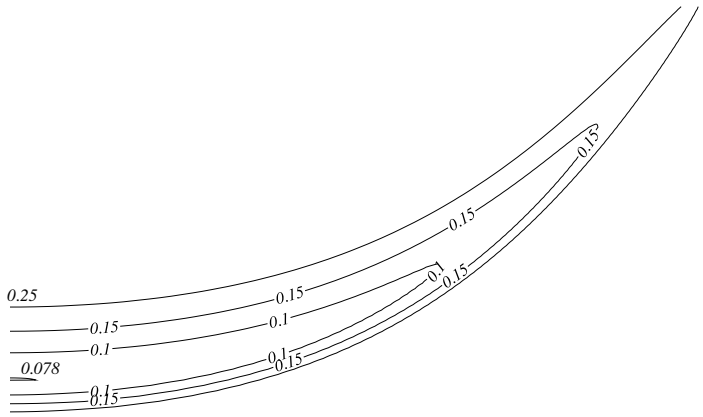

FIGURE 4.33. Contour lines of the Richardson number in the region of potential instability (half of the region represented) for the wave $a/h_1 = 1.51$ - see Figure 4.32.

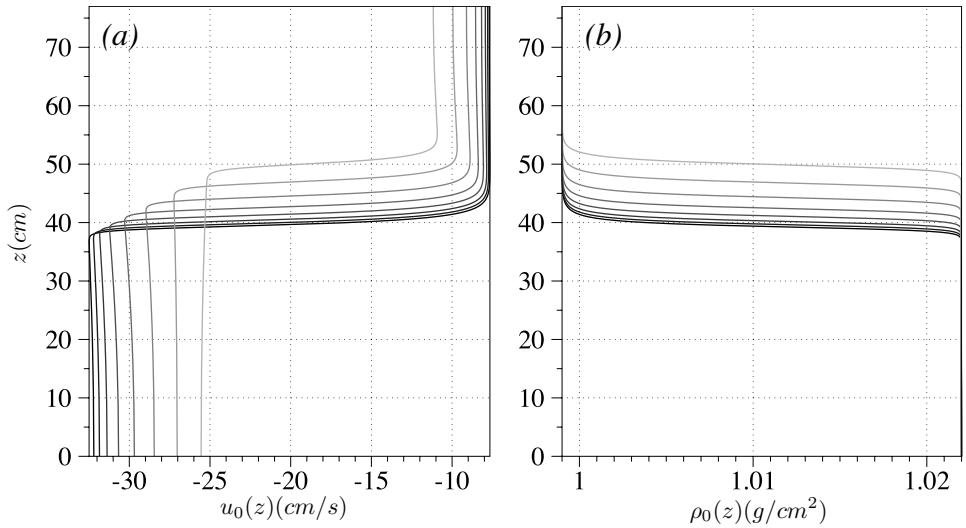

FIGURE 4.34. (a) Horizontal velocity profiles, (b) density profiles for a wave of amplitude $a/h_1 = 1.51$, for equidistant 8 locations in between $X = 0$ cm (peak of the wave) and $X = 134.75$ cm.

We construct the branch of unstable normal modes, for a given combination of density stratification $\rho_0(z)$ and shear $u_0(z)$, by a parameter continuation technique in the wave number k, extending the the eigenvalue search close to the real axis, where the eigenvalue problem becomes singular – see Figure 4.35 for the unstable branches in the complex plane $c = c_R + ic_I$ corresponding to eight equidistant horizontal locations across the region of potential local instability. All the stability computations are performed in the frame of reference of the wave (moving at horizontal speed c_{wave} with respect to the lab frame).

In Figure 4.36 we show the growth rates and the phase speed of the unstable modes for the eight combinations of shears and density stratifications shown in Figure 4.34. Note that the phase speed of the normal modes is negative, and moreover it decreases for increasing k, which implies that the group velocity $(d\omega_R/dk)$ is also negative.

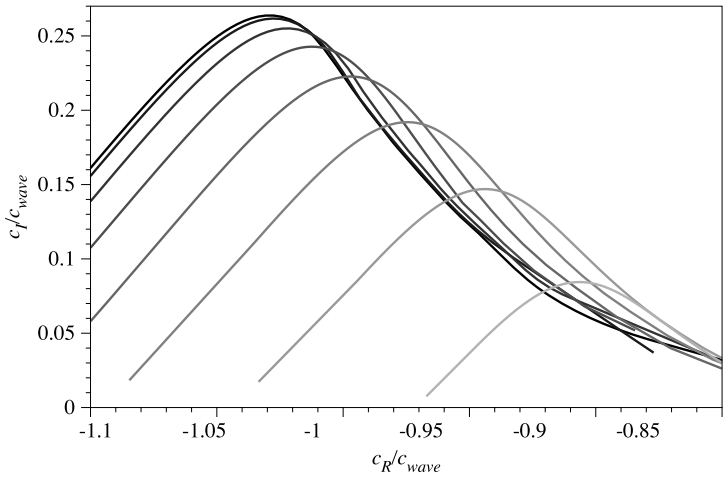

FIGURE 4.35. Unstable branches in the complex c plane for 8 equidistant locations in between $X = 0$ cm (peak of the wave) and $X = 134.75$ cm, for the solitary wave solution in Figure 4.32. Black - $X = 0$ cm, light gray - $X = 134.75$ cm.

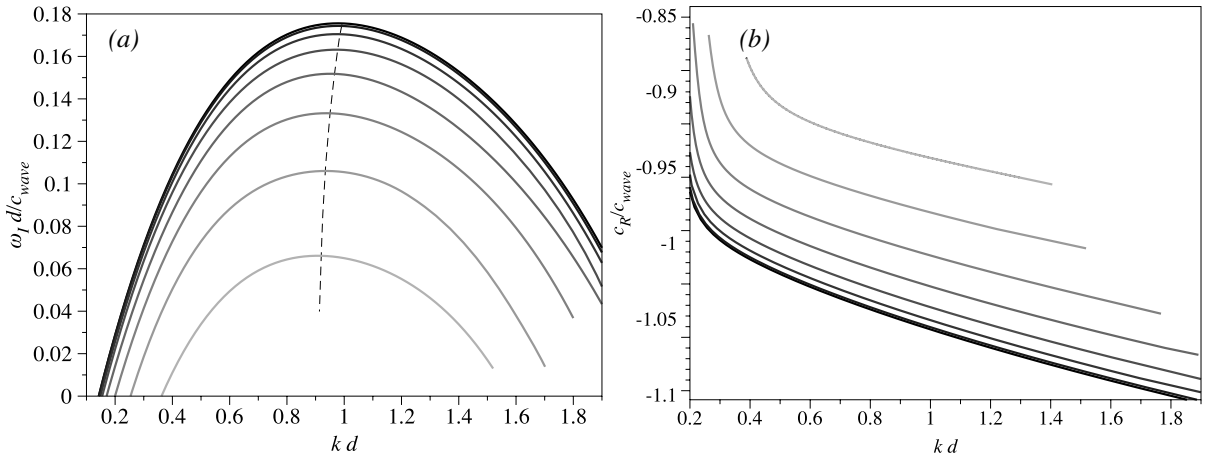

FIGURE 4.36. (a) Growth rates and (b) phase speed for 8 equidistant locations in between $X = 0$ cm (peak of the wave) and $X = 134.75$ cm, for the solitary wave solution in Figure 4.32. Black – $X = 0$ cm, light gray – $X = 134.75$ cm; $d = 2$ cm represents the thickness of the pycnocline.

Next, we illustrate the dependence of the unstable spectrum on the horizontal location across the region of local instability. First, we note that the normal mode that would be first visible in the evolution of a perturbed initial state is the mode corresponding to the maximum growth rate. We expect this to be the case as long as the horizontal extent of the area of local instability is larger than the periods associated with these modes,

which is the case for most of the waves considered in this analysis. From Figure 4.37 we can infer that the wave number associated with the most unstable mode does not vary significantly along the wave profile. Furthermore, in Figure 4.38, we can see that the

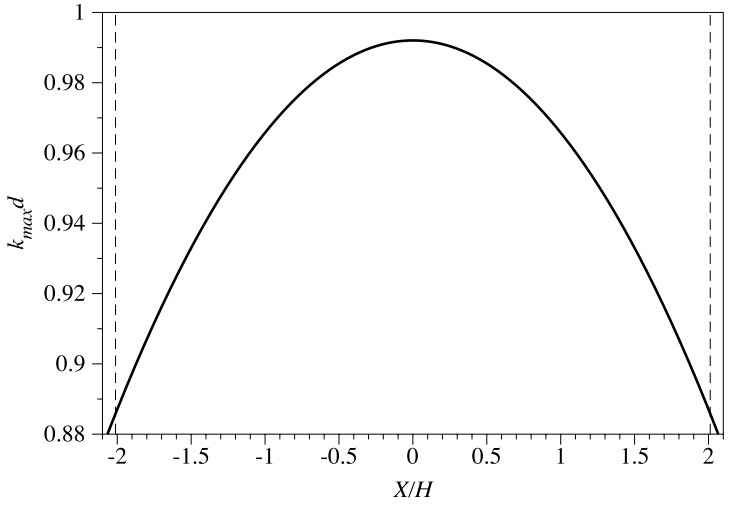

FIGURE 4.37. Wave number corresponding to the maximum growth unstable mode along the wave profile. The dashed lines mark the range of the region of potential local instability, $Ri < 1/4$.

period of the self-induced shear instability for an actual wave evolution falls in the range predicted by the local eigenvalue calculation (12.69 cm to 14.27 cm).

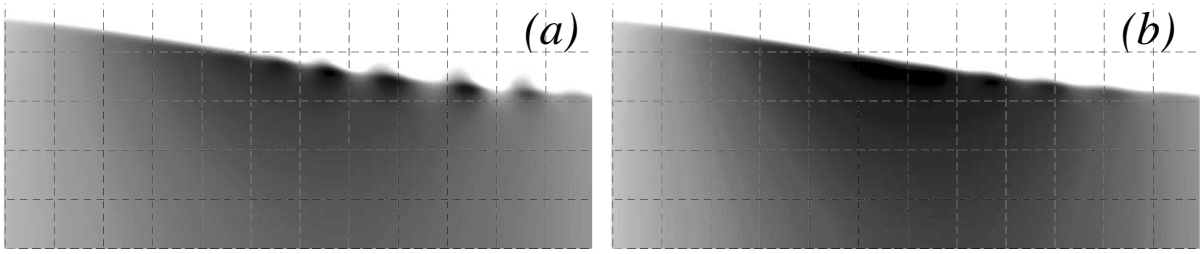

FIGURE 4.38. Portion of the horizontal pressure gradient p_x evidencing self-induced shear instability for a wave of amplitude $a/h_1 = 1.51$ at $t = 11$ s for a numerical simulation at resolution (a) 512, (b) 1024. Superimposed on each plot, a grid with spatial resolution of 10 cm, to evidence the wavelength of the perturbation.

In Figure 4.39 we show the variation of the growth rate associated with the most unstable normal mode in the horizontal direction. Note that the horizontal range of

potential local instability ($Ri < 1/4$) almost coincides with the range of *actual* local instability. Finally, in Figure 4.40 we show the phase speed and the group velocity

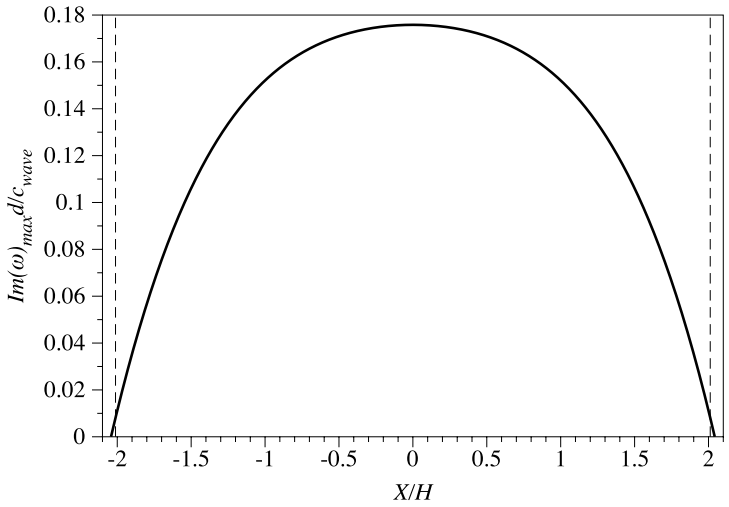

FIGURE 4.39. Maximum growth rate along the wave profile. The dashed lines mark the range of the region of potential local instability, $Ri < 1/4$.

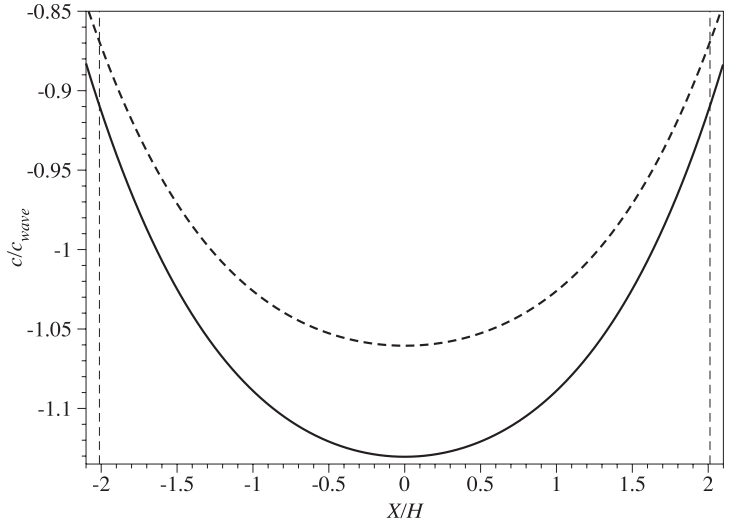

FIGURE 4.40. Dashed - phase speed, continuous - group velocity associated with the maximum growth rate along the wave profile. The thin dashed lines mark the range of the region of potential local instability, $Ri < 1/4$.

associated with the most unstable mode, which is negative at all horizontal locations in the region of local instability. This fact explains at first order the behavior described in

§4.3.1 – namely the initial perturbation located at the peak of the wave grows and it is advected away from the pocket of instability, with the wave reaching a state of equilibrium afterwards. Relatively recent advancements in the stability theory of spatially varying flows as presented in Huerre & Monkewitz [24, 25], Huerre [26], based on slowly varying asymptotics WKBJ analysis, support this veiwpoint. This approach assumes *scale separation*, i.e., the stream-wise variation of the flow must be slow over a typical wavelength of the perturbation, so that the local dispersion relation can be used in the global stability analysis of the flow, as a leading-order approximation. We note that the flow under consideration in this chapter meets these requirements.

The foundation of Huerre & Monkewitz [24, 25], Huerre [26] approach lies on the fundamental distinction between *absolute* and *convective* instability. A parallel shear flow is said to be convectively unstable if the growing wave train generated by an initial perturbation is advected away. Conversely, the flow is said to be absolutely unstable if the instability contaminates the entire medium. This distinction seems trivial in the case of strictly parallel stationary flows, which are frame invariant – a simple change of frame of reference renders a convectively unstable parallel flow in an absolutely unstable one. However, when considering spatially developing stationary flows, these concepts become relevant, since the frame of reference in which the flow is stationary is singled out. The main conjecture of the theory is that a necessary (although not sufficient) condition for the existence of time-periodic intrinsic oscillations (or self-sustained global modes) is the existence of a pocket of *absolute* instability somewhere in the flow field.

The flow considered here has a pocket of *convective* instability (confirmed by the *negative* group velocity of the local spectrum in the region of local instability), being

locally stable outside this region. Thus, in the framework of the above-described theory, this flow does not support self-sustained global modes – a conjecture supported by the numerical simulations.

We conclude this section by mentioning that the term convective is extensively used in the literature to qualify another mechanism of wave breaking that occurs when the fluid velocity approaches the phase speed of the wave, or equivalently zero in the frame of reference of the wave (see for instance Holyer [22]). The waves investigated in this work do not exhibit this property and thus throughout the remainder of this chapter we employ the term convective only in the context described in the paragraph above.

Ability of the evolution code to accurately capture linear growth of the shear instability.

In order to test the ability of the evolution code to capture instabilities, we simulate the time evolution of a parallel shear constructed with the density stratification and the shear from the maximum displacement of the pycnocline (for the wave with amplitude $a/h_1 = 1.51$) perturbed with monochromatic perturbation of wave number close to the maximum growth rate mode

$$\psi(x, z, 0) = \hat{\psi}_0 \, \mathrm{sech}^2 \left[\frac{\ln 9}{d} (z_p - z) \right] \cos kx \, ,$$

where d and z_p are the thickness and the center of the pycnocline , $kd \approx 0.8$ whereas $\hat{\psi}_0$ is the magnitude of the perturbation. We study the behavior of the instability by tracking a constant density isoline contained in an window of length comparable to the wavelength of the perturbation, monitoring the trajectory of the maximum displacement point – see Figures 4.41 and 4.42. We perform the simulation in the lab frame where

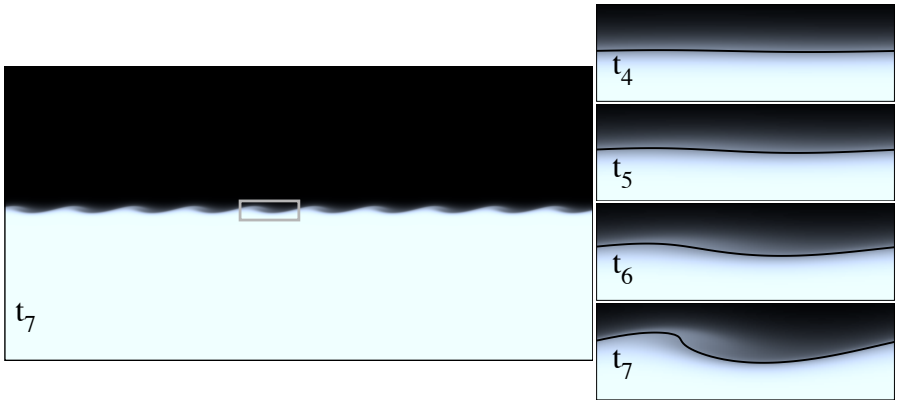

FIGURE 4.41. Right - density field at time $t = 4.45\,\mathrm{s}$ for the parallel shear from the maximum displacement of the wave of amplitude $a/h_1 = 1.51$, perturbed with monochromatic perturbation of wave number $kd = 0.8$. Left - portion of the density field (marked on the image at right) at time $t_4 = 2.79$ s, $t_5 = 3.35\,\mathrm{s}$, $t_6 = 3.8\,\mathrm{s}$ and $t_7 = 4.45\,\mathrm{s}$; black line - average density isoline.

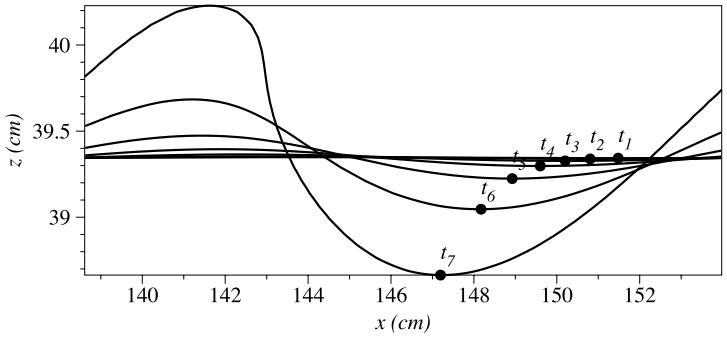

FIGURE 4.42. Density isolines corresponding to the average density for $t_1 = 1.12\,\mathrm{s}$, $t_2 = 1.17\,\mathrm{s}$, $t_3 = 2.23\,\mathrm{s}$, $t_4 = 2.79\,\mathrm{s}$, $t_5 = 3.35$ s, $t_6 = 3.8$ s and $t_7 = 4.45\,\mathrm{s}$.

the phase speed of growing normal modes (and hence the horizontal excursion of the the density isolines in the initial stage of linear growth) is relatively small ($\approx 1\,\mathrm{cm/s}$). From this trajectory, we are able to estimate the growth rate and the phase speed of the perturbation. In Figure 4.43 we compare the phase speed of the perturbation and its growth rate against the predictions of the Taylor-Goldstein stability theory. Note that while the comparison for growth rate is excellent, the phase speed comparison is less

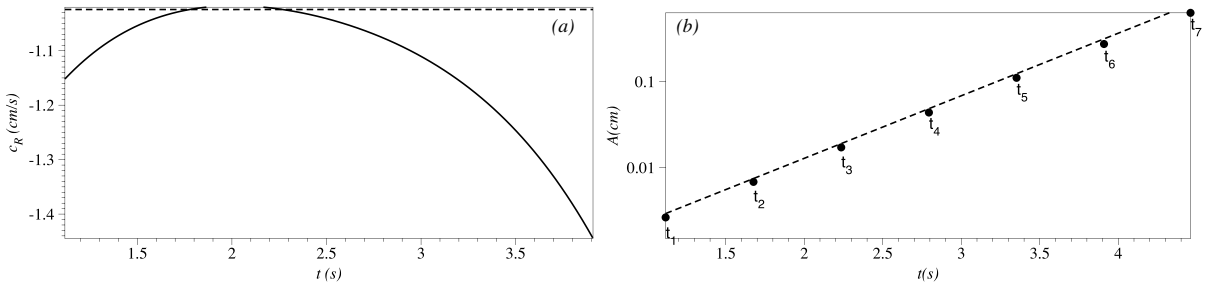

FIGURE 4.43. (a) Continuous - phase speed of the perturbation constructed from the average density isoline trajectory for the simulations described in Figure 4.41, dashed - estimate from the stability calculation. (b) Data points - maximum displacement of the average density isoline at $t_1 = 1.12\,\mathrm{s}$, $t_2 = 1.17\,\mathrm{s}$, $t_3 = 2.23\,\mathrm{s}$, $t_4 = 2.79\,\mathrm{s}$, $t_5 = 3.35$ s, $t_6 = 3.8\,\mathrm{s}$ and $t_7 = 4.45\,\mathrm{s}$; dashed line $A(t_1)e^{\omega_I(t-t_1)}$, where A is the displacement registered at $t = t_2$ and ω_I is the growth rate estimate from the stability calculation.

satisfactory, in particular after 2.5 s, albeit we can identify nonlinearity in the growth at around 3 s, as evidenced in the shapes of the average density isolines – see Figure 4.42.

4.3.3. Simple envelope equation for instability. We remark that in our numerical simulations (both the generation experiment and the evolution of the solitary wave solution) and in the experimental observations of Grue *et al.* [19] and Fructus *et al.* [13], Kelvin-Helmholtz billows develop *after* the point of maximum displacement of the wave, while no growth is observed in the front of the wave. We argue that while the *convective* character of the instability is partly responsible for this asymmetry, it does not explain it entirely. In the following, to illustrate this point, we use the local spectrum calculation developed in the previous section to construct a simple envelope equation for the perturbation evolution in the unstable region, and compare it qualitatively to numerical simulations.

We follow the strategy outlined in Troy & Koseff [50]. They performed experiments of generation and propagation of long progressive internal waves of *small* amplitude in a

near two-layer background stratification, given by a tangent hyperbolic density profile. They proposed a Richardson number criteria for breaking, based on the local stability properties of the flow, which compared well to the experimental observations. In the following, we briefly review the main features of their construction. The small amplitude regime and the long wave assumption allowed them to accurately model both the shear and the density stratification along the wave, with coincident tangent hyperbolic profiles (i.e. aligned in the pycnocline region, and with the same thicknesses). Detailed numerical stability computations for these type of shears have been performed by Hazel [20], under the Boussinesq approximation (i.e. neglecting the inertial terms in the stability equation (4.6)). Under this approximation, the growing normal modes are stationary in the frame of reference corresponding to the average of the shear (which in the case of periodic waves corresponds to the lab frame). Thus, in the *wave frame* the normal modes are advected in the opposite direction of the propagation of the wave, at constant phase speed coinciding with the phase speed of the wave. We note here that the group velocity of the unstable normal modes in this instance coincides with the phase speed. Furthermore, Hazel [20] results confirmed that the criteria $Ri < 1/4$ is both a necessary and sufficient condition for existence of growing normal modes, thus the horizontal extent of the regions with $Ri < 1/4$ is a reasonable estimate for the region of *local* instability (a result which we have verified in large amplitude regime, in the section above). Thus, Troy & Koseff [50] constructed an estimate of the time of travel of the perturbation in the unstable region (say T_w) based on the length of the area of local instability and the speed of propagation of instability. Next, they proposed the following model equation modeling the growth of

a perturbation

$$A_t + cA_X - \omega_I(X)A = 0\,,$$

where c is the speed of propagation of the wave, ω_I is the growth rate associated with the fastest growing normal mode and $X = x - ct$ (x being the lab frame coordinate). Thus a perturbation that enters the unstable region, will grow in the interval T_w (time of exit from the unstable region) to an amplitude

$$A = A_0 e^{\overline{\omega}_I T_w}\,,$$

where A_0 is the magnitude of the perturbation as it enters the region of local instability and $\overline{\omega}_I$ is the average (over the horizontal extent of the region of local instability) of the maximum growth rate. Finally, they proposed the following criteria for instability

$$A/A_0 \gg 1\,, \qquad \text{or, equivalently,} \qquad \overline{\omega}_I T_w \gg 0\,,$$

which they expressed in terms of the Richardson number, by fitting the growth rate from the stability calculation of Hazel [20] in terms of the Richardson number across the wave profile.

In the large amplitude regime investigate in this chapter, we note that both the phase speed and the group velocity of the normal mode varies considerably along the unstable region (within 10% of the speed of propagation of the wave). Following the reasoning in Troy & Koseff [50], while attempting to include the span-wise variation of both the phase speed and of the growth rate of the most unstable mode, we propose the following envelope equation for the evolution of a monochromatic perturbation with wave number

close to the maximum growth rate normal mode (as predicted by the local stability analysis)

$$A_t + c_R(X)A_X - \omega_I(X)A = 0\,, \tag{4.8}$$

where $A(X,t)$ is the amplitude of the perturbation, $c_R(X)$ is the phase speed corresponding to the maximum growth rate at location X and $\omega_I(X)$ is the maximum growth rate at location X. While Troy & Koseff [50] were interested only with an estimate of growth *at the end* of the unstable region, we monitor also the growth of the perturbation within this region.

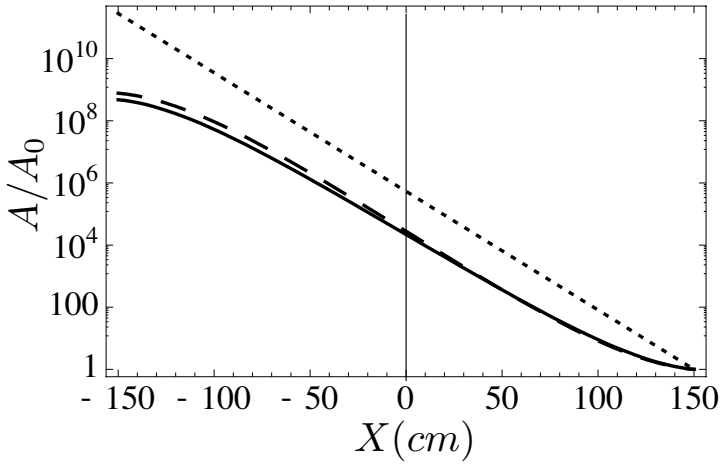

FIGURE 4.44. Amplification factor (A/A_0) for a perturbation initiated at the right boundary of the instability region. Black - taking into account the spatial variation of the phase speed and growth rate of the most unstable local mode, dashed - approximating the local phase speed with the phase speed of the wave, dotted - approximating the local growth rate with the growth rate at the maximum displacement.

We solve equation (4.8) by the method of characteristics. We denote the length of the region of local instability by $\widetilde{L}$, and place the coordinate system at the point of maximum displacement of the pycnocline. Then the time of travel of a perturbation

across the instability region is

$$T_w = F(\widetilde{L}/2) - F(-\widetilde{L}/2)\,,$$

where

$$F(X) = \int \frac{1}{c_R(X)} dX\,.$$

The characteristic curve initiating at the right boundary of the instability region is parametrized by $\{[X(s) = s\,, t(s) = F(s) - F(\widetilde{L}/2)] : -\widetilde{L}/2 < s < \widetilde{L}/2\}$, and the amplitude of the perturbation along this characteristic is

$$A(X, t(X)) = A_0(\widetilde{L}/2)\mathrm{Exp}\left[\int_{\widetilde{L}/2}^{X} \frac{\omega_I(s)}{c_R(s)} ds\right]\,, \qquad X \in [-\widetilde{L}/2\,, \widetilde{L}/2]\,. \tag{4.9}$$

In Figure 4.44, we show the amplification factor A/A_0 for the wave of amplitude $a/h_1 = 1.51$, computed by (i) taking into consideration the spatial variation of both the local group velocity and local growth rate, (ii) by approximating the group velocity with the wave speed and (iii) by approximating both the group velocity and the growth rate with the corresponding values at the peak of the wave. Not that (i) predicts the smallest amplification rates across the unstable region.

The amplification factor at the peak of the wave predicted by this simple model for the large amplitude wave a/h_1 is substantial (10^4), hence for a perturbation entering the unstable region from the front of the wave, we expect to see appreciable growth at this particular point. However, as shown in Figure 4.45, no significant growth is noticeable at point of maximum displacement, and practically no growth is detected in the front of the

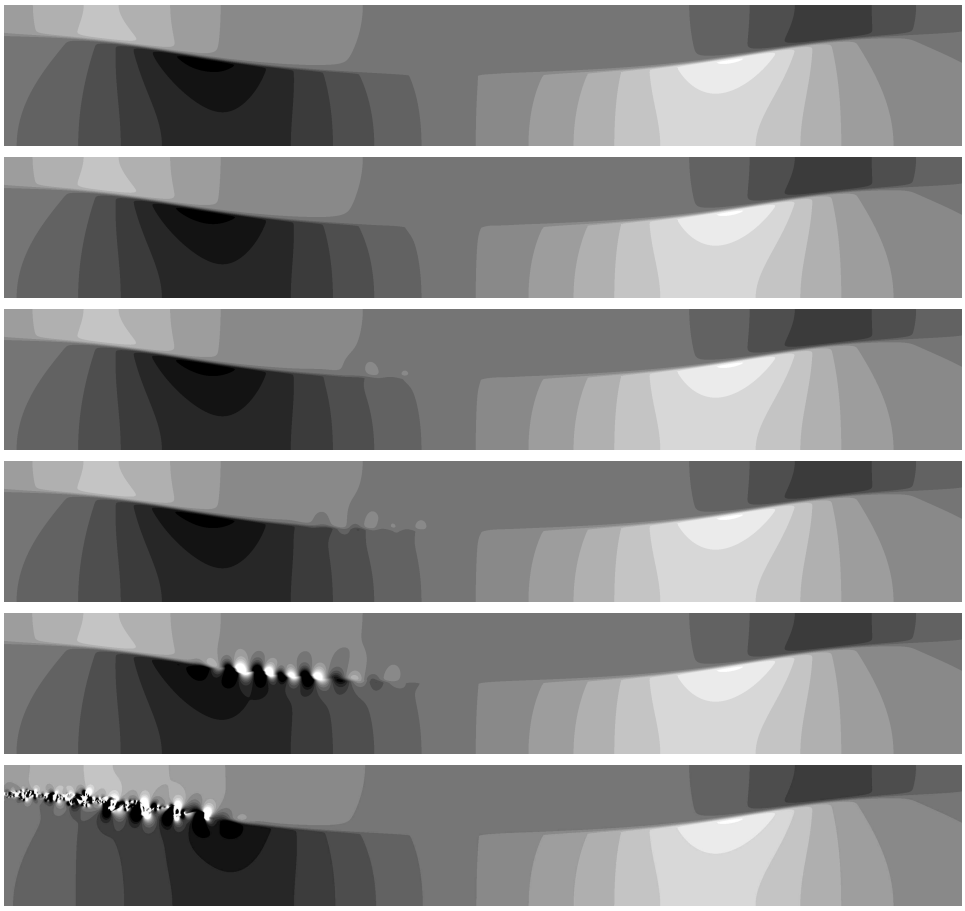

FIGURE 4.45. Portion of the horizontal pressure gradient p_x during the time evolution of a wave of amplitude $a/h_1 = 1.51$, seeded with a perturbation of magnitude 10^{-5} in the stream function, initially located at distance $X = 616$ cm from the maximum displacement, in front of the wave. Snapshots at times $26\,, 28\,, 30\,, 32\,,$ and 40 s, respectively.

wave, even if the perturbation, initially of (non-dimensional) magnitude 10^{-5}, traverses the entire region of local instability.

4.3.4. Amplitude threshold for manifestation of shear instability. In this final section we explore the stability properties of waves of various amplitudes on the same background stratification as the large amplitude wave ($a/h_1 = 1.51$) investigated in the section above, in an effort to determine a threshold amplitude for the manifestation of instability. We focus on the stability properties at the peak of the wave, where

the shear is maximal (and thus, when the flow is locally unstable, the growth rates of the unstable normal modes are maximal). We found that for all the locally unstable waves investigated, the group velocity of the unstable modes at this particular location is negative, suggesting that the flows under consideration can only be *convectively* unstable. Under this assumption, we construct an estimate of the amplification of a perturbation that traverses the region of local instability (4.9) by taking the growth rate at the peak as an upper bound for the growth rate across the region of local instability. T_w, the time of travel of the perturbation in the unstable region, is approximated by L_{Ri}/c_R, where L_{Ri} is the length of the pocket with $Ri < 1/4$ (which as shown in the previous section, is a good estimate for the extent region of local instability), and c_R is the phase speed of the fastest growing mode at the peak of the wave.

We remark that Fructus *et al.* [13] constructed a similar estimate by considering only *half* of the pocket of $Ri < 1/4$, based on the assumption that the shear instability originates at the center of the wave. While our numerical experiments revealed that the local growth rates are inhibited in the front of the wave, this is expected to be a first order (in the long wave parameter) correction. Thus we argue that considering the full extent of the area of local instability offers a more robust estimate for the amplification factor.

In order to isolate an amplitude range for which we expect to identify local instability within the flow field, we first evaluate the minimum Richardson number at the peak of the wave. We thus identify a minimal amplitude $a_{min}/h_1 \approx 0.76$ – see Figure 4.46, which also shows that the two-layer approximation (see relation (D.9), Appendix D) furnishes a reasonable estimate of the minimum Richardson number at the peak of the wave, in

particular in large amplitude regimes. We first bracket the threshold amplitude a_{min} with

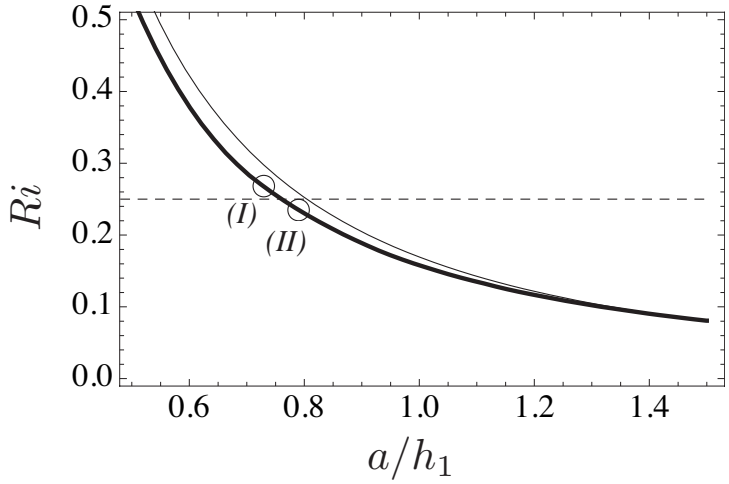

FIGURE 4.46. Minimum Richardson number at the peak of the wave as function of amplitude. Thick - continuos stratification, thin - prediction using the two-layer approximation. The circles mark waves of amplitudes a/h_1 0.73 , 0.79 respectively. The dashed line marks the critical Richardson number $Ri = 0.25$.

two amplitudes ((I) and (II) in Figure 4.46) and evaluate the corresponding spectrum at the peak. We are able to detect an unstable branch of normal modes only for the amplitude (II) – 0.79, and thus confirm again the the $Ri < 1/4$ is a good indicator of local instability. We next evaluate the unstable spectrum for a series of waves of amplitudes $a > a_{min}$.

In Figures 4.47 and 4.48 we display the maximum growth rate and the phase speed of the maximum growing normal mode, both corresponding to the peak location. Figure 4.49 depicts areas with $Ri < 1/4$ for several of the waves investigated whereas Figure 4.50 shows the dependence of the length of these areas on the amplitudes. As a side note, we remark on the fact that the height associated with the points that limit the horizontal extent of the pockets of $Ri < 1/4$ has a weak dependence on amplitude,

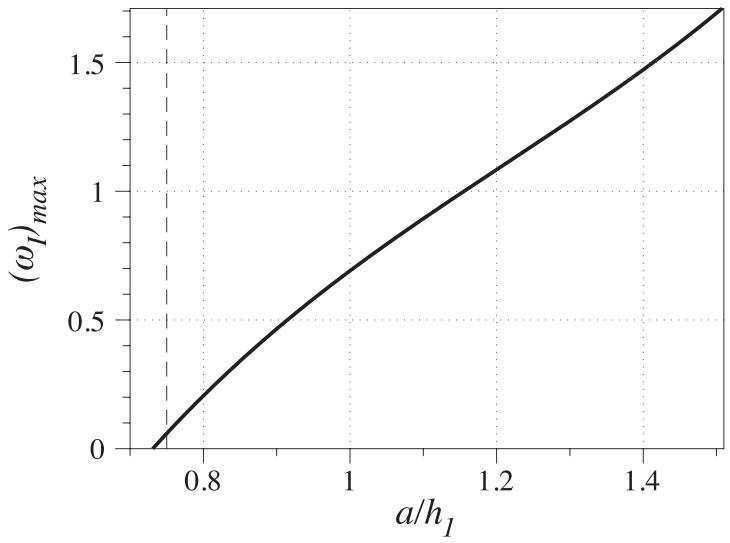

FIGURE 4.47. Maximum growth rate at the peak as a function of amplitude. The dashed lines marks the amplitude a_{min}, corresponding to $Ri = 0.25$.

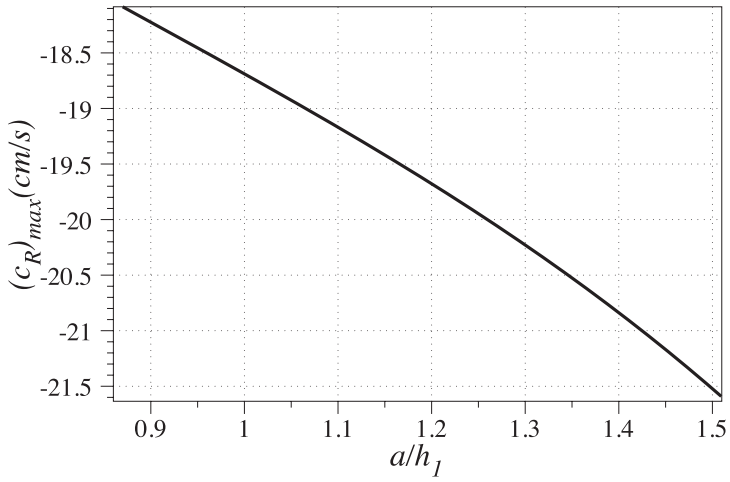

FIGURE 4.48. Phase speed of the maximum growing modes at the peak as a function of amplitude.

suggesting a critical height. (Further investigation is needed to elucidate what precisely selects this particular level.)

Finally, in Figure 4.51 we depict the dependence of the amplification factor on the amplitude of the wave. For waves of amplitude $a_{min}/h_1 < a/h_1 < 0.9$ the amplification factor is less than 10, thus we do not expect shear instability to manifest. Another factor that might inhibit shear instability development is when the length of the area of

instability becomes comparable to the the optimum instability wavelength. Note however that in our case, this happens when $a/h_1 < 0.8$, amplitude range excluded already by the criterion based on the amplification factor.

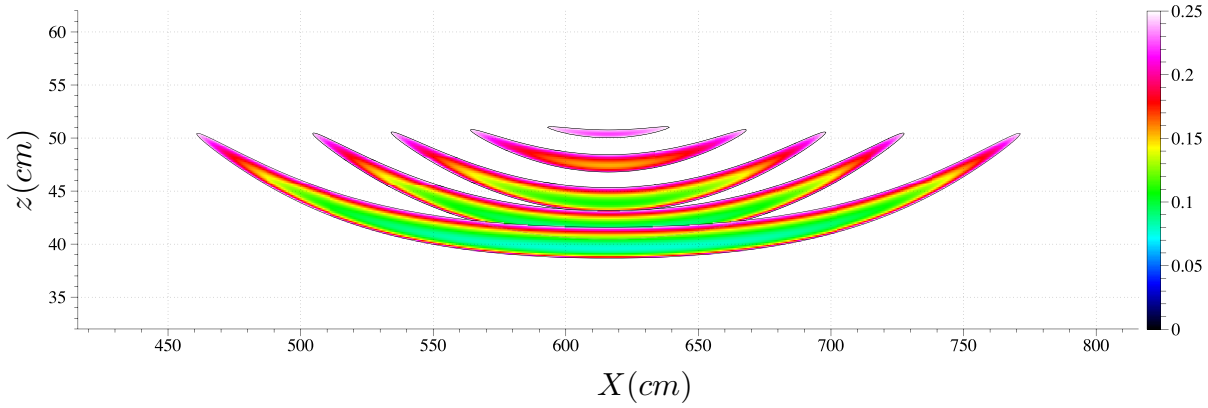

FIGURE 4.49. Regions with Richardson number smaller than 1/4 for waves of amplitudes a/h_1 0.79 , 0.98 , 1.14 , 1.23 , 1.48 and 1.51 respectively.

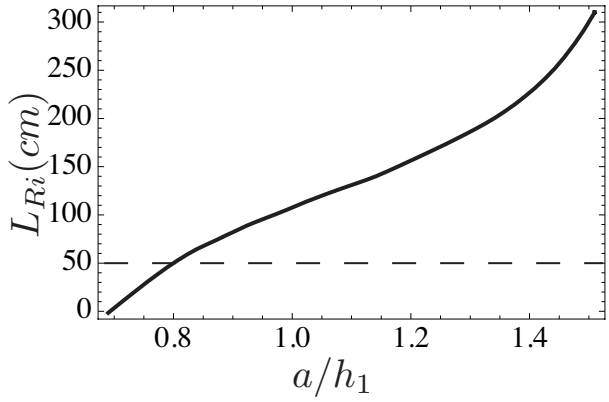

FIGURE 4.50. Dependence of the length of the area of local instability on the amplitude

To demonstrate the effectiveness of the threshold for the manifestation of shear instability identified above, we have performed numerical simulations for the evolution of several waves with amplitudes marked in Figure 4.51 (a/h_1 of 1.023 , 1.14 and 1.23 respectively – see Figures 4.52–4.54). In all instances, we use an initial perturbation

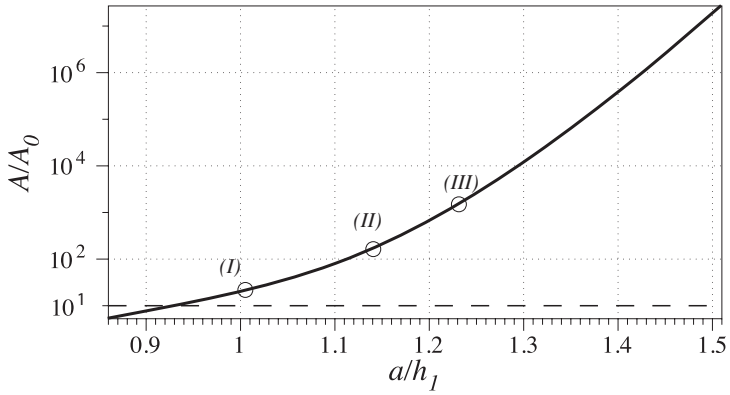

FIGURE 4.51. Amplification factor as a function of amplitude.

of non-dimensional magnitude 10^{-3} with wave number close to the optimum instability wave number

$$\psi(x,z,0) = \hat{\psi}_0 \operatorname{sech}^2\left[\frac{\ln 9}{d}(z_p - z)\right]\cos kx\,, \tag{4.10}$$

where z_p is the center of the pycnocline at the maximum displacement, $d = 10$ cm and $\hat{\psi}_0$ the magnitude of the perturbation.

Recall that the wave of amplitude $a/h_1 = 1.23$ generated from the step initial condition in density does not exhibit shear instability during its evolution – see Figure 4.18, §4.2.6. However, as shown in Figure 4.54 , we can detect shear instability when perturbing with a sufficiently large perturbation.

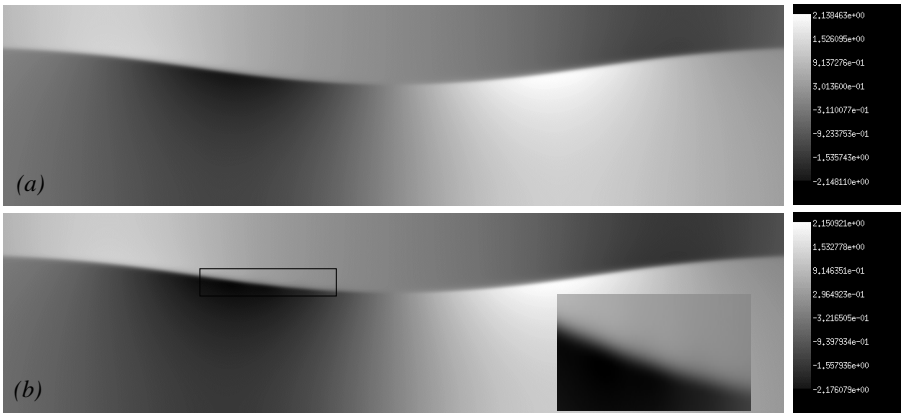

FIGURE 4.52. Portion of the horizontal pressure gradient for the evolution of a wave of amplitude $a/h_1 = 1.023$, perturbed with a monochromatic perturbation (4.10) of non-dimensional amplitude 10^{-3} at (a) $t = 0$ s and (b) $t = 5$ s.

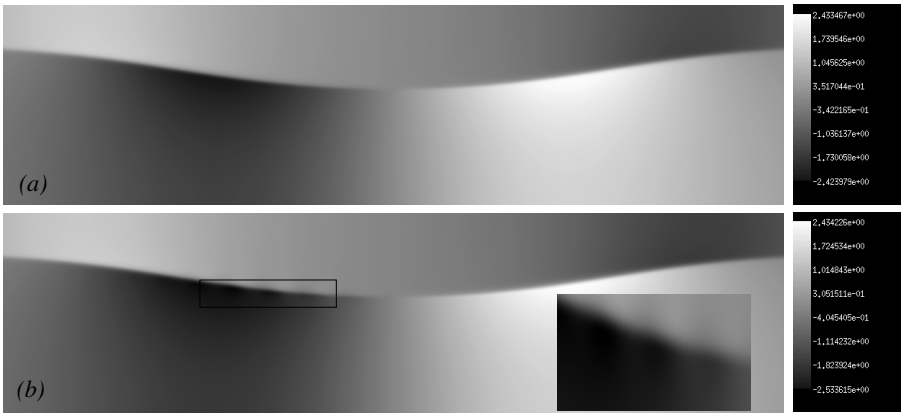

FIGURE 4.53. Same as Figure 4.52, $a/h_1 = 1.14$

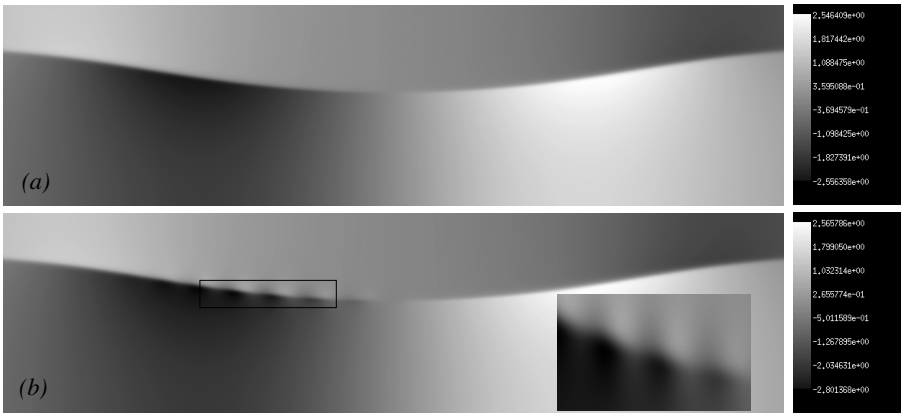

FIGURE 4.54. Same as Figure 4.52, $a/h_1 = 1.23$

4.4. Discussion

We have studied numerically the shear instability of solitary waves of large amplitude in a near-two layer stratification, with parameters from laboratory experiments reported in Grue *et al.* [19]. We have validated the evolution code used for simulating the generation and propagation of the waves considered, by emulating the experiments in Grue *et al.* [19], and comparing against solutions of the strongly nonlinear model, optimally adjusted to include the effect of a finite-width pycnocline. While the main dynamical features in Grue *et al.* [19] where successfully captured, there are some discrepancies in the wave shapes (in particular in the large amplitude regime) which so far are unaccounted for.

The numerical simulations of the generation experiments captured shear instability development in the same amplitude regime as in Grue *et al.* [19]. In order to identify whether the shear instability is an inherent property of the waves of large amplitude or is induced by the experimental generation, we have also studied the propagation of solitary wave solutions of Euler equations (obtained with a variant of the algorithm presented in Turkington *et al.* [51], which we describe in Appendix C). A resolution study for a wave of large amplitude has demonstrated the convergence of both the evolution code and of the initial condition. It has also revealed a interesting stability property of the flow: the numerical error induced a first episode of shear instability, the resulting Kelvin-Helmholtz billows being advected from the region of maximum displacement, leaving the wave in a state of equilibrium. Thus, no global self-sustained instability emerged.

In order to elucidate this, we have performed a local spectral stability analysis of the steady solution. The stability analysis revealed that the waves are locally unstable in

a finite region around the point of maximum displacement whose horizontal extent is very well approximated by $Ri < 1/4$ criterion. The phase speed and the group velocity associated with the unstable local modes are negative in the frame of reference of the wave, confirming that the flow is convectively unstable, and thus precluding the existence of a global self-sustained mode. Furthermore, the wave number associated with the optimally growing normal modes was found to be almost constant across the region of local instability, and consistent with the wave numbers observed in numerical simulations.

We next constructed a simple amplitude equation for the growth of a monochromatic perturbation (associated with the optimally growing normal modes) across the region of local instability. We have concluded that this simple model does not fully explain the marked front-back asymmetry in growth observed in our numerical simulations (and laboratory experiments such as Grue *et al.* [19], Fructus *et al.* [13]). Thus, the growth rates seem severely inhibited in front of the wave; conversely, they seem enhanced in the back of the wave. An extension to the next order in the long wave parameter would be necessary in order to assess whether the linear theory can capture this effect. However, it is unclear whether this analysis would shed some light on the the physical mechanism responsible for this asymmetry, which is without doubt a consequence of the spatial variation of the flow.

CHAPTER 5

On the use of the strongly nonlinear two-layer model for the spectral stability study of internal solitary waves in continuous stratification

While in Chapter 4 we have investigated numerically the shear instability of solitary waves on a specific background density stratification with narrow pycnocline (which we selected for referencing to actual experiments reported in Grue *et al.* [19]), the current chapter is aimed at stratifications with wider pycnoclines. The analysis presented here is rather limited, the scope of this chapter being mainly to suggest some possible avenues for a systematic study of linear stability of long solitary waves in density stratifications with one pycnocline.

We consider the class of prototype density profiles defined by

$$\overline{\rho}(z) = \rho_{min} + \frac{\rho_{max} - \rho_{min}}{2}\left(1 + \tanh\left[\frac{\ln\ 9}{d}(z_p - z)\right]\right), \tag{5.1}$$

where ρ_{min}, ρ_{max} are the densities below and above the pycnocline, z_p is the location of the inflection point (the center) of the density stratification, whereas d is the thickness of the pycnocline defined as usual (the distance between the vertical locations in the density stratification corresponding to $\rho_{min} + 0.1\Delta\rho$ and $\rho_{max} + 0.9\Delta\rho$ respectively). As in Chapter 3, we fix the densities $\rho_{min} = 0.999$ g/cm^3, $\rho_{max} = 1.022$ g/cm^3 and the total

height of the fluid column $H = 77$ cm and aim to study the two parameter family spanned by the thickness of the pycnocline d and the position of the center of the pycnocline z_p. We are considering only two configurations, that support solitary waves of depression ($z_p = 62$ cm) and elevation ($z_p = 17$ cm) respectively, with varying pycnocline thickness.

As shown in Chapter 3, solitary waves in background density stratifications such as (5.1) are well described (up to relatively thick pycnoclines ≈ 8 cm) by the strongly nonlinear two-layer model Choi & Camassa [7] when optimally choosing for the two-layer system parameters (density in the two layers and the position of the interface). Thus, the two-layer approximation predicts very well integral quantities such as the displacement of the isoline corresponding to the average density and the speed of propagation. However, for studying the spectral stability properties of the flows, we need accurate predictions for the local velocities. In §3.5, we suggested a method for constructing the velocity field for long solitary waves in such stratifications based on the strongly nonlinear model Choi & Camassa [7].

In the subsequent development, we want to assess how accurately this approximation of the velocity field captures the local spectral properties of solitary waves. For this we are investigating the linear stability at the maximum displacement of front solutions in continuous stratification, fronts which are limiting forms for the solitary waves branch. The horizontal velocity and density profiles corresponding to the conjugate state are computed using the method outlined in [31] (briefly described in §3.3.2). The shears associated with the limiting fronts are maximal for the corresponding solitary wave branch, thus we conjecture that if locally unstable, the front is the most unstable (in terms of

associated growth rates) of the entire branch of solitary waves. Conversely, when stable, the entire branch of solitary waves is stable.

First, in order to determine a range of pycnocline widths for which we expect local instability, we monitor the minimum Richardson number across the pycnocline with respect to the 0.25 threshold. As shown in Figure 5.1, the conjugate states are locally stable for pycnocline widths bigger than ≈ 9 cm for $z_p = 62$ cm and than ≈ 8 cm for $z_p = 17$ cm. Note also that the prediction of the two layer model (with optimal choice of parameters and velocity field reconstructed to include the effect of the finite width pycnocline) are reasonably accurate.

Furthermore, the range of pycnocline widths for which local instability can occur is in the range of validity of the optimal two layer approximation described in Chapter 3.

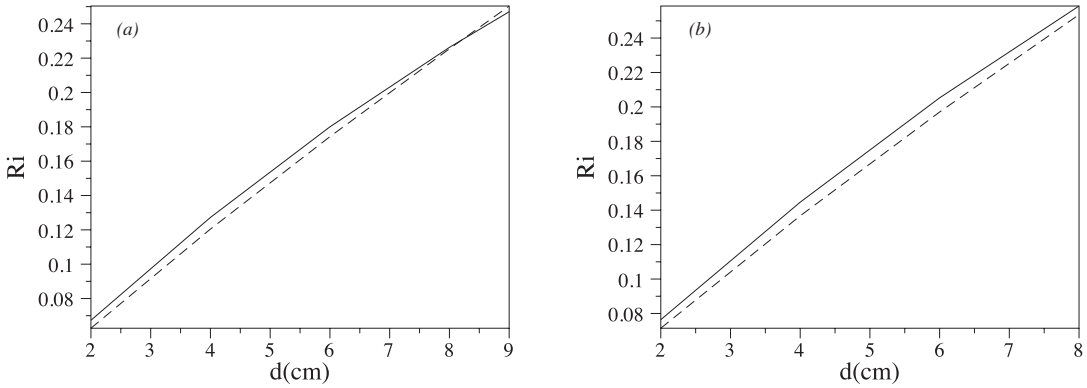

FIGURE 5.1. Continuous - minimum Richardson number at the maximum displacement of front solutions in density stratification (5.1) for (a) $z_p = 62$ cm and (b) $z_p = 17$ cm. Dashed - Richardson number computed based on the optimal two layer approximation, with the shear and density across the pycnocline region approximated with linear profiles.

The spectrum calculations suggest that the necessary condition for existence of unstable normal modes $Ri < 0.25$ is also a sufficient condition – see Figure 5.2, where the growth rates of the unstable local modes are shown for the configuration with $z_p = 62$ cm

and various pycnocline widths. Note that for $d = 9$ cm the minimum Richardson number corresponding to the conjugate state is 0.247024 (very close to the 0.25 threshold) and the associated growth rates are very small. Given that the optimal two-layer approximates very well the minimum Richardson number, one can thus estimate, based on this approximation, a minimum amplitude for which the corresponding solitary wave is locally unstable at the maximum displacement, and also determine the horizontal extent of the area of local instability for solitary waves of amplitudes above this minimal amplitude.

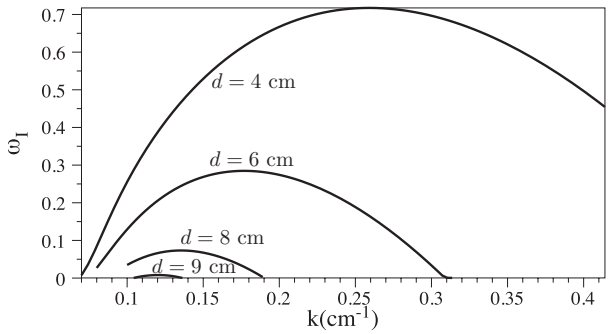

FIGURE 5.2. Growth rates at the maximum displacement of front solutions in density stratification (5.1) for $z_p = 62$ cm and various widths of the pycnocline.

The phase speeds of the unstable modes for the conjugate states are negative in the frame of reference of the front and decreasing with the wave number for both the configuration with $z_p = 62$ cm and $z_p = 17$ cm, as evidenced in Figure 5.3. This obviously implies that the group velocities are also negative. Thus the flow is locally convectively unstable, in the sense defined in §4.3.2. An interesting avenue for future research is to investigate whether the convective character of the shear instability holds for solitary waves of amplitudes smaller than the maximal amplitude defined by the front.

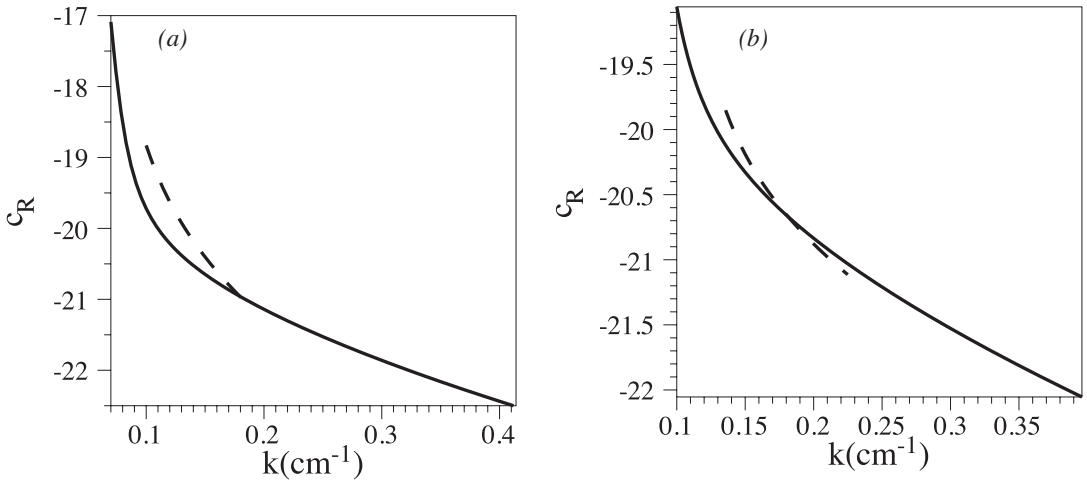

FIGURE 5.3. (a) Phase speed of normal unstable modes for conjugate state corresponding to the background density stratification (5.1) with $z_p = 62$ cm: continuous - $d = 4$ cm and dashed - $d = 6$ cm; (b) same as (a) for $z_p = 17$ cm.

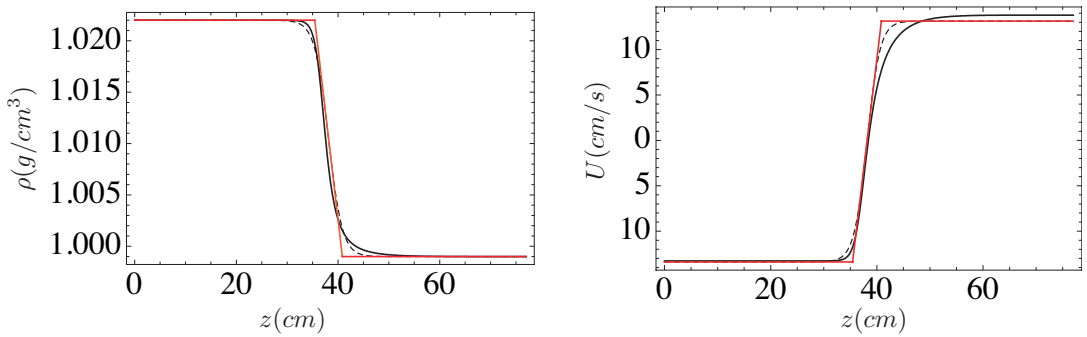

FIGURE 5.4. Black continuous - horizontal velocity and density profiles for conjugate states in density stratification (5.1) with $z_p = 62$ cm and $d = 6$ cm. Red - optimal two layer approximation, Dashed - approximation using tangent hyperbolic profile with thickness $d = 6$ cm.

Finally, we note that by using the optimal two layer prediction and assuming linear density and velocity in the pycnocline region when reconstructing the horizontal velocity profiles, the growth rates of the unstable modes are over-predicted – see Figure 5.5(a). We argue that this is due to the fact that the optimal two-layer approximation, while capturing the maximum slope of the density and velocity profile accurately, does not predict correctly the thickness of the pycnocline. The predicted phase speed is almost constant as opposed to the phase speed corresponding to the conjugate state normal

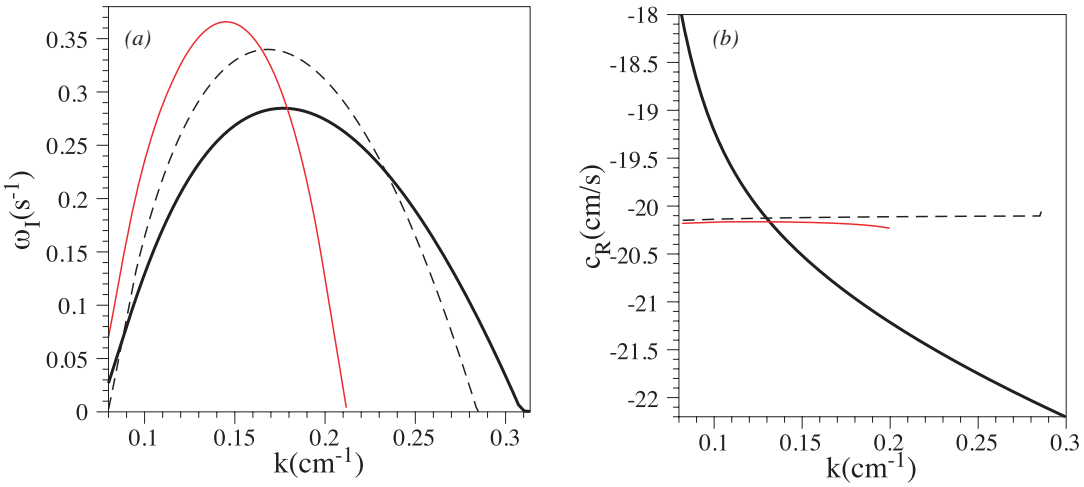

FIGURE 5.5. Black continuous - (a) growth rates, (b) phase speeds of normal unstable modes for the conjugate state corresponding to the background density stratification (5.1) with $z_p = 62$ cm with $d = 6$ cm; Red - spectrum calculation by approximating the density and horizontal velocity in the pycnocline region with a linear profile; Dashed - approximating the density and horizontal velocity with tangent hyperbolic profiles with thickness $d = 6$ cm – see Figure 5.4.

modes – see Figure 5.5(b). This can be attributed to the departure from antisymmetry that the actual shear and density profiles corresponding to the conjugate state exhibit – see Figure 5.4, as opposed to the linear approximation which is antisymmetric.

Thus, in order to be able to use the optimal two layer approximation for studying the unstable spectrum, better approximations for the horizontal velocity structure across the pycnocline are needed. Nonetheless, the optimal two layer predictions for the minimum Richardson number across the pycnocline are excellent. Since the criterion $Ri < 1/4$ for the class of density and shear profiles considered is a good indicator of existence of local unstable spectrum, the optimal two layer can be used to infer an amplitude threshold for locally unstable solitary waves and determine the horizontal extent of the area of local instability.

APPENDIX A: Solitary waves on uniform layer currents

Closed form solutions for solitary waves in the most physically common situation of fluid at rest at infinity can be found for the strongly nonlinear model Choi & Camassa [7]. In this appendix, we want to extend the analysis to the situation of layers of inviscid fluid in relative uniform motion. This setup is admittedly less likely to have physical relevance, as a (constant) velocity jump cannot be sustained indefinitely as $|x| \to \infty$ by real viscous fluids, however this investigation is relevant in the discussion of various classes of periodic waves, where velocity jumps occur locally within the period.

Recently, it came to our attention that solitary wave solutions on relative currents have been studied in laboratory experiments Gavrilov [16] where some comparison with analytic solutions based on a strongly nonlinear two-fluid model Makarenko & Maltseva [35] are reported.

Conditions of existence

In the following we will show that solitary wave solutions exist only for certain combinations of currents in the two layers. Throughout this Appendix, we shall work in the frame of reference of the waves, i.e., that of an observer who sees the wave profile as constant in time. We will thus study the two parameter family of solitary wave solutions on a given reference state (given by the "hardware" parameters of heights and densities of the undisturbed layers $h_1\,, h_2$ and ρ_1, ρ_2, respectively), parametrized by the uniform currents at infinity in each of the two layers $\widehat{u}_1|_\infty\,, \widehat{u}_2|_\infty$. We introduce the non-dimensional parameters $\rho \equiv \rho_1/\rho_2\,, h \equiv h_1/h_2\,,$ and note the relationships between the total height

$H = h_1 + h_2$ and the widths of the layers

$$h_1 = \frac{hH}{1+h} \qquad \text{and} \qquad h_2 = \frac{H}{1+h}\,. \tag{A.1}$$

First, we determine the quadrature form for arbitrary currents $\widehat{u}_1|_\infty$, $\widehat{u}_2|_\infty$ and subsequently determine the conditions which these currents must satisfy for solitary wave solutions to exist. We can integrate directly the ordinary differential equations corresponding to mass conservation (2.8), (2.9) and the two second order differential equations (2.14) and (2.20), by using the boundary conditions $\zeta|_{\pm\infty} = 0, \zeta_X|_{\pm\infty} = 0$, $\zeta_{XX}|_{\pm\infty} = 0$, respectively. We obtain the four integration constants in the quadrature as

$$C_1 = h_1\widehat{u}_1|_\infty\,, \tag{A.2}$$

$$C_2 = h_2\widehat{u}_2|_\infty\,, \tag{A.3}$$

$$C_3 = \frac{1}{2}\frac{\rho_1 C_1^2}{{h_1}^2} - \frac{1}{2}\frac{\rho_2 C_2^2}{h_2^2}\,, \tag{A.4}$$

$$C_4 = \frac{\rho_1 C_1^2}{h_1} + \frac{\rho_2 C_2^2}{h_2}\left(1 - \frac{H}{2h_2}\right)\,. \tag{A.5}$$

Notice that the quadrature coefficients depend exclusively on the squares of the currents in the wave frame $\widehat{u}_1^2|_\infty$ and $\widehat{u}_2^2|_\infty$, so for ease of notation we will use

$$U_1 \equiv \widehat{u}_1^2|_\infty\,, \qquad U_2 \equiv \widehat{u}_2^2|_\infty\,, \tag{A.6}$$

and suppress the dependence on these parameters as functional arguments, whenever this can be done safely without generating confusion.

The quadrature becomes

$$\zeta_X^2 = 3\gamma \frac{\zeta^2 \left[\zeta^2 + q_1(U_1, U_2)\zeta + q_2(U_1, U_2)\right]}{\rho_1 h_1^2 U_1 \eta_2 + \rho_2 h_2^2 U_2 \eta_1}\,, \tag{A.7}$$

where

$$q_1(U_1, U_2) = \frac{1-h}{1+h} H + \frac{1}{1-\rho} \frac{\rho U_1 - U_2}{g}\,, \tag{A.8}$$

$$q_2(U_1, U_2) = -\frac{h}{1+h} H^2 + \frac{1}{(1-\rho)(1+h)} \frac{\rho U_1 + h U_2}{g} H\,. \tag{A.9}$$

First, we observe that the root of the denominator in (A.7)

$$a_*(U_1, U_2) = \frac{h}{1+h} \frac{\rho h U_1 + U_2}{U_2 - \rho h^2 U_1} H\,, \tag{A.10}$$

is, in general, outside the physical domain except the limiting cases $U_1 = 0$ or $U_2 = 0$, when a_* equals h_1 or $-h_2$ respectively. The roots of the quadratic $\zeta^2 + q_1(U_1, U_2)\zeta + q_2(U_1, U_2)$ determine whether a solitary wave solution exists: the discriminant has to be positive

$$\Delta(U_1, U_2) \equiv q_1(U_1, U_2)^2 - 4 q_2(U_1, U_2) > 0\,, \tag{A.11}$$

and the roots

$$a_-(U_1, U_2) \equiv -\frac{q_1(U_1, U_2)}{2} - \frac{\sqrt{\Delta(U_1, U_2)}}{2}\,, \tag{A.12}$$

and

$$a_+(U_1, U_2) \equiv -\frac{q_1(U_1, U_2)}{2} + \frac{\sqrt{\Delta(U_1, U_2)}}{2}\,, \tag{A.13}$$

must have the same sign, since they cannot straddle the origin when the quartic has positive coefficient for the fourth power ζ^4 – see Figure A.1 for possible configurations. For the two roots to be of the same sign, we must have

$$q_2(U_1, U_2) > 0\,. \tag{A.14}$$

If these conditions are satisfied, the amplitude given by

$$a(U_1, U_2) = a_+(U_1, U_2) \qquad \text{if} \qquad a_- < a_+ < 0$$

or

$$a(U_1, U_2) = a_-(U_1, U_2) \qquad \text{if} \qquad 0 < a_- < a_+\,,$$

needs to be in the physical domain range

$$a(U_1, U_2) \in (-h_2, h_1)\,, \tag{A.15}$$

which imposes another constraint on the choice of parameters U_1 and U_2.

Next, we study the domain of existence of solitary waves in the quadrant for positive U_1 and U_2 by looking at the behavior of the roots a_-, a_+ on lines

$$U_2(\kappa) = \kappa U_1\,, \qquad \text{with} \qquad \kappa \in [0, \infty)\,.$$

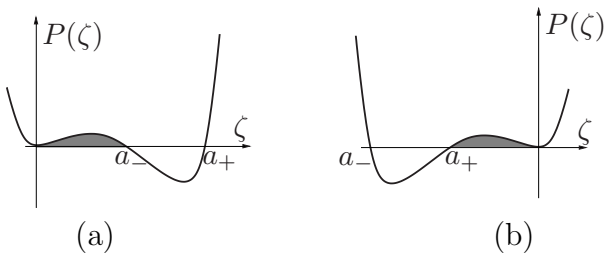

FIGURE A.1. Possible configurations for root positions of the quartic numerator of the quadrature (A.7).

The locus of the roots of the quadratic polynomial $\zeta^2 + q_1(U_1, \kappa U_1)\zeta + q_2(U_1, \kappa U_1)$ is a hyperbola in the semi-plane (U_1, ζ) given by

$$\zeta^2 + \frac{\rho - \kappa}{g(1-\rho)} U_1 \zeta + \frac{H(h\kappa + \rho)}{g(1-\rho)(1+h)} U_1 + \frac{H(1-h)}{1+h}\zeta - \frac{H^2}{(1+h)^2} = 0\,,$$

which degenerates into a parabola for $\kappa = \rho$ – see Figure A.2. The hyperbola has two branches, with vertices corresponding to vanishing of the discriminant Δ. Thus, to the merging of the two roots $a_\pm$ into a nonzero double root, gives rise to a front solution, i.e., a solution whose profile $\zeta(X)$ joins the asymptotic level as $|X| \to \infty$ of $\zeta = 0$ and $\zeta = a_+ = a_-$ (sometimes referred to as conjugate states in internal wave literature). The two vertices are

$$(U_1^{(1)}(\kappa), \zeta^{(1)}(\kappa)) = \left((1-\rho)\frac{(\sqrt{\rho} - \sqrt{\kappa})^2}{(\kappa - \rho)^2} gH\,, \frac{h\sqrt{\kappa} - \sqrt{\rho}}{(1+h)(\sqrt{\kappa} + \sqrt{\rho})} H \right)\,, \tag{A.16}$$

$$(U_1^{(2)}(\kappa), \zeta^{(2)}(\kappa)) = \left((1-\rho)\frac{(\sqrt{\rho} + \sqrt{\kappa})^2}{(\kappa - \rho)^2} gH\,, \frac{h\sqrt{\kappa} + \sqrt{\rho}}{(1+h)(\sqrt{\kappa} - \sqrt{\rho})} H \right)\,, \tag{A.17}$$

when $\kappa \neq \rho$. When $\kappa = \rho$ the vertex of the corresponding parabola is given by

$$(U_1^{(1)}(\kappa), \zeta^{(1)}(\kappa)) = \left(\frac{(1-\rho)}{4\rho} gH, \frac{(h-1)}{2(1+h)} H \right)\,.$$

We now show that only one of the hyperbola branches has a portion located inside the physical domain which corresponds to solitary wave solutions. Indeed,

$$\zeta^{(2)}(\kappa) > h_1 \qquad \text{for} \qquad \kappa > \rho\,,$$

and

$$\zeta^{(2)}(\kappa) < -h_2 \qquad \text{for} \qquad \kappa < \rho\,,$$

respectively.

The (transverse) axis of this hyperbola is the line

$$q_1(U_1, \kappa U_1) = 0\,,$$

while one asymptote is a horizontal line that goes through the center of the hyperbola. whose height is at

$$\zeta_c(\kappa) = -\frac{1}{D}\begin{vmatrix} 0 & \dfrac{H}{2g}\dfrac{h\kappa+\rho}{(1-\rho)(1+h)} \\ \dfrac{\rho-\kappa}{2g(1-\rho)} & \dfrac{H(h-1)}{2(1+h)} \end{vmatrix},$$

with

$$D = \begin{vmatrix} 0 & \dfrac{\rho-\kappa}{2g(1-\rho)} \\ \dfrac{\rho-\kappa}{2g(1-\rho)} & 1 \end{vmatrix},$$

hence

$$\zeta_c(\kappa) = \frac{H}{1+h}\frac{h\kappa+\rho}{\kappa-\rho}\,.$$

Thus, the center will be outside of the physical domain, since $\zeta_c(\kappa) > h_1$ for $\kappa > \rho$, or $\zeta_c(\kappa) < -h_2$ for $\kappa < \rho$, which implies the whole branch corresponding to the second

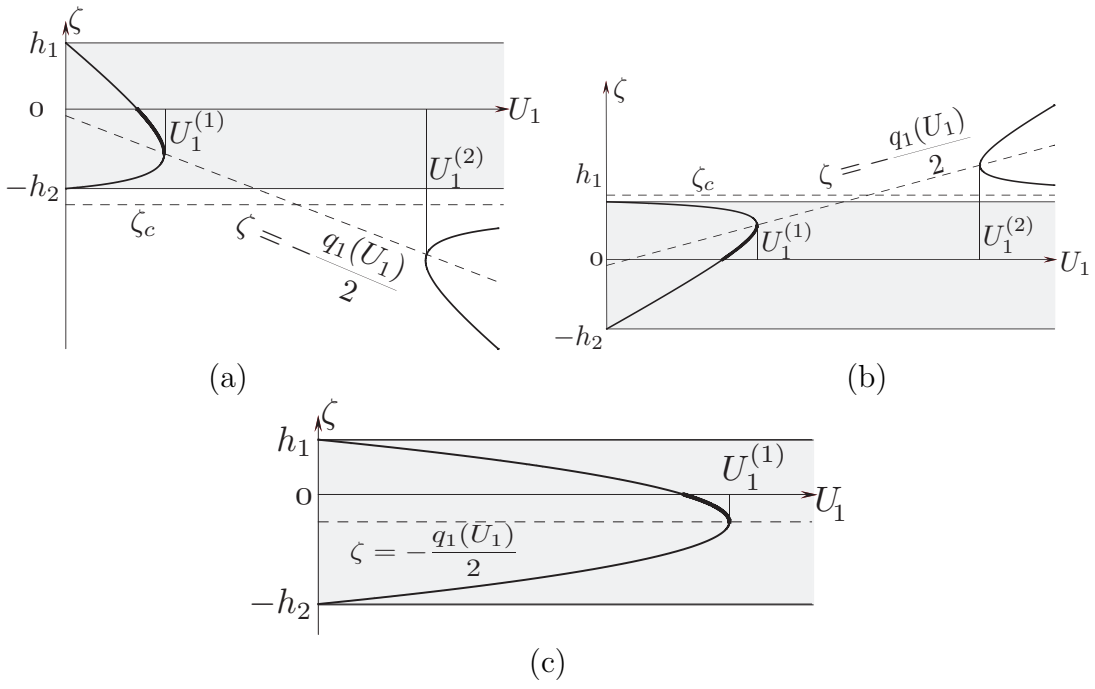

FIGURE A.2. Roots of the quadratic $\zeta^2 + q_1\zeta + q_2$ for (a) $\kappa < \rho$, (b) $\kappa > \rho$ and (c) $\kappa = \rho$. Thicker segments mark the amplitude of solitary wave solutions.

vertex (A.17) is. We remark that this second branch of solutions could still be useful for constructing weak solutions of the quadrature, which could then be interpreted as gravity currents. Such a study is worth pursuing but lies outside of the main focus of this paper and will be left for future work.

The first branch has a portion in the physical domain, since $a_+(0,0) = h_1$, $a_-(0,0) = -h_2$ and $\zeta^{(1)}(\kappa) \in (-h_2, h_1)$. However, only a segment of this branch corresponds to solitary wave solutions, namely the segment for which the condition

$$q_2(U_1, \kappa U_1) \geq 0\,,$$

holds. We infer that solitary wave solutions exist for

$$U_1 \in [U_{1min}(\kappa)\,, U_{1max}(\kappa)]\,,$$

with $U_{1min}(\kappa)$ root of equation $q_2(U_1, \kappa U_1) = 0\,,$

$$U_{1min}(\kappa) = \frac{(1-\rho)h}{(1+h)(\rho+h\kappa)} gH\,, \tag{A.18}$$

and

$$U_{1max}(\kappa) = U_1^{(1)}(\kappa) = (1-\rho)\frac{(\sqrt{\rho}-\sqrt{\kappa})^2}{(\kappa-\rho)^2} gH\,. \tag{A.19}$$

The amplitudes of the solitary waves along the line $U_2 = \kappa U_1$ for $U_1 \in [U_{1min}(\kappa)$, $U_{1max}(\kappa)]$ vary between zero and

$$a_{max}(\kappa) = \zeta^{(1)}(\kappa) = \frac{h\sqrt{\kappa}-\sqrt{\rho}}{(1+h)(\sqrt{\kappa}+\sqrt{\rho})} H\,, \tag{A.20}$$

having the sign given by the sign of $a_{max}(\kappa)$. We thus have

$$a(U_1, \kappa U_1) = \frac{-q_1(U_1, \kappa U_1) - \mathrm{sgn}(h\sqrt{\kappa}-\sqrt{\rho})\sqrt{\Delta(U_1, \kappa U_1)}}{2}\,. \tag{A.21}$$

We remark that in the limiting case $\kappa = 0$ (which implies $U_2 = 0$) the locus of the roots becomes a *degenerate hyperbola*, i.e., two straight crossing lines – see Figure A.4. The intersection point of the two lines is given by

$$(U_1^{(1)}, \zeta^{(1)}) = (U_1^{(2)}, \zeta^{(2)}) = ((1/\rho - 1)gH\,, -h_2)\,.$$

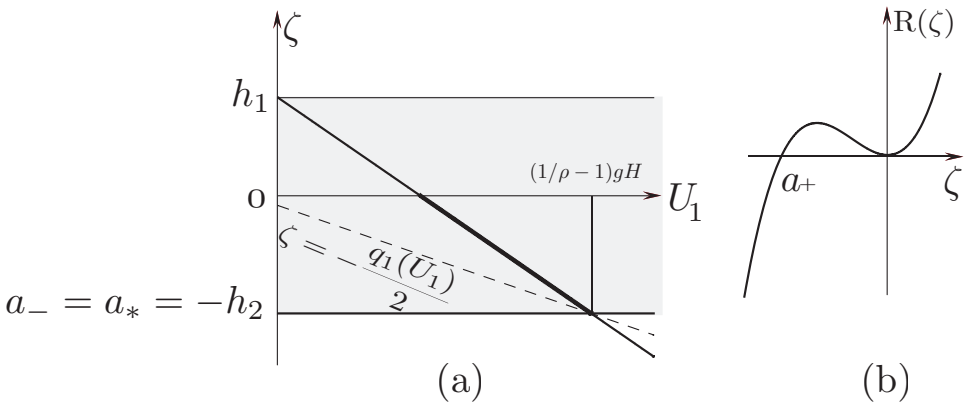

FIGURE A.3. (a) Roots of the quadratic $\zeta^2 + q_1\zeta + q_2$ for $U_2 = 0$. (b) The potential becomes a cubic polynomial since $a_- = a_*$.

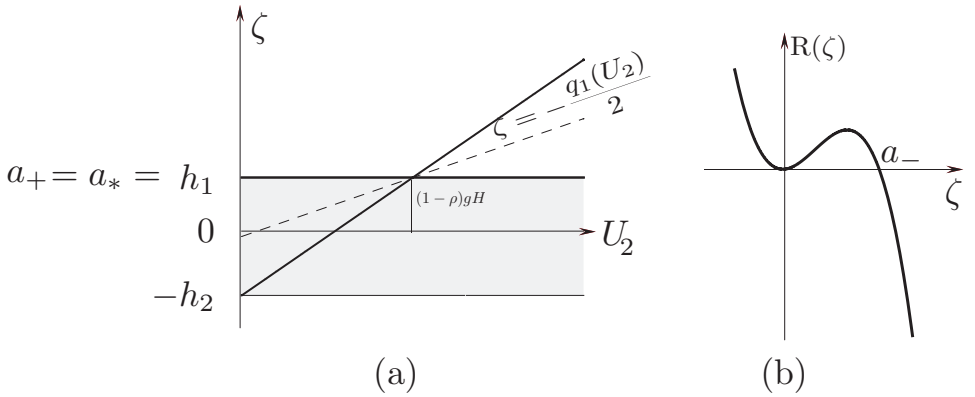

FIGURE A.4. (a) Roots of the quadratic $\zeta^2 + q_1\zeta + q_2$ for $U_1 = 0$. (b) The potential becomes a cubic polynomial since $a_+ = a_*$.

Note that for this degenerate case the whole segment including end points is populated by true solitary waves (not limiting to fronts), since the root of the denominator (A.10) becomes $a_* = a_- = -h_2$, so that the quadrature potential collapses to a cubic. Hence the solitary wave of maximum amplitude in this case is not a front, rather a solitary wave whose maximum depression (trough) touches the bottom wall. Conversely, when $\kappa \to \infty$ (which implies $U_1 = 0$) the locus of the roots is the *degenerate hyperbola*

$$\zeta^2 + \frac{1}{g(1-\rho)}U_2\zeta + \frac{Hh}{g(1-\rho)(1+h)}U_2 + \frac{H(h-1)}{1+h}\zeta - \frac{H^2h}{(1+h)^2} = 0$$

with the intersection point located at

$$(U_2^{(1)}, \zeta^{(1)}) = (U_2^{(2)}, \zeta^{(2)}) = ((1-\rho)gH\,, h_1)\ .$$

The root of the denominator becomes in this instance $a_* = a_+ = h_1$ hence the solitary wave of maximum amplitude is a solitary wave with the peak touching the top wall.

Domain of existence

We now can construct the domain in the parameter space $(U_1\,, U_2)$ for which traveling wave solutions exist – see Figure A.5. The curve $\Delta(U_1, U_2) = 0$ is a parabola in the plane $(U_1\,, U_2)$ tangent to the axis U_2, U_1 at the points

$$A = (0, (1-\rho)gH) \qquad \text{and} \quad B = ((1/\rho - 1)\, gH, 0)\ ,$$

and corresponds to front-like solutions. The domain in the plane (U_1, U_2) to the left of the parabola (so that $\Delta(U_1, U_2) > 0$ and roots are real) contains the origin. At the right of the parabola $\Delta(U_1, U_2)$ the roots are complex. Note that the curve $\Delta(U_1, U_2) = 0$ does not have explicit dependence on the ratio of the heights. We can determine an explicit formula for this branch

$$U_2(U_1) = \left(\sqrt{1-\rho}\sqrt{gH} + \sqrt{\rho}\sqrt{U_1}\right)^2\,, \qquad U_1 \in (0, (1/\rho - 1)gH)\,. \tag{A.22}$$

The amplitude of the corresponding fronts, by equation (A.16), is

$$a_f(U_1) = h_1 - \sqrt{\frac{\rho}{1-\rho}}\sqrt{\frac{U_1}{gH}}H\,. \tag{A.23}$$

The line $q_2(U_1, U_2) = 0$, which corresponds to the limiting amplitude zero, is tangent to the parabola at the point

$$C = \left(\frac{1-\rho}{\rho} \left(\frac{h}{1+h} \right)^2 gH \, , (1-\rho) \left(\frac{1}{h+1} \right)^2 gH \right) ,$$

and should correspond to the critical speed determined by the parent Euler system for infinitesimal amplitude waves on relative layer currents. The region in the (U_1, U_2) plane for which the roots have the same sign is delimited by this line, and does not contain the origin. We can conclude that the domain of existence for solitary waves is the domain in the plane (U_1, U_2) delimited by the arc of parabola $\widehat{ACB}$, the line $q_2(U_1, U_2) = 0$ and the two axes. The line $q_1(U_1, U_2) = 0$, which corresponds to roots equal and of opposite sign in the quadrature, intersects $q_2(U_1, U_2) = 0$ through the point C. This line divides the domain of existence in two sub domains. For $q_1 > 0$ we have $a_- < a_+ < 0$, which corresponds to solitary waves of depression, with amplitude given by a_+, whereas for $q_1 < 0$ we have $0 < a_- < a_+$, which corresponds to solitary waves of elevation, with amplitude given by a_-– see Figure A.1.

We note that when $\rho h^2 U_1 - U_2 = 0$ the denominator of the quadrature (A.7) degenerates into a constant. This equation corresponds to a line in the plane (U_1, U_2) on which the solitary wave solutions are given by elementary functions (combination of exponentials) rather than elliptic functions.

In Table 1 we summarize the analytical formulas for the wave shape and the effective wavelength for solitary wave solutions, for all possible relationships between the non-dimensional parameters κ, h and ρ. We also emphasize the afore-mentioned degeneracies of the elliptic functional form of solutions to elementary functions along the line $\rho h^2 U_1 -$

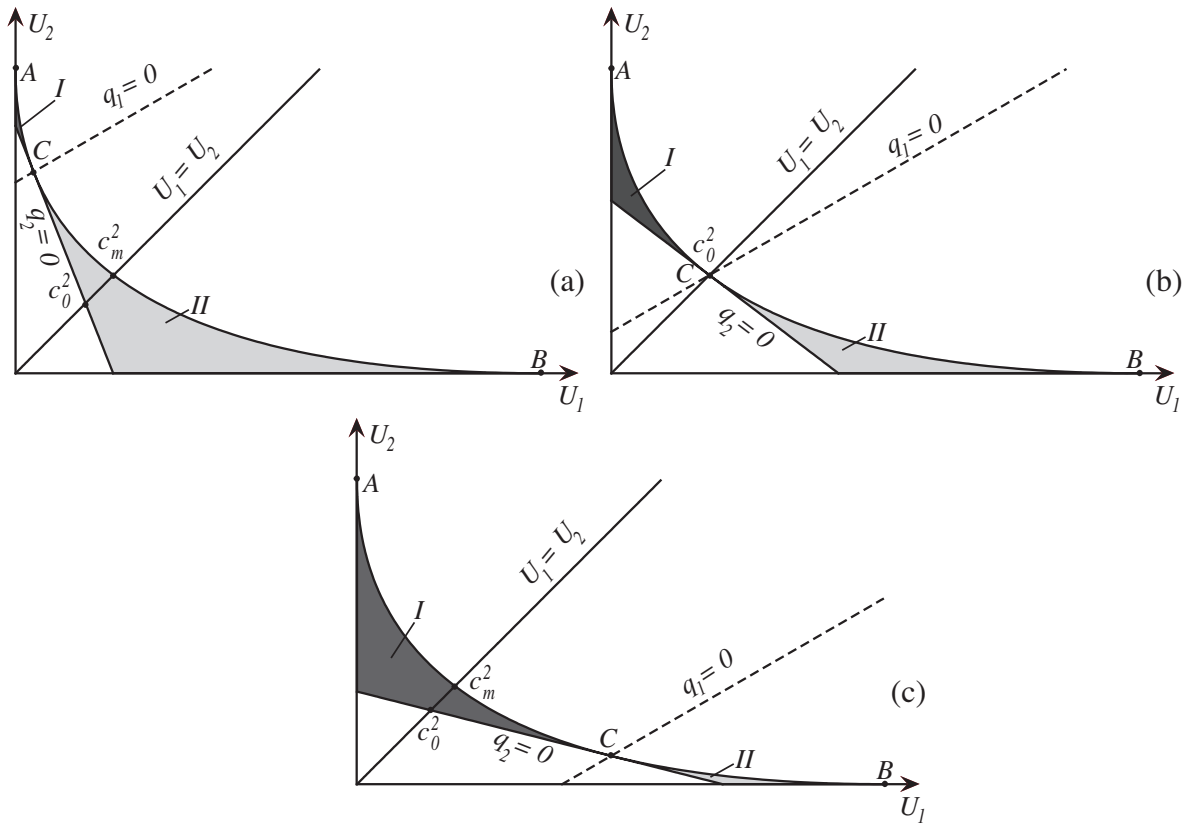

FIGURE A.5. Domain of existence for solitary waves on uniform current for (a) $h < \sqrt{\rho}$, (b) $h = \sqrt{\rho}$, (c) $h > \sqrt{\rho}$. Region I corresponds to solitary waves of elevation ($q_1 < 0$). Region II corresponds to solitary waves of depression ($q_1 > 0$).

$U_2 = 0$ (cases (v) and (vi)) and when either U_1 or U_2 is zero (case (vii)). In Table 2 we present closed form expressions for the wave shape of the front solutions.

Relation to solutions of full Euler two-layer system

In the neighborhood of the points A and B, on the front branch, the height of one of the two layers becomes infinitesimally small. Thus, this regime should rightly belong to the deep water configuration setup, for which a different asymptotic scaling from the shallow water approximation becomes necessary. We can in fact assess the validity of

	Case	$X(\zeta)$/ Effective wavelength
(i)	$\sqrt{\kappa} < \min(h\sqrt{\rho}, \frac{\sqrt{\rho}}{h})$,	$\mu X = \frac{2}{\sqrt{a_+ - a_*}}\left[\frac{a_*(a_+ - a_-)}{a_- a_+}\Pi(\phi, \alpha^2, k) + \frac{a_- - a_*}{a_+}F(\phi, k)\right]$,
	$a_* < a_- < a_+ < 0$.	$\lambda_I = \frac{2}{\mu a_+}\left[\sqrt{a_+ - a_*}(F(\delta, k) - E(\delta, k)) + \sqrt{\frac{a_+\lvert a_*\rvert}{a_-}}\right]$,
		$k^2 = \frac{a_- - a_*}{a_+ - a_*}$, $\sin\phi = \sqrt{\frac{a_+ - \zeta}{a_- - \zeta}}$, $\sin\delta = \sqrt{\frac{a_+}{a_-}}$.
(ii)	$h\sqrt{\rho} < \sqrt{\kappa} < \frac{\sqrt{\rho}}{h}$,	$\mu X = \frac{2}{\sqrt{a_* - a_-}}\left[\frac{a_*(a_+ - a_-)}{a_- a_+}\Pi(\phi, \alpha^2, k) + \frac{a_*(a_- - a_*)}{a_- a_+}F(\phi, k)\right]$,
	$a_- < a_+ < 0 < a_*$.	$\lambda_I = \frac{2}{\mu a_+}\left[\sqrt{a_* - a_-}(F(\delta, k) - E(\delta, k)) + \sqrt{\frac{a_+ a_*}{a_-}}\right]$,
		$k^2 = \frac{a_+ - a_*}{a_- - a_*}$, $\sin\phi = \sqrt{\frac{(a_* - a_-)(a_+ - \zeta)}{(a_* - a_+))(a_- - \zeta)}}$, $\sin\delta = \sqrt{\frac{a_+(a_* - a_-)}{a_-(a_* - a_+)}}$.
(iii)	$\frac{\sqrt{\rho}}{h} < \sqrt{\kappa} < h\sqrt{\rho}$,	$\mu X = \frac{2}{\sqrt{a_+ - a_*}}\left[\frac{a_*(a_- - a_+)}{a_- a_+}\Pi(\phi, \alpha^2, k) + \frac{a_+ - a_*}{a_+}F(\phi, k)\right]$,
	$a_* < 0 < a_- < a_+$.	$\lambda_I = \frac{2}{\mu a_-}\left[\sqrt{a_+ - a_*}(F(\delta, k) - E(\delta, k)) + \sqrt{\frac{a_-\lvert a_*\rvert}{a_+}}\right]$,
		$k^2 = \frac{a_- - a_*}{a_+ - a_*}$, $\sin\phi = \sqrt{\frac{(a_+ - a_*)(a_- - \zeta)}{(a_- - a_*)(a_+ - \zeta)}}$, $\sin\delta = \sqrt{\frac{a_-(a_+ - a_*)}{a_+(a_- - a_*)}}$.
(iv)	$\sqrt{\kappa} > \max(h\sqrt{\rho}, \frac{\sqrt{\rho}}{h})$,	$\mu X = \frac{2}{\sqrt{a_* - a_-}}\left[\frac{a_*(a_- - a_+)}{a_- a_+}\Pi(\phi, \alpha^2, k) + \frac{a_+ - a_*}{a_+}F(\phi, k)\right]$,
	$0 < a_- < a_+ < a_*$.	$\lambda_I = \frac{2}{\mu a_-}\left[\sqrt{a_* - a_-}(F(\delta, k) - E(\delta, k)) + \sqrt{\frac{a_* a_-}{a_+}}\right]$,
		$k^2 = \frac{a_+ - a_*}{a_- - a_*}$, $\sin\phi = \sqrt{\frac{a_- - \zeta}{a_+ - \zeta}}$, $\sin\delta = \sqrt{\frac{a_-}{a_+}}$.
(v)	$\sqrt{\kappa} = h\sqrt{\rho} < \frac{\sqrt{\rho}}{h}$,	$\tau X = \frac{1}{\sqrt{a_- a_+}}\log\left[\frac{(a_- - a_+)\zeta}{\left(\sqrt{a_-(a_+ - \zeta)} + \sqrt{a_+(a_- - \zeta)}\right)^2}\right]$,
	$a_- < a_+ < 0, a_* = +\infty$.	$\lambda_I = \frac{2}{\tau a_+}\log\frac{\sqrt{\lvert a_+\rvert} - \sqrt{\lvert a_-\rvert}}{\sqrt{\lvert a_+\rvert} - \sqrt{\lvert a_-\rvert}}$.
(vi)	$\sqrt{\kappa} = h\sqrt{\rho} > \frac{\sqrt{\rho}}{h}$,	$\tau X = \frac{2}{a_- a_+}\tanh^{-1}\left[\frac{a_+(a_- - \zeta)}{a_-(a_+ - \zeta)}\right]$,
	$0 < a_- < a_+, a_* = -\infty$.	$\lambda_I = \frac{2}{\tau a_-}\tanh^{-1}\sqrt{\frac{a_-}{a_+}}$.
(vii)	$a_* = a_- \le a \equiv a_+ < 0$,	$\mu X = \frac{1}{\sqrt{\lvert a\rvert}}\left[\log\frac{a}{\zeta} + 2\log\left(1 + \sqrt{1 - \frac{\zeta}{a}}\right)\right]$, $\lambda_I = \frac{2}{\mu\sqrt{\lvert a\rvert}}$.
	$0 < a \equiv a_- \le a_+ = a_*$.	

TABLE 1. Formulas for wave shapes and the effective wavelength of solitary wave solutions on uniform currents. (i) - (vi) The solutions are parametrized by U_1 and κ with $U_2 = \kappa U_1$. The roots a_-, a_+, a_* are given by relations (A.12), (A.13) and (A.10), respectively.
$\mu^2 = \frac{3g(1-\rho)}{h_2^2 U_1\lvert\rho h^2 - \kappa\rvert}$, $\tau^2 = \frac{3g(1-\rho)}{h_1 h_2^2 U_1(\rho + \kappa h)}$. F, E, Π are elliptic integrals of first, second and third kind. (vii) The solutions correspond to the cases $U_1 = 0$ and $U_2 = 0$, respectively.

each solitary wave solution in the domain of existence (see in particular Figure A.5), by

	Case	$X(\zeta)$
(i)	$\sqrt{\kappa} < \min(h\sqrt{\rho}, \frac{\sqrt{\rho}}{h})$, $a_* < a < 0$.	$\mu X = \frac{1}{a}\left[-X_f(\zeta, a, a_*) + X_f(\frac{a}{2}, a, a_*)]\right]$.
(ii)	$h\sqrt{\rho} < \sqrt{\kappa} < \frac{\sqrt{\rho}}{h}$, $a < 0 < a_*$.	$\mu X = \frac{1}{a}\left[-X_f(-\zeta, -a, -a_*) + X_f(-\frac{a}{2}, -a, -a_*)]\right]$.
(iii)	$\frac{\sqrt{\rho}}{h} < \sqrt{\kappa} < h\sqrt{\rho}$ $a_* < 0 < a$.	$\mu X = \frac{1}{a}\left[X_f(\zeta, a, a_*) - X_f(\frac{a}{2}, a, a_*)]\right]$.
(iv)	$\sqrt{\kappa} > \max(h\sqrt{\rho}, \frac{\sqrt{\rho}}{h})$, $0 < a < a_*$.	$\mu X = \frac{1}{a}\left[X_f(-\zeta, -a, -a_*) - X_f(-\frac{a}{2}, -a, -a_*)]\right]$.
(v)	$\sqrt{\kappa} = h\sqrt{\rho} < \frac{\sqrt{\rho}}{h}$, $a < 0$, $a_* = +\infty$, $\sqrt{\kappa} = h\sqrt{\rho} > \frac{\sqrt{\rho}}{h}$, $0 < a$, $a_* = -\infty$.	$\tau X = \frac{1}{a}\log\frac{\zeta}{a-\zeta}$.

TABLE 2. Formulas for wave shapes of front solutions on uniform currents. The solutions are parametrized by κ. $U_2 = \kappa U_1$ with U_1 given by (A.19). The roots $a = a_- = a_+$ and a_* are given by the relations (A.20) and (A.10), respectively. $\mu^2 = \frac{3g(1-\rho)}{|\rho h_1^2 - \kappa h_2^2|}$, $\tau^2 = \frac{3g(1-\rho)}{h_1 h_2^2 U_1(\rho+\kappa h)}$, $X_f(x, y, z) = (y - z)^{1/2}\log\left[\frac{(y-z)^{1/2}+(x-z)^{1/2}}{(y-z)^{1/2}-(x-z)^{1/2}}\right] - (-z)^{1/2}\log\left[\frac{(x-z)^{1/2}+(-z)^{1/2}}{(x-z)^{1/2}-(-z)^{1/2}}\right]$.

computing the associated long wave parameter based on maximum slope – see relation (2.84) (or on effective wavelength – see relation (2.83)).

The maximum slope of the wave profile is achieved at the inflection point ζ_I, which thus satisfies the equation

$$\zeta_{XX}(\zeta_I) = 0\,. \tag{A.24}$$

The second derivative ζ_{XX} can be computed by differentiating relation (A.7) while making use of the chain rule. Let $R(\zeta)$ denote the rational function at the LHS of (A.7). We

obtain

$$\zeta_{XX}(\zeta) = \frac{1}{2}\frac{\partial R}{\partial \zeta}\,. \tag{A.25}$$

With the second derivative ζ_{XX} now defined by the RHS of (A.25), equation (A.24) becomes a quadratic equation in the case of fronts or cubic equation in the case of solitary waves, respectively, with ζ_I being its root in the interval $(0, a)$. The maximum slope can thus be determined by

$$\max \zeta_X = \sqrt{R(\zeta_I)}\,. \tag{A.26}$$

The boundary of the domain of existence consisting of fronts represents in fact actual front solutions of Euler equations. [15] have derived relationships between speed and amplitude for front solutions of Euler equations (no assumption of constant currents at infinity) by using conservation of mass, of horizontal momentum and the continuity in pressure at the interface (which in fact is equivalent to the conservation of energy).

Below, following [15], we derive the current-amplitude relations for front (conjugate states) solutions for the Euler system, and show that we obtain the same relations as the ones derived from the strongly nonlinear model.

We fix the heights of the layers at $+\infty$ be h_1, h_2 and the densities in each layer. Let the currents at infinity in the wave frame be denoted by $\widehat{u}_1|_\infty$, $\widehat{u}_2|_\infty$ and $\widehat{u}_1|_{-\infty}$, $\widehat{u}_2|_{-\infty}$ at $\pm\infty$, respectively. We are looking for front solutions of amplitude a, that is, the heights at $-\infty$ are $h_1 - a$, $h_2 + a$. Therefore, the five quantities $\widehat{u}_1|_\infty$, $\widehat{u}_2|_\infty$, $\widehat{u}_1|_{-\infty}$, and $\widehat{u}_2|_{-\infty}$ and a are the free parameters. We have four constraints: mass conservation in each layer,

continuity of pressure at the interface and horizontal momentum conservation. Thus the fronts constitute a one parameter family of solutions. Mass conservation implies

$$(h_1 - a)\widehat{u}_1|_{-\infty} = h_1\widehat{u}_1|_{\infty}\,,$$

$$(h_2 + a)\widehat{u}_2|_{-\infty} = h_2\widehat{u}_2|_{\infty}\,.$$

We can thus express the currents in the wave frame at $-\infty$ in terms of the currents at $+\infty$,

$$\widehat{u}_1|_{-\infty} = \frac{h_1}{h_1 - a}\widehat{u}_1|_{\infty}\,, \tag{A.27}$$

$$\widehat{u}_2|_{-\infty} = \frac{h_2}{h_2 + a}\widehat{u}_2|_{\infty}\,. \tag{A.28}$$

The Bernoulli law (conservation of energy) in layer k is

$$R_k = p_k + \rho_k((\widehat{u}_k)^2 + (\widehat{v}_k)^2)/2 + \rho_k g z \equiv const\,. \tag{A.29}$$

We apply this at the interface in each layer to obtain, using again the notation defined by (A.6) modified in an obvious manner,

$$P_I^- + \frac{\rho_1 U_1^-}{2} + \rho_1 g a = P_I^+ + \frac{\rho_1 U_1^+}{2}\,, \tag{A.30}$$

$$P_I^- + \frac{\rho_2 U_2^-}{2} + \rho_2 g a = P_I^+ + \frac{\rho_2 U_2^+}{2}\,, \tag{A.31}$$

where P_I^- and P_I^+ are the pressures at the interface at $\pm\infty$, respectively. By substracting these two relations we have

$$U_2^- - U_2^+ + \rho(U_1^+ - U_1^-) + 2\,a\,g(1-\rho) = 0\,, \tag{A.32}$$

which by using (A.27)–(A.28) can be written as

$$\frac{\rho(a-2h_1)}{(h_1-a)^2}U_1^+ - \frac{(a+2h_2)}{(h_2+a)^2}U_2^+ + 2g(1-\rho) = 0\,. \tag{A.33}$$

For the conservation of the horizontal momentum we use the invariance of the "flow force" (horizontal momentum flux)

$$S = \int_{-h_2}^{h_1} (p + \rho\widehat{u}^2)dz\,. \tag{A.34}$$

At $-\infty$ the flow force is

$$S^- = \int_{-h_2}^{a} (p_2 + \rho_2 U_2^-)dz + \int_{a}^{h_1} (p_1 + \rho_1 U_1^-)dz\,. \tag{A.35}$$

By using the Bernoulli law (A.29) and again equations (A.27)–(A.28) we can write the above equation as

$$\begin{aligned} S^- &= \int_{-h_2}^{a} \left(R_2 - \rho_2 g z + \frac{\rho_2 U_2^-}{2}\right) dz + \int_{a}^{h_1} \left(R_1 - \rho_1 g z + \frac{\rho_1 U_1^-}{2}\right) dz \\ &= R_2(a+h_2) + R_1(h_1-a) + \frac{(\rho_1-\rho_2)ga^2}{2} + \frac{\rho_2 g h_2^2}{2} - \\ &- \frac{\rho_1 g h_1^2}{2} + \frac{\rho_1 U_1^+ h_1^2}{2(h_1-a)} + \frac{\rho_2 U_2^+ h_2^2}{2(h_2+a)}\,. \end{aligned} \tag{A.36}$$

The flow force at $+\infty$ is

$$S^+ = R_2 h_2 + R_1 h_1 + \frac{\rho_2 g h_2^2}{2} + \frac{\rho_1 g h_1^2}{2} + \frac{\rho_1 U_1^+ h_1}{2} + \frac{\rho_2 U_2^+ h_2}{2}\,. \tag{A.37}$$

The horizontal momentum conservation implies $S^- = S^+$ hence from (A.36) and (A.37) we obtain

$$R_2 - R_1 + \frac{(\rho_1 - \rho_2) g a}{2} + \frac{\rho_1 h_1}{2(h_1 - a)} U_1^+ - \frac{\rho_2 h_2}{2(h_2 + a)} U_2^+ = 0\,. \tag{A.38}$$

Continuity in pressure at the interface at $+\infty$ implies

$$R_2 - R_1 = \frac{\rho_2 U_2^+}{2} - \frac{\rho_1 U_1^+}{2}\,,$$

hence we can write (A.38) as

$$\frac{\rho U_1^+}{h_1 - a} + \frac{U_2^+}{h_2 + a} + (\rho - 1) g = 0 \tag{A.39}$$

We have obtained a system of two equations (A.33) and (A.39) for three unknowns $U_1^+\,, U_2^+$ and a. Solving for U_1^+ and U_2^+ as functions of a yields

$$U_1^+ = \frac{g(h_1 - a)^2 (1 - \rho)}{\rho H}\,, \tag{A.40}$$

$$U_2^+ = \frac{g(a + h_2)^2 (1 - \rho)}{H}\,. \tag{A.41}$$

Because $a < h_1$, a can be eliminated from the first equation to give

$$a = h_1 - \sqrt{\frac{\rho H}{(1 - \rho) g} U_1^+}\,, \tag{A.42}$$

which is identical to the amplitude formula from the quadrature (A.23). By replacing this in the second equation we obtain an explicit expression for the front branch in the parameter space U_1^+, U_2^+

$$U_2^+(U_1^+) = \left(\sqrt{Hg(1-\rho)} + \sqrt{\rho}\sqrt{U_1^+} \right)^2 ,$$

which is identical to the formula from the quadrature (A.22).

APPENDIX B: Solitary waves in "artificial" parameters

The domain of existence in the parameter space $(\beta\,, c)$ of solitary waves with the prescribed fluxes (2.70) can be found by fixing β and determining the range of speeds c for which solitary waves with property (2.70) exist.

From (2.70), with $\eta_k|_\infty = h_k + (-1)^k\beta$, we can determine the current at infinity in the wave frame in each layer

$$\widehat{u}_1|_\infty = -\frac{ch_1}{h_1-\beta}\,, \tag{B.1}$$

$$\widehat{u}_2|_\infty = -\frac{ch_2}{h_2+\beta}\,. \tag{B.2}$$

Note that for obtaining the range of phase speeds c for fixed β, we can mirror the discussion in Appendix A by shifting the heights of the asymptotic level as $|X| \to \infty$

$$h_1 \equiv h_1 - \beta\,, \quad h_2 \equiv h_2 + \beta\,, \quad h \equiv (h_1-\beta)/(h_2+\beta))\,, \tag{B.3}$$

and study solitary waves on currents parametrized by

$$U_1 = \frac{c^2h_1^2}{(h_1-\beta)^2}\,, \tag{B.4}$$

on a line in the parameter space $(U_1\,, U_2)$ given by

$$U_2 = \kappa U_1 \qquad \text{with} \qquad \kappa = \frac{h_2^2(h_1-\beta)^2}{h_1^2(h_2+\beta)^2}\,. \tag{B.5}$$

Thus, by using (B.1 - B.5), the relationships (A.7 - A.9) from Appendix A become

$$q_1(c\,;\beta) = -h_1 + h_2 + 2\beta + \frac{c^2}{\gamma}\left[\frac{\rho_1 h_1^2}{(h_1-\beta)^2} - \frac{\rho_2 h_2^2}{(h_2+\beta)^2}\right], \tag{B.6}$$

$$q_2(c\,;\beta) = -(h_1-\beta)(h_2+\beta) + \frac{c^2}{\gamma}\left[\frac{\rho_1 h_1^2(h_2+\beta)}{(h_1-\beta)^2} + \frac{\rho_2 h_2^2(h_1-\beta)}{(h_2+\beta)^2}\right]. \tag{B.7}$$

The discriminant of the quadratic form $\zeta^2 + q_1\zeta + q_2$ is

(B.8)

$$\Delta(c\,;\beta) = H^2 - \frac{2H}{\gamma}\left[\frac{\rho_1 h_1^2}{(h_1-\beta)^2} + \frac{\rho_2 h_2^2}{(h_2+\beta)^2}\right]c^2 + \frac{1}{\gamma^2}\left[\frac{\rho_1 h_1^2}{(h_1-\beta)^2} - \frac{\rho_2 h_2^2}{(h_2+\beta)^2}\right]^2 c^4,$$

whereas the root at the denominator (A.10) becomes

$$a_*(\beta) = \frac{\rho_r h_r^2(h_2+\beta) + h_1 - \beta}{1-\rho_r h_r^2}, \tag{B.9}$$

where $h_r = h_1/h_2$ and $\rho_r = \rho_1/\rho_2$.

Based on the results in Appendix A, and by using (B.1 - B.5) we can infer that solitary waves solutions with the property (2.70) for fixed β exist for

$$c \in [c_{min}(\beta), c_f(\beta)],$$

where relationships (A.18) and (A.19) for the speed of the limiting cases of solitary and front solutions turn into

$$c_{min}(\beta) = \sqrt{\frac{\gamma(h_1-\beta)^3(h_2+\beta)^3}{\rho_1 h_1^2(h_2+\beta)^3 + \rho_2 h_2^2(h_1-\beta)^3}}, \tag{B.10}$$

and

$$c_f(\beta) = \sqrt{g(1-\rho_r)H}\,\frac{(h_1-\beta)(h_2+\beta)}{\sqrt{\rho_r}h_1(h_2+\beta)+h_2(h_1-\beta)}\,, \tag{B.11}$$

respectively. The corresponding maximum amplitude is given by equation (A.20) modified by the new β-shifted asymptotic heights

$$a_f(\beta) = \frac{(h_1-\beta)^2 - h_r\sqrt{\rho_r}(h_2+\beta)^2}{(h_r\sqrt{\rho_r}-1)\beta + h_r\sqrt{\rho_r}h_2 + h_1}\,. \tag{B.12}$$

As in Appendix A, the polarity of the family of solitary waves parametrized by β is given by the sign of the amplitude of the front (B.12). We thus have, from (B.12),

$$a_f(\beta) < 0 \text{ for } \beta < \beta_0 \text{ and } a_f(\beta) > 0 \text{ for } \beta > \beta_0\,,$$

with

$$\beta_0 = \frac{H}{1+h_r}\frac{h_r - \sqrt{h_r\sqrt{\rho_r}}}{1+\sqrt{h_r\sqrt{\rho_r}}}\,. \tag{B.13}$$

The amplitude of the foliating family of solitary waves parametrized by β is therefore

$$a(c\,;\beta) = \frac{-q_1(c\,;\beta) + \mathrm{sgn}(\beta_0-\beta)\sqrt{\Delta(c\,;\beta)}}{2}\,, \qquad c \in [c_{min}(\beta), c_f(\beta)]\,. \tag{B.14}$$

We can eliminate β from (B.12) as root of the quadratic equation that is in the range $[-h_2, h_1]$,

$$\beta_f(a) = -\frac{a}{2} + \frac{h_1(\sqrt{\rho_r}+1)}{1-h_r\sqrt{\rho_r}} - \frac{\sqrt{a^2(1-h_r\sqrt{\rho_r})^2 + 4H^2h_r\sqrt{\rho_r}}}{2(1-h_r\sqrt{\rho_r})}\,, \tag{B.15}$$

and substituting in (B.11) we obtain an explicit formula for the amplitude-speed relation for the front branch subject to restriction $h_r\sqrt{\rho_r} \neq 1$

$$c_f(a) = \sqrt{Hg}\frac{(1+h_r)\sqrt{1-\rho_r}}{(h_r\sqrt{\rho_r}-1)^2}\left(h_r\sqrt{\rho_r}+1-\sqrt{\left(\frac{a}{H}\right)^2(h_r\sqrt{\rho_r}-1)^2+4h_r\sqrt{\rho_r}}\right).$$

For the special depth ratio $h_r\sqrt{\rho_r} = 1$ the above expression becomes invalid. In this case the dependence of a_f on β is linear and equation (B.12) becomes

$$a_f(\beta) = h_1 - h_2 - 2\beta\,, \tag{B.16}$$

with the maximum speed (B.11) for this case being

$$c_f(\beta) = \sqrt{Hg}\frac{(1+h_r)^2}{h_r}\sqrt{\frac{1-\sqrt{\rho_r}}{1+\sqrt{\rho_r}}}\frac{(h_1-\beta)(h_2+\beta)}{H^2}\,. \tag{B.17}$$

The front branch amplitude-speed relation in this special case $h_r\sqrt{\rho_r} = 1$ is therefore

$$c_f(a) = \sqrt{Hg}\frac{(1+h_r)^2}{4h_r}\sqrt{\frac{1-\sqrt{\rho_r}}{1+\sqrt{\rho_r}}}\left(1-\left(\frac{a}{H}\right)^2\right). \tag{B.18}$$

In order to emphasize the special cases $h_r = \sqrt{\rho_r}$ and $h_r = 1/\sqrt{\rho_r}$ and the associated degeneracies, we present in Figure B.1 the functions $a_f(\beta)$, $c_f(\beta)$ and $c_f(a)$ for two fixed depth ratios $h_r < 1$ and $h_r > 1$, respectively, and varying density ratios $\rho_r \in (0,1)$. We note that the front branch $c_f(a)$ is symmetric with respect to c axis; the level β corresponding to $a_f = 0$ is given by β_0.

Finally, we note how a simple geometric construction based on the effective wavelength can give an approximate relation speed-amplitude relation for given period, based

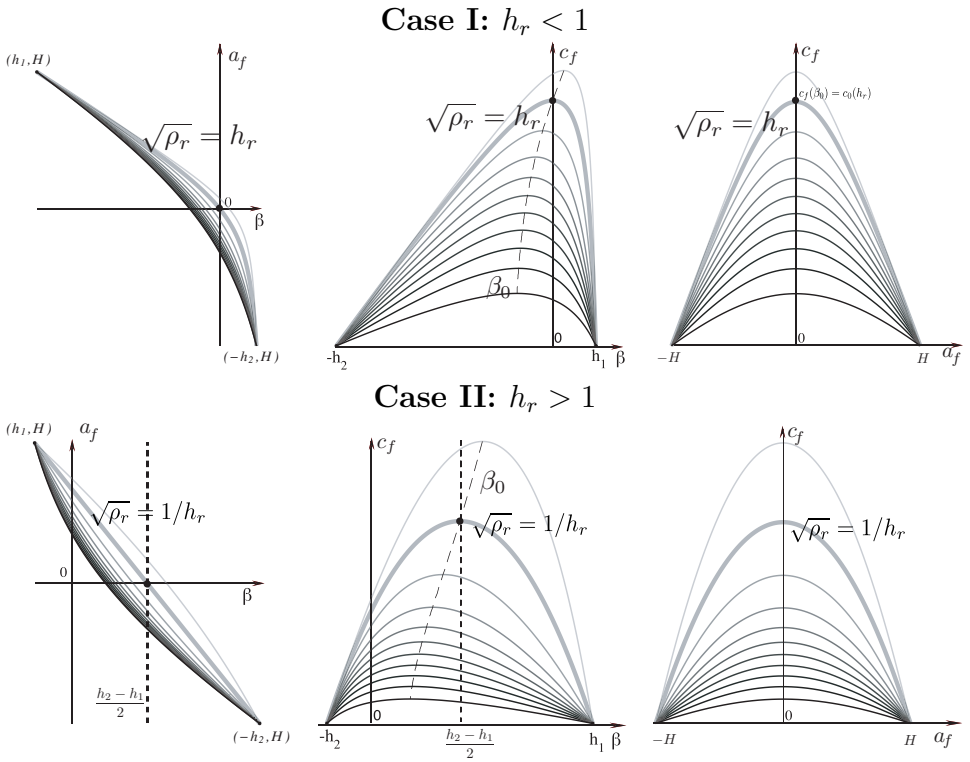

FIGURE B.1. Amplitude and speed of the front as functions of β; speed of the front as function of amplitude for values of $\rho_r \in (0,1)$.
(I) Depth ratio fixed $h_r < 1$. The thicker curve corresponds to $\sqrt{\rho_r} = h_r$, critical depth ratio. In this particular instance $\beta_0 = 0$.
(II) Depth ratio fixed $h_r > 1$. The thicker curve corresponds to $h_r\sqrt{\rho_r} = 1$. In this instance, the front branch $c(A)$ becomes a parabola.

on the observation that actual periodic solutions are very close to their limiting foliating solution if the period is sufficiently large. In fact, equating the area in the strip of height β and width L to the area under the solitary wave profile $2A\lambda_I$, gives, because the fast exponential decay of solitary waves, the position β and speed c corresponding to a mean-zero period-L wave in the constrained class. For a configuration of periodic waves approaching solitary waves of depression, this is determined by

$$\frac{\beta L}{2} = \frac{2}{\mu(\beta,A)}\left[\sqrt{a_*(\beta)-a_-(\beta,A)}\,(F(\delta,k)-E(\delta,k)) + \sqrt{\frac{A\,a_*(\beta)}{a_-(\beta,A)}}\right], \tag{B.19}$$

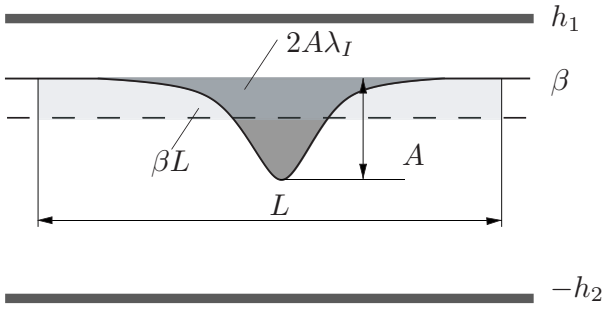

FIGURE B.2. Sketch of the approximation for periodic wave solutions close to their solitary wave limit. The crest position β of a periodic solution for given amplitude A and period L can be determined by equating the area under the foliating solitary wave profile with the area above the mean level over a period L.

where the modulus and argument of the elliptic functions depend on β and A through

$$k^2 = \frac{A + a_*(\beta)}{a_*(\beta) - a_-(\beta, A)}\,, m^2 = \frac{a_-(\beta, A)}{A}\frac{a_*(\beta) + A}{a_-(\beta, A) - a_*(\beta)}\,, \sin\delta = \frac{1}{m}\,,$$

$a_*(\beta)$ is given by (B.9), whereas

$$a_-(\beta, A) = A - q_1(c(\beta, A); \beta)\,,$$

with q_1 given by (B.6). We can obtain an explicit dependence of c on β and A by imposing that $\zeta = -A$ is a root of the quadratic $\zeta^2 + q_1(c;\beta)\zeta + q_2(c;\beta)$ and thus obtain a linear equation in c^2. This construction is illustrated in Figure B.2.

APPENDIX C: Implementation of the TEW algorithm for computing solitary internal waves solutions in continuously stratified fluid

In the current appendix, we first briefly review the computational method for determining fully nonlinear solitary wave solutions of Euler equations in continuous stratification presented in Turkington *et al.* [51] (TEW algorithm), and then describe our numerical implementation (the Fortran codes are included). While we have not modified the structure of the original algorithm, we propose an improved diagnostic for convergencevwhich becomes necessary when highly converged solutions are sought.

Furthermore, in this work (Chapters 3 and 4 of this thesis) we are interested in solitary wave solutions in stratifications with narrow pycnoclines. As observed in Turkington *et al.* [51] the convergence of the algorithm is greatly reduced in this particular limit. We remark that Lamb [32] has also observed slow converge rates of the TEW algorithm when the minimum Richardson number approaches the 0.25 threshold, being able to compute converged solutions with Richardson number as low as $Ri_{min} \approx 0.23$. For Richardson number under 0.23 however, his implementation failed to converge; Lamb attributed this convergence failure to the intrinsic instability of the solutions sought. While we do not necessarily disprove this conjecture, by adjusting some of the parameters that control the convergence of the scheme, we are able to determine converged solutions in stratifications with narrow pycnoclines that have regions with Richardson number as low as ≈ 0.07.

TEW Algorithm

Variational principle. The method described in Turkington *et al.* [51] relies on a variational formulation for the Dubreil Jacotin-Long (DJL) equation which governs the motion of steady flow in a continuously-stratified, inviscid, incompressible and non-diffusive fluid. Assuming that there are no close isopycnal surfaces, Turkington *et al.* [51] expressed the DJL equation in terms of a single unknown function $\eta(x\,,z)$, which represents the vertical displacement of the isopycnal surface passing through the point $(x\,,z)$ from its undisturbed level at $\pm\infty$. The resulting nonlinear eigenvalue problem is

$$M\eta = \frac{\lambda\eta}{H}\overline{\rho}(z-\eta) \quad \text{in} \quad D\,, \tag{C.1}$$

where $D = \{\{(x,z) \in \boldsymbol{R}^2 : -\infty < x < \infty\,, 0 < z < H\}\}$ denotes the fluid domain, $\overline{\rho}(z)$ is the background stratification, M denotes the quasilinear operator

$$M\eta := -(\overline{\rho}(z-\eta)\eta_x)_x - (\overline{\rho}(z-\eta)\eta_z)_z - \frac{1}{2}|\nabla\eta|^2\overline{\rho}'(z-\eta)\,,$$

whereas the eigenvalue parameter is defined by

$$\lambda = \frac{gH}{c^2}\,, \tag{C.2}$$

with c being the phase speed of the wave. The boundary conditions for the vertical displacement are

$$\eta = 0 \quad \text{on} \quad \partial D\,, \quad \eta \to 0 \quad \text{as} \quad x \to \pm\infty\,. \tag{C.3}$$

The equation (C.1) admits a variational formulation as follows. Let the objective and constraint functionals, respectively, be defined as

$$E(\eta) = \int_D \frac{1}{2}|\nabla\eta|^2\overline{\rho}(z-\eta)dx\ dz\,, \tag{C.4}$$

and

$$F(\eta) = \int_D f(z\,,\eta)dx\ dz\,, \tag{C.5}$$

with

$$f(z\,,\eta) = \frac{1}{H}\int_0^\eta \left[\overline{\rho}(z-\eta) - \overline{\rho}(z-\xi)\right] d\xi\,.$$

Then a pair $(\eta\,,\lambda)$ (with η satisfying the boundary conditions (C.8)) that satisfies the condition

$$E(\eta) \to \min \quad \text{subject to} \quad F(\eta) = A > 0\,,$$

is a solution of equation (C.1). It is straightforward to verify that if η is a minimizer and λ the associated Lagrange multiplier then (C.1) holds, since

$$E'(\eta) = M\eta\,, \qquad F'(\eta) = -\frac{\eta}{H}\overline{\rho}'(z-\eta)\,,$$

where prime denotes the functional derivative in η.

Note that c^2E represents the kinetic energy of the wave in the lab frame whereas $gHF(\eta)$ represents the potential energy of the wave disturbance. Thus the physical interpretation of the variational principle mentioned above is quite appealing: a solitary

wave solution minimizes the kinetic energy of the admissible variations for a prescribed potential energy.

Semilinear form of the eigenvalue problem. The first step in the numerical solution of (C.1) consists in a change of variable that transforms the *quasilinear* eigenvalue problem (C.1) in η into a *semilinear* eigenvalue problem in ϕ, which in turn can be solved numerically via a constrained-optimization technique. Thus by setting

$$\phi = s(z) - z(z-\eta) \quad \text{with} \quad s(z) = \int_{z_0}^{z} \sqrt{\overline{\rho}(\xi)}d\xi\,. \tag{C.6}$$

the eigenvalue problem (C.1) becomes

$$-\Delta\phi + s''(z) - s''(s^{-1}(s(z)-\phi)) = -\frac{2\lambda}{H}\left[z - s^{-1}(s(z)-\phi)\right] s''(s^{-1}(s(z)-\phi))\,, \tag{C.7}$$

with boundary conditions

$$\phi = 0 \quad \text{on} \quad \partial D\,, \quad \phi \to 0 \quad \text{as} \quad x \to \pm\infty\,. \tag{C.8}$$

The objective and constraint functionals become

$$E(\phi) = \int_D \left[\frac{1}{2}|\nabla\phi|^2 + e(z\,,\phi)\right] dx\; dz\,, \tag{C.9}$$

and

$$F(\phi) = \int_D f(z\,,\phi)dx\; dz\,, \tag{C.10}$$

where

$$e(z\,,\phi) = \int_0^\phi \left[s''(z) - s''(s^{-1}(s(z) - \xi))\right] d\xi\,, \tag{C.11}$$

and

$$f(z\,,\phi) = -\frac{2}{H}\int_0^\phi \left[z - s^{-1}(s(z) - \xi)\right] s''(s^{-1}(s(z) - \xi))d\xi\,. \tag{C.12}$$

The semilinear eigenvalue problem (C.7) can be written in terms of the functional derivatives of f and e

$$-\Delta\phi + e_\phi(z\,,\phi) - \lambda f_\phi(z\,,\phi) = 0\,. \tag{C.13}$$

We record here the functional derivatives of f and e which are going to be useful in the subsequent development. Thus

$$\begin{aligned}
e_\phi &= s''(z) - s''(s^{-1}(s(z) - \phi))\,,\\
f_\phi &= -\frac{2}{H}\left[z - s^{-1}(s(z) - \phi)\right] s''(s^{-1}(s(z) - \phi))\,,\\
e_{\phi\phi} &= \frac{s'''(s^{-1}(s(z) - \phi))}{s'(s^{-1}(s(z) - \phi))}\,,\\
f_{\phi\phi} &= -\frac{2}{H}\frac{s''(s^{-1}(s(z) - \phi))}{s'(s^{-1}(s(z) - \phi))} + \frac{2}{H}\left[z - s^{-1}(s(z) - \phi)\right]\frac{s'''(s^{-1}(s(z) - \phi))}{s'(s^{-1}(s(z) - \phi))}\,,
\end{aligned}$$

We also record the bounds

$$a = \max[e_{\phi\phi}(z\,,\phi)]_-\,, \tag{C.14}$$

(C.15) $$b = \max[f_{\phi\phi}(z\,,\phi)]_-\,,$$

Finally, at the basis of the minimization technique lays the assumption that the objective functional E is convex, which Turkington *et al.* [51] enforced by requiring

$$a < (\pi/H)^2\,.$$

It is important to mention here that the above condition is not a necessary condition for convexity; furthermore it is not met in the case of many of the stratifications with narrow pycnoclines considered throughout this thesis.

Iterative scheme. Turkington *et al.* [51] introduced a globally convergent iterative algorithm that solves the semilinear problem (C.7) by casting it in the form of a quadratic programming subproblem. In the following, we succinctly present their strategy, emphasizing the steps which are relevant to our numerical implementation. The convergence of the iterative scheme relies upon the convexity of two functionals: $F + \beta E$ and E respectively. β is chosen such that

(C.16) $$\beta(\pi^2/H^2 - a) - b > 0\,,$$

with a, b given by (C.14)-(C.15). Then by choosing

(C.17) $$\alpha = \max[e_{\phi\phi}(z\,,\phi)]_+\,,$$

E can be split as

$$E = E_+ - E_-\,,$$

with

$$E_+ = \int \left[\frac{1}{2}|\nabla\phi|^2 + \frac{\alpha}{2}\phi^2\right] dx\ dz\,,$$

convex and quadratic and

$$E_- = \int \left[\frac{\alpha}{2}\phi^2 - e(z\,,\phi)\right] dx\ dz\,,$$

convex.

Thus, with the above notation, the iterative algorithm is described as follows. Let ϕ^0 be an initial condition satisfying $F(\phi^0) = A$. The iterative step $\phi^k \to \phi^{k+1}$ consists in solving the problem

$$E_+(\phi) - E_-(\phi^k) - \langle E'_-(\phi^k), \phi - \phi^k\rangle \to \min \text{ over } F(\phi^k) + \langle F'(\phi^k) + \beta E'(\phi^k), \phi - \phi^k\rangle \geq A\,,$$

where $\langle\cdot\,,\cdot\rangle$ denotes the inner product

$$\langle u\,, v\rangle = \int_D uv\ dz\ dx\,.$$

The explicit construction of the iterative scheme is reducible to the following three parts:

(1) Solve the two elliptic boundary value problems (in v^k and w^k)

$$(-\Delta + \alpha)v^k = \alpha\phi^k - e_\phi(z,\phi) \quad \text{in } D\,, \quad v^k = 0 \text{ on } \partial D\,, \tag{C.18}$$

$$(-\Delta + \alpha)w^k = f_\phi(z,\phi) \quad \text{in } D\,, \quad w^k = 0 \text{ on } \partial D\,. \tag{C.19}$$

(2) Evaluate the four integrals

$$S_1 = \int_D f_\phi(z,\phi^k) w^k \; dx \; dz \,, \tag{C.20}$$

$$S_2 = \int_D f_\phi(z,\phi^k)(\phi^k - v^k) \; dx \; dz \,, \tag{C.21}$$

$$S_3 = \int_D \left[|\nabla(\phi^k - v^k)|^2 + \alpha(\phi^k - v^k)^2 \right] \; dx \; dz \,, \tag{C.22}$$

$$F(\phi^k) = \int_D f(z\,,\phi^k) \; dx \; dz \,, \tag{C.23}$$

(3) Define

$$\mu^{k+1} = \max\left[0, \frac{A - F(\phi^k) + S_2 + \beta S_3}{S_1 + 2\beta S_2 + \beta^2 S_3}\right] , \tag{C.24}$$

$$\phi^{k+1} = v^k + \mu^{k+1}\left[w^k + \beta(\phi^k - v^k)\right] , \tag{C.25}$$

$$\lambda^k = \frac{\mu^k}{1 - \beta\mu^k} \,. \tag{C.26}$$

Numerical implementation

In our implementation of the TEW algorithm the Poisson problems (C.18), (C.19) are solved by a FFT method as follows. First, the infinite strip domain D is truncated assuming periodicity in the horizontal direction. The period is chosen large enough so to ensure adequate decay at the horizontal boundaries. Taking advantage of the homogeneous boundary conditions at the top and bottom boundaries, we mirror the domain in the vertical direction, imposing periodic boundary conditions in both directions on the resulting domain. The equations are thus solved in Fourier space, the ensuing method having order of convergence four.

The integral (C.22) can be rewritten by using integration by parts and relation (C.18) as follows

$$S_3 = \int_D (\phi^k - v^k) \left[-\Delta(\phi^k - v^k) + \alpha(\phi^k - v^k) \right] \, dx \, dz =$$

$$\int_D (\phi^k - v^k) \left[e_\phi(z\,, \phi^k) - \Delta\phi^k \right] \, dx \, dz\,.$$

and the laplacian $\Delta\phi^k$ in the integrand is evaluated with a nine point stencil. For evaluating the integrals (C.20-C.23), we use a fourth order Simpson rule.

The integrands themselves involve the transformation function s and its inverse (see (C.6) for the definition) for which two discretized look-up tables with $1,000,000$ uniformly spaced points are pre-computed. For determining the inverse we use a quadratic interpolation scheme.

The computational domain is scaled such that $z \in [0\,, 1]$. The computational results referred to through the remainder of this Appendix pertain to the class of stratifications

$$\overline{\rho}(z) = \rho_{min} + \frac{\rho_{max} - \rho_{min}}{2} \left(1 + \tanh \left[\frac{\ln\ 9}{d} (z_p - z) \right] \right) \,, \tag{C.27}$$

with $\rho_{min} = 0.999$ g/cm^3, $\rho_{max} = 1.022$ g/cm^3 and the total height of the fluid column $H = 77$ cm, the thickness of the pycnocline d and position of the center of the pycnocline z_p.

Stopping criterion

The iterative scheme stopping criterion suggested in Turkington *et al.* [51] ($5 \cdot 10^{-3}$ in the L_2 norm of the relative error in the eigenfunction ϕ) is not sufficient for our purposes. In fact, for stratifications with narrow pycnoclines, we found this criterion to be

sometimes misleading, suggesting convergence in instances in which other tests indicate that the numerical solution is not in fact a traveling wave solution – see Figure C.1 where the mass flux (a quantity that is conserved by a truly stationary solution) is shown for a solution with infinite norm of the relative error in ϕ of 10^{-5}.

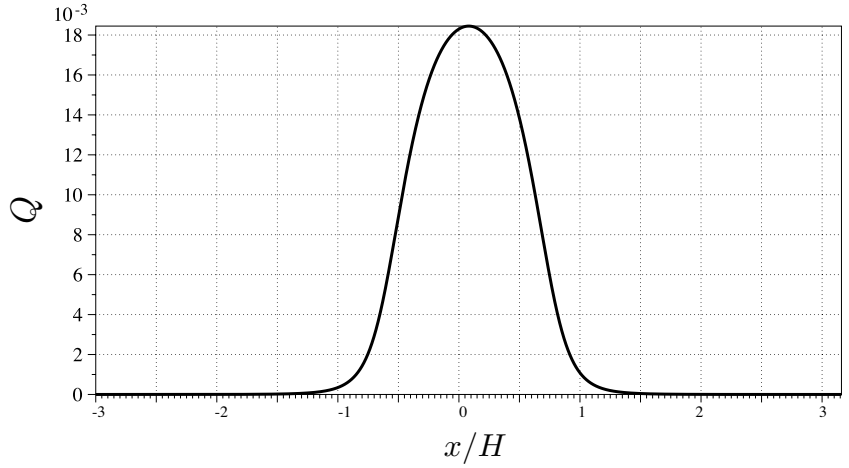

FIGURE C.1. Non-dimensionalized mass flux $\int_0^H \rho U(z)dz / \int_0^H \overline{\rho}(z)cdz$ for a solution with infinite norm of the relative error in ϕ of 10^{-5}, in background stratification (C.27) with $d = 2$ cm and $z_p = 15$ cm. The resolution of the scheme is 512 discretization points in the vertical.

Thus, apart from monitoring convergence in the relative error in the eigenfunction ϕ and the eigenvalue λ as suggested in Turkington *et al.* [51], we also monitor the residual of the DJL equation in the transformed variable ϕ (C.13). An estimate of this residual can be constructed inside the iterative loop. Thus by subtracting ϕ^k from relation (C.25) and applying the operator $(\alpha - \Delta)$ we obtain

$$(\alpha - \Delta)(\phi^{k+1} - \phi^k) = \frac{\mu}{\lambda}\left[(\alpha - \Delta)(v^k + \lambda w^k) + (\alpha - \Delta)\phi^k\right] ,$$

which, by using relations (C.18) and (C.19) we can rewrite as

$$(\alpha - \Delta)(\phi^{k+1} - \phi^k) = \frac{\mu^{k+1}}{\lambda^{k+1}} \left[-\Delta\phi^k + e_\phi(z\,, \phi^k) - \lambda^{k+1} f_\phi(z\,, \phi^k) \right] ,$$

We recongnize in the RHS of the above relation the residual of equation (C.13). As shown in Figure C.2, for the case from Figure C.1, the magnitude of the residual is substantial when the relative error in ϕ suggests convergence.

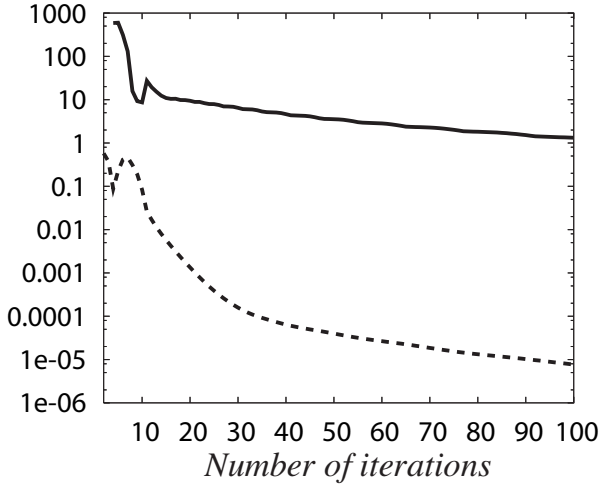

FIGURE C.2. Dashed - relative error in ϕ, continuous - residual for the case from Figure C.1.

Order and rate of convergence

We have monitored the convergence of the eigenvalue λ (C.2) by fixing a threshold for the residual and looking at the relative convergence of λ as the discretization of the system was refined. As expected based on the fourth order construction of all portions of the numerical scheme, the order of convergence was found to be four. The rate of convergence however is strongly dependent on the parameters α and β, parameters that control the convexity of the functionals involved in the iterative scheme. We note that

choosing α substantially bigger than the estimate provided by relation (C.17) greatly accelerates convergence. We thus used $\alpha \approx 200$ in the majority of the numerical results presented.

The rate of convergence is also smaller when the sought solutions are strongly nonlinear: as exemplified in Figure C.3 where we show (a) the residual versus the number of iterations for three numerical solutions in the stratification (C.27) with $d = 2$ cm and $z_p = 65$ cm, for three values of the parameter A and (b) the corresponding wave profiles. The minimum Richardson number corresponding to the largest amplitude wave with $A = 3.2 \cdot 10^{-3}$ is 0.076.

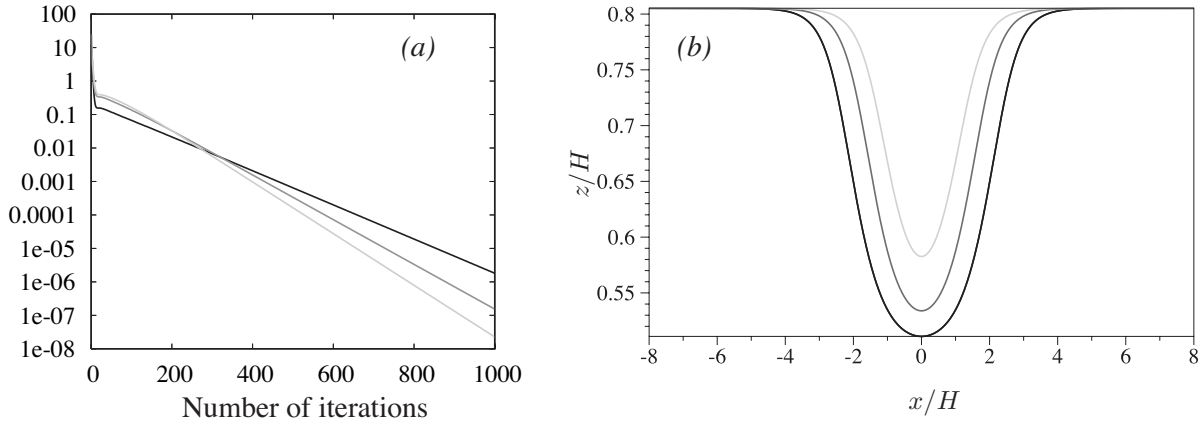

FIGURE C.3. (a) Residual versus the number of iterations for three numerical solutions in the stratification (C.27) with $d = 2$ cm and $z_p = 65$ cm, for $A = 3.2 \cdot 10^{-3}$, $2 \cdot 10^{-3}$ and 10^{-3} (from black to light gray). (b) the corresponding isolines of density corresponding to the average density.

Numerical codes

Main code

```
program IterFFT
!*****************************************************
! Iterative Algorithm Turkington,Wang and Eydeland (1990)
! Solves the 2 Helmholtz equations in Fourier space
! homogeneous boundary conditions in vertical direction
! periodic boundary conditions in horizontal direction
!*****************************************************
implicit none
include 'FFTinput.f'
integer nx,ny
parameter(nx=ngridx-1)
parameter(ny=2*(ngridy-1))
integer kx,ky
integer jiter
!Scalar quantities
double precision hdom
double precision pi,g
double precision hy,hs,ymin,ymax,smin,smax
integer k
integer iloc
double precision fl,fc,fr,fac
```

```
double precision tempy

double precision diff,normtemp

double precision t,rhot,rhoprimet

integer iter

double precision S1,S2,S3,S4

double precision temp1,temp2,part1,part2,den

double precision miu,eig,cphys

double precision alphanew,betanew

double precision temp,massflux,aux,res

double precision miuold,cold

double precision errmiu,erreig,errc

!Dimensioned by nfit

double precision yy(nfit+2),stemp(nfit+2)

double precision  ytemp(nfit+2),ss(nfit+2)

double precision prho(nfit+2)

!Dimensioned by ngridx

double precision work(ngridx)

!Dimensioned by ngridy

double precision y(ngridy),sy(ngridy)

double precision etareadx(ngridx),etaread(ngridy)

double precision seta(ngridy),sdp(ngridy)

!Dimensioned by ngridx X ngridy

double precision ,dimension(:,:),allocatable :: eta,phi
```

```
double precision v(ngridx,ngridy),w(ngridx,ngridy)
double precision shift(ngridx,ngridy),sinvshift(ngridx,ngridy)
double precision sdpsinvshift(ngridx,ngridy)
double precision ephi(ngridx,ngridy),fphi(ngridx,ngridy)
double complex ,dimension(:,:),allocatable:: cRHS
double precision temparray(ngridx,ngridy),laplphi(ngridx,ngridy)
double precision DLANGE,DNRM2
external DLANGE,DNRM2
double precision ,dimension(:,:),allocatable :: rho,psi
double precision phiold(ngridx,ngridy)
pi=4.d0*datan(1.d0)
g=981.d0
write(*,*)'dx, dy : ',dx,dy
hdom = d - c
write(*,*)'alpha,beta: ',alpha,beta
write(*,*)'maxiter:  ',maxiter
!*******************************************************
! Setting up the grid in the vertical direction
!*******************************************************
do ky = 1, ngridy
y(ky)= c + dble(ky-1)*dy
end do
!*******************************************************
```

```
! Reading the look up tables for s, s inverse and the integral of density
!*****************************************************
open(11, FILE= 'ytempss.dat')
open(12, FILE= 'yystemp.dat')
open(13, FILE= 'prho.dat')
write(*,*)'Reading data files...'
do k=1,nfit+1
read(12,*)yy(k),stemp(k)
read(11,*)ytemp(k),ss(k)
read(13,*)prho(k)
end do
read(11,*)ytemp(nfit+2),ss(nfit+2)
read(13,*)prho(nfit+2)
close(11)
close(12)
close(13)
write(*,*)'Done reading data files'
ymax=ytemp(nfit+1)
ymin=ytemp(1)
smax=ss(nfit+1)
smin=ss(1)
hy = (ymax-ymin)/dble(nfit)
hs= (smax-smin)/dble(nfit)
```

```
!*******************************************************
!Determine the s values at the grid points
!*******************************************************
do ky=1,ngridy
iloc = int((y(ky)-ymin)/hy)
fl=ss(iloc+1)
fc=ss(iloc+2)
fr=ss(iloc+3)
fac=(y(ky)-ytemp(iloc+2))/hy
sy(ky)=0.5d0*((fac**2)*(fl-2.d0*fc+fr)-fac*(fl-fr)+2.d0*fc)
end do
! close(20)
!*******************************************************
! Initialize eta
! eta is the vertical displacement defined as rhoinf( y-eta(x,y) ) = rho(x,y)
! a good initial guess accelerates the convergence
!*******************************************************
allocate(eta(ngridx,ngridy))
allocate(phi(ngridx,ngridy))
if(input.eq.'new')then
open(21, FILE=inputeta)
do ky=1,ngridy
read(21,*)(etareadx(kx),kx=1,ngridx)
```

```
eta(1:ngridx,ky)=etareadx(1:ngridx)
end do
else
open(21,FILE=inputeta)
do kx=2,ngridx
read(21,*)(etaread(ky),ky=1,ngridy)
eta(kx,1:ngridy)=etaread(1:ngridy)
end do
end if
close(21)
!*******************************************************
! Compute phi = s(y)-s(y-eta)
!*******************************************************
do kx=1,ngridx
do ky=1,ngridy
tempy=y(ky)-eta(kx,ky)
iloc=int((tempy-ymin)/hy)
fl=ss(iloc+1)
fc=ss(iloc+2)
fr=ss(iloc+3)
fac=(tempy-ytemp(iloc+2))/hy
seta(ky)=0.5d0*((fac**2)*(fl-2.d0*fc+fr)-fac*(fl-fr)+2.d0*fc)
phi(kx,ky)=sy(ky)-seta(ky)
```

```
phi(kx,ky)=sy(ky)-seta(ky)

end do

end do

!Compute the inf norm of phi to use as loop iterating criteria

normtemp=DLANGE('m',ngridx,ngridy,phi,ngridx,work)

!*******************************************************

! Compute (sdp)  s''(y)=rhoinf'(y)/(2* Sqrt(rhoinf) )

!*******************************************************

do ky=1,ngridy

t=dtanh(lambda*(y0-y(ky)))

rhot=rho1+0.5d0*rhodiff*(1.d0+t)

rhoprimet=-0.5d0*lambda*rhodiff*(1.d0-t**2)

sdp(ky)=0.5d0*rhoprimet/dsqrt(rhot)

end do

!*******************************************************

!  Iterative Loop

!*******************************************************

iter=0

diff=10.d0

res=10.d0

open(200, FILE= 'FFTconv.test')

write (200,*)'# itercphysmueigAmpres'

miuold=0.d0
```

```
cold=0.d0
do while (res.gt.tol.and.iter.lt.maxiter)
iter=iter+1
write(*,*)'Iteration  ',iter
do kx=1,ngridx
do ky=1,ngridy
!******  Compute shift=s(y)-phi
shift(kx,ky)=sy(ky)-phi(kx,ky)
!**** Interpolate to get sinvshift=sinverse(s(y)-phi)
iloc=int((shift(kx,ky)-smin)/hs)
fl=yy(iloc+1)
fc=yy(iloc+2)
fr=yy(iloc+3)
fac=(shift(kx,ky)-stemp(iloc+2))/hs
sinvshift(kx,ky)=0.5d0*((fac**2)*(fl-2.d0*fc+fr)-fac*(fl-fr)+2.d0*fc)
 !******* Compute s''(sinvshivt)
t=dtanh(lambda*(y0-sinvshift(kx,ky)))
rhot=rho1+0.5d0*rhodiff*(1.d0+t)
rhoprimet=-0.5d0*lambda*rhodiff*(1.d0-t**2)
sdpsinvshift(kx,ky)=0.5d0*rhoprimet/dsqrt(rhot)
 !******* Compute ephi & RHS 1st Helmholtz equation
ephi(kx,ky)=sdp(ky)-sdpsinvshift(kx,ky)
v(kx,ky)=-alpha*phi(kx,ky)+ephi(kx,ky)
```

```
 !******* Compute fphi & RHS 2nd Helmholtz equation
fphi(kx,ky)=-2.d0/hdom*(y(ky)-sinvshift(kx,ky))*sdpsinvshift(kx,ky)
w(kx,ky)=-fphi(kx,ky)
end do
 end do
!***************** First Helmholtz equation
! Copy real matrix in complex matrix extended
allocate(cRHS(nx,ny))
cRHS(1:nx,1:ngridy-1)=dcmplx(v(1:nx,1:ngridy-1),0.d0)
cRHS(1:nx,ngridy+1:ny)=dcmplx(- v(1:nx,ngridy-1:2:-1),0.d0)
! Solve the Helmholtz problem
call helm(nx,ny,cRHS,alpha,b-a,2*hdom)
! Extract  real part of complex matrix
v(1:nx,1:ngridy)=real(cRHS(1:nx,1:ngridy))
v(ngridx,1:ngridy)=v(1,1:ngridy)
! Extract imaginary part of complex matrix to compute norm
! temparray(1:nx,1:ngridy)=dimag(cRHS(1:nx,1:ngridy))
! temparray(ngridx,1:ngridy)=temparray(1,1:ngridy)
!write(*,*)'img',DLANGE('M',ngridx,ngridy,temparray,ngridx,work)
!write(*,*)'mag v',DLANGE('M',ngridx,ngridy,v,ngridx,work)
!write(*,*)'mag ephi',DLANGE('M',ngridx,ngridy,ephi,ngridx,work)
!***************** Second Helmhotz equation
! Copy real matrix in complex matrix extended
```

```
 cRHS(1:nx,1:ngridy-1)=dcmplx(w(1:nx,1:ngridy-1),0.d0)
 cRHS(1:nx,ngridy+1:ny)=dcmplx(- w(1:nx,ngridy-1:2:-1),0.d0)
! Solve the Helmholtz problem
call helm(nx,ny,cRHS,alpha,b-a,2*hdom)
! Extract  real part of complex matrix
w(1:nx,1:ngridy)=real(cRHS(1:nx,1:ngridy))
w(ngridx,1:ngridy)=w(1,1:ngridy)
! Extract imaginary part of complex matrix to compute norm
! temparray(1:nx,1:ngridy)=dimag(cRHS(1:nx,1:ngridy))
! temparray(ngridx,1:ngridy)=temparray(1,1:ngridy)
!write(*,*)'img',DLANGE('M',ngridx,ngridy,temparray,ngridx,work)
!write(*,*)'mag w',DLANGE('M',ngridx,ngridy,w,ngridx,work)
!write(*,*)'mag fphi',DLANGE('M',ngridx,ngridy,fphi,ngridx,work)
!************** Integral S 1
temparray=fphi*w
call simpson9(ngridx,ngridy,temparray,dx,dy,S1)
write(*,*)'S1',S1
!************** Integral S 2
temparray=fphi*(phi-v)
call simpson9(ngridx,ngridy,temparray,dx,dy,S2)
write(*,*)'S2',S2
!************** Integral S 3
!call laplacian2(ngridx,ngridy,phi,dx,dy,laplphi)
```

```
! Copy real matrix in complex matrix extended
cRHS(1:nx,1:ngridy-1)=dcmplx(phi(1:nx,1:ngridy-1),0.d0)
cRHS(1:nx,ngridy+1:ny)=dcmplx(- phi(1:nx,ngridy-1:2:-1),0.d0)
call laplacian(nx,ny,cRHS,b-a,2*hdom)
! Extract  real part of complex matrix
laplphi(1:nx,1:ngridy)=real(cRHS(1:nx,1:ngridy))
laplphi(ngridx,1:ngridy)=laplphi(1,1:ngridy)
! Extract imaginary part of complex matrix to compute norm
!temparray(1:nx,1:ngridy)=dimag(cRHS(1:nx,1:ngridy))
!temparray(ngridx,1:ngridy)=temparray(1,1:ngridy)
!write(*,*)'img',DLANGE('M',ngridx,ngridy,temparray,ngridx,work)
temparray=(phi-v)*(-laplphi+ephi)
call simpson9(ngridx,ngridy,temparray,dx,dy,S3)
write(*,*)'S3', S3
!********** Integral S 4
do kx=1,ngridx
do ky=1,ngridy
t=dtanh(lambda*(y0-sinvshift(kx,ky)))
rhot=rho1+0.5d0*rhodiff*(1.d0+t)
part1=(y(ky)-sinvshift(kx,ky))/hdom * rhot
iloc = int((y(ky)-ymin)/hy)
fl=prho(iloc+1)
fc=prho(iloc+2)
```

```
fr=prho(iloc+3)

fac=(y(ky)-ytemp(iloc+2))/hy

temp1=0.5d0*((fac**2)*(fl-2.d0*fc+fr)-fac*(fl-fr)+2.d0*fc)

iloc = int((sinvshift(kx,ky)-ymin)/hy)

fl=prho(iloc+1)

fc=prho(iloc+2)

fr=prho(iloc+3)

fac=(sinvshift(kx,ky)-ytemp(iloc+2))/hy

temp2=0.5d0*((fac**2)*(fl-2.d0*fc+fr)-fac*(fl-fr)+2.d0*fc)

part2=(temp2-temp1)/hdom

temparray(kx,ky)=part1+part2

end do

end do

call simpson9(ngridx,ngridy,temparray,dx,dy,S4)

write(*,*)'S4',S4

!compute eigenvalue

miu=(Amp-S4+S2+beta*S3)/(S1+2*beta*S2+(beta**2)*S3)

if(miu.lt.0.d0) then

miu=0.d0

write(*,*)'!!!!!!!!! zero miu'

end if

errmiu=dabs((miu-miuold)/miu)

eig=miu/(1.d0-beta*miu)
```

```
miuold=miu
cphys=dsqrt(g*hdom/eig)
errc=dabs((cphys-cold)/cphys)
cold=cphys
den=1.d0-beta*miu
write(*,*)'1-beta*miu',den
write(*,*)'miu    ',miu
write(*,*)'eig',eig
write(*,*)'speed',cphys
phiold=phi
!update phi
phi=v+miu*(w+beta*(phi-v))
temparray=0.d0
phiold=phi-phiold
do kx=2,ngridx-1
do ky=2,ngridy-1
aux=phiold(kx+1,ky)+phiold(kx-1,ky)+&
phiold(kx,ky-1)+phiold(kx,ky+1)-4.d0*phiold(kx,ky)
temparray(kx,ky)=alpha*phiold(kx,ky)-aux/(dx**2)
end do
end do
res=DLANGE('M',ngridx,ngridy,temparray,ngridx,work)
write(*,*)'Max value of (alpha-lap)*(phi-phiold)/den',res/den
```

```
! evaluate infinite norm for convergence check
 temp1=DLANGE('m',ngridx,ngridy,phi,ngridx,work)
 diff=dabs(temp1-normtemp)
 normtemp=temp1
 write(*,*)'relative error max norm phi',diff/normtemp
 write(*,*)'relative error Amp-S4 ',Amp-S4
!call convexitycheck(ngridx,ngridy,sinvshift,rho1,rho2,lambda,y0,&
  alphanew,betanew)
 deallocate(cRHS)
 write (200,*)iter,errc,errmiu,dabs((Amp-S4)/Amp),res/den
end do
write(200,*)'#',cphys*scalvel
close(200)
!*****************************************************
! Write to data files
 allocate(rho(ngridx,ngridy))
 allocate(psi(ngridx,ngridy))
 do kx=1,ngridx
do ky=1,ngridy
 shift(kx,ky)=sy(ky)-phi(kx,ky)
 iloc=int((shift(kx,ky)-smin)/hs)
 fl=yy(iloc+1)
 fc=yy(iloc+2)
```

```
 fr=yy(iloc+3)
 fac=(shift(kx,ky)-stemp(iloc+2))/hs
 sinvshift(kx,ky)=0.5d0*((fac**2)*(fl-2.d0*fc+fr)-fac*(fl-fr)+2.d0*fc)
 eta(kx,ky)=y(ky)-sinvshift(kx,ky)
 temp1=y(ky)-eta(kx,ky)
 t=dtanh(lambda*(y0-temp1) )
 rho(kx,ky)=rho1+0.5d0*rhodiff*(1.d0+t)
 psi(kx,ky)=eta(kx,ky)*cphys!-cphys*y(ky)
 end do
end do
open(20,FILE='FFTeta.'//gridtype)
open(50,FILE='FFTphi.'//gridtype)
open(30,FILE='FFTrho.'//gridtype)
open(40,FILE='FFTpsi.'//gridtype)
do ky=1,ngridy
write(20,505)(eta(kx,ky),kx=1,ngridx)
write(30,505)(rho(kx,ky),kx=1,ngridx)
write(40,505)(scal*psi(kx,ky),kx=1,ngridx)
write(50,505)(phi(kx,ky),kx=1,ngridx)
end do
close(20)
close(30)
close(40)
```

```
close(50)
! compute the mass flux for each section
call velu(ngridx,ngridy,psi,temparray,dy)
open(60,FILE='FFTmass.flux')
iloc = int((hdom-ymin)/hy)
fl=prho(iloc+1)
fc=prho(iloc+2)
fr=prho(iloc+3)
fac=(hdom-ytemp(iloc+2))/hy
temp1=0.5d0*((fac**2)*(fl-2.d0*fc+fr)-fac*(fl-fr)+2.d0*fc)
temp1=temp1*cphys
do  kx=1,ngridx
massflux=0.d0
do ky=1,ngridy
massflux=massflux+rho(kx,ky)*(temparray(kx,ky)-cphys)
end do
temp=rho(kx,1)*(temparray(kx,1)-cphys)+&
   rho(kx,ngridy)*(temparray(kx,ngridy)-cphys)
massflux=massflux - 0.5d0*temp
massflux=dy*massflux
write(60,*)dx*dble(kx-1),massflux+temp1
end do
close(60)
```

```
501 format(2049(D30.20,1x),1x)

502 format(4097(D30.20,1x),1x)

503 format(8193(D30.20,1x),1x)

504 format(16385(D30.20,1x),1x)

505 format(20481(D30.20,1x),1x)

deallocate(eta)

deallocate(phi)

deallocate(rho)

deallocate(psi)

stop

end

!*******************************************************

subroutine helm(nx,ny,RHS,alpha,L,h)

!  external

implicit none

include 'fftw3.f'

integer nx,ny

double complex RHS(nx,ny)

double precision alpha,L,H

integer*8 plan,info

! internal

integer kx,ky,k

double precision tempx,tempy,temp
```

```
double precision fx(nx),fy(ny),pi
pi=4.d0*datan(1.d0)
! precompute the wave number multipliers
fx(1)=0.d0
do kx=2,nx/2+1
fx(kx)=(2.d0*pi*dble(kx-1)/L)**2
fx(nx-kx+2)=fx(kx)
end do
fy(1)=0.d0
do ky=2,ny/2+1
fy(ky)=(2.d0*pi*dble(ky-1)/h)**2
fy(ny-ky+2)=fy(ky)
end do
!*******************************************************
!  2D FFT transform
!  solve periodic Helmholtz problem for each line
!*******************************************************
call dfftw_plan_dft_2d(plan,nx,ny,RHS,RHS,&
FFTW_FORWARD,FFTW_ESTIMATE)
call dfftw_execute(plan)
call dfftw_destroy_plan(plan)
do ky=1,ny
!   Solve the 1D poisson problem
```

```
tempy=fy(ky)
do kx=1,nx
tempx=fx(kx)
RHS (kx,ky)=-RHS(kx,ky)/(tempx+tempy+alpha)
end do
end do
!  Invert FFT
call dfftw_plan_dft_2d(plan,nx,ny,RHS,RHS,&
FFTW_BACKWARD,FFTW_ESTIMATE)
call dfftw_execute(plan)
call dfftw_destroy_plan(plan)
temp=dble(nx*ny)
!Normalize (multiply by 1/(nx*ny)
call ZLASCL('G','N','N',temp,1.d0,nx,ny,RHS,nx,info)
return
end
!*******************************************************
subroutine simpson9(ngridx,ngridy,A,dx,dy,S)
!************ ngridx, ngridy -  odd numbers
implicit none
integer ngridx,ngridy
double precision A(ngridx,ngridy)
double precision dx,dy,S
```

```
integer kx,ky
S=0.d0
do kx=2,(ngridx-1),2
do ky=2,(ngridy-1),2
S=S+16.d0*A(kx,ky)
S=S+4.d0*(A(kx-1,ky)+A(kx+1,ky)+A(kx,ky-1)+A(kx,ky+1))
S=S+(A(kx-1,ky-1)+A(kx-1,ky+1)+A(kx+1,ky-1)+A(kx+1,ky+1))
end do
end do
S=dx*dy/9.d0*S
return
end
!*****************************************************
subroutine laplacian(nx,ny,RHS,L,h)
!  external
implicit none
include 'fftw3.f'
integer nx,ny
double complex RHS(nx,ny)
double precision L,H
integer*8 plan,info
! internal
integer kx,ky,k
```

```
double precision tempx,tempy,temp
double precision fx(nx),fy(ny),pi
pi=4.d0*datan(1.d0)
! precompute the wave number multipliers
fx(1)=0.d0
do kx=2,nx/2+1
fx(kx)=(2.d0*pi*dble(kx-1)/L)**2
fx(nx-kx+2)=fx(kx)
end do
fy(1)=0.d0
do ky=2,ny/2+1
fy(ky)=(2.d0*pi*dble(ky-1)/h)**2
fy(ny-ky+2)=fy(ky)
end do
!*********************************************************
!  2D FFT transform
!*********************************************************
call dfftw_plan_dft_2d(plan,nx,ny,RHS,RHS,&
FFTW_FORWARD,FFTW_ESTIMATE)
call dfftw_execute(plan)
call dfftw_destroy_plan(plan)
do ky=1,ny
tempy=fy(ky)
```

```
do kx=1,nx
tempx=fx(kx)
RHS (kx,ky)=-RHS(kx,ky)*(tempx+tempy)
end do
end do
!  Invert FFT
call dfftw_plan_dft_2d(plan,nx,ny,RHS,RHS,&
FFTW_BACKWARD,FFTW_ESTIMATE)
call dfftw_execute(plan)
call dfftw_destroy_plan(plan)
temp=dble(nx*ny)
call ZLASCL('G','N','N',temp,1.d0,nx,ny,RHS,nx,info)
return
end
!*******************************************************
subroutine convexitycheck(ngridx,ngridy,sinvshift,rho1,rho2,&
lambda,y0,alpha,beta)
implicit none
integer ngridx,ngridy
double precision sinvshift(ngridx,ngridy)
double precision rho1,rho2,lambda,y0
double precision alpha,beta,t
integer kx,ky
```

```
double precision rhodiff,emax,emin,fmax,fmin
double precision pi,dy,y,rhot,rhoprimet,rhodpt
double precision epp, fpp,a,b
rhodiff= rho2 -rho1
pi = 4.d0*datan(1.d0)
emax = -1.d20
emin=  1.d20
fmax = -1.d20
fmin=  1.d20
dy=1.d0/dble(ngridy-1)
do kx=1,ngridx
do ky=1,ngridy
y=dy*dble(ky-1)
t=dtanh(lambda*(y0-sinvshift(kx,ky)))
rhot=rho1+0.5d0*rhodiff*(1.d0+t)
rhoprimet=-0.5d0*lambda*rhodiff*(1.d0-t**2)
rhodpt= -rhodiff*(lambda**2)*t*(1-t**2)
epp = -(0.5d0*rhoprimet/rhot)**2+0.5d0*rhodpt/rhot
fpp = -(rhoprimet / rhot) + 2.d0 *epp* (y-sinvshift(kx,ky))
emax=max(epp,emax)
emin=min(epp,emin)
fmax=max(fpp,fmax)
fmin=min(fpp,fmin)
```

```
end do
end do
a=abs(min(0.d0,emin))
b=abs(min(0.d0,fmin))
alpha=emax
beta=b/(pi**2-a)
write(*,*)'a,b',a,b
write(*,*)'alpha,beta', alpha, beta
write(*,*)'emax,emin', emax, emin
write(*,*)'fmax,fmin', fmax, fmin
write(*,*)'piˆ2-a', pi**2-a
return
end
!*****************************************************
subroutine velu(ngridx,ngridy,psi,vel,dy)
!******** computes the horizontal velocity order 2 formulas
implicit none
integer ngridx, ngridy
double precision psi(ngridx,ngridy)
double precision vel(ngridx,ngridy)
double precision ddy,dy
integer kx,ky
ddy=2.d0*dy
```

```
do kx=1,ngridx
vel(kx,1) = -(3.d0* psi(kx,1)-4.d0*psi(kx,2)+psi(kx,3))/ddy
vel(kx,ngridy) = (3.d0* psi(kx,ngridy)-4.d0*psi(kx,ngridy-1)&
+psi(kx,ngridy-2))/ddy
do ky=2,ngridy-1
vel(kx,ky)=(psi(kx,ky+1)-psi(kx,ky-1))/ddy
end do
end do
return
end
!*****************************************************
subroutine laplacian2(ngridx,ngridy,A,dx,dy,laplacian)
implicit none
integer ngridx,ngridy
double precision A(ngridx,ngridy),laplacian(ngridx,ngridy)
double precision dx,dy
integer kx,ky
do kx=2,ngridx-1
do ky=2,ngridy-1
laplacian(kx,ky)=1.d0/(6.d0*dx**2)*(A(kx-1,ky-1)+A(kx-1,ky+1)&
                    +A(kx+1,ky-1)+A(kx+1,ky+1)+&
4.d0*(A(kx,ky-1)+A(kx,ky+1)+A(kx-1,ky)+A(kx+1,ky))&
-20.d0*A(kx,ky))
```

```
end do
end do
do kx=2,ngridx-1
laplacian(kx,1)=1.d0/(6.d0*dx**2)*(A(kx-1,ngridy-1)-A(kx-1,2)-&
                A(kx+1,ngridy-1)+A(kx+1,2)+&
4.d0*(-A(kx,ngridy-1)+A(kx,2)+A(kx-1,1)+A(kx+1,1))-20.d0*A(kx,1))
laplacian(kx,ngridy)=1.d0/(6.d0*dx**2)*(A(kx-1,ngridy-1)-A(kx-1,2)&
                +A(kx+1,ngridy-1)-A(kx+1,2)+&
4.d0*(A(kx,ngridy-1)-A(kx,2)+A(kx-1,ngridy)+A(kx+1,ngridy))&
-20.d0*A(kx,ngridy))
end do
do ky=2,ngridy-1
laplacian(1,ky)=1.d0/(6.d0*dx**2)*(A(ngridx-1,ky-1)&
                +A(ngridx-1,ky+1)+A(2,ky-1)+A(2,ky+1)+&
4.d0*(A(1,ky-1)+A(1,ky+1)+A(ngridx-1,ky)+A(2,ky))&
-20.d0*A(1,ky))
laplacian(ngridx,ky)=1.d0/(6.d0*dx**2)*(A(ngridx-1,ky-1)&
                +A(ngridx-1,ky+1)+A(2,ky-1)+A(2,ky+1)+&
4.d0*(A(ngridx,ky-1)+A(ngridx,ky+1)+A(ngridx-1,ky)+A(2,ky))&
-20.d0*A(ngridx,ky))
end do
laplacian(1,1)=0.d0
laplacian(ngridx,1)=0.d0
```

```
laplacian(ngridx,ngridy)=0.d0

laplacian(1,ngridy)=0.d0

return

end


integer ngridx,ngridy !number of nodes in x,y direction

! Coarse

!     parameter(ngridx=2049)

!     parameter(ngridy=129)

!Medium

!    parameter(ngridx=4097)

!    parameter(ngridy=257)

!Fine

parameter(ngridx=8193)

parameter(ngridy=513)

!Finest

!     parameter(ngridx=16385)

!     parameter(ngridy=1025)

character(len=6)::gridtype

parameter(gridtype='fine')

double precision tol  !tolerance for relative error inside loop

integer maxiter,printiter  !maximum number of iterations

parameter(tol=1.d-16)
```

```
parameter(maxiter= 3)
parameter(printiter= 200)
double precision scal
!  parameter(scal=77.d0*dsqrt(77.d0))
parameter(scal=1.d0)
double precision scalvel
!  parameter(scalvel=dsqrt(77.d0))
parameter(scalvel=1.d0)
integer nfit     !number of points in s table
parameter(nfit=1000000)
!*******************************************************
! Parameters depending on the density profile
!*******************************************************
!!!!!!!!!! For the profile rho=rho1+rhodiff/2(1+tanh(lambda(y0-y)))
double precision rho1,rho2,rhodiff,y0,lambda
parameter(rho1 = 0.999d0)    !asymptotic value first layer
parameter(rho2 = 1.022d0)    !asymptotic value second layer
parameter(rhodiff = rho2- rho1)
parameter(y0=62.0d0/77.d0)    !position of the pycnoclyne
parameter(lambda=80.d0)!thickness of the pycnoclyne
!*******************************************************
! Parameters that control the convergence
!*******************************************************
```

```
double precision alpha,beta
parameter(alpha =200.0d0)
parameter( beta = 0.001d0)
!*******************************************************
! Amp is the objective functional - the potential energy of the wave
!*******************************************************
double precision Amp
parameter( Amp=3.2d-3)
!*******************************************************
! a,b,c,d - domain frontiers
! dx - step in x direction
! dy - step in y direction
! hdom - height of the domain
!*******************************************************
double precision a,b,c,d,dx,dy
parameter(a=-8.d0)
parameter(   b=8.d0)
parameter(   c=0.d0)
parameter(   d=1.d0)
parameter (dx=(b-a)/dble(ngridx-1))
parameter (dy=(d-c)/dble(ngridy-1))
! read the ngridy per line input files - old or ngridx -new
character(len=3)::input
```

```
parameter(input='new')

! the input eta file name

character(len=30)::inputeta

parameter(inputeta='eta.fine')
```

Code for generating the inversion table

```
PROGRAM TABLE

!*******************************************************

C  nfit - size of table

C  all double precision variables

!*******************************************************

implicit none

integer nfit

parameter (nfit= 1000000)

integer i,j,k,key

double precision rho1,rho2,rhodiff,rhomid

double precision  lambda, y0

double precision yy(nfit+2),ss(nfit+2)

double precision  ymin,ymax,smin,smax

double precision yl,yr,sl,sr,yp,sp

double precision  ytemp(nfit+2),stemp(nfit+2)

double precision  hy,hs,prho(nfit+2)

double precision s1,s2,s3,y1,y2,y3
```

```
double precision temp
double precision  ps,pr,ymid
double precision  templ,tempm,tempr
double precision  temp2l,temp2m,temp2r
!*******************************************************
C  rho1  density of top layer
C  rho2  density of lower layer
C  y0  height of  center of interface
C  lambda  density profile parameter
C  determining thickness
C ymin¡y0 ¡ymax
!*******************************************************
rho1 = 0.999d0
rho2 = 1.022d0
rhomid = 0.5d0 * (rho1 + rho2)
rhodiff = rho2 - rho1
y0 = 62.d0/77.d0
lambda =20.0d0
!*******************************************************
C Creating y, s gridding C
!*******************************************************
ymin=0.d0
ymax=2.d0
```

```
hy=(ymax-ymin)/dble(nfit)
ytemp(1)= ymin
do i=2,nfit+1
ytemp(i)= ytemp(i-1) + hy
end do
!*******************************************************
C     compute the integral from ymin to y
C     evaluate integral from ymin to y0
C     s = integralyminˆy - integralyminˆy0
C     use Simpson rule order 3
!*******************************************************
ss(1)=0.d0
prho(1)=0.d0
ps=0.d0
pr=0.d0
do i=2,nfit+1
ymid=0.5d0*(ytemp(i-1)+ytemp(i))
temp2l= rho1+ 0.5d0 * rhodiff *
  1(1.d0 + dtanh(lambda*(y0-ytemp(i-1))))
templ = dsqrt(temp2l)
temp2m= rho1+ 0.5d0 * rhodiff *
  1(1.d0 + dtanh(lambda*(y0-ymid)))
tempm = dsqrt(temp2m)
```

```
temp2r= rho1+ 0.5d0 * rhodiff *
  1(1.d0 + dtanh(lambda*(y0-ytemp(i))))
tempr = dsqrt(temp2r)
ps  = ps  +  (templ+4.d0*tempm+tempr)
pr = pr +  (temp2l+4.d0*temp2m+temp2r)
ss(i) = ps
prho(i) = pr
end do
C Evaluate the s integral from ymin to y0
key=int((y0-ymin)/hy)
ymid=5.d-1*(ytemp(key+1)+y0)
temp2l= rho1+ 0.5d0 * rhodiff *
  1(1.d0 + dtanh(lambda*(y0-ytemp(key+1))))
templ = dsqrt(temp2l)
temp2m= rho1+ 0.5d0 * rhodiff *
  1(1.d0 + dtanh(lambda*(y0-ymid)))
tempm = dsqrt(temp2m)
temp2r= rhomid
tempr = dsqrt(temp2m)
temp=(y0-ytemp(key+1))/hy
ps  = templ+4.d0*tempm+tempr
ps=temp*ps+ss(key+1)
do i=1,nfit+1
```

```
ss(i) = hy/6.d0*(ss(i)-ps)

prho(i)=hy/6.d0*prho(i)

end do

!*******************************************************

C  Regridding values in s-direction

C  New evenly spaced s values are stored in stemp.

C  inversion based on points in stemp are stored in yy

C  Quadratic interpolation

!*******************************************************

smin=ss(1)

smax=ss(nfit+1)

hs=(smax-smin)/dble(nfit)

stemp(1)= smin

do i=2,nfit+1

stemp(i)= stemp(i-1) + hs

end do

yy(1)=ymin

yy(nfit+1)=ymax

key = 1

do j=2,nfit

sp=stemp(j)

do i=key,nfit+1

if (ss(i).lt.sp) then
```

```
key=i
else
goto 351
endif
end do
351    continue
C quadratic interpolation
s1=ss(key-1)
s2=ss(key)
s3=ss(key+1)
y1=ytemp(key-1)
y2=y1+hy
y3=y2+hy
temp=y1*(sp-s2)*(sp-s3)/((s1-s2)*(s1-s3))
temp=temp+y2*(sp-s1)*(sp-s3)/((s2-s1)*(s2-s3))
temp=temp+y3*(sp-s1)*(sp-s2)/((s3-s1)*(s3-s2))
yy(j)= temp
end do
open(91, FILE = 'ytempss.dat', STATUS = 'Unknown')
open(92, FILE = 'yystemp.dat', STATUS = 'Unknown')
open(93, FILE = 'prho.dat', STATUS = 'Unknown')
do i=1,nfit+2
write(91,1001) ytemp(i),ss(i)
```

```
write(92,1001) yy(i),stemp(i)

write(93,1002) prho(i)

end do

1001  format(d20.16,1x,d20.16)

1002  format(d20.16)

close(91)

close(92)

close(93)

STOP

END
```

APPENDIX D: Approximation for Richardson number based on the strongly nonlinear model

In the current Appendix, we deduce a simple approximation for the Richardson number along the profile of a solitary wave in a continuous stratification with thin pycnocline, using the predictions of the strongly nonlinear model Choi & Camassa [7]. We assume that the pycnocline thickness d is constant along the wave profile.

In the following discussion, we fix the location $X = x - ct$ along the wave profile. Richardson number is defined as

$$Ri(z) = \frac{\beta(z) g}{u'(z)^2}\,, \tag{D.1}$$

where $\beta(z) = -\rho'(z)/\rho(z)$. First we approximate the derivative of the horizontal velocity u and of the density ρ by $u'(z) \approx \dfrac{\Delta u}{d}$ and $\rho'(z) \approx -\dfrac{\Delta \rho}{d}$, respectively, where Δu is the jump in velocity across the interface, $\Delta\rho = \rho_2 - \rho_1$, the difference between the densities of the two layers and d the thickness of the pycnocline. We also approximate the density inside the pycnocline by the average value ρ_{med}. We thus have

$$Ri \approx \frac{g d \Delta\rho}{\rho_{med} (\Delta u)^2}\,. \tag{D.2}$$

The asymptotic relation for the horizontal velocity at the interface is

$$u_k|_{z=\zeta} = c\left[1 - \frac{h_k}{\eta_k}\left(1 + \frac{\eta_{kXX}\eta_k^2}{3} - \frac{2h_k(\eta_{kX})^2}{3}\right)\right],\ k = 1, 2\,, \tag{D.3}$$

where ζ is the interface displacement, η_k are the widths of the two layers layers (see §2.2, Figure 2.1 for notations) and c is the phase speed of the wave. The velocity jump at the interface is therefore

$$\Delta u = u_2 - u_1 = c\left[\frac{h_1}{\eta_1}\left(1 - \frac{\zeta_{XX}\eta_1^2}{3} - \frac{2h_1\zeta_X^2}{3}\right) - \frac{h_2}{\eta_2}\left(1 + \frac{\zeta_{XX}\eta_2^2}{3} - \frac{2h_2\zeta_X^2}{3}\right)\right]. \tag{D.4}$$

ζ_X can be expressed in terms of interfacial displacement and the speed c by using the quadrature formula for the interface ζ (Choi & Camassa [7])

$$\zeta_X^2 = \frac{3\zeta^2}{c^2}\frac{c^2\rho_1\eta_2 + c^2\rho_2\eta_1 - g(\rho_2 - \rho_1)\eta_1\eta_2}{\rho_1 h_1^2\eta_2 + \rho_1 h_2^2\eta_1} = F(\zeta)\,, \tag{D.5}$$

from where we obtain

$$\zeta_{XX} = \frac{1}{2}\frac{\partial F(\zeta)}{\partial \zeta}\,. \tag{D.6}$$

By replacing (D.5) and (D.6) in (D.4) we can express the velocity jump across the interface (D.4) solely in terms of the displacement of the interface and thus obtain the Richardson number at any X location of the wave profile only in terms of the interfacial displacement

$$Ri(X) = \frac{gd\Delta\rho}{\rho_{med}\Delta u(\zeta(X))^2}\,. \tag{D.7}$$

By neglecting $O(\epsilon^2)$ correction terms in the formula for horizontal velocity (D.3) (where $\epsilon = H/L$, the long wave parameter), the velocity jump at the interface Δu can be written

as

$$\Delta U(\zeta) = c\left(\frac{h_1}{\eta_1} - \frac{h_2}{\eta_2}\right),$$

and thus

$$Ri(X) = \frac{gd\Delta\rho}{\rho_{med}}\left[\frac{(h_1 - \zeta(X))(h_2 + \zeta(X))}{cH\zeta(X)}\right]^2. \tag{D.8}$$

This approximation is legitimate because we already have neglected the variation of the width of the pycnocline along the wave profile, which induces a more significant error.

Finally, the minimum Richardson number along the wave profile is located at the maximum displacement of the pycnocline ($\zeta = a$), where the velocity jump is maximum. By substituting the phase speed of the solitary wave in terms of the wave amplitude a (Choi & Camassa [7])

$$\frac{c^2}{c_0^2} = \frac{(h_1 - a)(h_2 + a)}{h_1 h_2 - (c_0^2/g)a},$$

with c_0 being the critical speed, we obtain the Richardson at the maximum displacement of the pycnocline in terms of the amplitude of the wave

$$Ri_{min}(a) = \frac{g\ d\Delta\rho}{\rho_{med}H^2c_0^2}\left[h_1h_2 - (c_0^2/g)a\right](h_1 - a)(h_2 + a). \tag{D.9}$$

BIBLIOGRAPHY

[1] Almgren, A.S., Bell, J.B., Colella, P., Howell, L.H., Welcome, M.L. 1998 A conservative adaptive projection method for the variable density incompressible Navier-Stokes equations. *Journal of Computational Physics*, **142**, 1–46.

[2] Benjamin, T.B. 1971 The stability of solitary waves. *Royal Society of London Proceedings Series A* **328**, 153–182.

[3] Benjamin, T.B. 1995 Verification of the Benjamin-Lighthill conjecture about steady water waves. *Journal of Fluid Mechanics* **295**, 337–356.

[4] Benjamin, T.B. & Lighthill, M.J. 1954 On Cnoidal Waves and Bores. *Royal Society of London Proceedings Series A* **224**, 448–460.

[5] Bona, J.L., Lannes, D. & Saut, J.-C. 2008 Asymptotic models for internal waves *J. Math. Pures Appl.* **89**, 536–566.

[6] Choi, W. & Camassa, R. 1996 Weakly nonlinear internal waves in a two-fluid system. *J. Fluid Mech.* **313**, 83–103.

[7] Choi, W. & Camassa, R. 1999 Fully nonlinear internal waves in a two-fluid system. *Journal of Fluid Mechanics* **396**, 1–36.

[8] Camassa, R., Choi, W., Michallet, H., Rusås, P.-O. & Sveen, J.K. 2006 On the realm of validity of strongly nonlinear asymptotic approximations for internal waves. *Journal of Fluid Mechanics* **549**, 1–23.

[9] Dias, F. & Vanden-Broeck, J.-M. 2003 On internal fronts. *Journal of Fluid Mechanics* **479**, 145–156.

[10] Drazin, R.J. & Howard,L.N. 1996 Hydrodynamic stability of parallel flow of inviscid fluid. *Advances of Applied Mechanics* **9**, 1–89.

[11] Drociuk, R.J. 2004 On the closed form solution for the geodesics in sds space.*ArXiv General Relativity and Quantum Cosmology e-prints*, arXiv:gr-qc/0402093

[12] Duda, T.F., Lynch, J.F., Irish, J.D., Beardsley, R.C., Ramp, S.R., Chiu, C.-S., Tang, T.Y. & Yang, Y.J. 2004 Internal tide and nonlinear internal wave behavior at the continental slope in the northern South China Sea. *IEEE Journal of Ocean Engineering* **29**, 1105–1130.

[13] Fructus, D. Carr,M. Grue,J. Jensen,A.& Davies, P. 2008 Shear-induced breaking of large internal solitary waves. *Journal of Fluid Mechanics* **000**, 1–29.

[14] Fructus, D. & Grue, J. 2004 Fully nonlinear solitary waves in a layered stratified fluid. *Journal of Fluid Mechanics* **505**, 323–347.

[15] Funakoshi, M. & Oikawa, M. 1986 Long internal waves of large amplitude in a two layer fluid. *Journal of the Physical Society of Japan* **55**, 128-144.

[16] Gavrilov, N.V. 1994 Internal solitary waves and smooth bores which are stationary in a laboratory coordinate system. *Journal of Applied Mechanics and Technical Physics.* **35**, 29–33.

[17] Goldstein, S. 1931 On the stability of superposed streams of fluids of different densities. *Proceedings of the Royal Society of London, Series A* **132**, 524–548.

[18] Green, A.E. & Naghdi, P.M. 1976 A derivation of equations for wave propagation in water of variable depth. *Journal of Fluid Mechanics* **78**, 237–246.

[19] Grue, J., Jensen, A., Rusås, P.-O. & Sveen, J.K. 1999 Properties of large-amplitude internal waves. *Journal of Fluid Mechanics* **380**, 257–278.

[20] Hazel, P. 1972 Numerical studies of the stability of stratified shear flows. *Annual Review of Fluid Mechanics* **38**, 395–425.

[21] Helfrich, K. & Melville, K. 2006 Long nonlinear internal waves. *Annual Review of Fluid Mechanics* **38**, 395–425.

[22] Holyer, J.Y. 1979 Large amplitude progressive interfacial waves. *Journal of Fluid Mechanics* **93**, 433–448.

[23] Howard, L.N 1961Note on a paper of John W. Miles. *Journal of Fluid Mechanics*, **10**, 509–512.

[24] Huerre, P. & Monkewitz, P. 1985 Absolute and convective instabilities in free shear layers. *Journal of Fluid Mechanics* **159**, 151–168.

[25] Huerre, P. & Monkewitz, P. 1990 Local and global instabilities in spatially developing flows. *Annual Review of Fluid Mechanics* **22**, 473–537.

[26] Huerre, P. 2007 Open shear flow instabilities.*Perspectives in Fluid Dynamics: a collective introduction to current research*, 6th edn. Cambridge, England, Cambridge University Press, 159–229.

[27] Kelvin, W. 1871 The influence of wind on waves in water supposed frictionless. *Phil. Magn.* **42**, 368–274.

[28] Klopman, G. 1990 A note on integral properties of periodic gravity waves in the case of a non-zero mean Eulerian velocity. *Journal of Fluid Mechanics* **211**, 609–615.

[29] Koop, C.G. & Butler, G. 1981 An inverstigation of internal solitary waves in a two-fluid system. *Journal of Fluid Mechanics* **112**, 225–251.

[30] K.-K. Tung, T.F. Chan, and T. Kubota. 1984 Large amplitude internal waves of permanent form *Studies in Applied Mathematics* **66**.

[31] Lamb, K.G. & Wan, B. 1998 Conjugate flows and flat solitary waves for a continuously stratified fluid.*Physics of Fluids* **10**, 2061–2079.

[32] Lamb, K.G. 2002 A numerical investigation of solitary internal waves with trapped cores formed via shoaling.*Journal of Fluid Mechanics.* **451**, 109–144.

[33] Lamb, H. 1932 *Hydrodynamics*, 6th edn. Cambridge, England, Cambridge University Press.

[34] Longuet-Higgins, M.S. 1975 Integral Properties of Periodic Gravity Waves of Finite Amplitude. *Royal Society of London Proceedings Series A* **342**, 157–174.

[35] Makarenko, N.I.. & Maltseva, Zh.L. 2007 Phase velocity spectrum of internal waves in a weakly-stratied two-layer fluid. *Fluid Dynamics* **2**, 278–294.

[36] Maslowe, S.A.. & Thompson, J.M. 1971 Stability of a stratified free shear layer. *Physics of Fluids* **14**, 453–458.

[37] Meiron, D.I.. & Saffman, P.G. 1983 Overhanging interfacial gravity waves of large amplitude. *Journal of Fluid Mechanics* **129**, 213–218.

[38] Miles, J.W.. 1961 On the stability of heterogeneous shear flows. *Journal of Fluid Mechanics*, **10**, 496–508.

[39] Miyata M. 1985 An internal solitary wave of large amplitude. *La Mer* **23**, 4348.

[40] Miyata M. 1988 Long internal waves of large amplitude.In *Nonlinear Water Waves, IUTAM Symp.*, Tokyo 1987, ed. K Horikawa, H Maruo, pp. 399406. Berlin, Germany, Springer-Verlag.

[41] Miyata, M. 2000 A note on broad narrow solitary waves. *PRC Report 00-01, SOEST* **00-05**, 1–26.

[42] Moum, J.N., Farmer, D.M., Smyth, W.D., Armi, L., Vagle, L. 2003 Structure and generation of turbulence at interfaces strained by internal solitary

waves propagating shoreward over the continental shelf. *Journal of Physical Oceanography* **33**, 2093–112.

[43] Rusås, P-.O. & Grue, J 2002 Solitary waves and conjugate flows in a three-layer fluid. *European Journal of Mechanics, B/Fluids* **21**, 185—206.

[44] Rusås, P.-O. 2001 Stationary waves in a three-layer fluid. PhD thesis. University of Oslo.

[45] Sallerson, A.B. 2006 A numerical study of Kelvin-Helmholtz instability of large amplitude internal waves. M.S thesis. University of North Carolina at Chapel Hill.

[46] Squire, H.B. 1933 On the stability of three-dimensional disturbances of viscous flow between parallel flows. *Proceedings of the Royal Society A.* **142**, 621–628.

[47] Su, C.H. & Gardner, C.S. 1969 Korteweg-de Vries Equation and generalization III: Derivation of the Korteweg-de Vries Equation and Burgers Equation. *Journal of Mathematical Physics* **10**, 536–539.

[48] Taylor, G.I. 1931 Effect of variation in density on the stability of superposed streams of fluid. *Proceedings of the Royal Society of London, Series A* **132**, 499–523.

[49] Thorpe, S.A. 1968 On the shape of progressive internal waves. *Philosophical Transactions of the Royal Society of London, Series A.* **263**, 563–614.

[50] Troy, D. & Koseff, J. R. 2005 The instability and breaking of long internal waves. *Journal of Fluid Mechanics* **543**, 107–136.

[51] Turkington, B. Eydeland, A. Wang S. 1991 A computational method for solitary internal waves in a continuously stratified fluid. *Studies in Applied Mathematics* **85**, 93–127.

[52] Turner, R.E.L. Vanden-Broeck, J.-M. 1985 The limiting configuration of interfacial gravity waves. *Physics of Fluids* **29**, 372–375.

[53] Vlasenko,V. Stashchuk,N. Hutter,K. 2005 *Baroclinic Tides. Theoretical Modeling and Observational Evidence.*, 1st edn. Cambridge, England, Cambridge University Press.

[54] Yih,C.-S. 1959 Gravity waves in a stratified fluid. *Journal of Fluid Mechanics* **8**, 481–508.